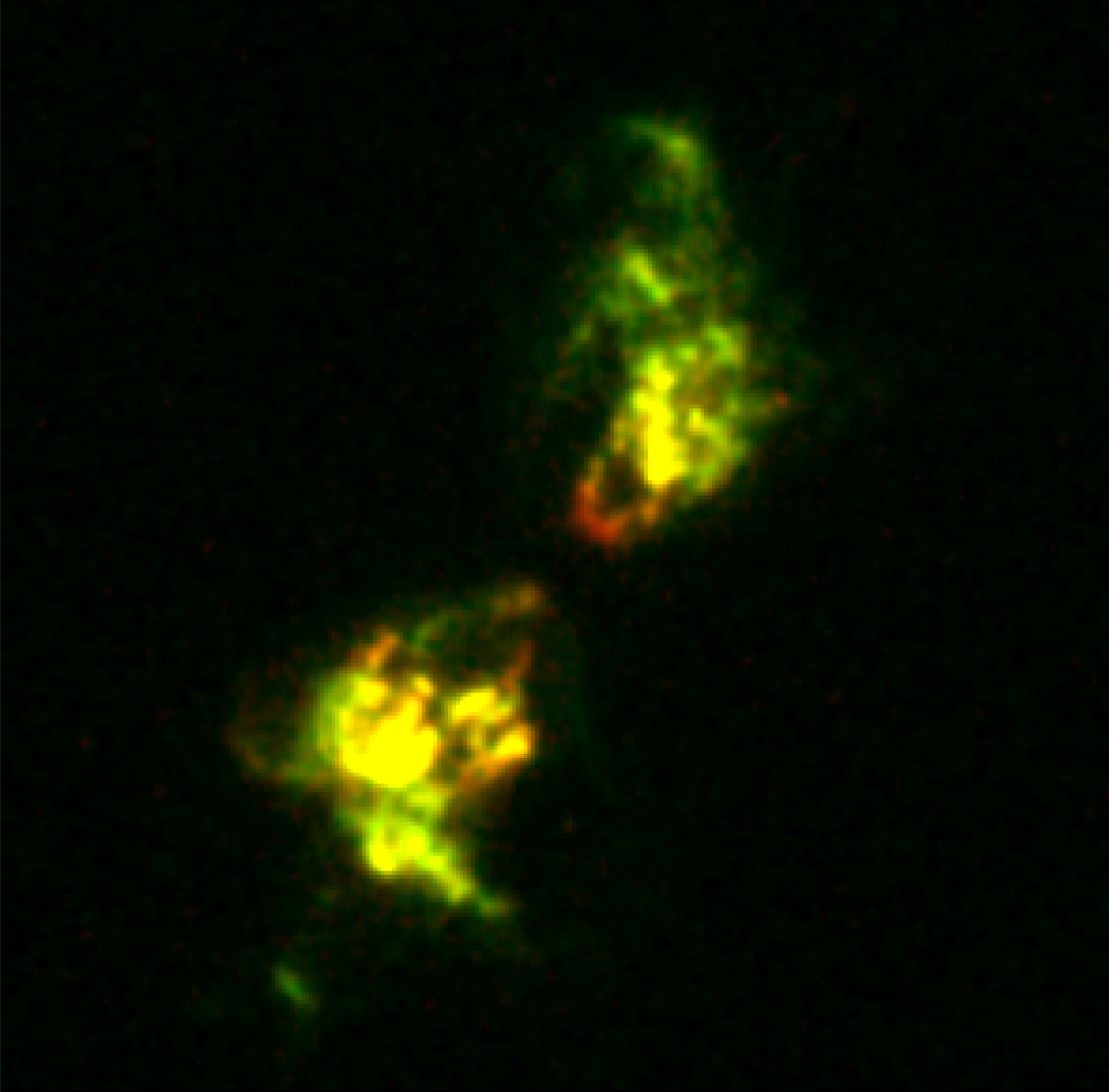

IRAS 22568+6141

filters f814w (red) and f606w (green)

Hubble Space Telescope

UNIVERSIDAD
DE GRANADA

Identification and characterization of nascent planetary nebulae

Roldán Alonso Cala Barón

Supervisors:

Dr. José Francisco Gómez Rivero

Dr. Luis Felipe Miranda Palacios

Thesis submitted for the degree of

Doctor of Philosophy

Programa de Doctorado en Física y Matemáticas

April 2026

Agradecimientos

Recuerdo cuando alcancé edad y me trepé por primera vez al árbol de carambola del patio de la otra casa. Quería alcanzar una fruta cuyo contraste destellaba sobre las demás. Me dejó un sabor agridulce al probarla.

A mi madre y a mi padre, Doris y Josué, a quienes atesoro en deuda por el amanecer, el cuidado y el apoyo en la vida. Porque emprendimos un viaje con Manue y Juan, inesperadamente, por el mundo, pero un jardín con luciérnagas, junto a la hoguera, nos aguarda, adonde reposar y compartir orquídeas del tiempo.

José Francisco, Luis: Gracias por hacer de hacedores de sueños estos años y del doctorado una linda experiencia. Día a día, ardua o sencilla, entre hojarascas de Sakura, cenizas del Sakurajima, fantásticas empedradas o estrellas fugaces en las alturas de los Andes.

Felipe, Omar: Gracias por las conversaciones refrescantes, en especial desde ese verano oscuro en el que relució otra vez nuestra amistad.

Julián, el juego y diálogo acumulado de tantos años de alguna manera me condujeron desde Los Trinitarios hasta Los Cármenes.

To David, Gabor, Kaito, Keisuke, Yosuke, and Imai-san: Thank you for your kindness, hospitality and active memories in Kagoshima.

Agradezco el apoyo y la formación en el grupo Star Planet Formation and Evolution (proyectos PID2020-114461GB-I0, PID2023-146295NB-I00) y en el Instituto de Astrofísica de Andalucía (SEV-2017-0709 y CEX2021-001131-S), financiados por MICIU/AEI/10.13039/501100011033. Agradezco también el apoyo y la formación en la European Southern Observatory y la ayuda predoctoral PRE2018-085518, financiada por MICIU/AEI/10.13039/501100011033 y por el ESF 'Invirtiendo en tu futuro'.

Abstract

The morphology of stars with initial masses ($M_{\rm i}$) $\simeq 0.8-8\,{\rm M}_{\odot}$ (e.g., including the Sun) is roughly spherical during most of their evolution, but during the planetary nebula (PN) phase it tends to show spectacular non-spherical shapes (e.g., butterfly or ring-like morphologies), whose origins are not fully understood. We aim to improve our understanding of the PN formation by identifying and characterizing new nascent PNe and candidates by means of maser and non-thermal radio continuum emission. To achieve this, we consulted maser databases and radio continuum surveys, gathered published and archival optical and infrared imaging and spectroscopy, and complemented these data with our own infrared, optical and radio observations. After our careful multiwavelength analysis, including an assessment of the ionized emission using newly developed diagnostic diagrams to distinguish between shocks and photoionization, we increased the number of maser-emitting PNe and candidates from 10 to 23, and of non-thermal PNe and candidates in the centimeter regime from 1 to 23. The significant increase in the number of confirmed and candidate PNe with maser and/or non-thermal radio continuum emission opens the possibility, for the first time, to carry out robust statistical investigations of the nascent PN phase. In addition, we identified 3 'water fountains' (WFs) and one WF candidate, increasing the number of confirmed WFs from 15 to 18. Notably, we reported the discovery of the first known 'low-velocity' WFs with ionized emission, an emergent group of sources whose study could be relevant to determine the chronology of the onset of ionization in evolved stars. Although maser-emitting PNe and candidates seem to be a heterogeneous group, some of them show oxygen-rich circumstellar envelopes and carbon-rich central stars, an evolutionary channel consistent with a recent thermal pulse and/or common-envelope (CE) evolution. The radio spectral indices (between -1.1 and -0.3) of non-thermal PNe and candidates would imply that intense magnetic fields are active during the PN formation. We report that low-velocity WFs exhibit CO absorption bands characteristic of cool giant stars, while classical, high-velocity WFs show emission lines from shocks around post-AGB stars or photoionization from PNe. This suggests that the difference between low- and high- velocity WFs reflects intrinsically different evolutionary stages. Moreover, the nature of the newly identified source IRAS 18443−0231 is consistent with a nascent PN from a magnetized WF and could thus be one of the youngest PNe known. We also studied in detail illustrative cases of ionized emission dominated by shocks (IRAS 22568+6141) and photoionization (Vy 2-2). In IRAS 22568+6141, we reported on an energetic event that occurred around 1990, and that manifested itself as a sudden and rapid increase in the nebular brightness. A late thermal pulse in the central star provides a simple and consistent explanation for this energetic event and for its subsequent photometric and spectral evolution. In Vy 2-2, our intermediate resolution spectra revealed many new nebular recombination and forbidden emission lines that were crucial in accurately determining the new value of the abundance discrepancy factor (*adf*) of 13.6±2.6, which is unusually

high for PNe. Our analysis of high resolution spectra reveal a high-excitation central region and a pair of low-excitation bipolar lobes. We derived a kinematical age of only $\simeq$210 yr for this nascent PN. Stellar emission lines are also detected, suggesting a *wels* type central star, although they could more probably be related to an irradiated close companion. This possibility is compatible with the unusually high *adf*, the observed nebular structures, and other emission properties which suggest that Vy 2-2 may host a post-CE binary. Chemical abundances and circumstellar mass estimates indicate $M_{\rm i} \lesssim 0.9\,M_{\odot}$ for the star progenitor of Vy 2-2. Therefore, Vy 2-2 would be an illustrative observational case of the CE evolutionary phase. For the future, we have obtained near-infrared spectroscopy of nascent PNe with masers to assess their ionized emission using our previously and newly developed diagnostic diagrams, which constitute a novel methodological contribution and provide a powerful tool for the classification of obscured sources, particularly in the context of upcoming datasets from facilities such as the James Webb Space Telescope. Moreover, we envision that the technical capabilities of wide-field galactic surveys of ionized emission (traced by radio continuum emission and infrared/optical emission lines), in synergy with an artificial intelligence (AI) pipeline, could help to discover a new generation of nascent PNe. In particular, the application of an AI pipeline could provide a robust classification of sources as post-AGB stars or PNe.

Resumen

La morfología de las estrellas con masas iniciales (M_i) $\simeq 0.8 - 8\,\mathrm{M}_\odot$ (p.e., incluyendo el Sol) es aproximadamente esférica durante la mayor parte de su evolución, pero durante la fase de nebulosa planetaria (NP) tiende a mostrar espectaculares formas no esféricas (p.e., tipo mariposa o anulares), cuyas causas aún no se comprenden completamente. El objetivo de esta tesis es mejorar nuestra comprensión de las etapas más tempranas de la formación de NPs mediante la identificación y caracterización de nuevas NPs nacientes y candidatas trazadas por la emisión máser y el continuo de radio no-térmico. Para ello, consultamos bases de datos de máseres y catálogos de continuo de radio, recopilamos imágenes y espectroscopía óptica e infrarroja publicada y de archivo, y complementamos estos datos con nuestras propias observaciones en el infrarrojo, óptico y radio. Tras un cuidadoso análisis multibanda, que incluyó la evaluación de la emisión ionizada mediante diagramas diagnósticos novedosos para distinguir entre excitación por choques y fotoionización, incrementamos el número de NPs emisoras de máser y candidatas de 10 a 23 y el de NPs no-térmicas y candidatas en el régimen centimétrico de 1 a 23. El incremento significativo en el número de NPs confirmadas y candidatas con emisión máser y/o continuo de radio no-térmico abre la posibilidad, por primera vez, de realizar estudios estadísticos robustos de la fase naciente de las NPs. Además, identificamos 3 'Fuentes de Agua' (FA) y una candidata a FA, aumentando el número de FA confirmadas de 15 a 18. Destacamos el descubrimiento de las primeras FA de baja velocidad con emisión ionizada, un grupo emergente de fuentes cuyo estudio podría ser relevante para determinar la cronología del inicio de la ionización en estrellas evolucionadas. Aunque las NPs emisoras de máser y candidatas parecen constituir un grupo heterogéneo, algunas presentan envolturas circunestelares ricas en oxígeno y estrellas centrales ricas en carbono, un canal evolutivo compatible con un pulso térmico reciente y/o evolución en envoltura común (EC). Los índices espectrales de radio (entre -1.1 y -0.3) de las NPs no-térmicas y candidatas implicarían que campos magnéticos intensos están activos durante la formación de las NPs. Reportamos que las FA de baja velocidad exhiben bandas de absorción de CO características de estrellas gigantes frías, mientras que las FA clásicas de alta velocidad presentan líneas de emisión producidas por choques en torno a estrellas post-AGB o fotoionización en NPs. Esto sugiere que la diferencia entre FA de baja y alta velocidad refleja etapas evolutivas intrínsecamente distintas. Además, la naturaleza de la fuente recientemente identificada IRAS 18443$-$0231 es consistente con una NP naciente procedente de una FA magnetizada y podría ser una de las NPs más jóvenes conocidas. También estudiamos en detalle casos ilustrativos de emisión ionizada dominada por choques (IRAS 22568+6141) y por fotoionización (Vy 2-2). En IRAS 22568+6141, reportamos un evento energético ocurrido alrededor de 1990, que se manifestó como un aumento súbito y rápido del brillo nebular. Un pulso térmico tardío en la estrella central proporciona una explicación simple y coherente para este evento y su posterior evolución fotométrica y espectral. En Vy 2-2, nuestros espectros

de resolución intermedia revelaron numerosas líneas nuevas de recombinación y prohibidas que fueron cruciales para determinar con precisión un nuevo valor del factor de discrepancia de abundancias (*fda*) de 13.6±2.6, inusualmente alto para NPs. Nuestro análisis de espectros de alta resolución revela una región central de alta excitación y un par de lóbulos bipolares de baja excitación. Determinamos una edad cinemática de $\simeq$210 yr para esta NP naciente. También detectamos líneas de emisión estelar que sugieren una estrella central de tipo *wels*, aunque probablemente estén relacionadas con una compañera cercana irradiada. Esta posibilidad es compatible con el valor inusualmente alto del *fda*, las estructuras nebulares observadas y otras propiedades de emisión, lo que sugiere que Vy 2-2 podría albergar un sistema binario post-EC. Las abundancias químicas y estimaciones de masa circunestelar indican $M_{\rm i} \lesssim 0.9\,M_{\odot}$ para la estrella progenitora de Vy 2-2. Por tanto, Vy 2-2 sería un caso observacional ilustrativo de la fase evolutiva de envoltura común. Para el futuro, hemos obtenido espectroscopía en el infrarrojo cercano de NPs nacientes con máseres para evaluar su emisión ionizada utilizando nuestros previamente desarrollados y nuevos diagramas de diagnóstico, que constituyen una contribución metodológica novedosa y proporcionan una herramienta potente para la clasificación de fuentes oscurecidas, particularmente en el contexto de futuros catálogos de instalaciones como el James Webb Space Telescope. Además, prevemos que las capacidades técnicas de los cartografiados galácticos de emisión ionizada (trazada mediante emisión de radio continuo y líneas ópticas/infrarrojas), en sinergia con una pipeline basada en inteligencia artificial (IA), podrían ayudar a descubrir una nueva generación de NPs nacientes. En particular, la aplicación de esta pipeline de IA podría proporcionar una clasificación robusta de fuentes como estrellas post-AGB o NPs.

Contents

List of Figures

List of Tables

Chapter 1

Introduction

Planetary nebulae (PNe) constitute one of the final evolutionary stages of stars with initial masses $\simeq 0.8 - 8\,M_{\odot}$ (e.g., eventually including the Sun). They emerge when the central star becomes hot enough to create and maintain a photoionized region within the circumstellar envelope expelled in previous evolutionary phases. Interestingly, while the morphology of stars is roughly spherical during most of their evolution, PNe show spectacular non-spherical morphologies, including bipolar and multipolar structures, equatorial rings and rotating disks. The reasons for this morphological diversity are not fully understood. It is clear, however, that the roughly spherical symmetry of the circumstellar envelope must break during the evolutionary phases immediately before a PN is created and/or during the PN phase itself. The physical processes taking place at the onset of the PN phase, i.e., when photoionization starts, may hold important clues to understanding the origin of this panoply in the shaping of PNe. This thesis thus focuses on nascent PNe, in which photoionization is just beginning, trying to identify and characterize new candidate objects in an elusive evolutionary stage.

1.1 Stellar evolution until the AGB phase

Stars with low and intermediate masses ($< 8\ M_{\odot}$) expend most of their lives in the main sequence. This phase is characterized by nuclear hydrogen burning, in which hydrogen (H) nuclei are converted into helium (He) nuclei, lasting around 10^{8}–10^{10} yr depending on their initial mass (Vassiliadis & Wood 1993). When the H in the stellar core is exhausted, nuclear burning continues in an H shell surrounding an inert He core, leading to expansion of the outer stellar layers and the formation of a red giant. During the red giant branch (RGB) phase, the stellar radius increases significantly (by factors of tens to hundreds), while the effective temperature ($T_{\rm eff}$) decreases, causing the star to move toward the upper right region of the Hertzsprung-Russell diagram (HRD; Fig. 1.1). The RGB phase ends with the first He flash, which occurs when the core reaches the temperature required for the ignition of He fusion, marking the transition from the RGB onto the horizontal branch (HB). The subsequent He

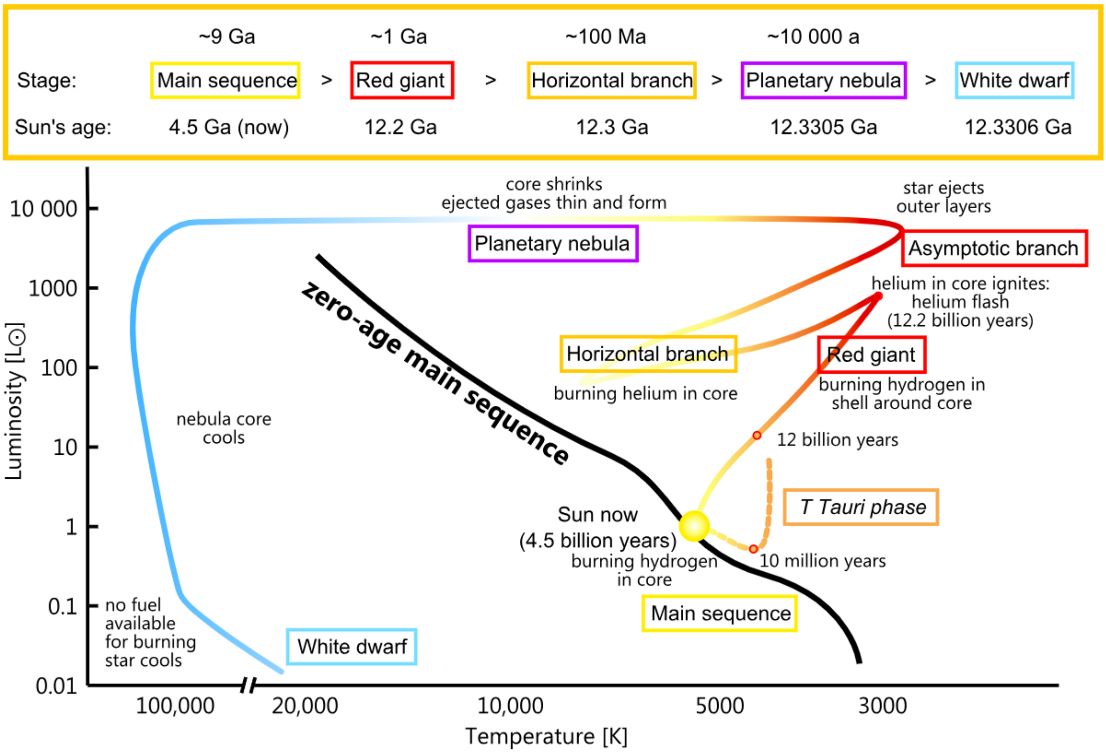

FIGURE 1.1: Possible evolutionary track of the Sun across the Hertzsprung-Russell diagram. Credit: Wikimedia Commons

burning phases, lasting around 10^7–10^9 years (depending also on the initial mass of the star, Vassiliadis & Wood 1993), governs the evolution through the horizontal branch (HB) and later ascent to the Asymptotic Giant Branch (AGB).

1.2 From AGB stars to white dwarfs

When the main nuclear burning cycles of H and He in the stellar core are completed, stars with initial masses (M_i) up to $8\,\mathrm{M}_\odot$ enter the AGB phase. During this phase, the evolved star is mainly composed of an electron-degenerate nucleus with significant amounts of C and O, which is surrounded by a He-rich intershell layer and a burning layer rich in H (Miller Bertolami 2016). This AGB phase is thus mainly characterized by nuclear reactions within layers, rather than at the stellar nucleus. The fusion of H gradually adds mass onto the He-rich intershell material. When the He-rich material reaches a critical mass, a sudden ignition of the He fusion is activated, producing a He-shell flash or thermal pulse.

The energy released in a thermal pulse expands and cools the He-burning layer, while the nuclear reactions proceed again only in the H-burning layer for a while. During this shell interplay, lasting 10^3-10^5 yr, depending on the initial mass of the star (Vassiliadis & Wood 1993; Marigo et al. 2017), each thermal pulse is followed by a short dredge-up event (lasting only $\lesssim 10^2$ yr; Vassiliadis & Wood 1993; Marigo et al. 2017), which transports heavy elements, produced by nucleosynthesis processes, from the core to the outer surface of the star (Marigo et al. 2017). Furthermore, in the extended atmosphere of the star, the enriched material cools down and condenses into molecules and dust grains, which are expelled mainly due to radiation pressure (e.g. Kwok 1975), forming an expanding circumstellar envelope. These processes in the AGB phase channelize the chemical enrichment of the interstellar medium with elements heavier than the primordial H and He.

These nucleosynthesis processes are also responsible for the development of C- and O-rich stars at the AGB phase, depending especially on their initial masses (Marigo et al. 2017). Observations and evolutionary models agree that the progenitors of C-rich stars (surface abundance ratio of C/O>1) are main-sequence stars with initial masses $2.5\,\mathrm{M}_{\odot} \leq M_{\mathrm{i}} \leq 4\,\mathrm{M}_{\odot}$, while those stars with initial masses $M_{\mathrm{i}} \leq 2.5\,\mathrm{M}_{\odot}$ and $M_{\mathrm{i}} \geq 4\,\mathrm{M}_{\odot}$ are expected to develop O-rich stars (C/O<1) during the AGB phase (Miller Bertolami 2016; Marigo et al. 2017). Interestingly, during this phase, the greater the number of thermal pulses, the more C-rich the star becomes, although in the more massive stars ($M_{\mathrm{i}} \gtrsim 3.5\,\mathrm{M}_{\odot}$) the hot bottom burning converts C into N, preventing the star from becoming C-rich (Miller Bertolami 2016; Marigo et al. 2017).

Mass-loss rates in AGB stars range from 10^{-5} to $10^{-7}\,\mathrm{M}_{\odot}\,\mathrm{yr}^{-1}$ from the beginning to the end of this phase (Vassiliadis & Wood 1993; Decin et al. 2019), and the circumstellar envelope grows at these rates. Defining the exact moment when this phase is terminated has been challenging both in terms of observations and modeling. It is usually assumed to begin when the outer H-burning layer mass decreases to $\sim 10^{-2}$–$10^{-3}\,\mathrm{M}_{\odot}$, and the circumstellar envelope gets detached from the central star (Miller Bertolami 2016). During the post-AGB phase, mass-loss rates drop to 10^{-7}–$10^{-8}\,\mathrm{M}_{\odot}\,\mathrm{yr}^{-1}$ (Miller Bertolami 2016; Sánchez Contreras et al. 2017), while the circumstellar envelope cools and expands. At some point, it usually absorbs the optical radiation from the star and re-emits it at longer wavelengths. The O and C isotopologues lock to form gas molecules of CO and, if the C/O ratio is unbalanced, dust features rich in either O (e.g. water ice or amorphous and crystalline silicates) or C (e.g. polycyclic aromatic hydrocarbons) are formed (Perea-Calderón et al. 2009). The roughly spherical symmetry can be broken and anisotropies can develop during the post-AGB phase (see Section 1.4). Simultaneously, the central star shrinks at constant luminosity, increasing its $\mathrm{T}_{\mathrm{eff}}$ until it reaches $\simeq$25000–30000 K, when a photoionized region is created within the detached circumstellar envelope. At this point, the star enter its PN phase, and the circumstellar envelope becomes a PN (Manchado et al. 1996a).

Central stars of PNe are expected to evolve at almost constant luminosity toward higher $\mathrm{T}_{\mathrm{eff}}$ (see Fig. 1.1) until the cooling white dwarf phase (Vassiliadis & Wood 1994; Blöcker 1995; Miller Bertolami 2016). However, thermal pulses can reoccur unexpectedly when the central star is in the post-AGB and PN phases (e.g., Iben et al. 1983). These thermal pulses cause expansion and cooling of the central stars, before restarting their evolution along the horizontal and PN tracks in the HRD, in what is called 'born-again' phenomenon (see

Montoro-Molina 2024). These thermal pulses are called late (LTP) if they occur at the post-AGB or PN phases, or very late (VLTP) if they occur in the cooling track toward the white dwarf phase. The LTP and VLTP are exotic events, the subject of numerous theoretical studies both as a general phenomenon (Iben et al. 1983; Blöcker 2001; Lawlor & MacDonald 2003; Lawlor 2023) and as a test for individual cases (e.g. Hajduk et al. 2005; Lawlor 2021). These thermal pulses provide a special opportunity to track the evolution of the central stars in timescales of years and decades, instead of the usual centuries and millennia. However, to date only few VLTP (e.g., Duerbeck & Benetti 1996; Clayton & De Marco 1997; Gonzalez et al. 1998; Guerrero et al. 2018, and references therein) and LTP (e.g., Reindl et al. 2017; Toalá et al. 2019) have been identified.

1.3 Observational properties of PNe

1.3.1 Emission properties

The main source of the radiation processes observed in PNe is the presence of a photoionized region in its circumstellar envelope. The central stars of PNe usually have $T_{\rm eff} \simeq 30000 - 200000\,$K, and in this regime they produce enough ultraviolet photons above the ionization potential of H ($h\nu \geq 13.6\,$eV) to maintain a photoionized region when the rates of ionizations and recombinations are balanced. Essentially, an ionizing photon absorbed by a H atom liberates an electron with kinetic energy equal to the excess photon energy. These free electrons are the primary agents of heating of the photoionized regions and through electrostatic (Coulomb) interactions they share their kinetic energy with the photoionized regions. If the flux of ionizing photons is sufficiently high compared with the total H column density, the size of the photoionized region, which is usually characterized by the Strömgren radius (Strömgren 1939), exceeds the nebular radius and a fraction of the ionizing photons escape into the interstellar medium, rendering the nebula density-bounded. Conversely, if all ionizing photons are absorbed within the nebula, then it is radiation-bounded, since the Strömgren radius is smaller than the nebular radius.

Thermal balance in PNe thus arises from an interplay between heating by free electrons and cooling by radiative processes within the photoionized region. In gas dominated by H, recombination is a fundamental cooling mechanism: when free electrons recombine with ions, they release energy as line emission under conditions that are typically optically thick to Lyman photons but optically thin to most other recombination lines (see Peimbert et al. 2017, and references therein). These discrete transitions produce the recombination lines (e.g., Lyman, Balmer, Paschen, etc.) that are observable from the ultraviolet to the radio regime depending on transition energy and optical depth. The emissivities of recombination line emission depend on the electron energy distribution (usually approximated by a Maxwellian distribution at the electron temperature $T_{\rm e}$), on $T_{\rm e}$ (which sets the collisional excitation and recombination rates), and on the electron density $N_{\rm e}$, although their dependence on

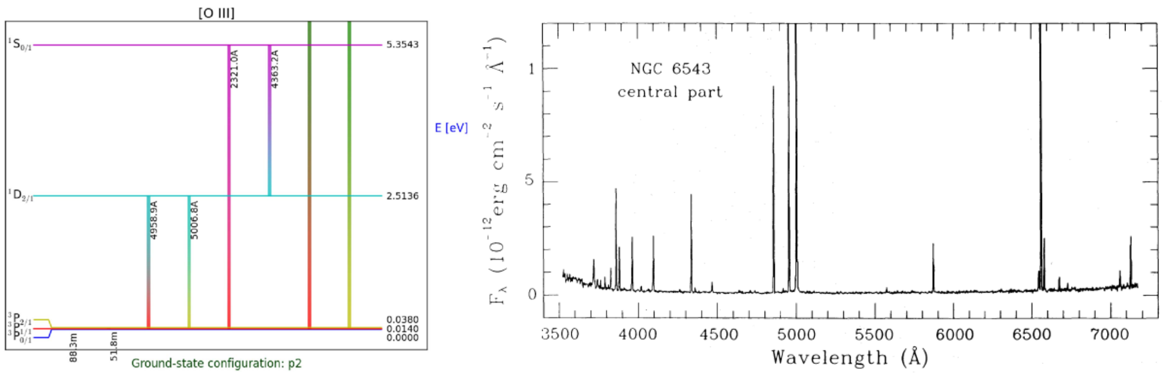

FIGURE 1.2: ***Left.*** Grotian diagram for O^{++} taken from (Peimbert et al. 2017) and created with PyNeb (Luridiana et al. 2015). ***Right.*** Optical spectrum of NGC 6543 in the central region taken from Manchado & Pottasch (1989).

T_e is relatively weak compared to that of collisionally excited lines. In fact, in most PNe, the abundances of heavier elements introduce efficient cooling through collisionally excited (including forbidden) lines from the ultraviolet to the far-infrared. These emission lines are denoted in brackets (e.g., [O III], [N II], [S II]), and are produced when electrons collide with ions, promoting them to metastable states from which they decay radiatively (Osterbrock & Ferland 2006).

These forbidden emission lines play a fundamental role in determining the physical conditions of the ionized gas, particularly the electron density (N_e) and temperature (T_e). Ratios of specific forbidden transitions, such as [O III]λ4363/(λ4959+λ5007) for T_e and [S II]λ6716/λ6731 for N_e, provide robust diagnostics that are largely independent of elemental abundances (see Peimbert et al. 2017, and references therein). This diagnostic is based on the different excitation energies of the levels involved, since the [O III]λ4363 line arises from a much higher-energy level than the [O III]$\lambda\lambda$4959,5007 lines, so their ratio is highly sensitive to the electron temperature T_e. Consequently, hotter nebulae exhibit higher [O III]λ4363/(λ4959+λ5007) ratios (see Fig. 1.2, left). Analogous temperature-sensitive diagnostics based on auroral-to-nebular line ratios are known for other ions, such as [N II], [Ne III], and [S III], while density-sensitive ratios such as the [S III] doublet depend primarily on the balance between radiative decay and collisional de-excitation. Analytical expressions and a comprehensive discussion of these diagnostics are presented in Osterbrock & Ferland (2006, Chapter 5). Accurate measurements of these line intensities therefore constitute a cornerstone of quantitative nebular spectroscopy and are essential for constraining the thermal and density structure of PNe. These physical parameters tend to be in the range of $T_e \simeq 5000 - 20000\,\mathrm{K}$ and $N_e \simeq 500 - 10000\,\mathrm{K}$ (Acker et al. 1992)

Optical emission lines were identified in the spectra of PNe as early as the 19th century. For instance, Fig. 1.2 shows a modern spectrum of the PN NGC 6543 (see also Fig. 1.5), which was one of the first PNe observed spectroscopically. It was included as No. 4373.37 H. IV in the spectroscopic study of (Huggins & Miller 1864a,b), displaying emission lines which coincide with those of H and O. These lines are representative of the recombination lines

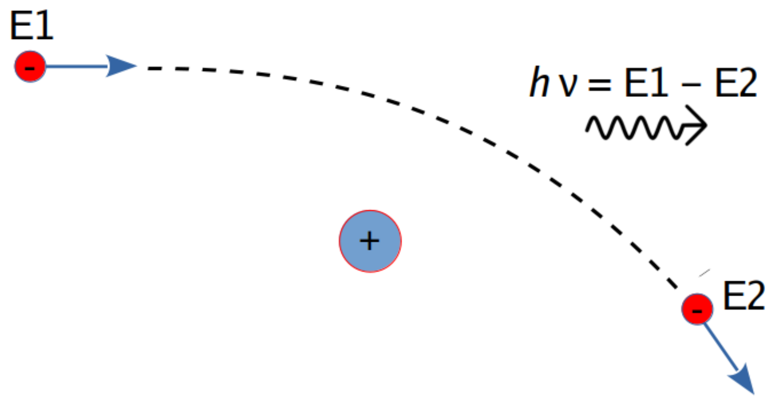

Figure 1.3: Free-free emission by a free electron (red circle) deflected in the electric field of an atomic nucleus (blue circle). E1 and E2 represent the initial and final energy of the electron, and $h\nu$ is the energy of the emitted photon, where h is Planck's constant and ν is the photon frequency.

and collisionally excited, respectively, that characterize the emission from the photoionized regions of PNe. Their spectra are characterized by multiple emission lines on top of a continuum emission.

Apart from the collisionally excited and recombination lines, free-moving particles can also cool the photoionized region significantly through electrostatic interactions. Specifically, when a free electron interacts with a free proton, the electron is deflected, emitting a photon that carries away part of its kinetic energy. Since both particles remain free before and after the interaction, the resulting radiation is called free-free emission, or bremsstrahlung ("braking") radiation due to this deflection (Fig. 1.3). Since these particles do not have quantized energy states, the changes in their kinetic energy do not result in monochromatic emission lines, but instead in a continuum emission. This continuum emission dominates and characterizes PNe at radio frequencies.

The dependence of the flux density (S_ν) of the radio continuum emission with frequency (ν) that characterizes PNe tend to show ranges of spectral indices (α, with $S_\nu \propto \nu^\alpha$) for the thermal (free-free) emission from +2 at low frequencies (optically thick regime) and −0.1 at high frequencies (optically thin regime). The observed radio spectra of PNe usually show two different ranges (Taylor et al. 1987; Aaquist & Kwok 1991; Gruenwald & Aleman 2007). At low frequencies, α ranges from $\simeq +0.6$ to $+2$, corresponding with (partially) optically thick emission, while at higher frequencies the slope flattens to values $\alpha \simeq -0.1$ (see Fig 6.3, left).

The Spectral Energy Distribution (SED) of PNe can be a key diagnostic tool for distinguishing them from other kinds of astronomical sources (e.g., Zhang & Kwok 1991; Ramos-Larios et al. 2009, 2012). The SED represents the flux density emitted by the circumstellar envelope and its central star as a function of wavelength or frequency, and it provides a comprehensive view of the different physical components contributing to their total emission. In the optical and ultraviolet ranges the SED is usually dominated by the stellar continuum

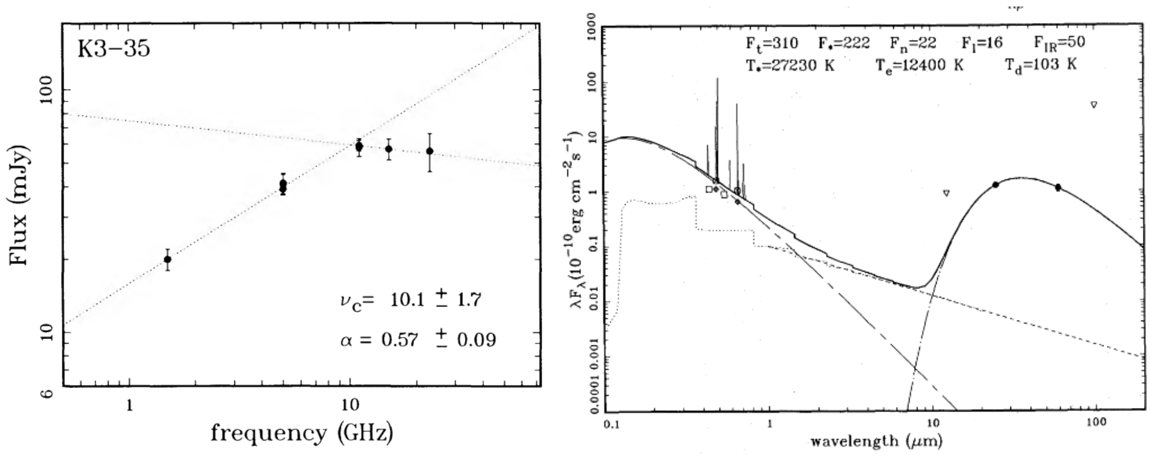

FIGURE 1.4: ***Left.*** Radio continuum spectrum of the nascent PN K3-35 taken from Aaquist & Kwok (1991). ***Right.*** SED of a compact PN taken from Zhang & Kwok (1991).

and winds from the central star and by recombination and collisionally excited lines from the photoionized region. At longer wavelengths, from the near- to mid-infrared, the emission arises mainly from warm dust grains that absorb stellar radiation and re-emit it thermally, while emission features from dust rich in C (e.g., polycyclic aromatic hydrocarbons) or rich in O (e.g., water ice or crystalline silicates) may also be present. In the far-infrared and sub-millimeter regimes, cooler dust and molecular gas dominate the emission, whereas at radio wavelengths, as mentioned before, the continuum is typically produced by thermal (free–free) emission. The combination of these contributions results in a characteristic multi-peaked SED that reflects the evolutionary stage, chemical composition, morphological structures and physical conditions of the PN and its central star (see Fig. 6.3, right).

1.3.2 Morphological properties

Unknown astrophysical objects with visual resemblance to planets, but showing blurred instead of compact appearance, were coined "planetary nebulae" when they were discovered (Messier 1781; Herschel 1791). These sources also displayed spectacular extended and non-spherical shapes, with predominant large-scale elliptical, bipolar and irregular structures of unknown origin. This made PNe astrophysical objects of special scientific interest. With the continuous improvement of the technical capabilities of optical telescopes, including the transition from photographic plates to charge-coupled devices, such morphologies of PNe have been resolved into growing intrinsic complexities (Manchado et al. 1996a). This improvement is also reflected in classification schemes, since early ones usually include the large-scales morphologies mentioned above as their primary designation (Balick 1987; Corradi & Schwarz 1995), while the more modern ones include multipolar shapes and secondary classifications that describe in more detail a possible combination of non-spherical features (Manchado et al. 1996b; Sahai et al. 2007, 2011). In Fig. 1.5 and Fig. 1.6 a few representative morphologies of PNe are shown.

A primary classification as roughly spherical shape is represented in Fig. 1.5 by the PN Abell 39 (top left). There, the top right panels shows color-composite imaging of NGC 6826, NGC 6543 (called "Cat's Eye"), NGC 7009, and NGC 7662 as seen by the Hubble Space Telescope (HST) and the Chandra X-ray observatory. In particular, NGC 6826 and NGC 7662 are representative of elliptical PNe. These PNe are composed of two elliptical shells, and thin or linear high-surface brightness features present in the outer shell. In the case of NGC 6826, such features could represent secondary nebular characteristics such as diametrically opposed ansae or jets. These jets are also observed in NGC 6543 and NGC 7009 (Miranda & Solf 1992; Balick et al. 1998; Gonçalves et al. 2003), although in these two PNe the jets trace a more extended linear to S-shaped region, which is especially noticeable in the latter PN. In the case of NGC 6543 (the Cat's eye), apart from these jets, it is composed of a halo with centrosymmetric arclike features according to the classification scheme of Sahai et al. (2007, 2011). In addition, in that figure the X-ray emission (pink color) is representative of the higher temperatures in the environment closer to the central stars.

Bipolar morphologies are among the most striking structures observed in PNe. A well-known example is NGC 6302 (Fig. 1.5, bottom panels), which is also broadly point-symmetric (Sahai et al. 2007). While its large-scale lobes define its overall morphology in the optical (Fig. 1.5, bottom left), observations at other wavelengths reveal a much higher degree of structural complexity in the central regions (Fig. 1.5, bottom right). The bottom panels therefore emphasize the importance of an integral multiwavelength approach to fully understand the shaping and mass-loss evolutionary history of each individual PNe.

Other impressive examples of the diverse shapes of PNe are shown in Fig. 1.6. They can exhibit non-spherical morphologies with peculiar appearances. For instance, some PNe display multipolar structures with point-symmetric lobes, as shown by Kn 26 (top left panel), which exhibits a quadrupolar morphology. Others present more unusual geometries, such as NGC 1514 (top right panel), whose morphology has been suggested to arise from shaping processes analogous to those operating in supernova remnants (see Soker 2024). In addition, collimated outflows in the form of point-symmetric, S-shaped jets are also observed in PNe, often accompanied by density-enhanced equatorial regions, as illustrated by Fleming 1 (bottom panel).

Surveys including large samples of post-AGB stars (Sahai et al. 2007, e.g.,) have shown predominantly non-spherical nebulae, in contrast with analyses based on smaller samples which reported roughly spherical morphologies (Manchado et al. 2025). Searching for nascent PN would therefore be useful to find precursors of the diverse morphologies seen immediately before and after this elusive evolutionary phase.

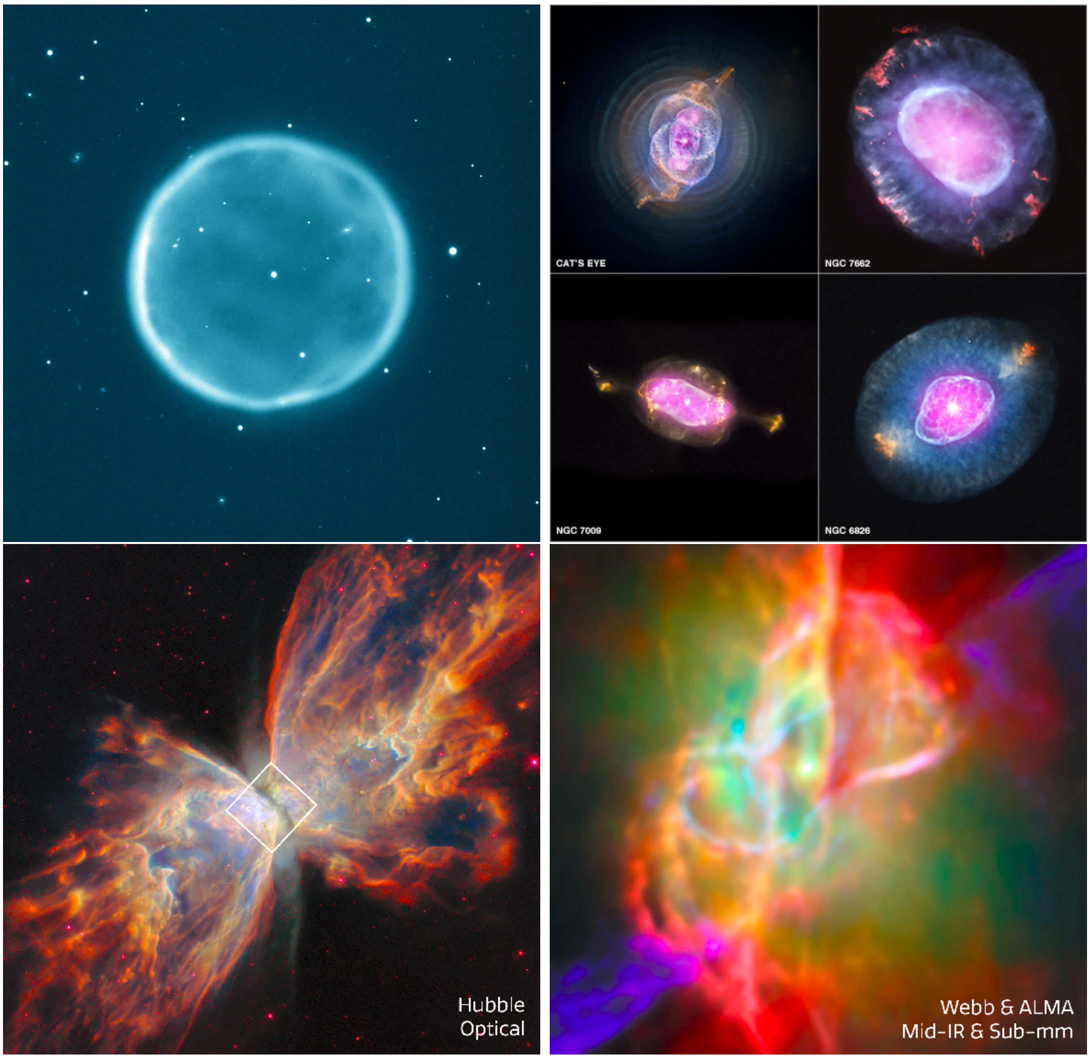

FIGURE 1.5: Morphologies of PNe. **Top left:** Monochromatic image of Abell 39 as seen by [O III] of the WIYN 3.5-meter Telescope. Credit: G. Jacoby, G. Ferland, K. Korista, and WIYN/NOIRLab/NSF. **Top right:** Color-composite imaging of NGC 6543, NGC 7662, NGC 7009, and NGC 6826 combining X-ray and optical data from Chandra Observatory and the HST. X-ray emission in the 0.3–2.0 keV band, shown in pink. Optical data as seen by narrow-band filters F502N (blue), F656N (green), and F658N (red). **Bottom left and right:** Color-composite images of NGC 6302 as seen by the HST (left) and zoom in in the central region (right) as seen by the James Webb and Atacama Large Millimeter/summillimeter Array (ALMA). Credit: ESA/Webb, ALMA (ESO/NAOJ/NRAO) NASA & CSA.

1.3.3 Central stars

Central stars of PNe are characterized by intense ultraviolet radiation and diverse atmospheric chemical compositions and wind properties. In fact, central stars can also be classified into several spectral classes: H-rich objects (e.g. O-type, Of, and hot subdwarfs such as sdO/sdB), H-deficient Wolf–Rayet–like stars denoted [WC] and [WO], PG1159 stars that show C– and He-rich atmospheres, and a population of weak emission-line stars (Acker & Neiner 2003; Weidmann & Gamen 2011). Additionally, some central stars are already at the beginning of the white-dwarf track or present peculiar spectra produced by binary

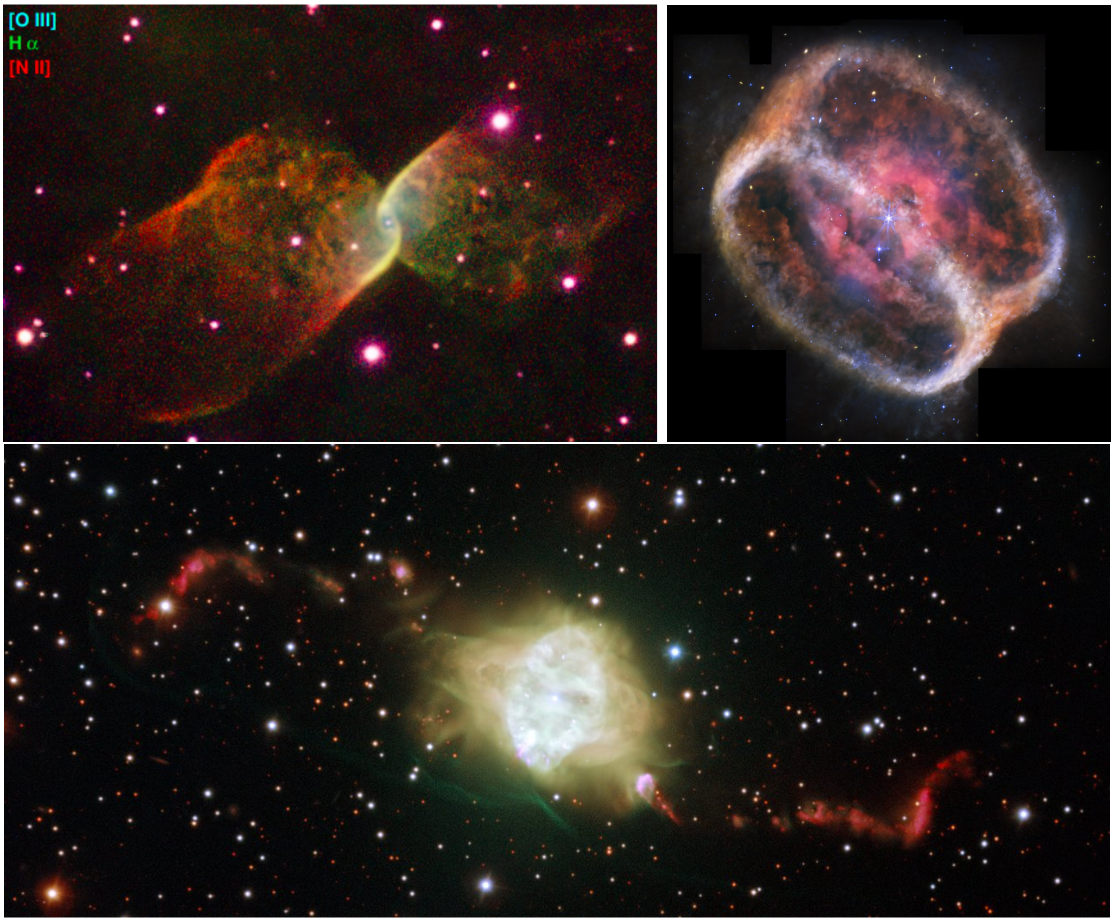

FIGURE 1.6: Morphologies of PNe. Color-composite imaging of **Top left:** Kn 26 as seen by the Nordic Optical Telescope taken from Guerrero et al. (2013). **Top right:** NGC 1514 as seen by the James Webb Space Telescope taken from Ressler et al. (2025). **Bottom:** Fleming 1 as seen by the Very Large Telescope taken from Boffin et al. (2012).

interaction (Weidmann et al. 2020). These spectral types reflect differences in surface abundance chemistry, mass-loss rates and evolutionary history, and the observational evidence indicates that the evolution of binary star systems is essential for understanding both the central star properties and the morphologies of PNe (e.g., Jones & Boffin 2017; Boffin & Jones 2019). High-resolution optical spectroscopy and monitoring photometric observations can further reveal multiple absorption features originating from the photosphere of different stars (Santander-García et al. 2015), or the form of weak emission lines from highly ionized species due to irradiation of a secondary star, which can be easily confused with nebular emission lines in the spectra of PNe when observed at intermediate resolution (e.g., Pollacco & Bell 1993, 1994; Jones & Boffin 2017).

1.4 Formation and shaping of PNe

The discovery of photospheric absorption lines in the spectra of AGB stars showing a Doppler shift with respect to circumstellar emission lines provided fundamental observational evidence that these stars were losing their mass in the form of winds with velocities of $\sim 10\,\mathrm{km\,s^{-1}}$ (Deutsch 1956; Reimers 1977), probably driven by radiation pressure on dust grains (Kwok 1975). Similarly, it was found that central stars of PNe continue to lose mass through winds after the onset of the photoionization phase, producing an emission-line wind driven by radiation pressure on the gas that can reach up velocities of $10^4\,\mathrm{km\,s^{-1}}$ (Osterbrock 1964; Guerrero & De Marco 2013).

Since winds expelled during the PN phase propagate about one or two orders of magnitude faster than those of the previous AGB phase, it is reasonable to assume that these winds will interact significantly, which led to the Interacting Stellar Winds (ISW) model to explain the shaping of PNe (Kwok et al. 1978). In this model, the fast, emission-line wind from the ionizing central star propagates through the slower, expanding circumstellar envelope expelled in the previous evolutionary phases. This interaction produces a bright contact discontinuity, similar to those observed in the PNe shown in Fig. 1.5 (top right), and has successfully explained the roughly spherical and elliptical morphologies seen in some PNe (e.g., Fig. 1.5). Such morphologies are seen in ionized gas in PNe and in molecular gas around AGB stars (e.g., in CO molecules; Olofsson et al. 2000).

However, most observed morphologies of PNe significantly deviate from ideal spherical bubbles (see Section 1.3.2). This means that during the transition from the AGB to the PN phase, other mass-loss modes and wind properties must interplay simultaneously or intermittently, beyond the simple ISW framework. In particular, the presence of density-enhanced equatorial regions around the central stars of bipolar PNe led to the development of the Generalized ISW (GISW) model (Balick et al. 1987; Balick & Frank 2002). In this scenario, the formation of bipolar and butterfly morphologies (e.g., NGC 6302 in Fig. 1.5) were successfully reproduced assuming the presence of a toroidal structure that provided an inertial confinement that collimates the radiation-driven stellar wind (Icke et al. 1989; Mellema & Frank 1995). However, it was unclear how is the toroidal structure developed before the onset of this wind.

In addition to this question, other morphological structures with distinctive kinematical properties were discovered. High-velocity bipolar jets (Carsenty & Solf 1982; Gieseking et al. 1985; Guerrero et al. 2021), with characteristics consistent with low-ionization emission regions (Balick 1987; Balick et al. 1998; Mari et al. 2023a,b), as well as S-shaped, point-symmetric jets accompanied by density-enhanced equatorial regions (e.g., NGC 6543 in Fig. 1.5 and Fleming 1 in Fig. 1.6), were identified. These latter structures are commonly interpreted as the result of precessing, highly collimated outflows (Miranda & Solf 1992; Lopez et al. 1993; Guerrero et al. 2008; Miranda et al. 2024). Such features cannot be easily explained within the framework of the GISW model and therefore motivated the investigation of additional mass-loss mechanisms (Sahai & Trauger 1998). Observations of post-AGB stars with optically bright non-spherical nebulae revealed that the shaping mechanisms of some PNe are already active before the onset of photoionization (Kwok et al. 1996). Moreover, the kinetic energy of high-velocity bipolar molecular outflows in post-AGB stars and young

PNe exceeds what can be provided by radiation pressure alone, implying the presence of an additional energetic source activated during the brief transition between these evolutionary stages (Bujarrabal et al. 2001).

Binary stellar evolution has been identified as a natural channel to develop a density contrast between the equatorial and polar directions and, therefore, as a key shaping mechanism of PNe (Soker & Livio 1989; Soker 1997; Jones & Boffin 2017; Boffin & Jones 2019). During the AGB phase, the interaction between the winds expelled by the giant primary star and a compact companion can temporarily develop a circumstellar disk around the companion, circumbinary disks, or both, from which material can be accreted and expelled along polar directions (Livio et al. 1979; Morris 1981, 1987; Sánchez Contreras et al. 2022). Such accretion–outflow processes would be analogous to those in active galactic nuclei and young stellar objects, and are responsible for shaping some PNe (Soker & Livio 1994; Sánchez Contreras et al. 2022).

The evolution of binary stellar systems sensitively depends on its orbital separation: wide binaries may undergo Bondi–Hoyle accretion (Bondi & Hoyle 1944; Edgar 2004), intermediate separations favor Wind Roche Lobe Overflow (WRLOF) (Podsiadlowski & Mohamed 2007; Mohamed & Podsiadlowski 2007), and close systems undergo Roche Lobe Overflow (RLOF; Paczyński 1971). The latter triggers the Common Envelope (CE) evolutionary phase (Paczynski 1976; Livio & Soker 1988) during which the companion rapidly removes a significant fraction of the circumstellar envelope of the primary star (Nordhaus & Blackman 2006; Ricker & Taam 2012). Interestingly, a common outcome of this phase are density-enhanced equatorial regions (Ivanova et al. 2013). The observed link between binary central stars and bipolar morphologies supports this scenario (Miszalski et al. 2009), and numerical simulations indicate that CE evolution plus radiatively-driven winds can transform spherical circumstellar envelopes into bipolar morphologies (García-Segura et al. 2018; Zou et al. 2020). In any case, binary central stars of PNe have been detected in a wide range of configurations, including close post–CE systems with orbital periods of hours to days, as well as wider binaries with periods of months to years (De Marco 2009; De Marco et al. 2015; Jones & Boffin 2017).

Post-AGB stars with SEDs consistent with Keplerian disks (de Ruyter et al. 2006) further strengthen this picture. Such disks often show rotation and expansion (Bujarrabal et al. 2003, 2013) and are commonly found around binary post-AGB stars with active accretion processes (Oomen et al. 2018, 2019). Hence, accretion and disk-related mechanisms play a significant role in shaping and evolution of some PNe (see Sánchez Contreras et al. 2022).

Magnetic fields have long been proposed as a potential sculpting mechanism of PNe, both in single- and binary-star evolution (Balick & Frank 2002). In the former case, roughly spherical winds expelled during the AGB phase can be modify by significant magnetic pressure and tension generated by stellar dynamos and rotation, leading to bipolar and point-symmetric morphologies in magnetohydrodynamic (MHD) simulations (Garcia-Segura 1997; García-Segura et al. 2005, 2014). In binary systems, these simulations indicate that magnetic fields are amplified through interaction-driven mechanisms, such as accretion disks alone or during the CE evolutionary phase that lead to the launching of magnetically collimated winds (Huarte-Espinosa et al. 2012; García-Segura et al. 2020; Balick et al. 2020; Zou et al. 2020; Ondratschek et al. 2022). Observationally, maser-emitting molecules of high-velocity molecular outflows have been associated with toroidal magnetic fields of the order of milliGauss (Vlemmings et al. 2006). Similarly, the dust grains seems to be organized in the central region by magnetic field lines that are perpendicular to bipolar lobes (Sabin et al. 2007, 2015). This may be also the case for maser-emitting molecules during the nascent PN phase (see Section 1.5.1). On the other hand, it is interesting to note that magnetic fields have been found to be extremely weak or not present at all on the stellar surfaces of post-AGB stars and central stars of PNe (Leone et al. 2014). However, they might have certainly been involved in the shaping of bipolar and multipolar structures in PNe (Hajduk et al. 2025). Therefore, observational studies of magnetic shaping in PNe are only just beginning, and further research is needed to advance this field.

It is therefore imaginable a combination of these shaping mechanisms, including slow and fast stellar winds, magnetic field effects, CE evolutionary phase, active accretion disks, and photoionization (see also Kwok 2010; García-Segura 2010), could together account for the large variety of PNe morphologies. Further variations, such as the influence of thermal pulses, sub-stellar companions (Decin et al. 2020), including planets or brown dwarfs (Soker 1996; De Marco & Soker 2011; Miranda et al. 2024), may also contribute to the panoply of PNe.

1.5 Nascent PNe

This thesis focuses on evolved stars in their first centuries of the photoionization phase (which we call nascent PNe), a very small fraction of the PN lifetime ($\sim 10^4$-10^5 yr depending on M_i; Miller Bertolami 2016; García-Segura et al. 2025). In fact, apart from the incipient ionizing radiation from the central star, the physical conditions of nascent PNe are expected to be similar to those of late post-AGB stars, which complicates their identification.

The increasing number of ionizing photons due to the rapid increase of the $T_{\rm eff}$ of the central star produces a large number of tracers and variable conditions that are trackable over a few decades after the onset of photoionization. First, with the ionization front advancing at supersonic velocities (R-type ionization front, Kahn 1954; Franco et al. 1990), while the rate of ionization is still higher than that of recombination. During this fast advance of the ionization front, the emerging plasma should still briefly maintains the density distribution of the circumstellar envelope expelled in the previous evolutionary phases, with a radial dependence of the electron density of $N_e \propto r^{-2}$. This density structure produces thermal (free-free) radiation with a radio spectral index of around +0.6 (partially optically thick) in most of the centimeter domain (Olnon 1975; Panagia & Felli 1975). Thus, finding an evolved star with a spectral index of that order could be an indication that it is transiting the nascent PN phase (Gómez et al. 2005). However, we note that a shock-ionized wind would have exactly the same spectral index. Therefore, an independent determination of the origin of the ionized gas (whether ultraviolet photons or shocks) is necessary to classify a source as a nascent PN based on its radio spectral index. This could be obtained, for instance, with optical and infrared spectroscopy, or estimating whether the mass-loss rates required to explain the observed flux densities under the assumption of an ionized wind are reasonable (Uscanga et al. 2014). Another expected property of the radio emission during this phase of rapid growth of the ionized region is a monotonically rising flux density, due to the increase of the size of the nascent PN (Tafoya et al. 2009).

When the ionization front reaches the Strömgren radius, ionization and recombination are balanced and the supersonic initial expansion of the PN stops. At this point, the pressure of the hot ionized gas is 2-3 orders of magnitude larger than the colder surrounding envelope, which causes further expansion of the plasma, at nearly sound speed. This tends to homogenize the density structure of the PN, and the radio spectral index departs from +0.6. The radio spectrum is then expected to show a spectral index of +2 at low frequency and -0.1 at high frequency. The turn-over frequency separating optically thin from optically thick emission allows estimating the emission measure (EM) of the ionized gas. This parameter has also been used as an age tracer, with younger PNe having higher EM, and this turn-over frequency would tend to decrease with time (Kwok & Feldman 1981). We note that this is different from the interpretation of a possible turnover frequency during the previous phase of R-type expansion, where the frequency at which the spectral index changes from +0.6 to -0.1 would be related with the size of an inner hole in the ionized nebula with an electron density dependence as r^{-2} (Anglada et al. 2018). Such a turn-over frequency, however, has never been unambiguously determined in any PNe at this early phase.

An optimal search for new nascent PNe and candidates would thus require the identification of short-lived observational aging tracers and the mining of multiepoch archival data complemented with new observations. From the ultraviolet to the radio wavelengths, witnessing the emergence of forbidden and recombination emission lines in evolved stars would tend to identify nascent PNe (e.g., Parthasarathy et al. 1993), although these spectroscopic data are not available to date. On the other hand, while the infrared properties and the molecular content of evolved stars transiting between the late post-AGB and nascent PN phases are expected to be virtually identical, two observational characteristics that can only coexist with the first centuries of the photoionization phase are molecular masers and non-thermal radio continuum emission. Moreover, in the case of the molecular maser emission, the multiple observations over the past years have allowed gathering information on tens of thousands of maser-emitting sources located across the northern and southern sky, which can be consulted in public astronomical databases (Forster & Caswell 1989a; Benson et al. 1990; Engels & Bunzel 2015; Ladeyschikov et al. 2019). Furthermore, in the case of non-thermal radio continuum emission, the updated capabilities of radio interferometers, which can perform wideband (1-8 GHz bandwidth) continuum observations from which intraband spectral indices have been reported over multiple epochs in the last years (Wang et al. 2018;

Medina et al. 2019; Yang et al. 2023), allowing to robustly confirm the presence of variable flux densities and negative spectral indices in evolved stars transiting between the post-AGB and PN phases (Cerrigone et al. 2011, 2017) and the identification of new post-AGB stars and PNe with non-thermal radio continuum emission.

Interestingly, key sculpting mechanisms intimately related with the PN formation and particularly observed during the onset of the photoionization, such as collimated jets traced by molecular masers, non-thermal radio continuum emission, strong shocks, and magnetic-field activity, are also observed in young stellar objects (YSOs) (Carrasco-González et al. 2010; Anglada et al. 2018). This phenomenological convergence highlights a striking analogy between nascent PNe and YSOs, despite representing opposite evolutionary stages (stellar birth versus death). Such similarities suggest that the physical processes governing jet formation and collimation may be universal across different astrophysical environments (see Rodríguez-Kamenetzky et al. 2025). Thus, the study of nascent PNe not only improves our understanding of PN formation, but could potentially offer new invaluable comparative laboratories for jet-launching mechanisms.

An essential assessment in the context of the nascent PN phase is therefore how to distinguish ionized emission from radiative shocks alone, photoionization alone, or a mixture of both. An ideal diagnosis would thus require the modeling of ionized emission produced by different contributions of shocks and photoionization. However, to date, such hybrid models have not yet been developed. Instead, ionized emission has been modeled independently, either due to shocks alone (Allen et al. 2008; Sutherland & Dopita 2017) or photoionization (Ferland et al. 2017). Each of these models reproduce a synthetic spectrum with emission lines of different intensities from the ultraviolet to the radio wavelengths. The intensities of the emission lines of shock models are sensitive to physical parameters such as shock velocity, magnetic fields, or chemical abundances, whereas the intensities of the emission lines in photoionization models are more sensitive to the $T_{\rm eff}$, N_e, or chemical abundances. Furthermore, the entire collection of these synthetic spectra have been stored in the Mexican Million Models Database (Morisset et al. 2015; Alarie & Morisset 2019). Therefore, it is possible to compare all the possible combination of the emission line ratios determined by shock models, together with those from photoionization models, and compare them with those obtained from spectroscopic observations.

1.5.1 Molecular maser emission

Molecular maser emission originating from circumstellar envelopes, rather than from the interstellar or extragalactic medium, is widespread among AGB stars (e.g., Elitzur 1992; Lo 2005). During the AGB phase, SiO, H_2O, and OH maser emission is usually emitted by O-rich stars (e.g., Reid & Moran 1981a; Elitzur 1992). The SiO maser emission tend to show a single spectral peak, whereas H_2O and OH masers often present two peaks of similar intensity but separated in velocity. The SiO maser peak generally lies between the two H_2O maser peaks, which themselves fall within the broader velocity range defined by the OH maser emission. High-angular resolution observations show that these maser species tend to be stratified in the circumstellar envelope, being located at increasing distances from the star: SiO masers within ~10 au (e.g., Diamond et al. 1994), H_2O up to $\sim 10^2$ au, and OH up to $\sim 10^3$ au, tracing the inner and large-scale kinematics of the roughly spherical circumstellar envelope (e.g., Reid & Moran 1981a; Elitzur 1992; Diamond et al. 1994). In particular, the OH maser emission, associated with the approaching and receding sides of the circumstellar envelope, tend to trace terminal expansion velocities in the envelope, ranging from 10-25 km s^{-1} (e.g., te Lintel Hekkert et al. 1991; Goldman et al. 2017). On the other hand, in C-rich AGB stars the molecular maser emission of HCN and SiS molecules instead traces the kinematics beyond the stellar photosphere (e.g., Menten et al. 2018).

Astonishing deviations from this stratified pattern of the circumstellar maser emission drew scientific attention (Likkel & Morris 1988; te Lintel Hekkert et al. 1988). In particular, H_2O maser emission exhibiting multiple components and spanning larger velocities than those of the OH, were discovered in evolved stars such as IRAS 16342−3814, IRAS 19134+2131, and W43A (Likkel et al. 1992). High-angular resolution observations of this H_2O maser emission display small-scale bipolar to S-shape structures and outflowing motions of hundreds of kilometers per second, revealing the activation of at least one distinct, non-spherical mass-loss mechanism (Imai et al. 2002, 2004; Claussen et al. 2009, and see Fig. 1.7). Such emergent group of high-velocity H_2O maser-emitting sources was subsequently coined “water fountains” (WFs). Moreover, since the kinematical ages of WF jets ($\lesssim 10^2$ yr; Day et al. 2010; Yung et al. 2011; Orosz et al. 2019; Tafoya et al. 2020) turned to be similar to the timescales over which H_2O maser emission fades after the AGB phase ($\lesssim 10^2$ yr; Gómez et al. 1990), these sources may represent one of the first manifestation of collimated mass loss during the transition to the PN phase.

To date, fifteen evolved stars have been identified as WFs (Imai 2007; Gómez et al. 2017; Imai et al. 2023). These sources present mass-loss rates of $\sim 10^{-3}$–10^{-4} $M_\odot$ yr^{-1}, which are not consistent with single stellar evolution, but instead with the intense mass-loss rates after the CE evolutionary phase, suggesting that WFs may hold close binary systems (Khouri et al. 2021). Among them, “Classical” WFs display velocity ranges of up to several hundred km s^{-1}, while others show narrower H_2O maser spectra ($\lesssim 50$ km s^{-1}) and were coined “low-velocity” WFs (Boboltz & Marvel 2007; Yung et al. 2013). The spectral properties of WFs seems to be consistent with those of the post-AGB phase (Gledhill & Forde 2012; Pérez-Sánchez et al. 2017; Yung et al. 2017), although the emission properties of one WF (W43A) are more compatible with those of the AGB phase (Imai et al. 2005) and another one (IRAS 15103−5754) has ionized emission compatible with a PN (Gómez et al. 2015b). In fact, the evolutionary stage of a potential new group of WF PNe might correspond with the onset of photoionization (Gómez et al. 2015b). Moreover, such WF PN-evolutionary channel would therefore correspond with an outcome of the CE evolutionary phase (Khouri et al. 2021).

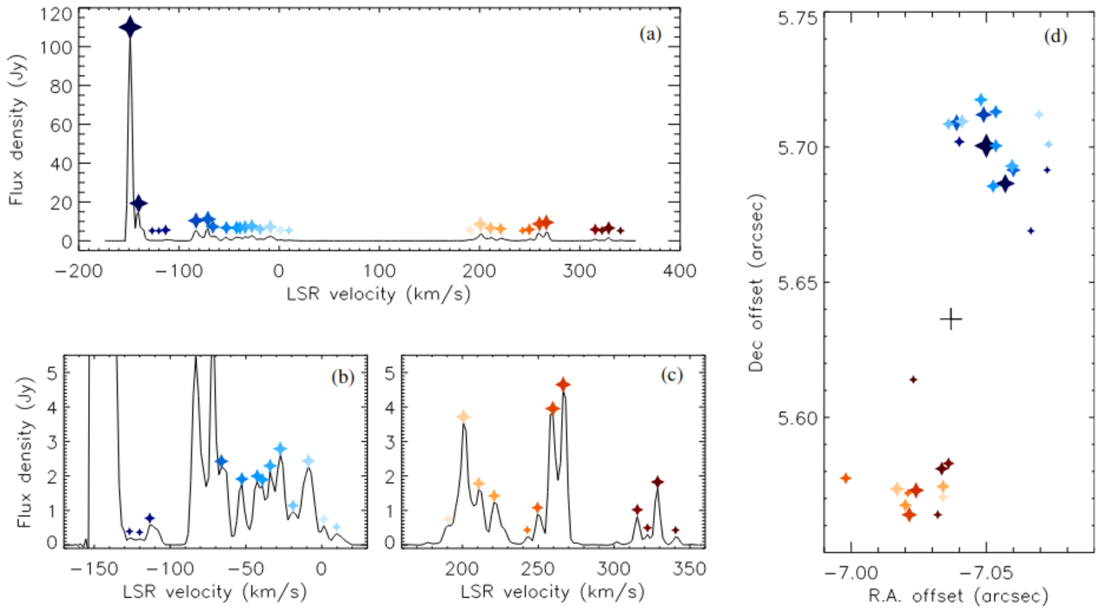

FIGURE 1.7: H_2O maser emission and spatial distribution of the H_2O maser spots in the WF IRAS 18113−2503 (Gómez et al. 2011).

During the post-AGB phase, mass-loss rates decrease up to $10^{-8}\,M_\odot\,yr^{-1}$ (Blöcker 1995; Miller Bertolami 2016), leading to the gradual disappearance of circumstellar masers. Since SiO, H_2O, and OH masers tend to occupy regions within 10, 10^2, and 10^3 au from the stellar surface, they are expected to vanish on timescales of about 10, 10^2, and 10^3 yr, respectively (Lewis 1989; Gómez et al. 1990). Comparing this with the duration of the post-AGB phase (10^3-10^4 yr), only nascent PNe are thus expected to be maser emitters, and the presence of different species could eventually be used as an aging tracer of PNe.

To date, only eight nascent PNe have been identified through their association with OH and H_2O maser emission, and have been coined OHPNe and H_2OPNe, respectively. These PNe are Vy 2-2, OH 0.9+1.3, K 3-35, IRAS 17347−3139, JaSt 23, IRAS 18061−2505, IRAS 15103−5754, and IRAS 16333−3807(Davis et al. 1979; Pottasch et al. 1987; Zijlstra et al. 1989; Miranda et al. 2001; de Gregorio-Monsalvo et al. 2004; Suárez et al. 2007; Tafoya et al. 2007; Gómez et al. 2008; Uscanga et al. 2012, 2014; Gómez et al. 2015b; Qiao et al. 2016a). So far, no SiO maser emission has been identified in a PN (Nyman et al. 1998; Yoon et al. 2014). These nascent PNe tend to show bipolar morphologies, collimated outflows and density-enhanced equatorial regions and have been consequently associated with the CE evolutionary phase (Gómez et al. 2018b; Miranda et al. 2021). These morphological characteristics are illustrated in Fig. 1.8 by the unpublished near-infrared high-angular resolution images of K 3-35 and IRAS 17347−3139.

The first OHPN identified by means of the 1612 MHz OH ground-state transition was Vy 2-2 (Davis et al. 1979; Seaquist & Davis 1983). The OH maser emission exhibited a single blueshifted component, which differs from the double-peak maser profile tracing the receding and approaching sides of the roughly spherical circumstellar envelope has been interpreted as

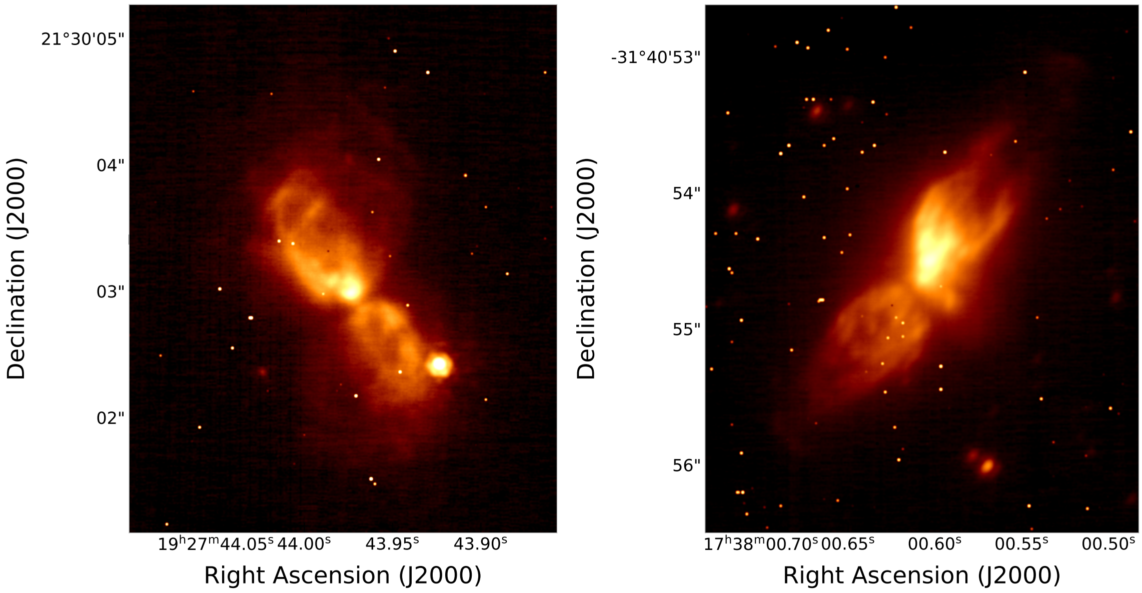

FIGURE 1.8: Narrowband K_s-filter imaging of the OHPNe and H_2OPNe K 3-35 (left) and IRAS 17347−3139 (right) obtained with the adaptive optic system of the Keck II telescope.

the redshifted component being absorbed by an optically thick photoionized region (Seaquist & Davis 1983). Since then, single to irregular 1612 MHz OH maser emission has been found to be common among maser-emitting PNe (Uscanga et al. 2012; Qiao et al. 2016b).

K 3-35 was the first H_2OPN identified (Miranda et al. 2000, 2001). This nascent PN also shows emission from the four (1612, 1665, 1667 and 1720 MHz) ground-state OH maser transitions (Miranda et al. 2001). Interestingly, this source shows radio continuum emission with an S-shaped morphology, and the H_2O maser spots are emitted from a density-enhanced equatorial region and the tips of this S structure (see Fig. 1.8, left Miranda et al. 2001). Furthermore, multi-epoch maser observations of these maser spots suggests that the molecular gas in this equatorial region is undergoing a combination of rotation and expansion (Uscanga et al. 2008). In addition, the detection of Zeeman splitting in the OH maser lines provides evidence for the presence of a magnetic field in this molecular gas (Gómez et al. 2009). However, the inferred field strength is likely insufficient to strongly couple to or align dust grains in this region (Sabin et al. 2025).

The fact that molecular maser emission emitted by nascent PNe and WFs can trace bipolar outflows and equatorial regions indicates that this emission may not necessarily be the remnant of that tracing the roughly spherical circumstellar envelope created during the AGB phase, and instead it reflects more recently developed physical conditions favorable for the maser emission. This would be also the case of OH masers in non-spherical post-AGB stars (Zijlstra et al. 2001). Alternatively (or complementarily), this emission could have been developed in regions of nascent PNe with special shielding mechanisms that protect maser-emitting molecules from photodissociation (Tafoya et al. 2007). In any case, the propagation of the ionization front and the growth of the photoionized region must end up photodissociating the maser-emitting regions in more evolved PNe.

Apart from the previously mentioned case of K 3-35, polarimetric studies of OH masers in nascent PNe have revealed the presence of large-scale magnetic fields (Gómez et al. 2016). In addition, observations of toroidal OH-emitting structures around post-AGB stars indicate that temporal variations in the magnetic field may be associated with the onset of new mass-loss episodes, potentially linked to the transition toward the PN phase (Szymczak & Gérard 2004; Gonidakis et al. 2014). Consequently, nascent PNe traced by maser emission are promising sources for direct comparison with MHD models of PNe (e.g., García-Segura et al. 2020; Ondratschek et al. 2022). In this context, multi-epoch polarimetric observations would be a powerful approach to test the possible evolution of magnetic fields during the nascent PN phase.

Another interesting case to remark is the H_2OPN and OHPN IRAS 17347−3139 (de Gregorio-Monsalvo et al. 2004; Tafoya et al. 2009). Near-infrared K-band imaging reveals an angularly small bipolar morphology and an obscured equatorial structure within which H_2O masers seem to trace expanding and rotating motions (see Fig. 1.8, right; de Gregorio-Monsalvo et al. 2004). A radio spectral index of around +0.6, a high turn-over frequency ($<$ 20 GHz), and a brightening of the radio continuum emission in few years, are consistent with the propagation of the ionization front and the expansion of the photoionized region at the moment when the photoionization phase has just begun (Gómez et al. 2005; Tafoya et al. 2007).

Central stars remain undetected in most of these maser-emitting PNe, with the exception of the H_2OPN IRAS 18061−2505, which unexpectedly hosts a [WC]-type central star (Górny et al. 2004). The H_2O maser is located in the central region of this PN (Suárez et al. 2007; Gómez et al. 2008), and its current evolutionary stage is controversial, since observational data would be compatible with that of a post-CE evolutionary phase that may have undergone a LTP or VLTP (Miranda et al. 2021).

Maser monitoring and variability in the nascent PNe K 3-35 and IRAS 15103−5754 have provided further insight in the evolution of these sources. In K 3-35, the H_2O masers at the tips of the bipolar emission have shown intermittent activity over two decades (de Gregorio-Monsalvo et al. 2004; Gómez et al. 2018a). In IRAS 15103−5754, the maser morphology has evolved from a fast bipolar jet to a slower perpendicular distribution in the central region within the past decade (Gómez et al. 2023), which could correspond with the development of a a toroidal structure, as observed at high-angular resolution submillimeter continuum observations (Gómez et al. 2018b).

Maser emission also allows distance determination via parallax measurements, as was done for K 3-35 using very long baseline interferometry (Tafoya et al. 2011). Similar measurements have been achieved for OH masers in AGB and post-AGB stars (e.g., Orosz et al. 2017). Accurate distances are required for deriving physical properties of nascent PNe.

1.5.2 Non-thermal radio continuum emission

High-velocity stellar winds expelled during the post-AGB phase are known to reach to velocities of the order of $\sim 10^3\,\mathrm{km\,s^{-1}}$ (Sánchez Contreras & Sahai 2001; Uscanga et al. 2023) when they interact for the first time or recurrently within their circumstellar envelope, creating shocks that can free electrons that, in their turn, can produce free-free emission with similar spectral characteristics as that of PNe, but before the photoionization phase (Cerrigone et al. 2011, 2017). However, if energetic electrons move in a medium permeated by a strong magnetic field, they travel in spiral motions along the magnetic-field lines due to strong Lorentz forces. This process is called magneto-bremsstrahlung, and can produce different types of emission, such as gyro-synchrotron (for low-velocity electrons) or synchrotron radiation (for relativistic electrons).

Across the centimeter domain, non-thermal continuum emission is characterized by variable flux densities and negative spectral indices. Such emission is also particularly strong in environments where high-energy phenomena dominate, such as active galactic nuclei and quasars (Blandford & Königl 1979), microquasars (Mirabel et al. 1992), and supernova remnants (Weiler & Sramek 1988). Interestingly, the molecular jets traced by WFs have been also associated with ionized emission consistent with synchrotron radiation (Pérez-Sánchez et al. 2013a; Pérez-Sánchez et al. 2017). Moreover, this radiation could still be present during the PN phase, but its contribution in the radio continuum could be, in general, overwhelmed by the more intense thermal (free-free) emission from the photoionized region (Casali et al. 2007). Only in the nascent PN phase would therefore be possible to detect synchrotron radiation, when the photoionized region is small, and the thermal emission is weaker than the non-thermal emission. On the other hand, we note the recent detection at 144 MHz of non-thermal radiation from PNe (Hajduk et al. 2025). The thermal (free-free) radiation is naturally weak at such low frequencies, allowing the identification of non-thermal emission in more evolved PNe, possibly linking magneto-bremsstrahlung processes with their morphologies. Thus, the highest frequency at which non-thermal emission can be effectively detected may be considered as an aging indicator. In this thesis, we will use the term "non-thermal PNe" to refer to PNe in which non-thermal radio continuum emission has been detected.

In this context, it is worth mentioning the case of the previously mentioned nascent PN IRAS 15103−5754, where the H_2O maser emission tracing a WF outflow indicates it is at an exceptionally young stage, and the presence of ionized gas reported from mid-infrared imaging and spectroscopic observations (Gómez et al. 2015b) is still not dominated by thermal (free-free) emission at radio frequencies, and instead it showed an initial spectral index $\alpha \simeq -0.54$, which would be more consistent with the presence of non-thermal (possibly synchrotron) emission (Suárez et al. 2015). Furthermore, the observed variability of the flux density and negative spectral index are not consistent with non-thermal radio continuum emission alone, and instead suggests the presence of a newly developed and growing ionized region, a scenario consistent with the beginning of the photoionization phase (Suárez et al. 2015). This further suggests that non-thermal radio continuum emission is potentially an aging tracer of PNe.

This is interesting for the comparison between these PNe with non-thermal radio continuum emission at centimeter wavelengths and most of the maser-emitting PNe mentioned above, which predominantly show free-free continuum emission. It is possible that maser-emitting PNe with thermal emission, while still young, are in a slightly more evolved stage than the emerging group of non-thermal PNe. Moreover, searching for more non-thermal PNe at centimeter wavelengths could potentially assess the role of magnetic fields as an sculpting mechanism from the nascent to more evolved PN phases.

Chapter 2

Goals, Methodology and Results

2.1 Goals

The main purpose of this thesis is to improve our understanding of the very earliest stages of PN formation by studying in detail evolved stars that may be transiting between the brief post-AGB phase and the elusive nascent PN phase. Throughout this thesis, the term “nascent PN candidate” refers to an object whose observational properties are consistent with those expected for a PN at the onset of photoionization, but whose nature as a bona fide PN has not yet been confirmed. We have pursued the following specific goals:

1. **Identification of new nascent PNe and candidates.** The scarce number of confirmed nascent PNe limits our ability to constrain the physical mechanisms operating at the onset of PN formation. Therefore, this thesis aims at identify possible PNe showing maser lines and/or non-thermal radio continuum emission, using both types of radiation as tracers of a nascent PN nature. For the case of maser-emitting PNe, we search for maser emission arising from evolved stars that show possible evidence for the presence of the photoionized regions that characterize PNe (e.g., free-free emission). Regarding non-thermal PNe, their identification necessarily requires to check the frequency dependence of radio continuum emission, to determine the cases in which the spectral index is negative.

2. **Characterization of nascent PNe and candidates, and analysis of evolutionary pathways.** Shocks from post-AGB stars can produce ionized emission prior to the onset of the photoionization phase from PNe. Distinguishing between shocks and photoionization is therefore an essential issue to assess, and it is addressable through a detailed analysis of emission lines from the optical to the far-infrared. In addition, binary-star progenitors of PNe tend to develop characteristic morpho-kinematical patterns (e.g, spirals, toroidal structures, and collimated outflows) and their ionized emission have been related in some cases with special physical conditions (e.g., low

values of N_e, and discrepant chemical abundances). Examining these properties may therefore provide hints about the evolutionary pathway of nascent PNe.

3. **Variability during the nascent PN phase.** The rapid increase in the effective temperature of the central star during the nascent PN phase leads to time-variable ionization, shock conditions, and emission properties on timescales of years to decades. Thus, through the analysis of archival multi-epoch photometric, spectroscopic, and radio continuum observations, we aim to identify temporal changes in continuum flux densities, emission-line excitation, light curves, and radio spectral indices. Such variability provides direct constraints on the evolution of the ionized gas and helps discriminate between transient shocks and the progressive onset of photoionization.

2.2 Methodology

In order to increase the known number of evolved stars at the nascent PN phase, this thesis mines public databases, surveys available in the literature, and published and archival imaging and spectroscopic data stored in open telescope archives worldwide. These data are complemented with new multiwavelength imaging and spectroscopic observations focused on the most promising sources resulting from the cross-identification procedure described below.

2.2.1 Cross-identification procedure using databases

In order to increase the chances of identifying new nascent PNe and candidates, the search must rely on carefully selected aging tracers from sources located in both the northern and southern hemispheres that have been reported to date.

Sources included in surveys based on single-dish maser observations are therefore foundational to this aim. Fortunately, the positions of a large fraction of these sources are stored in the maser databases of Benson et al. (1990), Forster & Caswell (1999a), Engels & Bunzel (2015), and Ladeyschikov et al. (2019). Furthermore, these databases also include the positions of sources reported by radio interferometers located in both hemispheres. Cross-identifying these positions with those of sources reported in radio continuum surveys can potentially lead to the identification of new nascent PNe and candidates, considering radio continuum emission as a tracer of the thermal (free-free) emission from the photoionized regions that characterize PNe. However, many of the reported maser detections arise from single-dish observations, whose positional accuracy is typically on the order of several arcminutes, which makes the true origin of these emissions uncertain. Hence, in order to improve the positional accuracy to arcsecond scales and to corroborate the maser–continuum spatial association, new radio interferometric observations are required. Ideally, the continuum observations should be conducted at frequencies close to those of the maser lines, so that they can be performed simultaneously with the same telescope, sharing the same amplitude and phase calibration. Such observations have already been carried out in the northern hemisphere by The HI/OH/Recombination line survey of the Milky Way (THOR; Beuther et al. 2019; Wang et al. 2020), and in the southern hemisphere through the Australia Telescope Compact Array (ATCA) interferometric follow-up of the Southern Parkes Large Area Survey in Hydroxyl (SPLASH; Qiao et al. 2016b, 2018, 2020). However, the continuum data associated with the SPLASH follow-up survey remain unpublished. Thus, in this thesis, these unpublished continuum data is reduced, with the aim of searching for possible nascent PNe and candidates exhibiting OH maser–continuum spatial associations.

To search for non-thermal PNe, this thesis takes advantage of the new technical capabilities of the Very Large Array (VLA), which is currently conducting large-area surveys with sensitivities of the order of milliJanskys and gigahertz-wide continuum bandwidths. These capabilities allow the determination of intraband spectral indices for new and known radio continuum sources in the northern sky. In particular, the THOR survey has reported such data between 1 and 2 GHz. Furthermore, the Global View of Star Formation in the Milky Way (GLOSTAR) survey has reported similar information between 4 and 8 GHz. Moreover, GLOSTAR has released data from two different observing epochs, first obtained with the VLA in the D configuration (Medina et al. 2019, 2024), and subsequently through a follow-up with the VLA in the B configuration (Dzib et al. 2023; Yang et al. 2023). This combination potentially allows the identification of sources with variable flux densities and/or negative spectral indices, and therefore the discovery of new non-thermal PNe and candidates.

The resulting catalog of sources identified through maser and non-thermal radio continuum emission were further cross-identified with sources in public astronomical databases. In particular, the Hong Kong/AAO/Strasbourg PN database (HASH; Parker et al. 2016), which compiles an updated list of sources classified as evolved stars and PNe to date, will be exhaustively used in this search for new objects in the nascent PN phase.

2.2.2 Processing of further archival data and execution of new observations

The core of this search is the mining of available data to date, complemented with new multiwavelength observations. Hence, in synergy with the cross-identification procedure described above, public telescope archives will be exhaustively consulted in order to search for unpublished data containing the cross-identified sources, either as dedicated science targets or as marginal detections within the field of view of random observations.

Cross-identified sources from single-dish maser observations were first searched for available radio interferometric data in the public archives of the ATCA and the VLA, depending on whether their positions are located in the southern or northern hemispheres, respectively. This initial step is necessary to optimize telescope legacy time and to justify the need for new radio interferometric observations.

Evolved stars transiting between the brief post-AGB phase and the nascent PN phase are primarily distinguished by whether their ionized emission is consistent with photoionization processes typical of PNe, or with shock ionization alone, as expected for post-AGB stars. However, this distinction is not straightforward. In particular, constructing the radio continuum spectrum to assess the presence of photoionized gas is often insufficient, since ionized jets from post-AGB stars can produce spectral indices of approximately +0.6, similar to the values expected from the photoionized gas during the nascent PN phase. In this context, and considering that these sources tend to be obscured at optical wavelengths, it becomes necessary to analyze recombination and/or forbidden emission lines at infrared wavelengths, and to develop new diagnostic diagrams based on photoionization and shock models for infrared lines.

The cross-identified sources were therefore searched for in photometric r-band catalogs. Optical spectroscopy was subsequently applied to those sources with reported magnitudes brighter than ≃18. In the remaining optically obscured cases, near-infrared spectroscopic observations were conducted. Interestingly, unpublished mid-infrared spectroscopy was found for some cross-identified sources in the open archive of *Spitzer*. These unpublished spectra, together with published mid-infrared spectra of known nascent PNe obtained with *Spitzer* and the Infrared Space Observatory (ISO), can be used in synergy to robustly test the new mid-infrared diagnostic diagrams in the context of the nascent PN phase, and to justify the need for new infrared spectroscopic observations in future work.

For completeness, the following summarizes the observations we have performed in the chapters of this thesis:

- **Radio interferometry:** New ATCA and VLA observations were carried out to obtain simultaneous continuum and (SiO, H_2O, and OH) maser data, allowing the determination of maser–continuum spatial separations with accuracies of the order of arcseconds, which is optimal for associating these emissions. The correlator is configured to improve the spectral resolution and velocity coverage of previous maser observations, while the continuum bandwidth is set to its maximum capacity, aiming to achieve a signal-to-noise (S/N) ratio of S/N≥10.

- **Optical spectroscopy:** Intermediate-resolution long-slit optical spectroscopy was applied with the Calar Alto Faint Object Spectrograph (CAFOS) instrumentation mounted on the 2.2m telescope of the Centro Astronómico Hispano en Andalucía (CAHA) to analyze emission lines in the wavelength ranges 3200–6200 Å and 5800–9600 Å for sources with reported optical photometric values brighter than ≃18 magnitudes. For both compact and extended sources, slit widths are selected to integrate the total emission, and the slit orientation is aligned with the extended structure when present. This strategy allows the measurement of nebular emission lines and the determination of extinction-corrected flux ratios, which are fundamental for determining the physical conditions and chemical abundances of the ionized gas, as well as for performing robust diagnostic line-ratio analyses to distinguish between photoionization and shock ionization. This analysis, essential for this thesis, is further extended at these wavelengths by means of high-resolution long-slit and fiber spectroscopy in carefully selected sources, in order to assess whether the internal kinematics of the ionized gas are consistent with the results obtained at coarser spectral resolution. These observations were performed with the Manchester Echelle Spectrometer (MES) at the 2.1 m telescope on the San Pedro Mártir (SPM) Observatory and the Calar Alto high-Resolution search for M dwarfs with Exoearths with Near-infrared and optical Echelle Spectrographs (CARMENES) mounted on the 3.5m telescope at CAHA.

- **Near-infrared spectroscopy:** Intermediate-resolution long-slit near-infrared spectroscopy was applied to cross-identified sources with reported optical photometric values weaker than ≃18 magnitudes, using the Son of ISAAC (SOFI) instrument on the New Technology Telescope (NTT). In particular, K-band observations (2.0–2.3 μm) aimed to detect the H (Br γ) and He I emission lines in this wavelength range. These recombination lines may provide a key near-infrared diagnostic to assess whether the ionized emission in these sources is more consistent with photoionization from PNe or with shock ionization alone from post-AGB stars.

The doctoral candidate actively participated in co-authoring and preparing observational proposals for these telescopes, designing the observing strategies, and taking part in the execution of observing runs (both remote and on-site). Given the high success rate for the submitted proposals, not all these data could be used in this thesis, and some of them will be used for future work during the upcoming post-doctoral research. Table 2.1 list accepted proposals in the context of this thesis.

2.2.3 Data reduction and software

Data reduction follows standard procedures for radio interferometry and optical and near-infrared spectroscopy:

- **Radio:** The calibration of ATCA data was performed using the MIRIAD software package, including flagging of bad data and standard amplitude and phase calibration of the visibilities. For VLA observations, the initial calibration was carried out using the VLA calibration pipeline within CASA. Subsequent imaging of the calibrated visibilities was performed using both CASA and AIPS, particularly for the generation of spectral-line datacubes. When sufficiently bright maser channels or continuum sources were available, self-calibration was applied in order to improve the signal-to-noise ratio and the dynamic range of the final images.

- **Optical:** Optical spectroscopic data were reduced following standard procedures, including bias and dark subtraction, flat-field correction, wavelength calibration, sky

TABLE 2.1: Summary of proposal of observations accepted in the context of this thesis.

Title	Date	Telescope	Project ID	Principal Investigator	Chapter[a]
Capturing a planetary nebula eclosion	2019	ALMA	2019.1.00232.S	R.A. Cala	10
HCN masers: a new tool to observe the innermost regions of nascent planetary nebulae	2024	APEX	C114F-970006	K. Ohnaka	10
Confirmation of new OH-maser-emitting planetary nebulae	2020	ATCA	C3390	R.A. Cala	6
Confirming the first SiO maser emission ever in planetary nebulae	2020	ATCA	C3324	R.A. Cala	5
IRAS 18019−2216: A planetary nebula emerging from a "water fountain"?	2023	ATCA	2023OCTS-DG	R.A. Cala	10
Searching for close binary central stars of planetary nebulae	2016	CAHA-2.2m	H16-2.2-024	L.F. Miranda	8
The formation of planetary nebulae at high spectral resolution	2016	CAHA-3.5m	H16-3.5-036	L.F. Miranda	8
Non-thermal planetary nebulae as a new type of astronomical object	2021	CAHA-2.2m	F21-2.2-0.17	R.A. Cala	5, 9
The central star of a planetary nebula evolves	2023	CAHA	DDT23B.320	R.A. Cala	5
A late thermal pulse in a central star?	2024	CAHA	DDT24B.324	R.A. Cala	10
Monitoring the recombining planetary nebula IRAS 22568+6141	2025	CAHA	25B-2.2-030	R.A. Cala	10
HCN masers: a new tool to observe the innermost regions of nascent planetary nebulae	2024	IRAM-30m	066-24	J.F Gómez	10
Confirming new maser-emitting planetary nebulae	2021	VLA	21A-138	R.A. Cala	6
A nascent planetary nebula from a magnetized water fountain	2023	VLA	24A-401	R.A. Cala	10
The first candidate planetary nebula with SiO masers	2024	VLA	25A-173	R.A. Cala	4
Identification of nascent planetary nebulae	2023	NTT	111.24T1.001	R.A. Cala	7, 10
Morfocinemática del material ionizado por choques y fotoionizado en nebulosas planetarias nacientes	2023	MES-2.2m	FM-15	R. Vásquez	5
Seguimiento morfocinemático de IRAS 22568+6141	2024	MES-2.2m	FM-15	R. Vásquez	10
A nascent planetary nebula from a magnetized water fountain	2023	Gran Telescopio Canarias	GTC2023-214	R.A. Cala	10
The magnetized 'water fountain' and circumstellar structure of a nascent planetary nebula	2024	European VLBI Network	E24B011	R.A. Cala	10

[a] The observational projects marked as pertaining to Chapter 10 refer to data intended for future research.

subtraction, and flux calibration. The values of N_e and T_e were derived by comparing observed emission-line intensities with theoretical predictions for a suitable set of collisionally excited lines and recombination lines. These calculations were carried out using IRAF and PyNeb, allowing the determination of ionic abundances from both type of emission lines.

- **Near-infrared:** Dark-current correction, flat fielding, slit curvature distortion, combination of frames, and wavelength calibration of near-infrared spectroscopy was reduced using the SOFI/NTT pipeline executed through esorex. Additional processing, including extraction and telluric correction, was carried out using IRAF. Flux calibration was performed with a specific programming code we developed.

2.3 Results

This section summarizes principal results obtained in the chapters that constitute this thesis.

2.3.1 Searching for nascent planetary nebulae: OHPNe candidates in the SPLASH survey

In order to identify and characterize more OHPNe, we processed the unpublished continuum data of the interferometric follow-up of the Southern Parkes Large-Area Survey in Hydroxyl (SPLASH). We then matched the interferometric positions of OH maser and radio continuum emission, considering the latter as a possible tracer of free–free emission from photoionized gas, characteristic of PNe. We report eight objects with a positive coincidence, four of which are classified as candidate OHPNe here for the first time (IRAS 16372−4808, IRAS 17494−2645, IRAS 18019−2216, and OH 341.6811+00.2634). Available evidence strongly indicates that they are evolved stars, while the comparison with confirmed OHPNe indicates that they are likely to be PNe. Their final confirmation as bona fide PNe, however, requires optical/infrared spectroscopy. The obtained spectral indices of the radio continuum emission (between $\simeq$ 0.4–1.3) are consistent with partially optically thick free–free emission from photoionized gas.

2.3.2 An interferometric search for SiO maser emission in planetary nebulae

We intend to obtain the first detection of a SiO maser from a PN. Such a detection would provide us with a useful tool to probe mass loss in PNe at a scales of a few AU from the central star, much shorter than the scales traced by H_2O or OH masers. We compiled two different samples. The first one comprises all known PNe with confirmed OH and/or H_2O maser emission, as well as two candidate PNe showing OH masers. For the second sample, we compiled single-dish SiO maser detections in the literature, and compared them with catalogs of PNe and radio continuum emission (which could trace photoionized gas in PNe). We identified five targets (either PN or radio continuum sources) within the beam of the single-dish SiO maser observations. We then carried out interferometric observations of both samples with the Australia Telescope Compact Array, to confirm the spatial association between continuum and SiO maser emission. We find no SiO maser emission associated with any confirmed or candidate PN. In all targets, except IRAS 17390−3014, there is no spatial coincidence between SiO masers and radio continuum emission. While in IRAS 17390−3014 we cannot completely rule out a possible association, it is unlikely that the radio continuum emission arises from a PN. The absence of SiO maser emission in PNe showing OH or H_2O masers is of special interest, since thermal SiO emission has been reported in at least one of these targets, indicating that SiO molecules can be present in the gas phase.

2.3.3 Long- and short-term variability of the possible nascent planetary nebula IRAS 22568+6141: A late thermal pulse?

IRAS 22568+6141 has been classified as a low-ionisation planetary nebula (PN) and presents non-thermal radio continuum emission, which could be a signature of a nascent PN. We present intermediate-resolution long-slit spectra obtained in 2021 and 2023, high-resolution long-slit spectra taken in 2023, and a light curve at the r filter between 1953 and 2019. They all reveal changes in IRAS 22568+6141 with timescales of decades and a few years. The object underwent an energetic event around 1990 that suddenly increased its brightness, which has been fading since then. A comparison with a published spectrum from 1988 shows an increase in the Hβ flux in 2021 by factor of $\simeq$6 and the [O III] emission lines, which were absent in 1988. Between 2021 and 2023, the Hβ flux decreased by a factor of $\simeq$1.7, and the [O III] emission lines almost vanished. These results and the variability observed in other emission lines indicate that IRAS 22568+6141 was recombining and cooling down between 2021 and 2023, and probably since 2005, as suggested by archival radio continuum and mid-IR observations. The intermediate- and high-resolution spectra show that the excitation of the emission lines was dominated by shocks in 2021 and 2023, and probably also in 1988, which may be related to the non-thermal radio continuum emission from the object. Although the variability might be due to changes in the physical conditions in the shocks or in a nova-like eruption, it better accommodates that expected from a late thermal pulse, which is further suggested by a comparison with other similar objects.

2.3.4 Identification and characterization of nascent planetary nebulae with OH and H_2O masers

In order to identify more OHPNe and H_2OPNe, we used public databases and our own ATCA/VLA observations to match the positions of OH and H_2O masers with known PNe and radio continuum emitters, considering radio continuum emission as a possible tracer of the photoionized gas that characterizes PNe. Here we report the confirmation of positional coincidence of maser emission with one more PN, and 12 PN candidates. Moreover, we have confirmed three evolved stars as 'water fountains' (WFs) hosting H_2O masers. These WFs are associated with radio continuum emission, but their possible nature as PNe has not yet been confirmed. Although a final characterization of maser-emitting PNe as a group still requires confirmation of more objects, their distribution in the infrared color-color diagrams suggests that they are a heterogeneous group of PNe. In particular, the new OHPN IRAS 07027−7934 has been reported to contain a late [WC]-type central star, while the maser emission implies an O-rich envelope. This property is found in only one other known maser-emitting PN, although we found evidence that other confirmed and candidate OHPNe may also have mixed chemistry, since they show emission from polycyclic aromatic hydrocarbons. The new WF IRAS 18443−0231 shows radio continuum that is dominated by strong and variable non-thermal emission, as in magnetized outflows.

2.3.5 Low- and high-velocity "water fountains": Different evolutionary stages

"Water fountains" (WFs) are optically obscured evolved stars. Most of them are thought to be in the post-asymptotic giant branch (post-AGB) phase, and they are characterized by H_2O maser emission tracing molecular jets. Interestingly, four WFs (IRAS 15445−5449, IRAS 18019−2216, IRAS 18443−0231, and IRAS 18464−0140) and one WF candidate (IRAS 18480+0008) are potentially planetary nebulae (PNe) because they exhibit radio continuum emission, suggesting the presence of a photoionized region characteristic of PNe. To classify these objects, we obtained K-band (2.0-2.3 μm) spectra of these WFs, including the only WF PN known (IRAS 15103−5754) for comparison. Our spectra reveal two groups of sources: (i) "low-velocity" WFs with an H_2O maser velocity spread of $\lesssim$50 km s^{-1} (IRAS 18019−2216, IRAS 18464−0140, and IRAS 18480+0008) showing the CO band at 2.29 μm in absorption, typical of cool giant stars, and no emission lines, and (ii) "high-velocity" WFs, velocity spread of $\gtrsim$50 km s^{-1} (IRAS 15103−5754, IRAS 15445−5449, and IRAS 18443−0231), exhibiting emission lines of Brγ, He I, and H_2, consistent with hotter central stars and/or shock-excited emission. The emission line ratios of these lines in IRAS 18443−0231 indicate that it may be a nascent PN. The spectrum of IRAS 15445−5449 also shows a CO band and Na I doublet in emission, suggesting the presence of a compact circumstellar disk and/or active mass loss. These results favor the previously suggested notion that the difference between low- and high-velocity WFs is not simply a projection effect but a reflection of intrinsically different evolutionary stages. Moreover, the results are also consistent with the idea of an increase in the jet ejection velocity as the post-AGB evolution proceeds.

2.3.6 Near-infrared and optical spectroscopy on the nascent planetary nebula Vy 2-2: Evidence of binary-star evolution

We present and analyze new intermediate- and échelle high-resolution spectra of the nascent PN Vy 2-2 to obtain its chemical abundances and a new value for its controversial abundance discrepancy factor (*adf*), investigate the internal kinematics and ionization of the nebula, and infer its possible formation processes. Our intermediate resolution spectra reveal many previously unreported nebular recombination (e.g., N^+) and forbidden (e.g., [F IV]) emission lines as well as stellar emission lines. Some of the newly detected nebular lines are important to determine the *adf*. The derived abundances are subsolar and agree with previous values, while the new value of the *adf*(O^{2+})=13.6$\pm$2.6 indicates that Vy 2-2 belongs to the group of PNe with unusually high *adf*. Our morphokinematical and ionization structure analysis reveals that Vy 2-2 consists of a relatively high-excitation central region and two low-excitation bipolar lobes. Our data show that shock excitation does not exist in the main ionized shell of this PN. A distance of $\simeq$1.68 kpc to Vy 2-2 is obtained from the published angular expansion of the central region and its expansion velocity in H^+. The inferred kinematical age of $\simeq$210 yr supports that Vy 2-2 is a nascent PN. The stellar emission lines suggest a *wels*-like spectrum although more likely associated with an irradiated close companion than with the central star. Actually, the very high *adf*, the observed nebular structures, presence of fluorine, among others, point to Vy2-2 hosting a post-common-envelope binary system. Chemical abundances and circumstellar mass estimates suggest an initial mass $\lesssim 0.9\,M_\odot$ for the star progenitor of Vy 2-2.

2.3.7 A search for possible planetary nebulae with non-thermal radio continuum emission.

From our cross-identification procedure, we selected 23 objects with non-thermal radio continuum emission. The observed radio spectral indices ($-1.1 \leq \alpha \leq -0.3$) provide evidence for the presence of non-thermal emission in a regime traditionally assumed to be dominated by purely thermal processes. This implies that magnetic fields could be key in the PN formation. The combination of toroidal structures and/or bipolar morphologies, low N_e and high [N II]/Hα ratios, observed in some of our objects, is also observed in post-CE binary systems but more investigation is required to firmly established this apparent link. Alternatively, the presence of non-thermal radio continuum emission at cm wavelengths could also be a tracer of the nascent PN phase. This interpretation is also compatible with scenarios involving close post-CE binary systems, where shocks and magnetic fields may coexist with the onset of photoionization. Approximately $\sim$40% of the selected sources exhibits significant variations in α, which depend systematically on observing frequency, angular resolution, and epoch. This behavior could be explained by the superposition of a photoionized region and compact non-thermal structures, such as the case of M 3-28. Among the selected objects with non-thermal radio continuum emission, M 3-28 has been classified as a PN based on recombination-line diagnostics (He I λ5876, He I λ6678, and He I λ7065), 19 as PN candidates, one (G33.448 +00.318) is discarded as a PN, and two (G19.2356+0.4951 and IRAS 18551 +0159) are classified as evolved star candidates.

Chapter 3

Searching for nascent planetary nebulae: OHPNe candidates in the SPLASH survey

3.1 Introduction

Stars with initial masses ($M_{\rm i}$) between 0.8 and 8 $M_\odot$ will undergo the phase to form a planetary nebula (PN) before becoming a white dwarf. PNe are conspicuous objects in optical images showing round, elliptical, bipolar, multipolar or point-symmetric morphologies (e.g., Manchado et al. 1996a; Sahai et al. 2011) that are a result of the particular mass–loss history during the previous evolutionary stages: the asymptotic giant branch (AGB) and the post–AGB phases.

The AGB phase is characterized by strong mass–loss episodes, with rates up to 10^{-4} $M_\odot$ yr^{-1} (Vassiliadis & Wood 1993; Bloecker 1995). This creates an expanding circumstellar envelope (CSE), whose kinematics is traceable with spectral lines at radio wavelengths. Maser line emission from different molecules has been widely used in these studies. In particular, stars with $M_{\rm i} = 0.8 - 1.5$ $M_\odot$ and $M_{\rm i} = 4 - 8$ $M_\odot$ are expected to develop an oxygen-rich (C/O < 1) CSE (Groenewegen et al. 1995). In oxygen-rich AGBs, the CSE seems to be stratified with SiO, H_2O and OH masers located up to $\sim$10 AU, $\sim 10^2$ AU and $\sim 10^4$ AU from the central star, respectively (Reid & Moran 1981a; Elitzur 1992; Diamond et al. 1994). Thus, OH masers typically trace the front and back sides of the CSE (Reid 1976) with a typical terminal expansion velocity of $\sim 15 - 30$ km s^{-1} (te Lintel Hekkert et al. 1991), whereas the H_2O and SiO ones trace inner regions that expand more slowly.

This chapter is derived from the following publication:

- Cala et al. (2022)

During a brief post–AGB transition period ($\sim 10^2 - 10^4$ yr) between the AGB and PN phases (depending on M_i; Bloecker 1995; Miller Bertolami 2016), the mass–loss rate drops down to $10^{-7} - 10^{-8}$ $M_\odot$ yr^{-1} (Vassiliadis & Wood 1994). The star shrinks at a constant luminosity, and its effective temperature (T_{eff}) gradually increases, while the CSE continues expanding. With this sudden decline of mass–loss, the favorable conditions for maser-pumping are expected to disappear soon after the end of the AGB phase, on timescales of ∼10 yr, ∼100 yr and ∼1000 yr for SiO, H_2O and OH masers, respectively (Lewis 1989; Gómez et al. 1990). When the surface temperature of the central star reaches $T_{eff} \simeq 25{,}000 - 30{,}000$ K, it emits enough ultraviolet (UV) photons to develop and sustain a photoionized nebula in its CSE. When this photoionized region is maintained, we can consider that the star is in the PN phase. Molecules such as SiO, H_2O and OH are rapidly destroyed as the ionization front advances. Thus, comparing these maser lifetimes with the duration of the post–AGB phase, masers have been expected to be detected only in nascent PNe. However, special physical conditions in the CSE can temporarily shield these molecules from dissociation (Miranda et al. 2001) and maser-pumping can also be produced in collimated mass ejections with lower mass–loss rates than in the strong AGB winds (Suárez et al. 2009). In particular, OH masers can trace bipolar outflows in the AGB and post–AGB phases (Chapman 1988; Zijlstra et al. 2001), and so far, there are fifteen known cases where H_2O masers trace high-velocity collimated jets ($\simeq 50 - 300$ km s^{-1}; Imai 2007; Gómez et al. 2017). These objects are called water fountains (WFs).

Considering that maser emission is expected to disappear soon after the onset of the PN phase, it naturally follows that the number of maser-emitting-PNe must be small. So far, only 8 PNe have been confirmed to harbour maser emission, consistent with these short timescales of maser survival. Among these, 6 PNe display OH maser emission (OHPNe; Uscanga et al. 2012; Qiao et al. 2016a) and 5 ones show H_2O maser emission (H_2O-PNe; Miranda et al. 2001; de Gregorio-Monsalvo et al. 2004; Gómez et al. 2008; Uscanga et al. 2014; Gómez et al. 2015b), 3 of which harboring both species. SiO maser emission has never been detected in a PN (e.g. Nyman et al. 1998; Deguchi et al. 2001). With such scarcity, it is difficult to draw strong conclusions on the nature of maser-emitting PNe. Hence, detecting more of these sources is so crucial that the physical processes occurring at the beginning of photoionization could determine the subsequent morphological, kinematical and chemical evolution of evolved stars through the PN phase. Thus, further studies of these maser-emitting PNe can provide a deeper understanding about the end of low- and intermediate-mass stellar evolution. In principle, all confirmed maser detections in PNe trace O-rich CSE, although at least in one case (the H_2O-PNe IRAS 18061–2505; Gómez et al. 2008) dual chemistry is present, with a C-rich central star and an O-rich circumstellar ring (Miranda et al. 2021, and references therein). Another possible case of maser emission in dual-chemistry in a PN is the OH detection towards IRAS 07027–7934 (e.g., Zijlstra et al. 1991), but the association of the maser with the PN requires confirmation with interferometric radio observations. The relationship of these peculiar PNe with other dual-chemistry evolved objects with maser emission in previous evolutionary phases (Ohnaka et al. 2013) remains to be determined. Regarding C-rich stars, maser emission of molecules such as HCN is present at the AGB phase (Menten et al. 2018), but so far, no such maser has been reported in PNe. Thus, as a consequence of their different chemical evolution, it has not been possible to use the presence of masers as a putative signpost of the youth of C-rich PNe.

Focusing on the particular case of OH, Davis et al. (1979) reported Vy 2–2 as the first possible case of PN with 1612 MHz maser emission, based on Arecibo observations. Afterwards, Zijlstra et al. (1989) cataloged 12 OHPNe candidates, mostly based on single-dish observations. To date, only 6 PNe have been confirmed interferometrically to be associated with OH maser emission. These objects are Vy 2–2, IRAS 17393–2727, K 3–35, IRAS 17347–3139, JaSt 23, and IRAS 16333–4807 (Uscanga et al. 2012; Qiao et al. 2016a). There is an additional PN, NGC 6302, that is known to be associated with OH emission, but it has been argued that its emission could be of thermal nature (not maser), since the CO and the 1720 MHz line profiles (the latter in absorption) are similar to that of OH at 1612 MHz (Gómez et al. 2016), and that the 1612 MHz OH line is not detected at the longest baselines of ATCA (Qiao et al. 2020). In this case, we cannot confidently include NGC 6302 in the group of bona fide OHPNe. OH masers in PNe seem to preferentially trace magnetized toroidal structures, perpendicular to the lobes of the nebulae. This is suggested in IRAS 17347–3139 (based on the spatial distribution of the H_2O masers; de Gregorio-Monsalvo et al. 2004; Tafoya et al. 2009), and is observed in K 3–35 and IRAS 16333–4807 (Miranda et al. 2001; Uscanga et al. 2008; Gómez et al. 2009; Qiao et al. 2016a). In Vy 2–2, IRAS 17393–2727 and JaSt 23, the spatial distribution of OH masers is still to be determined.

In order to increase the number of known maser-emitting PNe, we searched for OHPNe candidates in data from the interferometric follow-up observations of the Southern Parkes Large-Area Survey in Hydroxyl (SPLASH).

The SPLASH project (Dawson et al. 2022) performed a fully-sampled, high-sensitivity, unbiased survey of the four OH ground-state transitions ($^2\Pi_{3/2}$, $J = 3/2$ at 1612.231, 1665.402, 1667.359 and 1720.530 MHz), covering 176 deg^2 of the southern Galactic plane and Galactic Center: $332° \leq l \leq 10°$, $|b| = 2°$ and $358° \leq l \leq 4°$, $+2° \leq b \leq +6°$. The four OH transitions were observed with the 64-m radio telescope at the Parkes Observatory ($\sim$15 arcmin resolution). The scientific goals of SPLASH included both thermal and maser emission of OH. Regarding OH masers, in contrast to other surveys, which were targeted toward a sample of selected sources (Chengalur, Lewis, Eder, & Terzian 1993; Deacon, Chapman, & Green 2004) and/or covered only one of the transitions (e.g., the ATCA/VLA OH 1612 MHz survey of Sevenster et al. 1997a,b, 2001), SPLASH allows a direct comparison among all four OH lines, while its large spatial coverage and high sensitivity provides an unbiased view of the nature and pumping mechanism of circumstellar masers.

Candidate maser sources detected at first in SPLASH were subsequently observed with the Australia Telescope Compact Array (ATCA), which allowed us to confirm unambiguously the OH maser detections, as well as an accurate determination of their positions. In this chapter, we will refer to Qiao et al. (2016b, 2018, 2020) interferometric follow-up maser observations as SPLASH–ATCA.

In SPLASH–ATCA, 934 individual sources were found to produce OH maser emission in at least one of the ground-state transitions, 432 of which were sources detected for the first time. The detected objects were then classified depending on available literature, their infrared colours and compactness, the number of OH maser transitions and/or their spectral profiles: 629 evolved stars, 158 star forming regions (SFRs), 14 supernova remnants and 132 objects of unknown nature.

OHPNe candidates can be identified using radio continuum emission as a possible tracer of the presence of photoionized gas. Free-moving electrons in the ionized region of PNe produce bremsstrahlung (free-free) radiation that can be detected at radio wavelengths. Thus, cross-matching OH-masers with radio continuum sources can be used to identify candidate OHPNe (Zijlstra et al. 1989; Uscanga et al. 2012). However, other objects, such as H II regions associated with massive young stellar objects (YSOs) can also show both radio continuum and OH maser emission.

The ATCA correlator used in SPLASH–ATCA allows the simultaneous observation of line and continuum emission. Qiao et al. (2016b, 2018, 2020) only reported the results of the OH line data. Therefore, we used the unpublished continuum data of SPLASH–ATCA as the main focus of this chapter, in order to find positional coincidence between the OH-emitters and radio continuum sources, considering continuum emission as a tracer of photoionized gas in PNe.

We note that not all OH maser detections in SPLASH were followed-up with SPLASH–ATCA, since those sources already observed in the Mapping the Galactic Magnetic field through OH masers (MAGMO) project with ATCA (Green et al. 2012) were not included. However, the MAGMO targets were most likely to be star-forming regions, so we do not think our data processing left out any evolved star covered by the original SPLASH survey.

3.2 Observations and data processing

3.2.1 SPLASH–ATCA continuum data

SPLASH–ATCA observations (project C2872) were carried out in several sessions from 2013-Oct-24 to 2016-Mar-04. The Compact Array Broadband Backend (CABB) correlator of ATCA was set in its 1M-0.5k mode, total bandwidth of 2 GHz centered at 2.1 GHz, and sampled over 2048 wideband channels of 1 MHz width each. These are used in this chapter to obtain the continuum emission of the sources. Zoom windows were placed at several of these wideband channels to obtain line data at a higher spectral resolution, presented in Qiao et al. (2016b, 2018, 2020). We refer the reader to these chapters for further details on the technical setup of the observations.

Observations at 1.1 – 3.1 GHz are severely affected by radio-frequency interference (RFI), specially from terrestrial and satellite communications. Hence, a careful flagging of RFI was manually applied to the continuum data. This RFI flagging was carried out with the MIRIAD package using standard procedures. The flux density scale and the bandpass response were calibrated with the standard flux calibrator PKS 1934–638. The complex-gain calibrators were chosen to be within 7° of each target. The calibrators were PKS 1613–586, MRC 1646–506 and PKS 1710–269.

We flagged the broadband channels that contained the detected OH emission with the Common Astronomy Software Applications (CASA) package, in order to avoid line contamination of the radio continuum. Images were obtained using Brigg's weighting of visibilities with a robust parameter of 0.5 (as defined in CASA), and deconvolved using multi-frequency synthesis in task tclean.

Regarding the particular fields containing the objects introduced in Section 3.3.1, we noticed the presence of extended galactic background contamination in the data containing the position of IRAS 18019–2216, which significantly worsened the image quality. We thus imaged it again restricting the visibilities to baselines longer than 7 kilolambda.

We also tried in CASA phase self-calibration with solution intervals of 10 seconds (the integration time of individual visibilities), which was only successful for IRAS 17494-2645. For the other sources presented in Section 3.3.1, we used longer intervals, of 30 seconds. Full widths at half maximum (FWHM) of the synthesized beams in final images vary depending on the individual *uv* coverage of the observations, but were typically $\simeq 3''.5 \times 9''$.

As an additional test, we tried self-calibration and imaging of the final list of OHPNe candidates included in Section 3.3.1 using the Astronomical Image Processing System (AIPS). No significant difference in signal-to-noise (S/N) ratio was found with respect with the processing with CASA.

3.2.2 Additional VLA and ATCA data

We searched the archives of ATCA, and *Karl G. Jansky Very Large Array* (VLA) for additional radio continuum data at different frequencies, in the fields containing the OHPNe candidates mentioned in section 3.3.1 within the primary beam of the antennas. We also included data at a wavelength of 7 mm from our own observations of the project C3324 with ATCA. Details of all these additional observations are shown in Table 3.1.

For the published data, we used the flux density values reported in the chapters cited in Table 3.1. For the unpublished data, we carried out a complete process of data reduction.

The unpublished ATCA data were processed, calibrated and imaged following the same procedures mentioned in section 3.2.1, applying self-calibration when the S/N ratio was high enough. In the particular case of the project code C1977, we combined the visibilities

Table 3.1: Additional ATCA and VLA data.

Telescope	Configuration[a]	Project Id.	Date	Frequency[b] GHz	Bandwidth[c] MHz
VLA	CnB	AB573	1990-Oct-03[d]	4.9	25
ATCA	6D	C1088	2004-Apr-07[e]	4.8	128
				8.6	128
ATCA	6A	C1450	2005-Apr-02[f]	4.8	128
				8.6	128
			2010-Feb-02	5.5	2000
				9.0	2000
ATCA	6B	C1610	2006-Dec-08	1.4	128
				2.4	128
			2006-Dec-10	4.8	128
				8.6	128
ATCA	6A	C1977	2010-Dec-25	5.5	2000
				9.0	2000
			2010-Dec-28	5.5	2000
				9.0	2000
VLA	C	16A-174	2016-Jun-09	5.8	3324
			2016-Jun-25	5.8	3324
VLA	D	17A-197	2017-Mar-31	5.8	3224
ATCA	H168	C3324	2019-Oct-21	43.0	2000
				45.0	2000
VLA	C	20A-160	2020-Apr-07[g]	3.0	2000

[a] Configuration of the antenna array during the observations.
[b] Central frequency of the observed band.
[c] Total bandwidth.
[d] Results published by White, Becker, & Helfand (2005).
[e] Results published by Urquhart et al. (2007).
[f] Results published by Bains et al. (2009).
[g] Results published by Gordon et al. (2021).

obtained in two different epochs (of observations 3 days apart), to obtain a single image with improved *uv* coverage and sensitivity. For the C3324 observations, performed at 43 and 45 GHz, we tested self-calibration with CASA and AIPS. It turned out that the final images obtained with AIPS procedures had a better S/N ratio, by a factor of about two. Thus, the results presented for those data are the ones obtained with AIPS self-calibration and imaging. In particular, we applied amplitude and phase self-calibration with solution intervals of 6 seconds. We note that the definition of the robust parameter of Brigg's weighting in AIPS is different from that of CASA. We set a robust parameter of zero in AIPS, which is equivalent of 0.5 in CASA.

The unpublished archival VLA data from 2016 and 2017 (project codes 16A-174 and 17A-197, respectively) were processed with CASA. Calibration was carried out with the VLA pipeline implemented in CASA, and further processing was also performed using standard CASA procedures. These observations were composed of different fields with phase centers located relatively close to one another. Two of our sources were included within the primary

TABLE 3.2: Confirmed OHPNe and new candidates discovered in SPLASH–ATCA data.

Source name[a]	Radio continuum emission peak RA (J2000) DEC (J2000)	Maser coordinates[b] RA (J2000) DEC (J2000)	Transition MHz	δ^c arcsec	$\Delta\sigma_m{}^d$ arcsec	Classification[e]
IRAS 16333–4807	16 37 06.603 –48 13 42.74	16 37 06.581 –48 13 42.54	1612	0.22	0.08	PN
		16 37 06.567 –48 13 42.32	1667	0.42	0.03	
		16 37 06.588 –48 13 42.39	1720	0.35	0.03	
		16 37 06.535 –48 13 42.35	1720	0.39	0.03	
		16 37 06.636 –48 13 41.44	1720	0.30	0.03	
		16 37 06.628 –48 13 42.43	1720	0.31	0.03	
		16 37 06.634 –48 13 42.46	1720	0.28	0.03	
IRAS 16372–4808[f]	16 40 55.812 –48 13 59.84	16 40 55.824 –48 13 59.82	1612	0.21	0.03	ES
OH 341.6811+00.2634	16 51 53.637 –43 47 16.48	16 51 53.641 –43 47 16.47	1612	0.11	0.19	U
JaSt 23	17 40 23.068 –27 49 12.13	17 40 23.057 –27 49 12.16	1612	0.04	0.03	PN
		17 40 23.064 –27 49 12.18	1612	0.09	0.03	
		17 40 23.056 –27 49 12.87	1665	0.86	0.03	
IRAS 17375–2759	17 40 38.575 –28 01 04.91	17 40 38.562 –28 01 02.28	1612	2.64	0.03	ES[g]
		17 40 38.591 –28 01 02.39	1667	2.54	0.03	
IRAS 17393–2727	17 42 33.139 –27 28 25.34	17 42 33.123 –27 28 25.05	1612	0.31	0.03	PN
		17 42 33.124 –27 28 25.03	1612	0.33	0.03	
		17 42 33.120 –27 28 25.02	1612	0.34	0.03	
		17 42 33.125 –27 28 25.17	1612	0.18	0.03	
		17 42 33.117 –27 28 25.13	1612	0.21	0.03	
		17 42 33.110 –27 28 25.11	1612	0.26	0.03	
		17 42 33.121 –27 28 25.22	1665	0.14	0.03	
		17 42 33.100 –27 28 25.41	1667	0.11	0.03	
		17 42 33.115 –27 28 25.03	1667	0.33	0.03	
		17 42 33.119 –27 28 24.93	1667	0.43	0.03	
		17 42 33.100 –27 28 25.06	1667	0.31	0.03	
IRAS 17494–2645	17 52 30.817 –26 46 17.68	17 52 30.815 –26 46 16.68	1612	1.00	1.00	U
IRAS 18019–2216	18 04 57.391 –22 15 50.97	18 04 57.387 –22 15 51.28	1612	0.31	0.25	U
		18 04 57.391 –22 15 50.58	1612	0.39	0.03	
		18 04 57.413 –22 15 49.41	1612	1.19	0.03	

[a] Source names in boldface indicate those for which the association between OH maser and radio continuum emission is reported here for the first time.
[b] Coordinates reported in Qiao et al. (2016b, 2018, 2020).
[c] Relative distance between the radio continuum emission peak and the OH maser spot.
[d] Relative positional accuracy between maser and continuum at 2.1 GHz.
[e] Classification in Qiao et al. (2016b, 2018, 2020). ES, PN, and U represent evolved star, planetary nebula, and object of unknown nature, respectively.
[f] The association between radio continuum and OH maser emission was reported by Bains et al. (2009), although these authors did not consider it to be an OHPN.
[g] The nature of this source as a PN will be discussed in Cala et al. (in preparation).

beam of several of these pointings. Thus, for each of our targets, we created mosaic maps with the fields containing them, in order to increase the final S/N ratio at the target position. As in the case of the SPLASH–ATCA data described above, the images containing IRAS 18019-2216 were obtained by using only baselines longer than 7 kilolamda. We attempted self calibration, but we did not obtain any improvement in the image quality of these data.

3.3 Results

3.3.1 OHPNe candidates in SPLASH–ATCA

We searched in the processed continuum images the catalogued positions of the OH maser-emitters sources of Qiao et al. (2016b, 2018, 2020). We kept only those where the coincidence between the OH maser relative to the continuum source were smaller than the FWHM synthesized beam ($\theta \simeq 3''.5 \times 9''$) of the continuum. Afterwards, we discarded all objects

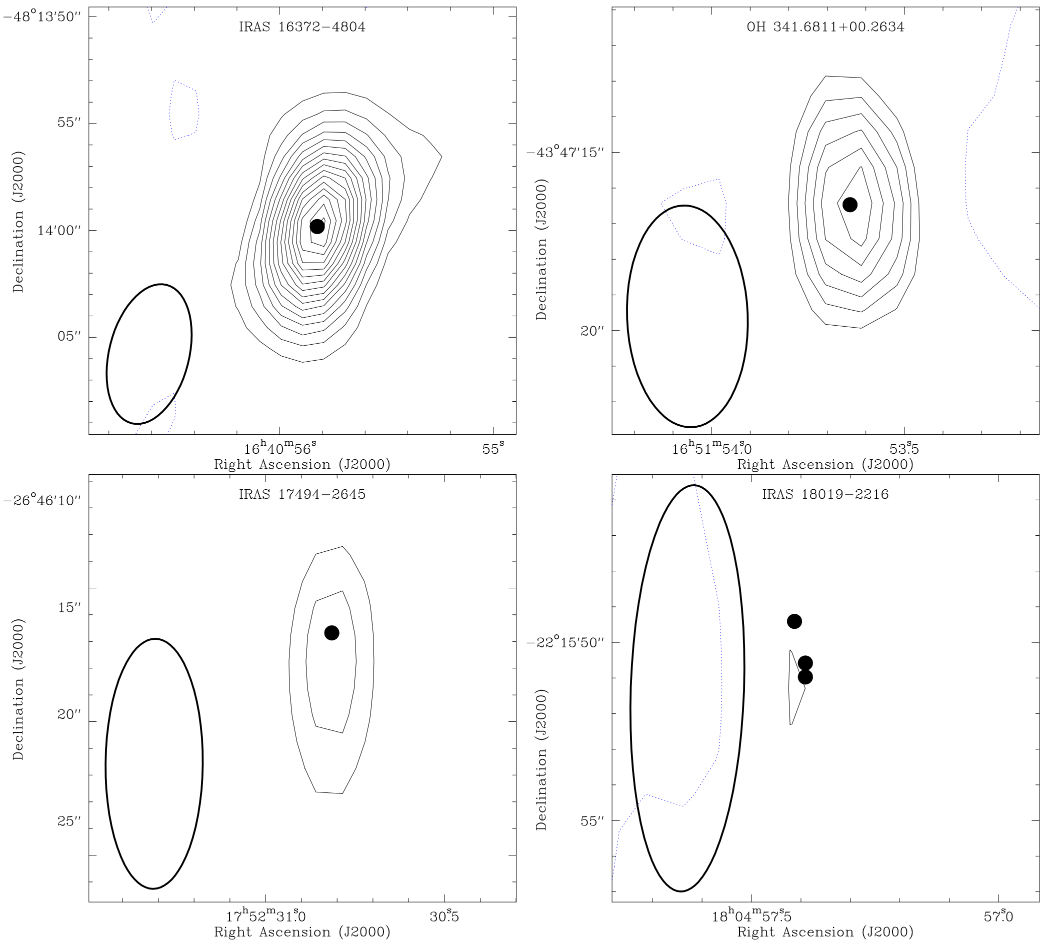

FIGURE 3.1: Contour maps of the radio continuum emission at 2.1 GHz of the new OHPNe candidates (Table 3.2). The black filled circles mark the location of the spectral OH maser features at 1612 MHz. The thick-lined ellipse represents the FWHM of the synthesized beam of each continuum image. Solid black and dotted blue contours represent positive and negative intensity values, respectively. *Top left.* IRAS 16372–4808: the first contour level and the increment step are two times σ (where σ = 0.24 mJy beam^{-1} is the rms of the map). The beam size is (6.68″ × 3.75″, p.a. = −14°). *Top right.* OH 341.6811+00.2634: the first contour level is 2σ and the increment step is 1σ (σ = 0.31 mJy beam^{-1}). The beam size is (6.23″ × 3.39″, p.a. = 2°). *Bottom left.* IRAS 17494–2645: the contour levels are 2σ and 3σ (σ = 0.31 mJy beam^{-1}). The beam size is (9.36″ × 3.64″, p.a. = 0°). *Bottom right.* IRAS 18019–2216: the contour levels are −2σ and 2σ (σ = 0.20 mJy beam^{-1}). The beam size is (11.41″ × 3.18″, p.a. = −2°). See also Fig. 3.2.

classified as SFRs or supernova remnants in Qiao et al. (2016b, 2018, 2020), and kept only with those identified as evolved stars or objects of unknown nature that could be evolved stars. We also rejected two cases (G359.567+1.147 and G008.483+0.176) of relatively close spatial match between maser and continuum emission (within ≃ 5″), even if the maser might be associated with an evolved star, but a literature search showed that the continuum emission traces an extragalactic object. We also detect IRAS 18043–2116, a WF post–AGB star (Walsh et al. 2009), whose radio continuum emission has been studied by Pérez-Sánchez et al. (2017). The remaining sources with a positive match, are reported in Table 3.2.

This match criterion of OH masers being within one synthesized beam of the continuum

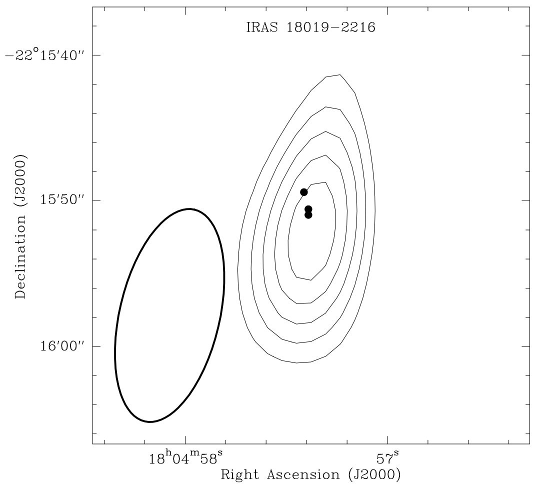

FIGURE 3.2: Contour map of the continuum emission at 5 GHz in IRAS 18019–2216, taken on 2017 March 31. The black circles mark the location of the spectral OH maser features at 1612 MHz. The first contour level is $2 \times \sigma$, and the increment step is $1 \times \sigma$ ($\sigma = 90$ μJy beam^{-1}. The thick-lined ellipse represents the FWHM of the synthesized beam of the continuum image ($14''.93 \times 6''.87$, p.a. = –13°).

emission seems adequate, since interferometric observations consistently show at least one OH spectral component and OH transition very close to the peak of the radio continuum emission in OHPNe ($\leq 1''$; Uscanga et al. 2012; Gómez et al. 2016). Moreover, OHPNe are angularly small in images (at optical, infrared or radio wavelengths), with sizes extending $\leq 3''$ from the nebular center (e.g., Miranda et al. 2001; de Gregorio-Monsalvo et al. 2004; Uscanga et al. 2014). Thus, even if OH emission was to be excited at the tip of the lobes, our match criterion would associate continuum and maser emission. In any case, the largest distance between OH and continuum emission in Table 3.2 is $\sim 1''$, whereas the shortest distance for sources that did not fulfill our criterion is $\sim 15''$. Therefore, we believe that our distance criterion did not reject any true association, whereas false positives are highly unlikely.

Table 3.2 gives the parameters of the continuum emission peaks at 2.1 GHz for these sources, as well as the coordinates of the OH maser components associated with the continuum sources. The distances of the maser components to the continuum sources (δ) are also derived. Since the maser and continuum observations were simultaneous, they share the same interferometric fringe phase calibration. Therefore, the 1-σ error of the relative position between maser and continuum emission is $\Delta\sigma_m \sim \theta/(2 \times \mathrm{S/N})$ (Reid et al. 1988), where θ is the apparent source size (corresponding to the FWHM of the beam for unresolved sources), and S/N is the signal-to-noise ratio of the emission. The absolute astrometric accuracy in SPLASH–ATCA is $< 1''$ (Qiao et al. 2016b).

In total, over the area of 176 deg^2 covered by SPLASH–ATCA, we found a match between OH maser and radio continuum emission in eight objects that are likely to be OHPNe. Three of these objects are already known OH emitters that are bona-fide PNe (IRAS 17393–2727, JaSt 23, and IRAS 16333–4807; Uscanga et al. 2012; Qiao et al. 2016b). The association of

OH maser and continuum emission in IRAS 17375–2759 was confirmed by Uscanga et al. (2012), but these authors classified it as an OHPN candidate. The nature of this source as a PN will be discussed in a forthcoming paper (Cala et al. in preparation). Three more objects of unknown nature are reported here for the first time: OH 341.6811+00.2634, IRAS 17194–2645, and IRAS 18019–2216. Finally, for IRAS 16372–4808 the association between OH maser and radio continuum emission was reported by Uscanga et al. (2012), but it was not considered to be an OHPN, based on its previous classification as a post–AGB star by Bains et al. (2009). However, as discussed below, there is not enough evidence to discard the nature of IRAS 16372–4808 as PN. Considering this re-evaluation of the source, we included it in the remaining of this chapter as a new OHPN candidate.

Radio continuum images at 2.1 GHz of these 4 new OHPN candidates using SPLASH–ATCA data are shown in Fig. 3.1. In the case of IRAS 18019–2216, this emission was only at a 2-sigma level, although coincident with the position of the maser components. The archival VLA observations at 5 GHz have confirmed the presence of radio continuum emission (Fig. 3.2).

3.3.2 Radio continuum emission and spectral indices

We have explored the flux density (S_ν) dependence on frequency (ν) of the radio continuum emission. In data with high S/N, the observed band of individual observations was separated on smaller frequency subbands ($\simeq$ 500 MHz). The dependence of flux density on frequency is presented in Table 3.3 and Fig. 3.3. The resulting spectral indices, α (defined as $S_\nu \propto \nu^\alpha$) are also presented in the individual panels of that figure.

The spectral indices of the radio continuum provide useful information on the nature of these sources. For all four OHPNe candidates of SPLASH, they are consistent with the expected values for thermal (free-free) radiation from photoionized gas, which ranges between $\alpha = +2$ (optically thick regime) at low frequencies and $\alpha = -0.1$ (optically thin regime) at high frequencies. The values we obtained suggest the presence of an ionized region that is partially optically thick at radio wavelengths.

For ionized regions with nearly constant electron density, one would expect a relatively abrupt transition between the optically thick emission at low frequencies and the optically thin regime at high ones. This is the common trend observed in PNe (see, e.g., Aaquist & Kwok 1991). This transition between opacity regimes determines a turnover frequency that is directly related to the emission measure of the ionized gas ($EM = \int n_e^2 dl$, where n_e is the electron density profile, and l is the linear distance along the line of sight). Thus, a higher n_e would result in a higher turnover frequency. In our candidates, the radio spectrum does not flatten to $\alpha = -0.1$, at the frequencies sampled (up to $\sim 2 - 45$ GHz). Such high turnover frequencies are considered to be a sign of youth in PNe (Kwok et al. 1981).

TABLE 3.3: Radio continuum flux density of the OHPNe candidates.

No.	OHPNe candidate	Frequency GHz	S_ν mJy	rms mJy beam^{-1}	Date
1	IRAS 16372–4808	1.38	4.8 ± 1.0	0.4	2006-Dec-08
		2.10	8.3 ± 0.4	0.24	2013-Oct-25
		2.38	10.0 ± 0.5	0.21	2006-Dec-08
		4.73	19.0 ± 1.1	0.5	2010-Feb-02
		4.80	15.10 ± 0.5	0.3	2004-Apr-07[a]
			15.17 ± 0.20	0.10	2005-Apr-02[b]
			15.03 ± 0.4	0.18	2006-Dec-10
		5.23	18.25 ± 1.0	0.5	2010-Feb-02
		5.73	21.8 ± 1.25	0.4	2010-Feb-02
		6.23	24.1 ± 1.0	0.4	2010-Feb-02
		8.23	29.20 ± 0.8	0.22	2010-Feb-02
		8.64	27.8 ± 0.6	0.3	2004-Apr-07[a]
			24.6 ± 0.5	0.25	2005-Apr-02[b]
			23.6 ± 0.6	0.21	2006-Dec-10
		8.73	30.1 ± 0.7	0.21	2010-Feb-02
		9.23	32.4 ± 0.7	0.23	2010-Feb-02
		9.73	33.6 ± 0.7	0.23	2010-Feb-02
		43.0	58.0 ± 0.1	0.03	2019-Oct-21
		45.0	58.6 ± 0.034	0.01	2019-Oct-21
2	OH 341.6811+00.2634	2.10	1.5 ± 0.5	0.3	2013-Oct-28
		5.50	2.8 ± 0.9	0.6	2010-Dec-28
		9.00	3.9 ± 1.0	0.7	2010-Dec-28
		43.0	16.4 ± 0.1	0.03	2019-Oct-21
		45.0	16.6 ± 0.13	0.1	2019-Oct-21
3	IRAS 17494–2645	2.10	1.4 ± 0.4	0.3	2006-Feb-26
		3.0[c]	1.9 ± 0.3	0.01	2020-Apr-07
		4.65	3.6 ± 0.14	0.1	2016-Jun-09
		4.85[d]	1.8 ± 0.34	0.3	1990-Oct-03
		6.95	6.2 ± 0.13	0.1	2016-Jun-09
4	IRAS 18019–2216	2.10	0.2 ± 0.07[e]	0.1	2016-Mar-01
		4.65	0.7 ± 0.1	0.1	2016-Jun-25
			0.4 ± 0.14	0.1	2017-Mar-31
		6.95	0.8 ± 0.14	0.1	2016-Jun-25
			0.6 ± 0.14	0.1	2017-Mar-31

Reported in Urquhart et al. (2007).
[b] Reported in Bains et al. (2009).
[c] Reported in Gordon et al. (2021).
[d] Reported in White et al. (2005).
[e] Detected with S/N ≃ 2.

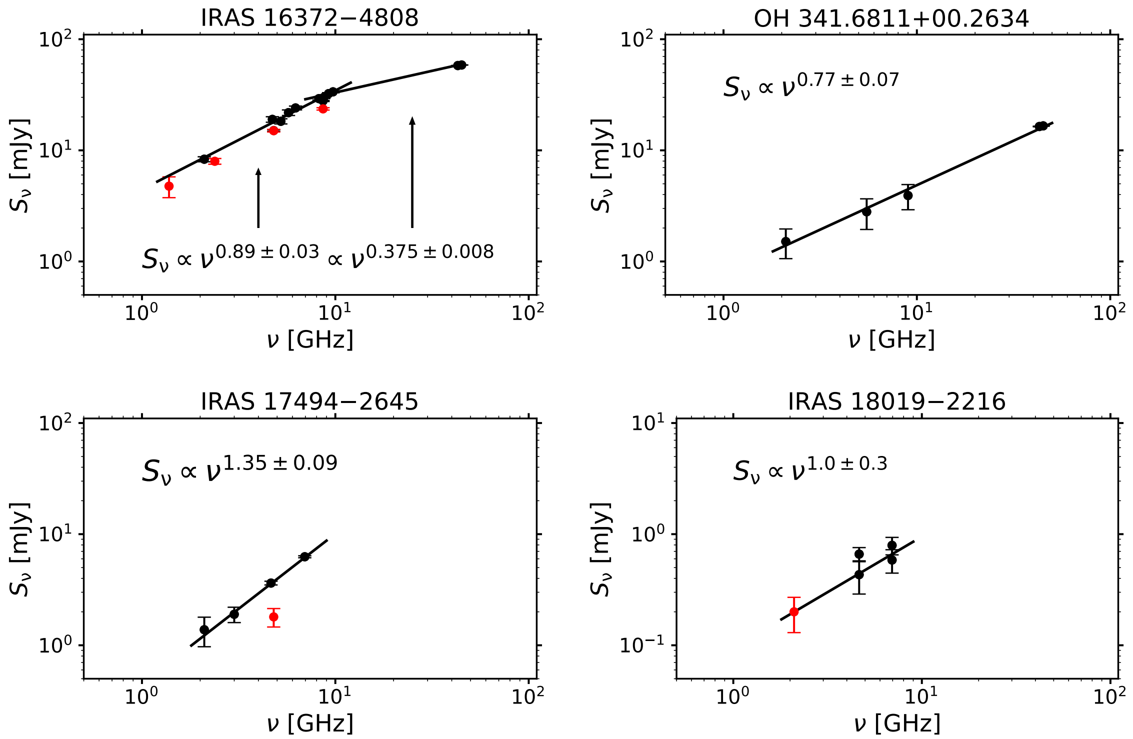

FIGURE 3.3: Radio continuum spectra of the new OHPNe candidates. Black and red circles represent the flux densities and its errors at different epochs (see below and Table 3.3). In some data points, the errors are smaller than the symbol sizes. The solid lines are least-square linear fits to $\log(S_\nu)$ vs $\log(\nu)$, whose slope gives the estimated spectral index. These fits were obtained using the data marked as black circles (see below). Notes: *IRAS 16372–4808:* Spectral indices shown in the figure were obtained with data taken on or after 2010 (black points), resulting in $\alpha = 0.89 \pm 0.03$ between 2.1 – 9.7 GHz, and $\alpha = 0.39 \pm 0.04$ between 8.7 – 45 GHz. A comparison with data taken on or before 2006 (red points) shows an increase of flux density with time, while maintaining a similar spectral index of 0.082 ± 0.04. *IRAS 17494–2645:* The red circle represents the flux density at 5 GHz in 1990, which seems to have increased by a factor of 2.0 ± 0.45 in 26 yr. *IRAS 18019–2216:* The red point represents the flux density detected with an S/N $\simeq 2$ at 2.1 GHz in this chapter. The spectral index was obtained using at 4.65 and 6.95 GHz the arithmetic mean (weighted by the inverse of noise squared) of data at the different epochs. A value of $\alpha = 0.59 \pm 0.75$ is obtained if the value of flux density at 2.1 GHz is ignored in the computation.

We also note that the spectral indices are relatively constant over a wide range of frequencies. This behaviour is also consistent with these objects being nascent PNe. At the very first stages of photoionization of the previously expelled CSE, the electron density of the ionized gas should be consistent with that of the envelope ($n_e \propto r^{-2}$, where r is the distance from the central star). An ionized region with that radial dependence would be partially optically thick over a wide range of frequencies, with spectral index $\alpha \simeq 0.6$ (Olnon 1975). The radio spectrum of the new OHPNe candidates shown in Fig 3.3 are, in some cases, relatively close to that value of $\alpha = 0.6$, specially for OH 341.6811+00.2634. The data at 43–45 GHz for IRAS 16372–4808 suggest that the source is becoming optically thinner at high frequencies, but a better frequency sampling above 10 GHz would be needed to accurately determine the spectral index in that range. These spectral indices ~ 0.6, are also found in confirmed OHPNe (e.g., K 3–35 and IRAS 17347-3139; Aaquist 1993; Gómez et al. 2005; Tafoya et al. 2009). Assuming a power-law distribution of ionized gas density with spherical symmetry ($n_e \propto r^{-q}$; Olnon 1975), values for $q = 2.2$, 2.4 and 2.6 are obtained for OH 341.6811+00.2634, IRAS 16372–4808, and IRAS 18019–2216, using the obtained spectral indices $\alpha \simeq 0.77$, 0.89, and 1.0 respectively. For the case of IRAS 17494–2645, the spectral index of 1.35 would imply, in principle, a steep power-law index $q = 3.4$. However, the emission of this source is supposed to be in the optically thick regime, and the spectral index may not reflect such a radial dependence on electron density. This could happen if the electron density is higher than those in the other candidates. We speculate that observations at $\nu > 10$ GHz may derive a flatter spectral index, closer to 0.6.

Another interesting property is time variation of the radio continuum emission. We have consistently found an increase of flux density, both in the four new OHPNe candidates discussed here, as well as several of the already confirmed OHPNe in Table 3.2. Regarding the known OHPNe whose continuum emission we detected in SPLASH–ATCA, the flux density at 2.1 GHz of JaSt 23 has increased, in around 3.5 yr, by a factor of 1.49 ± 0.26, with respect to the value reported by Gómez et al. (2016).

For our new OHPNe candidates, in IRAS 16372–4808 the flux densities at 4.8 and 8.4 GHz increased by a factor of 1.26 ± 0.11 and 1.26 ± 0.06 in around 6 and 5 yr, respectively (see Table 3.3). White et al. (2005) reported for IRAS 17494–2645 an $S_\nu = 1.8 \pm 0.3$ at 5 GHz. We obtained $S_\nu = 3.6 \pm 0.14$ mJy and $S_\nu = 6.3 \pm 0.14$ mJy at 4.65 and 6.95 GHz, respectively (see Table 3.3). Hence, the flux density of this source has increased by a factor of 2.0 ± 0.45 in around 26 yr. These variations are further discussed in Section 3.4.

The increase in flux density of radio continuum emission in nascent PNe could be interpreted as expansion of the ionization front. In this case, the flux density would be proportional to R^2, where R is the radius of the ionized region. This was the interpretation given by Gómez et al. (2005) and Tafoya et al. (2009) for the increasing emission in the OHPN IRAS 17347–3139. This source also fell within the sky coverage of SPLASH, although we did not detect its OH maser emission, which was weaker than the detection limit of the survey. We did detect, however, its continuum emission, and confirmed its increasing flux density, with $S_\nu = 54.5 \pm 4.4$ mJy. This means that, with respect to the flux density expected at 2.1 GHz in Tafoya et al. (2009), it has increased by a factor of 1.74 ± 0.23 in around 11 yr. This increase is roughly consistent with the factor of 1.31 ± 0.05 at 9.4 GHz in 13 yr found by (Gómez et al. 2005).

It is obvious that, considering this variability, spectral indices should be taken with care. A more accurate determination of spectral indices would require observations that are simultaneous or at least taken over a very short time interval. Despite this intrinsic uncertainty in obtaining numerical values, the radio spectra in Fig. 3.3 show robust trends for these objects.

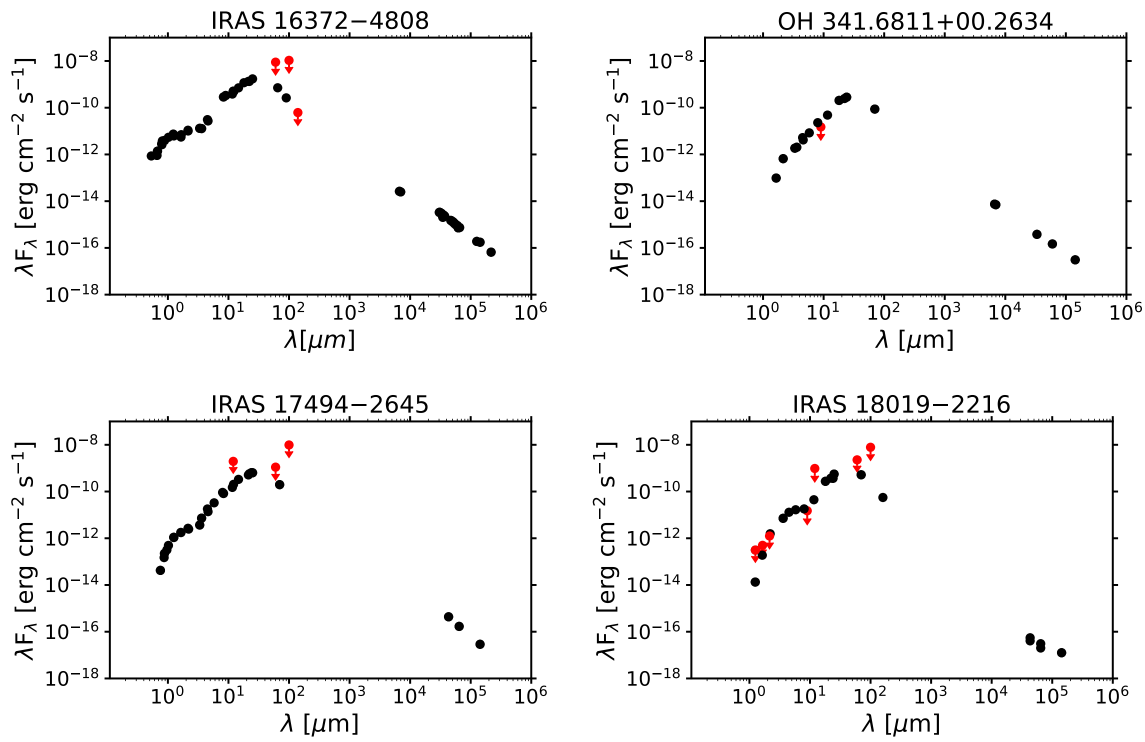

FIGURE 3.4: SED of the new OHPNe candidates, using optical and infrared photometric data mentioned in Section 3.3.3 and radio continuum emission from Table 3.3. Filled black circles are the photometric measurements, while red symbols and arrows represent upper limits.

3.3.3 Optical-Infrared spectral energy distribution (SED)

In order to better understand the circumstellar material surrounding these possible PNe, we obtained the optical-infrared SED of the four OHPNe candidates using archival data from $\sim$ 1 - 140 μm. To this end, we gathered information from the Two Micron All Sky Survey (*2MASS*), *AKARI*, the Deep Near Infrared Survey of the Southern Sky (*DENIS*), *Gaia*, the *Herschel Space Observatory*, Infrared Astronomical Satellite (*IRAS*), the Midcourse Space Experiment (*MSX*), the Panoramic Survey Telescope and Rapid Response System (*Pan-STARRS*), the *Spitzer Space Telescope*, the United Kingdom Infra-Red Telescope (*UKIDSS*), the *USNO-B* catalog, the Visible and Infrared Survey Telescope for Astronomy (VISTA) variable survey (*VVV*) and the Wide-field Infrared Survey Explorer (all-*WISE* survey). These photometric data are presented in Fig. 3.4, which includes also the radio continuum data previously plotted in Fig. 3.3.

The SEDs of all four objects are similar to each other, with a peak at $\lambda < 70$ μm. This is also consistent with the SEDs observed in the rest of confirmed OHPNe (Uscanga et al. 2012), as well as in obscured post–AGB stars and PNe, in general (e.g. Ramos-Larios et al. 2009, 2012). This peak of the SED is characteristic of PNe, rather than H II regions around massive YSOs, which also show thermal radio continuum emission but whose SED tends to peak at longer wavelengths ($\geq$ 100 μm; Wood & Churchwell 1989; Anderson et al. 2012).

3.4 Notes on the new OHPN candidates

A summary of the radio continuum and OH maser parameters of the four OHPN candidates is given in Tables 3.3 and 3.4, respectively. In particular, Table 3.4 illustrate the number of OH maser components in each source, and the figure number in Qiao et al. papers where their OH spectra can be consulted. In this section, we provide a detailed description for each object.

3.4.1 IRAS 16372–4808

The OH emission from this source was first reported in the ATCA/VLA survey of Sevenster et al. (1997a), showing a single-peaked spectrum with a flux density of $S_\nu = 2.25 \pm 0.03$ Jy at 1612 MHz in 1994. Its flux density has remained relatively stable in subsequent observations (Deacon et al. 2004; Qiao et al. 2016b). No H_2O maser emission has been detected towards this source (Deacon et al. 2007).

The radio continuum emission in this object was first reported by Urquhart et al. (2007). As mentioned above, our results show that the radio continuum of this object has increased by a factor of ~ 1.2 in around 10 yr (Table 3.3).

Bains et al. (2009) noticed the spacial coincidence between radio continuum and OH maser emission using interferometric data. They argue that this object is a post–AGB star. This conclusion is based on an DUSTY modeling (Ivezic et al. 1999) of its CSE, from which was obtained an $T_{\rm eff} \simeq$ 14,400 K for its central star, which is significantly lower than ∼25,000 K necessary to sustain a photoionized nebula. Thus, Bains et al. (2009) suggested that the radio continuum emission may arise from a shock-ionized nebula. However, we note that DUSTY assumes spherical symmetry of the CSE, but post–AGB stars with radio continuum emission usually have non-spherical morphologies (e.g. M 1–92, Hen 3–1475, the Red Rectangle, IRAS 15445–5449 or IRAS 18043–2116 in Bujarrabal et al. 1994; Borkowski et al. 1997; Cohen et al. 2004; Pérez-Sánchez et al. 2011, 2017, respectively). Furthermore, the spatially resolved emission from radio, infared and/or optical observations of the OHPNe K 3-35, IRAS 17347–3139 and IRAS 16333–4807 show bipolar nebulae with a toroidal structure at their equatorial plane (see Miranda et al. 2001; de Gregorio-Monsalvo et al. 2004; Uscanga et al. 2008; Tafoya et al. 2009; Sánchez Contreras & Sahai 2012; Uscanga et al. 2014). Therefore, the effective temperature obtained with DUSTY may not be accurate. Our results are compatible with the radio continuum emission arising from photoionized gas (see Sections 3.3.2 and 3.5.2).

We found a source (GAIA EDR3 5941005128417236224) in the GAIA EDR3 catalog (Gaia Collaboration et al. 2021), whose reported position is $\simeq 1.''4$ away from the radio continuum emission peak. Considering that this distance is small, but somehow larger than the estimated astrometric uncertainty of SPLASH–ATCA ($\simeq 1''$), the association of IRAS 16372–4808 with this optical source is uncertain. Furthermore, infrared J and K images from the *VVV* survey (Fig. 3.5) show at least two distinct sources, separated by $\simeq 1.''4$. The source detected in GAIA (R.A. [J2000] = 16:40:55.690559 ($\pm 0.00008''$), DEC [J2000] –48:13:59.20725 ($\pm 0.00005''$) coincides with the western *VVV* source, while the OH maser and radio continuum, as well as the mid and far infrared emission (e.g, all-WISE survey) is spatially coincident with the eastern source. Therefore, this OHPN candidate could be a different object from the one showing the optical counterpart. Alternatively, the two infrared sources may trace two lobes of the same PN, tracing a bipolar morphology. Spectroscopic observations will also be useful to ascertain the true optical/infrared counterpart of the OHPN candidate.

3.4.2 OH 341.6811+00.2634

The 1612 MHz OH maser emission was reported for the first time with the SPLASH–ATCA observations (Qiao et al. 2016b). The spectrum of the OH maser emission is single-peaked, with $S_\nu = 0.66 \pm 0.07$ Jy. No H_2O maser was detected in the H_2O Southern Galactic Plane Survey (HOPS; Walsh et al. 2011, 2014).

With the SPLASH–ATCA data we also report for the first time this object as a radio continuum-emitter, as well as the interferometric coincidence between the radio continuum source and the 1612 MHz OH maser emission (Fig. 3.1, top right).

No obvious optical counterpart can be identified in DSS images and in the GAIA EDR3 catalog. We found, however, an *IRAS* source relatively close ($\sim 27''$) to the position of the radio continuum peak at 2.1 GHz of OH 341.6811+00.2634. This source is IRAS 16483-4342. However, the flux densities reported for IRAS 16483-4342 (3.59 Jy and 191 Jy at 25 μm and 100 μm, respectively) are higher than the ones reported in *MIPSGAL* and by the *Herschel* telescope (2.26 Jy and 2.04 Jy at 24 μm and 70μm, respectively) at a location close to the radio continuum emission. Therefore, IRAS 16483-4342 and OH 341.6811+00.2634 seem to be two different sources.

This OHPN candidate is associated in SIMBAD with the infrared source SSTGLMC 341.6811+00.2634, and for which infrared images in K band retrieved from the *VVV* survey (spatial resolution $\sim 0.''42$) show unresolved emission.

3.4.3 IRAS 17494–2645

Single-peaked 1612 MHz OH maser emission was discovered by Sevenster et al. (1997a), showing $S_\nu = 2.62 \pm 0.03$ Jy. The spectrum reported in SPLASH–ATCA by Qiao et al. (2018) shows $S_\nu = 3.05 \pm 0.07$ Jy. Variability in the maser emission cannot be confirmed because the spectral resolution of the spectrum presented in Sevenster et al. (1997a) is different from that of Qiao et al. (2018) (1.36 km s^{-1} and 0.09 km s^{-1}, respectively). No H_2O maser was detected in HOPS (Walsh et al. 2011, 2014).

The radio continuum emission at 5 GHz on this source was detected in observations made in 1990 (White et al. 2005). Its flux density seems to have increased by a factor of 2.0 ± 0.45 in around 26 yr, as mentioned above (Table 3.3 and Section 3.3.2). While both OH maser and radio continuum emission has been previously reported individually, our SPLASH–ATCA data allow us to accurately ascertain their mutual association (Fig 3.1, bottom left).

No obvious optical counterpart can be identified in either DSS images or the GAIA EDR3 catalog. However, the radio continuum emission peak at 2.1 GHz of IRAS 17494–2645 coincides with a star-like object in PanSTARRS (ID: 75872681281354413), with a reported mean AB magnitude in filter i (at ∼7545 Å) of 21.33 ± 0.03 mag. Infrared emission from Ks and J filters taken from the *VVV* survey (resolution of $0.''45$ and $0.''70$, respectively) show spatially unresolved emission from the object.

3.4.4 IRAS 18019–2216

Sevenster et al. (1997a) reported the 1612 MHz OH maser spectrum with a single feature showing $S_\nu = 1.33 \pm 0.03$ Jy at -31.8 ± 1.36 km s^{-1}. Sevenster et al. (2001) reported afterwards $S_\nu = 0.96 \pm 0.03$ Jy at -32.2 ± 1.36 km s^{-1}. With respect to these spectra, the spectrum presented in Qiao et al. (2020) shows two new additional maser features. The brightest single feature shows $S_\nu = 0.77 \pm 0.07$ Jy at -31.3 ± 0.1 km s^{-1}. With respect to this previously detected brightest feature, one of the two new observed maser spots is redshifted, whereas the other one is blueshifted. The former shows 0.74 ± 0.07 Jy at -35.6 ± 0.1 km s^{-1}, and the latter shows 0.23 ± 0.07 Jy at -27.2 ± 0.1 km s^{-1}. The three features show a rough north–south (N-S) distribution in Fig. 3.1, along a length of $\sim 1.''8$. However, given the N-S elongation of the synthesized beams, this distribution is highly uncertain. High–angular resolution observations, with a better *uv* coverage are needed to accurately determine the structure traced by the OH maser emission. No H_2O maser was detected in HOPS (Walsh et al. 2011, 2014).

With the SPLASH–ATCA data we detected this object for the first time in the radio continuum, as well as we reported here for the first time interferometric association between the radio continuum and the OH maser (Fig 3.1, bottom right). We found IRAS 18019–2216 with an $S/N \simeq 2$ at 2.1 GHz, and we were able to detected it in two different epochs from the VLA archive at 4.65 GHz and 6.95 GHz (see Table 3.3).

We did not find an optical counterpart for this source. In SIMBAD it is catalogued as the YSO candidate SSTGLMC G007.9579–00.3931. Infrared images in K band taken from the *VVV* survey show spatially unresolved emission (resolution $\sim 0.''40$).

TABLE 3.4: Properties of OH maser emission at 1612 MHz for the new OHPN candidates[a].

Name	SPLASH–ATCA ID	$\upsilon_{\rm LSR}$[b] km s^{-1}	S_ν[c] Jy	Figure[d]
IRAS 16372–4808	G337.064−1.173	−90.5	1.94	1, 40
OH 341.6811+0.2634	G341.681+0.264	54.0	2.16	1, 126
IRAS 17494–2645	G002.640−0.191	124.1	6.10	2, 295
IRAS 18019–2216	G007.958−0.393	−31.3	2.09	3, 325
		−35.6	1.47	
		−27.2	0.18	

[a] Values correspond to the individual OH maser components identified in the SPLASH–ATCA observations by Qiao et al. (2016b, 2018, 2020).
[b] Local standard of rest velocity of the OH maser components.
[c] Flux density of the OH maser components.
[d] Figure number for the OH spectrum in the corresponding references: 1: Qiao et al. (2016b); 2: Qiao et al. (2018); 3: Qiao et al. (2020).

3.5 Discussion

3.5.1 The nature of the OHPN candidates as evolved stars

Our main criterion to look for new nascent PNe is based on determining a spatial coincidence between OH maser and radio continuum sources, using interferometric observations. However, there are other sources, different from PNe, which can show both types of emission. The first step to ascertaining the nature of these sources is to determine whether they are evolved stars, or if they could be YSOs. Massive YSOs can sustain photoionized regions around them. However, the properties of our OHPNe candidates are more consistent with their being stars in the last stages of stellar evolution.

The first clue is the OH transition detected in these objects. While massive YSOs are commonly associated to the main-line OH masers at 1665 MHz and 1667 MHz transitions (e.g., Caswell, Haynes, & Goss 1980; Szymczak & Gérard 2004), our OHPNe candidates only show OH maser emission at 1612 MHz. This is a typical characteristic of OH masers in evolved stars. In fact, while stars from the AGB up to the PN phases can show also OH maser emission at other frequencies, the satellite line at 1612 MHz is generally brighter than the main-line OH masers in these type of objects (Lewis 1997). This is also the case of all confirmed OHPNe (Uscanga et al. 2012; Qiao et al. 2016a).

Line emission from different molecules can also provide further constraints. For instance, methanol maser emission is widespread in massive star-forming regions, often associated with interstellar OH masers (Menten 1991). Furthermore, methanol masers have never been detected in CSE (Breen et al. 2013; Gómez et al. 2014). The position of all our sources was covered by the Methanol Multibeam Survey, but none was detected (Caswell et al. 2010, 2011), again consistent with their being evolved stars.

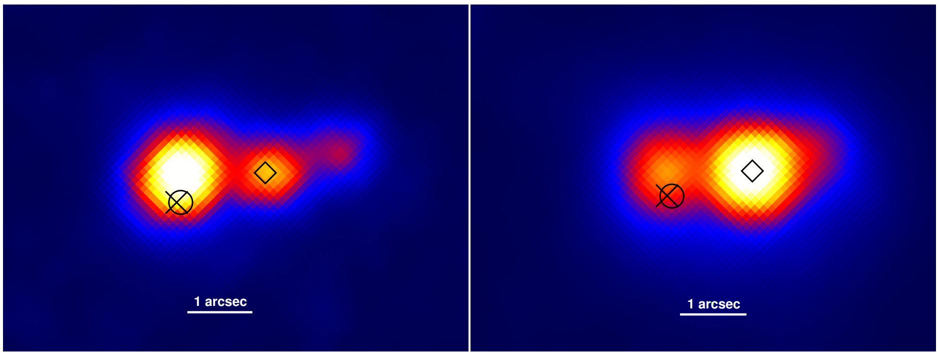

FIGURE 3.5: Infrared emission around IRAS 16372–4808 in *Ks* (left) and *J* (right) filters taken from the *VVV* survey, both in logarithm flux colour scale. The circle and cross are centered on the positions of the radio continuum emission peak at 2.1 GHz and the 1612 MHz OH maser spot of IRAS 16372-4808, respectively. The diamond is centered on the GAIA's source (see text for details). North is up and East is to the left.

We have also inspected the public data from HOPS[1], which included cubes of the emission from inversion transitions of ammonia at $\simeq$ 23 GHz (Purcell et al. 2012). These transitions are tracers of gas with high density ($> 10^3$ cm^{-3}, Ho & Townes 1983). Stars are born with dense cores in molecular clouds, and YSOs systematically host ammonia emission (e.g., Anglada et al. 1989; Verdes-Montenegro et al. 1989). The sources OH 341.6811+00.2634, IRAS 17494–2645, and IRAS 18019–2216 were within the sky section covered by HOPS, but no ammonia emission was found to be associated with them. The closest ammonia emission to these sources is associated with the compact dense core [PLW2012] G007.975-00.361+133.4, whose peak emission is located at $\sim$ 133 km s^{-1} and $\simeq$2 arcmin away from IRAS 18019-2216, which rules out an association with any of the 1612 MHz OH maser spots and continuum emission in this object.

The SEDs of the OHPNe candidates (Section 3.3.3, Fig. 3.4), with peaks at $\lambda < 70$ μm also suggest that they are evolved objects. On the other hand, in massive YSOs the peak emission is expected at $\lambda > 100$ μm (Wood & Churchwell 1989; Anderson et al. 2012). We also note that the wavelength of this peak emission in their SEDs is also similar to the confirmed OHPNe (Uscanga et al. 2012). Moreover, mid-infrared images from the *Spitzer Space Telescope* show bright, spatially unresolved, isolated sources (Qiao et al. 2016b, 2020), while massive star–forming regions usually show extended infrared emission, with filaments and diffuse nebulosities.

A more detailed analysis of the infrared colours of the OHPNe candidates can shed further light on the nature of these sources. In Fig. 6.4 we show an *MSX* colour–colour diagram, defined as $[a] - [b] = 2.5\ log(S_a/S_b)$, where a and b are wavelength in μm and S is flux density in Jy, which is useful to discriminate the mid–infrared colours typical of star-forming regions and of evolved stars (Sevenster 2002). The previously confirmed OHPNe and new candidates have similar colours, consistent with those in evolved stars, and in particular of those in the post–AGB phase.

[1]https://research.science.mq.edu.au/hops/public/data_cubes.php

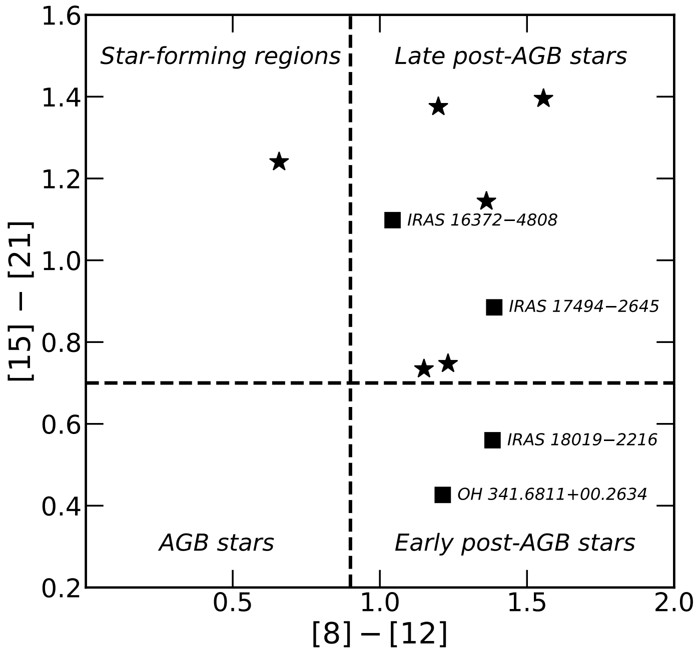

FIGURE 3.6: *MSX* colour-colour diagram, as defined by Sevenster (2002). The vertical and horizontal dashed lines separate the diagram into four quadrants, where different types of sources tend to cluster. The filled star and square symbols represent the known confirmed OHPNe and new candidates of SPLASH–ATCA, respectively.

While none of the criteria above can provide by themselves an unquestionable determination of the nature of these sources as evolved stars, the combined evidence from them all makes it highly unlikely that these objects belong to a different category of sources.

3.5.2 Radio continuum emission: photoionized nebulae or winds ionized by other processes?

We have argued above that these sources have a high probability of being evolved stars. But the determination of whether these objects have reached the PN phase requires ascertaining whether photoionization of the CSE has already started. A solid classification as PNe would require optical/infrared spectroscopy, which is not available for our candidates. However, the radio continuum emission can also provide important clues on the nature of these objects. In particular, we can study whether this emission is free-free radiation from ionized gas and, if so, whether the ionization is produced by UV radiation from the central star (i.e., it is in the PN phase), or by other processes, such as shocks in high-velocity winds (which can also be produced previously, in the AGB or post–AGB phases), with no significant contribution from photoionization. It is important to note that PNe can show both slowly expanding gas and high-velocity jets. Our discussion in this section, however, would focus on whether or not the mass–loss rates derived under the assumption of winds (ionized by shocks or other processes different from photoionization from the central star) are within reasonable values for objects in evolutionary stages before the PN phase.

As mentioned in Section 3.3.2, the spectral indices of the radio continuum emission in these OHPNe candidates are consistent with free-free radiation from photoionized gas. Even in some cases, the spectral indices are close to 0.6, which suggests a radial dependency of electron density as $n_e \propto r^{-2}$, as one would expect in the photoionized region in a nascent PNe. However, we note that the same spectral dependency would be obtained in the case of free-free radiation from an ionized wind (Panagia & Felli 1975; Reynolds 1986), which may be produced in the post–AGB phase, before the photoionization of the CSE takes place. This situation is seen in jets from YSOs (Anglada et al. 2018). Low-mass YSOs do not produce enough ionizing radiation to maintain an H II region around them, but radio continuum emission with spectral indices $\simeq 0.6$ are detected from collimated jets. In that case, the emission may arise from shock-ionized material.

Shock-ionized outflows can thus produce exactly the same radio spectral indices as a photoionized region, regardless of whether they represent an isotropic or a collimated mass–loss. It is mainly the radial dependency of the electron density which determines the spectral index. However, the values of flux density can be used to constrain the nature of the emission.

For instance, the radio continuum emission from an isotropic ionized outflow would have $\alpha = 0.6$, and an S_ν at a distance d from the Sun (Panagia & Felli 1975):

$$S_\nu = 5.12 \left[\frac{\nu}{10\,\mathrm{GHz}}\right]^{0.6} \left[\frac{T_e}{10^4\,\mathrm{K}}\right]^{0.1} \left[\frac{\dot{M}}{10^{-5}\,\mathrm{M_\odot\,yr^{-1}}}\right]^{4/3} \left[\frac{\mu}{1.2}\right]^{-4/3} \left[\frac{\upsilon_{\mathrm{exp}}}{10^3\,\mathrm{km\,s^{-1}}}\right]^{-4/3} \bar{Z}^{-2/3} \left[\frac{d}{\mathrm{kpc}}\right]^{-2} \tag{3.1}$$

The determination of mass–loss rates (under the assumption that the observed radio continuum emission arises from a shock-ionized wind) is hampered by the absence of accurate distance estimates for these sources, although we can still check whether the observed flux densities give reasonable values of those mass–loss rates. Using the flux densities at the measured frequency closest to 10 GHz for each source (see Table 3.3), an electron temperature of $T_\mathrm{e} = 10^4$ K, $\mu = 1.2$ for the mean atomic weight per electron, $\upsilon_{\mathrm{exp}} = 1 \times 10^3$ km s^{-1} for the velocity of a post–AGB fast wind, and $\bar{Z} = 1$ for metallicity, hence the mass–loss rate expected for the new OHPNe candidates would be $\dot{M} = 7.4 \times 10^{-5}$ (IRAS 16372–4808), 1.3×10^{-6} (OH 341.6811+00.2634), 8.5×10^{-6} (IRAS 17494–2645), 1.2×10^{-7} (IRAS 18019–2216) M$_\odot$ yr^{-1} $(d/\mathrm{kpc})^{3/2}$.

On the other hand, as mentioned above, a collimated, biconical ionized jet would also give a spectral index ($\alpha = 0.6$). In this case, departures from this spectral index can be interpreted as deviations from the biconical symmetry (Reynolds 1986). There is ample evidence for the presence of collimated winds in post–AGB stars, and they can play a key role in PN shaping (Sahai & Trauger 1998). For a collimated jet, the mass–loss rates required to explain the observed radio continuum emission, would be around one order of magnitude smaller than for the spherical ionized wind case, depending on the inclination of the jet with respect to the observer and, specially, on the degree of collimation of the jet (Reynolds 1986).

In the case of our candidate OHPNe, the mass–loss rates required to explain the observed radio continuum emission as shock-excited winds are probably too high when comparing with the values expected in classical post–AGB models (10^{-7}–10^{-8} $M_\odot$ yr^{-1}; Vassiliadis & Wood 1994; Blöcker 1995; Miller Bertolami 2016), but not so much if we consider the case of binary/multiple stellar systems. In these systems, large accretion rates between companions could be produced, with processes such as a common envelope (Ivanova et al. 2013). These processes can lead to extremely high mass–loss rates, as in the case of WF AGB and post–AGB stars (Imai 2007), with total mass–loss rates of $\simeq 10^{-3} - 10^{-4}$ $M_\odot$ yr^{-1} (Rizzo et al. 2013; Khouri et al. 2021). Thus, mass–loss rates from post–AGB stars in binary/multiple systems can be several orders of magnitude higher than rates expected from single stars. For instance, Bollen et al. (2021) estimate mass–loss rates of $10^{-4} - 10^{-8}$ $M_\odot$ yr^{-1} in a sample of jets in post–AGB binary systems.

We note, however, these large mass–loss rates at the AGB and post–AGB phases include mostly neutral material, which would not emit free-free radiation at radio wavelengths. The fraction of ionized material in winds and outflows from post–AGB stars is relatively low. For instance, while WFs are known to eject powerful collimated jets, their radio continuum emission is either extremely weak (cf. non-detections at 22 GHz with upper limits $30 - 40$ μJy in several of these objects, Gómez et al. 2017), or of non-thermal nature (Pérez-Sánchez et al. 2013b; Suárez et al. 2015). The WF IRAS 18043−2116 does have detectable radio continuum emission. From our SPLASH–ATCA data, we obtain a flux density of $\simeq 0.9$ mJy at 2.1 GHz, although the image is heavily contaminated by sidelobes from other sources in the field. A more reliable value of $\simeq 0.6$ mJy at 2 GHz was obtained by Pérez-Sánchez et al. (2017). These authors also showed that the spectral index of the radio continuum emission is consistent with free-free emission from an ionized jet. Their derived mass–loss rate under the assumption that the radio continuum emission arises from an ionized wind is $\leq \times 10^{-5}$ $M_\odot$ yr^{-1}, more than two orders of magnitude lower than the mass–loss rate derived by Khouri et al. (2021) from molecular line observations. In the case of the post–AGB binary system TW Cam, a source for which Bollen et al. (2021) derived a mass–loss rate in its jet (2×10^{-4} $M_\odot$ yr^{-1}), it is undetected in the NRAO VLA Sky Survey (NVSS; Condon et al. 1998), with a 3σ upper limit of $\simeq 1.5$ mJy at 1.4 GHz, and in the VLA Sky Survey (VLASS; Gordon et al. 2021), with a 3σ upper limit of $\simeq 0.4$ mJy at 3 GHz, while the source is at a distance of 1.8 kpc, probably much closer than our OHPN candidates. There is, of course, a caveat in this flux density comparison, since the distance to our OHPN candidates is unknown, but these objects are not conspicuously bright in the infrared (Fig. 3.4) compared with other post–AGB stars (see e.g., the SEDs in Ramos-Larios et al. 2012), and therefore, they do not seem located particularly nearby. Moreover, it is likely that at least some of these objects are in the Galactic Bulge, given their coordinates, which would place them at $\simeq 8 \pm 2$ kpc.

Other post–AGB stars with radio continuum emission also show weaker emission than these OHPN candidates. For instance, Hen 3-1475 displays a flat spectrum, with flux densities 0.3 – 0.4 mJy between 2.6 and 8.6 GHz (Cerrigone et al. 2017), while the Red Rectangle has a flux density of $\simeq$ 0.5 mJy at 8.4 GHz (Knapp et al. 1995; Jura et al. 1997). The object M 1–92 has radio fluxes comparable to those of our candidates (2.1 ± 0.4 mJy at 3 GHz; Gordon et al. 2021), although it is relatively nearby (2.5 kpc; Bujarrabal et al. 1997), consistent with its higher infrared emission (e.g., IRAS flux of 17.5 Jy at 12 μm, compared with 2 Jy for IRAS 16372-4808, our brightest object).

In summary, considering that the radio continuum emission of the new OHPNe candidates tends to be stronger than in post–AGB stars (e.g. Hen 3–1475, M 1–92 or the Red Rectangle), including those showing strong shocks (e.g. the WFs), we favour that this continuum emission is likely to arise from photoionized gas, especially for the sources with brighter radio flux densities. Therefore, the radio continuum detected in the OHPN candidates is indicative of fossil shells ionized by UV photons from the central star of a PN, and other sources of excitation seem to be improbable.

3.5.3 Comparison with known OHPNe and a possible evolutionary sequence

As shown above, the radio continuum emission alone cannot provide unambiguous evidence that these objects have already entered the PN phase. However, their common characteristics with the confirmed OHPNe can provide further support of their likely nature as PNe.

Three of our candidates show OH maser lines at 1612 MHz with a single spectral feature. Only IRAS 18019–2216 shows multiple spectral components with flux densities of the same order, although previous observations also reported a single peak. A dominant spectral feature can also be considered a common characteristic of known OHPNe. The OH spectra in these sources (Gómez et al. 2016; Qiao et al. 2016a) are irregular, but they tend to be dominated by several blended features that would appear as a single peak when observed with limited spectral resolution. Additional, spectrally resolved components are much weaker than the main features. The case of multiple, well-separated OH maser components in IRAS 18019–2216 could be considered similar to that of K 3-35, although this characteristic seems to be less frequent among OHPNe. In any case, the characteristics of OH maser spectra in our candidate sources are different from the double horned profile observed on AGB stars such as OH/IR stars that typically traces the receding front and back sides (Reid 1976), as well as the terminal expansion velocity of the CSE ($\simeq 15 - 30$ km s^{-1}; te Lintel Hekkert et al. 1991).

Another potentially interesting characteristic is the variation of the radio continuum flux density. Among the three cases in which we report data in more than one epoch (Table 3.3), there seems to be an increase of the emission in IRAS 16372–4808 and IRAS 17194–2645. In IRAS 18019–2216, the differences in flux density are not statistically significant. An enhancement of flux density has also been reported in the OHPNe Vy 2–2 and IRAS 17347–3139 (Christianto & Seaquist 1998; Gómez et al. 2005; Tafoya et al. 2009), and interpreted as a sign of the growth of the photoionized region, as expected in a nascent PN while the ionization front proceeds along the CSE. In addition to maser-emitting PNe, a similar increasing trend has been observed in other young PNe (e.g., Kwok et al. 1981; Knapp et al. 1995). In contrast, non-thermal radio continuum emission in evolved stars shows variability that could be either in a increasing or decreasing direction (Pérez-Sánchez et al. 2013b; Suárez et al. 2015; Cerrigone et al. 2017). In this sense, finding a decreasing flux density with time would be indicative of the presence of a non-thermal emission process. In the case of our candidates, the enhancement of radio continuum emission is consistent with a nature as nascent PNe.

As discussed in Sections 3.3.2 and 3.5.2 the spectral indices in our four OHPNe candidates are compatible with the ones expected in nascent PNe. This is further illustrated in Table 3.5, where we show the radio spectral indices of the previously reported OHPNe together with those of the candidates presented here. As mentioned before, a photoionized region would show free-free emission with spectral indices between 2 (optically thick) and -0.1 (optically thin). The optical depth of free-free emission decreases with frequency, so the same object can display both regimes, separated at a turnover frequency. We also mentioned that objects with a radial dependency of electron density of $n_e \propto r^{-2}$ can show a partially optically thick spectrum with $\alpha \simeq 0.6$ over a wide range of frequencies. It suggests a possible evolutionary sequence of nascent PNe based on their spectral indices. In this sense, the beginning of photoionization could be characterized by steep spectral indices (close to 2), when the densest parts of the CSE are photoionized. As the ionization front evolves, and the emission arises from regions both optically thin and thick, the resulting spectral indices would tend to be $\alpha \simeq 0.6$. The free-free emission would then become optically thin at high frequencies (with $\alpha \simeq -0.1$), with a turnover frequency that would decrease with time (Kwok & Feldman 1981). In general, we would expect that the radio continuum spectrum would flatten with time over a wider range of frequencies.

While this could be a general trend, it is difficult to set up a precise ranking of ages among confirmed and candidate OHPNe in Table 3.5, considering other possible parameters (e.g. the $M_{\rm i}$ of the stars, or binary evolution), and that the frequency coverage of the radio data is not homogeneous. However, we would suggest that sources like Vy 2–2 and IRAS 17494–2645 could be the youngest among the PNe in Table 3.5, since their spectral indices are steeper over a large frequency range, while K 3–35 and JaSt 23 would be relatively more evolved, since their radio spectra become optically thin within the range of sampled frequencies. A detailed and homogeneous study of the radio spectrum of these sources, as well as a monitoring of the radio continuum emission would be useful to better understand their evolutionary status.

TABLE 3.5: Radio spectral indices of the confirmed OHPNe and detected candidates.

Source name	α	Frequencies (GHz)	Confirmed
JaSt 23	0.57 ± 0.24[a]	2.1 – 5	Yes
	0.09 ± 0.25	5 – 10	
K 3–35	0.6 ± 0.1[b]	1.5 – 10	Yes
	-0.1 ± 0.2	10 – 22	
IRAS 17393–2727	0.66 ± 0.09[c]	2.1 – 15	Yes
IRAS 16333–4807	0.69 ± 0.01[d]	2.1 – 22.2	Yes
	1.39 ± 0.08[e]	1.38 – 2.41	
OH 341.6811+00.2634	0.77 ± 0.07	2.1 – 45	No
IRAS 17347–3139	0.79 ± 0.04[f]	4.3 – 8.9	Yes
	0.64 ± 0.06	16.1 – 24	
IRAS 16372–4808	0.90 ± 0.03	2.1 – 9.7	No
	0.375 ± 0.008	8.7 – 45	
IRAS 18019–2216	1.0 ± 0.3	2.1 – 6.5	No
Vy 2–2	1.30 ± 0.07[g]	1.5 – 15	Yes
IRAS 17494–2645	1.35 ± 0.09	2.1 – 6.5	No

[a] Using our data $S_\nu = 2.25 \pm 0.4$ mJy at 2.1 GHz, and $S_\nu = 3.7 \pm 0.4$ mJy and 3.9 ± 0.4 mJy at 5 and 10 GHz from Van de Steene & Jacoby (2001), respectively.
[b] Aaquist (1993).
[c] At 2.1 GHz, arithmetic mean (weighted by the inverse of the noise squared) of our data and Gómez et al. (2016); at 3 GHz from Gordon et al. (2021); at 5 and 15 GHz from Pottasch et al. (1987).
[d] Using our data $S_\nu = 19.10 \pm 0.54$ mJy at 2.1 GHz, and $S_\nu = 97 \pm 10$ mJy at $\sim$22.24 GHz from Uscanga et al. (2014).
[e] Qiao et al. (2016b).
[f] Gómez et al. (2005). For the central region of this PN, Tafoya et al. (2009) obtained spectral indices of $\sim$1.34 and $\sim$0.90 between 8.4–22.2 GHz and 22.2–43 GHz, respectively.
[g] Using the most recent data in Christianto & Seaquist (1998). Spectral indices of 1.43 ± 0.07, 1.28 ± 0.06, 1.24 ± 0.05, and 1.30 ± 0.07 were obtained from observations in 1982, 1987, 1992, and 1997, respectively.

3.5.4 New colour diagnostics for OHPNe

In Fig. 6.5 we show a *WISE* colour-colour diagram, where each colour is defined as $[a] - [b] = 2.5\, log(S_a/S_b)$, and where we compare the infrared colours of confirmed OHPNe and our new OHPNe candidates, with optically obscured post–AGB candidates from Ramos-Larios et al. (2009, 2012). A similar diagram was presented in Gómez et al. (2017), but comparing the obscured post–AGB candidates with WF objects. These authors did not find any significant difference in colours between WFs and obscured post–AGB stars.

However, in the case of our colour-colour diagram, the OHPNe (both candidate and bona-fide), seem to cluster together around $9.5 \leq [3.4] - [22] \leq 13.5$, and $4.0 \leq [4.6] - [12] \leq 7.0$.

The yet scarce number of known and candidate OHPNe precludes us to obtain strong statistical constraints, but a Kolmogorov-Smirnov test on the WISE colours suggests that the colour distribution between OHPNe and obscured post–AGB stars could be different (p value $\simeq 0.16$, is the probability to obtain the observed $[3.4] - [22]$ colours assuming that

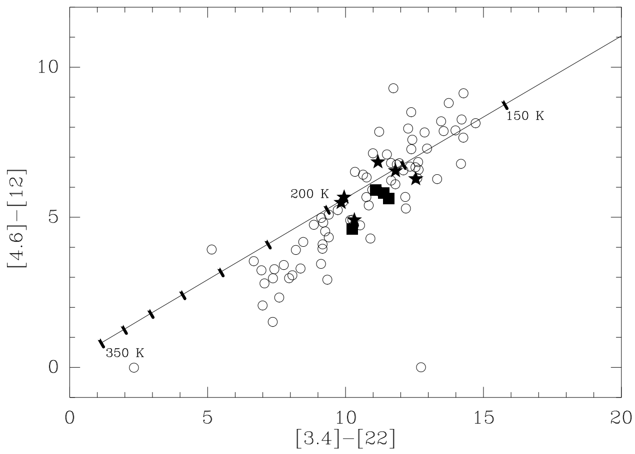

Figure 3.7: *WISE* colour-colour diagram (similar to the one presented in Gómez et al. 2017). The stars and squares represents the confirmed OHPNe and the new candidates of SPLASH–ATCA, respectively. The open circles represent obscured post–AGB candidates (Ramos-Larios et al. 2009, 2012). The solid line represents the locii of the colours for blackbody brightness distributions. The tick marks in the blackbody line go from 150 to 350 K at increment steps of 25 K. For IRAS 18019–2216, we have used measurements at 3.6 and 4.5 μm reported by *Spitzer* because at these wavelengths, the images of *WISE* show that the emission of this OHPN candidate is contaminated by a nearby source.

OHPNe and post–AGB stars are drawn from populations with the same colour distribution). If these different colours are confirmed, this would suggest that OHPNe are a particular type of objects, and not all evolved objects go through this phase, a particularity that is not observed in WF objects. This may also suggest that WFs are not the direct precursors of OHPNe, despite they share the property of being maser-emitting evolved objects, and that all, except three WFs, are also OH emitters (Gómez et al. 2017).

In any case, this apparent clustering of OHPNe in the WISE colour-colour diagram can be used as a diagnostic to support that our candidates are indeed bona fide OHPNe, since they have similar colours as the confirmed objects in this class. Moreover, this *WISE* colour-colour diagram could be used to identify more OHPNe candidates in the future.

3.6 Conclusions

We have used data from the ATCA follow-up of the SPLASH survey to identify new candidates to being PNe with OH maser emission. OHPNe seem to be extremely rare, consistent with their proposed nature as nascent PNe. So far, only 6 of such OHPNe have been confirmed in the literature. Our criterion to identify new OHPNe was to find a spatial coincidence between radio continuum at 2.1 GHz and OH maser emission, in objects classified in SPLASH as evolved stars and sources with unknown nature.

With these data, we have found four new candidates to being OHPNe: three in which we report the association between continuum and OH maser emission for the first time (OH 341.6811+00.2634, IRAS 17494–2645 and IRAS 18019–2216), and another one (IRAS 16372–4808) whose nature as a PN had been previously discarded. However, we discuss that there is not enough evidence for such a rejection, and should also be considered a OHPN candidate.

The radio continuum emission in all four candidates has spectral indices compatible with partially optically thick free-free emission from ionized gas and, in some cases, the spectral index is close to 0.6, the value expected from a ionized region with a radial dependency of density as r^{-2}, as it could be the case in nascent PNe.

Although massive YSOs can sustain photoionized regions (thus emitting free-free radio continuum emission) and present OH maser emission, these OHPN candidates are most likely evolved stars, based on the detection of OH ground-state maser emission only at 1612 MHz, the absence of methanol masers and of high-density molecular line tracers, their SED peaking at $\lambda < 70$ μm, and their infrared colours.

We also discuss whether the radio continuum emission actually arises from the photoionized region in a nascent PN, or from a shock-ionized wind (and therefore, the sources may still be in the post–AGB phase). While the mass–loss rates assuming an ionized wind are too high comparing with the expected ones in single post–AGB stars, we cannot completely discard that these rates could be enhanced by processes in binary/multiple systems, such as common envelope evolution. We suggest, however, that this is unlikely, since other post–AGB sources that have extremely high mass–loss rates show none or very weak radio continuum emission. Therefore, the radio continuum detected in the OHPN candidates is indicative of fossil shells ionized by UV photons from the central star of a PN. Their final confirmation as bona fide PNe would require optical/infrared spectroscopy.

However, these OHPN candidates show other similarities with confirmed OHPNe, such as the shape of the OH maser spectrum (in most cases dominated by a single spectral feature), or the increase of radio continuum flux density with time. Spectral indices of radio continuum emission are also similar to confirmed OHPNe. We propose a general trend, with younger OHPNe having steeper spectral indices, that would flatten as the object evolves. Moreover, we find evidence that OHPNe (including our candidates) tend to cluster in a definite area of a colour-colour diagram using WISE data, with $9.5 \leq [3.4] - [22] \leq 13.5$, and $4.0 \leq [4.6] - [12] \leq 7.0$, compared with the wider spread of obscured post–AGB stars in the same diagram. We also suggest that this colour diagram could be useful to identify new OHPNe in the future.

Acknowledgments

We thank our anonymous referee for his/her comments that have significantly improved the original manuscript. The Australia Telescope Compact Array is part of the Australia Telescope National Facility (grid.421683.a) which is funded by the Australian Government for operation as a National Facility managed by CSIRO. We acknowledge the Gomeroi people as the traditional owners of the Observatory site. The National Radio Astronomy Observatory is a facility of the National Science Foundation operated under cooperative agreement by Associated Universities, Inc. We used continuum images from the VLA Sky Survey, downloaded from the Canadian Initiative for Radio Astronomy Data Analysis (CIRADA), which is funded by a grant from the Canada Foundation for Innovation 2017 Innovation Fund (Project 35999), as well as by the Provinces of Ontario, British Columbia, Alberta, Manitoba and Quebec. This work has made use of the SIMBAD database, operated at the CDS, Strasbourg, France, and the NASA/IPAC Infrared Science Archive, which is operated by the Jet Propulsion Laboratory, California Institute of Technology, under contract with the National Aeronautics and Space Administration. It also makes use of data products from 2MASS (a joint project of the University of Massachusetts and the Infrared Processing and Analysis Center/California Institute of Technology, funded by NASA and the NSF), AKARI (a JAXA project with the participation of ESA), DENIS (partly funded by the SCIENCE and the HCM plans of the European Commission under grants CT920791 and CT940627), the services of the ESO Science Archive Facility, *Gaia* (the European Space Agency (ESA) mission *Gaia* (https://www.cosmos.esa.int/gaia), processed by the *Gaia* Data Processing and Analysis Consortium (DPAC, https://www.cosmos.esa.int/web/gaia/dpac/consortium). Funding for the DPAC has been provided by national institutions, in particular the institutions participating in the *Gaia* Multilateral Agreement), HERSCHEL (Herschel is an ESA space observatory with science instruments provided by European-led Principal Investigator consortia and with important participation from NASA), IRAS (was a joint project of the US, UK and the Netherlands), Pan-STARRS (have been made possible through contributions by the Institute for Astronomy, the University of Hawaii, the Pan-STARRS Project Office, the Max-Planck Society and its participating institutes), *Spitzer* Space Telescope (operated by the Jet Propulsion Laboratory, California Institute of Technology under a contract with NASA), MSX (funded by the Ballistic Missile Defense Organization with additional support from NASA Office of Space Science), UKIDSS (The project is defined in Lawrence et al. (2007) and uses the UKIRT Wide Field Camera (WFCAM; Casali et al. 2007) and a photometric system described in Hewett et al. (2006). The pipeline processing and science archive are described in Hambly et al. (2008)), USNO-B catalog (the construction and contents of the catalog can be found in Monet et al. (2003)), VVV survey (is supported by the European Southern Observatory, by BASAL Center for Astrophysics and Associated Technologies PFB-06, by FONDAP Center for Astrophysics 15010003, by the Chilean Ministry for the Economy, Development, and Tourism's Programa Iniciativa Científica Milenio through grant P07-021-F, awarded to The Milky Way Millennium Nucleus), and WISE (a joint project of the University of California, Los Angeles, and the Jet Propulsion Laboratory/-California Institute of Technology, funded by the NASA). RC, JFG, and LFM acknowledge support from grant PID2020-114461GB-I00 and the "Center of Excellence Severo Ochoa" award for the Instituto de Astrofísica de Andalucía (SEV-2017-0709), funded by MCIN/ AEI /10.13039/501100011033. RC is also supported by the predoctoral grant PRE2018-085518, funded by MCIN/AEI/ 10.13039/501100011033 and by ESF Investing in your future. This work is also partially supported by grants R18-RT-3082 (IAA4SKA) and P20-00880, funded by the Economic Transformation, Industry, Knowledge and Universities Council of the Regional Government of Andalusia and the European Regional Development Fund from the European Union. LU acknowledges support from the University of Guanajuato (Mexico) grant ID CIIC 164/2022. HI has been supported by JSPS KAKENHI (25610043, JP16H02167). H.-H.Q. is partially supported by the Special Funding for Advanced Users, budgeted and administrated by Center for Astronomical Mega-Science, Chinese Academy of Sciences (CAMS-CAS), CAS "Light of West China" Program and the National Natural Science Foundation of China (grant No. 11903038).

Data Availability

All data at radio wavelengths presented in this chapter are publicly accessible through the Australia Telescope Online Archive (http://atoa.atnf.csiro.au) and the NRAO Data Archive (https://archive.nrao.edu/), as uncalibrated visibilities. Relevant project numbers are listed in Table 3.1. The optical and infrared data we used are also accessible through their respective archives.

Chapter 4

An interferometric search for SiO maser emission in planetary nebulae

4.1 Introduction

Circumstellar maser emission of the SiO, H_2O, and OH molecules is widespread in asymptotic giant branch (AGB) stars with O-rich envelopes. These different species show a stratified distribution, with SiO masers located close to the star ≤ 10 au (Diamond et al. 1994; Desmurs et al. 2000; Reid & Menten 2007), and H_2O and OH farther away ($\simeq 10-10^2$ and 10^3-10^4 au, respectively; e.g., Bowers & Johnston 1994; Richards et al. 2012; Reimers 1977; Etoka & Diamond 2010), tracing a nearly spherical expansion of the envelope at different radii. This maser emission tends to disappear after the end of the AGB phase, when mass loss drops by several orders of magnitude, from rates up to $\simeq 10^{-4}$ $M_\odot$ yr^{-1} in the AGB (Vassiliadis & Wood 1993; Blöcker 1995) to $10^{-7}-10^{-8}$ $M_\odot$ yr^{-1} in the post-AGB phase (Vassiliadis & Wood 1994; Blöcker 1995).

Considering the estimated timescale of disappearance of these maser species after the end of the AGB (10, 100, and 1000 yr for SiO, H_2O, and OH, respectively; Gómez et al. 1990; Engels & Jiménez-Esteban 2007) and the duration of the transitional post-AGB phase (10^3-10^5 yr, Miller Bertolami 2016), no SiO nor H_2O maser emission was expected when the planetary nebula (PN) phase begins (i.e., when the central star becomes hot enough, $T_{\rm eff} \simeq 25000$ K, to photoionize its circumstellar environment), while only extremely young PNe (shortly after the onset of this photoionization) should show OH masers. This makes OH-maser emitting PNe (OHPNe, Zijlstra et al. 1989) very interesting objects to understand

This chapter is derived from the following publication:

- Cala et al. (2024b)

the early evolution of PNe. There are only six confirmed OHPNe (Uscanga et al. 2012; Qiao et al. 2016a), and several additional candidates (see Chapter 3).

Despite not being expected, five PNe are known to emit H_2O masers (Miranda et al. 2001; de Gregorio-Monsalvo et al. 2004; Gómez et al. 2008; Uscanga et al. 2014; Gómez et al. 2015b). The first identified case, K 3-35 (Miranda et al. 2001), actually emits both OH and H_2O masers. Two other PNe, IRAS 17347-3139 (de Gregorio-Monsalvo et al. 2004; Tafoya et al. 2009) and IRAS 16333-4807 (Uscanga et al. 2014; Qiao et al. 2016a), also show emission of both species. The unexpected detection of H_2O masers suggests that this emission in PNe is not the remnant of that seen in the AGB phase, which is related to isotropic winds, but it traces nonspherical mass-loss events instead (Suárez et al. 2007). In particular, interferometric observations usually show that OH and H_2O maser emission in PNe is associated with equatorial ejections (expanding tori) and/or collimated jets (Miranda et al. 2001; Uscanga et al. 2014; Gómez et al. 2015b; Qiao et al. 2016a). While these mass-loss phenomena allow the presence of maser emission in PNe for longer than previously expected, it is generally assumed that only extremely young PNe can be maser emitters, since the advance of the ionization front would eventually photodissociate OH and H_2O molecules at the locations where those masers can be produced. The assumption of extreme youth of maser-emitting PNe is compatible with their scarcity.

Considering that new, nonspherical mass-loss events in the post-AGB and PN phases can provide the conditions of population inversion of OH and H_2O levels (required for maser emission), it is reasonable to think that the same might happen in the case of SiO. In fact, a few late AGB and post-AGB stars are known to harbor SiO maser emission (e.g., Yoon et al. 2014; Nakashima & Deguchi 2003b; Amada et al. 2022), which is probably tracing either the base of collimated outflows (Imai et al. 2005) or circumstellar toroids (Sánchez Contreras et al. 2002). However, in the case of objects already in the PN phase, several attempts have been made to detect SiO masers, all with negative results (e.g., Bachiller et al. 1997; Nyman et al. 1998). In any case, SiO searches specifically targeting PNe remain scarce.

Obtaining a first detection of SiO masers in PNe would open a new window of research. It would allow us to probe mass loss at scales different from those traced by H_2O and OH, probably closer to the central star. Moreover, we could characterize the physical conditions that favor the presence of SiO masers, and determine how this correlates with the presence of other maser species.

In this chapter we present the results of a new sensitive survey for SiO masers in confirmed and candidate PNe, carried out with the Australia Telescope Compact Array (ATCA). We selected two different samples, which are described in Sec. 4.2. We present our results in Sec. 7.3, which we subsequently discuss in Sec. 4.5

4.2 Source samples

4.2.1 Sample 1: Planetary nebulae with known OH and/or H_2O masers

Planetary nebulae with either OH or H_2O maser emission are considered to be at the beginning of this evolutionary phase. Thus, these nascent PNe are among the best targets to search for SiO maser emission as well, since we expect it to disappear shortly after the end of the AGB phase, at even shorter timescales than the OH or H_2O masers. Our sample comprises 11 sources and includes all eight confirmed PN with OH or H_2O maser emission, as well as two additional objects whose nature as PN has not been confirmed, presented in Chapter 3: IRAS 16372−4808 and OH 341.6811+00.2634. We also included NGC 6302, a well known PN displaying OH line emission (Turner 1979; Zijlstra et al. 1989), although it has been suggested that this emission could be thermal, instead of maser (Gómez et al. 2016; Qiao et al. 2020). The list of sources is given in the first part of Table 4.1.

Some of these objects have already been observed in SiO transitions at 43 GHz (Jewell et al. 1991; Nyman et al. 1998), but with modest sensitivities (rms noise $\simeq$ 1 Jy). The observations in this chapter are significantly more sensitive (around two orders of magnitude).

4.2.2 Sample 2: Previous single-dish SiO maser detections near planetary nebulae and radio continuum sources

We carried out an extensive search in the literature and in publicly available catalogs for, on the one hand, reports on single-dish detections of SiO maser emission and, on the other hand, different catalogs of PNe and radio continuum emission, considering the latter as a possible tracer of free-free radiation from ionized gas in a PN (the list of references for the published works and catalogs we compiled would be too long to be detailed here, but some examples can be seen in references 21 to 30 in Table 4.1, and in the description of each source below). We then cross-matched these single-dish SiO detections with PNe and radio continuum sources, which resulted in five candidate sources (Table 4.1, bottom five sources) within the beam of the single-dish SiO observations. A definite confirmation of the association of maser emission with known PNe or with radio continuum emission requires interferometric confirmation, to ascertain that the SiO maser emission actually arises from the target object, and not from a different source within the single-dish beam.

4.3 Observations and data processing

ATCA observations were carried out in two sessions. The sample described in Sect. 4.2.1 (Sample 1, project C3324, PI: R. Cala) was observed on 2019 October 21, with the H168 configuration of ATCA (minimum and maximum baselines of 61 and 192 m, respectively,

TABLE 4.1: Parameters of our ATCA observations.

Source	R.A. (J2000)	Dec (J2000)	Gain calibrator	Beam size (arcsec)	Beam p.a. (deg)	T_{on} (h)	Refs.
Sample 1							
IRAS 15103−5754	15:14:18.397	−58:05:20.47	PMN J1515–5559	7.2 × 4.9	+85	0.65	1,2
IRAS 16333−4807	16:37:06.601	−48:13:42.88	IERS B1646–506	8.0 × 4.6	+78	0.65	3,4
IRAS 16372−4808	16:40:55.818	−48:13:59.93	IERS B1646–506	7.1 × 4.6	+82	0.65	5,6
OH 341.6811+00.2634	16:51:53.640	−43:47:16.50	IERS B1646–506	9.5 × 4.1	+81	0.65	5
NGC 6302	17:13:44.489	−37:06:11.71	IERS B1729–373	6.9 × 4.3	+75	0.65	7,8
IRAS 17347−3139	17:38:00.624	−31:40:54.91	IERS B1741–312	6.8 × 4.2	+75	0.66	9,10
JaSt 23	17:40:23.067	−27:49:12.00	IERS B1741–312	6.5 × 4.1	+88	0.67	11,12
IRAS 17393−2727	17:42:33.140	−27:28:24.70	IERS B1741–312	7.2 × 3.9	−88	0.65	13,14
IRAS 18061−2505	18:09:12.400	−25:04:34.50	IERS B1817–254	6.2 × 4.1	+72	0.65	15,16
Vy 2–2	19:24:22.218	+09:53:56.33	IVS B1936+046	6.8 × 5.7	+78	1.24	17,18
K 3–35	19:27:44.026	+21:30:03.57	IVS B1936+046	8.1 × 5.1	+31	0.66	19,20
Sample 2							
IRAS 17239−2812	17:27:05.030	−28:15:27.50	PKS 1710–269	0.76 × 0.18	+7	0.74	21,22
IRAS 17390−3014	17:42:18.870	−30:15:29.00	PKS 1710–269	0.73 × 0.17	+6	0.74	23,24
H 2–18	17:43:28.840	−21:09:52.50	PKS 1710–269	0.95 × 0.18	+3	0.74	25,26
IRAS 18052−2016	18:08:16.380	−20:16:11.30	IERS B1829–207	1.37 × 0.17	+4	0.74	27,28
IRAS 19508+2659	19:52:57.900	+27:07:44.70	VCS2 J1956+2820	1.12 × 0.16	+2	0.57	29,30

Right ascension and declination represent the coordinates of the phase center of the observations. "Gain calibrator" is the complex-gain calibrator used for each target. Beam sizes (full width at half maximum) and beam position angles (p.a., measured north to east) are those of the continuum images at 43 GHz. T_{on} is the total integration time on each source.

Sample 1 comprises PNe with known OH and/or H_2O masers. Sample 2 includes single-dish SiO maser detections near PNe and radio continuum sources.

References: (1) Gómez et al. (2015b), (2) Suárez et al. (2015), (3) Kimeswenger (2001), (4) Uscanga et al. (2014), (5) Chapter 3, (6) Sevenster et al. (1997b), (7) Payne et al. (1988), (8) Henize (1967), (9) de Gregorio-Monsalvo et al. (2004), (10) Gómez et al. (2005), (11) Jacoby & Van de Steene (2004), (12) Sevenster et al. (1997a), (13) Pottasch et al. (1987), (14) García-Hernández et al. (2007), (15) Suárez et al. (2006), (16) Gómez et al. (2008), (17) Vyssotsky et al. (1945), (18) Seaquist & Davis (1983), (19) Miranda et al. (1998), (20) Miranda et al. (2001), (21) Hall et al. (1990), (22) Douglas et al. (1996), (23) de Gregorio-Monsalvo et al. (2004), (24) Condon et al. (1998), (25) Gathier et al. (1983), (26) Izumiura et al. (1995), (27) Deacon et al. (2007), (28) Garwood et al. (1988), (29) White et al. (2005), (30) Nakashima & Deguchi (2003b).

when discarding antenna CA06) and the sample in Sect. 4.2.2 (Sample 2, project C3391, PI: R. Cala) on 2020 October 16 with the 6B configuration (baselines between 214 and 5969 m). In both sessions, we observed at two different intermediate frequencies (IFs), centered at 43 and 45 GHz, obtaining full linear polarization products with a bandwidth of 2 GHz each. We used the CFB 64M-32k mode of the Compact Array Broadband Backend (CABB) of ATCA, which samples each 2-GHz bandwidth into broadband channels with a width of 64 MHz, used for continuum observations. The CABB internally oversamples the total bandwidth, by obtaining broadband channels with separation of half the channel width, but only half of them (with final channel separation equal to the channel width) are provided to the user for the continuum dataset (a total of 32 channels of 64 MHz for the CFB 64M-32k mode). Five of the internal broadband channels were independently zoomed in with a finer spectral resolution, to obtain five individual spectral windows, each including one SiO transition and sampled into 2048 channels of 32 kHz width (velocity resolution 0.22 km s^{-1}). Of these channels, only the central 1847 ones were kept, providing a total coverage of $\simeq$ 404 km s^{-1}. An additional set of 5 adjacent internal broadband channels was combined and also zoomed in, providing a spectral window with 6144 channels, of which the central 5943 ones were kept (velocity resolution and coverage of 0.22 and 1296 km s^{-1}, respectively). This last set of channels includes both the hydrogen recombination line H53α (rest frequency = 42951.968 MHz), and the $^{29}Si^{16}O$ (v=0, J=1-0) line. Therefore, in total we observed six SiO transitions: four of the main isotopologue, $^{28}Si^{16}O$ (hereafter ^{28}SiO), and two of $^{29}Si^{16}O$ (hereafter ^{29}SiO). These transitions are listed in Table 4.2.

In both sessions, the bandpass calibrator was 3C 279 (PKS 1253-055), while the absolute flux calibrator was PKS 1934-638. Further information on our observational parameters, including the complex-gain calibrator for each target, is listed in Table 4.1. We note that the observations of project C3324 (sample 1) were carried out in the H168 configuration, in which five of the ATCA antennas have a relatively compact distribution, with maximum baseline of 192 m, and there is a sixth antenna (CA06) at a fixed position, $\simeq$ 4.5 km away from the main array. Although we included CA06 in our initial maps, the quality of the resulting maps was poor, given the highly inhomogeneous sampling of the uv-plane. Therefore, we excluded antenna CA06 from the data we presented for this project C3324. However, for project C3391 (sample 2) we used the whole array of six antennas, which gave good-quality maps, since the antenna distribution was optimized for observations at high angular resolution.

Data were calibrated with the Miriad software (Sault et al. 1995), following standard procedures for millimeter data processing in the ATCA users' guide. We then further processed the calibrated data using both the Common Astronomy Software Applications (CASA, CASA Team et al. 2022) and the Astronomical Image Processing System (AIPS, Fomalont 1981). We used CASA for initial data inspection, creating images and data cubes with task tclean. With this, we could identify the sources where line and continuum emission were detected. We also attempted self-calibration of the data with CASA, but its performance proved to be somewhat worse than AIPS self-calibration, at least for our data, using equivalent parameters. As an example, the signal-to-noise improvement of AIPS vs CASA was

TABLE 4.2: Observed SiO transitions.

Isotopologue	Transition	Rest frequency (MHz)
^{28}Si^{16}O	$v = 0,\ J = 1–0$	43423.853
^{28}Si^{16}O	$v = 1,\ J = 1–0$	43122.090
^{28}Si^{16}O	$v = 2,\ J = 1–0$	42820.570
^{28}Si^{16}O	$v = 3,\ J = 1–0$	42519.375
^{29}Si^{16}O	$v = 0,\ J = 1–0$	42879.941
^{29}Si^{16}O	$v = 1,\ J = 1–0$	42583.830

These rest frequencies were taken from the list of Manion et al. (2015). For the ^{29}Si^{16}O, $v = 1$, $J = 1–0$ transition, for which no frequency is available in that compilation, we adopted the value reported by Müller et al. (2005).

a factor of 2 when self-calibration was carried out with continuum data (sample 1), and a factor of $\simeq 1.5$ when using masers (sample 2). Even though this improvement may seem modest, it could be important for a detection project like ours, in case the emission is close the sensitivity limit. Therefore, we decided to continue all further data processing using AIPS. Tasks mentioned below correspond to the AIPS package, unless stated otherwise.

Since the ATCA does not correct the frequency drift due to the Earth's motion during the observing session, we carried out an off-line correction of the visibilities of the line spectral windows for this Doppler shift, using task CVEL, to align all data to the same velocity (with respect to the kinematical definition of the Local Standard of Rest, hereafter LSR). All radial velocities mentioned in this chapter are given with respect to the LSR. In the fields where obvious SiO emission was detected (most sources in sample 2), we selected the velocity channel with strongest emission of the ^{28}SiO v=1 line, and carried out phase and amplitude self-calibration. In most cases we could obtain solutions at intervals as short as the integration cycle time of the individual visibilities (6 seconds for sample 1, 10 seconds for sample 2). We then copied the solutions to the whole dataset, including all spectral lines and the continuum emission. For sample 1, where no SiO emission was detected, we carried out self-calibration on the radio continuum data at 43 GHz, and the solutions were then copied to the spectral line data and the continuum at 45 GHz. By using the same self-calibration solutions for all data in each source, we ensure a better relative accuracy in the flux density measurements.

Moreover, for sample 1, the sampling of the interferometric plane provided by the ATCA with the short time span covered by the observations of each source ($\simeq 45$ min in most cases) is poor, which results in point spread functions with strong sidelobes. In the case of the unresolved sources with a good signal-to-noise ratio, this is not a major problem, since the CLEAN algorithm can work properly and remove the sidelobes. However, the continuum emission in NGC 6302 is resolved, which significantly affects the image reconstruction. In fact, several of the resulting sidelobes of the maps are actually stronger than the peak closest to the expected location of the source. Even restricting deconvolution to this central peak, we could not obtain continuum maps with good enough fidelity to provide reliable source parameters. The interferometric visibilities, however, clearly show the presence of emission. Thus, the parameters of the continuum emission in this source, presented below, were obtained by fitting an elliptical Gaussian function to the visibilities using task uvmodelfit of CASA.

We subtracted the continuum emission from the visibilities of the spectral lines using task UVLIN, by selecting channels without line emission in the spectral window of each transition. For the continuum emission, we used the broadband channels covering 2 GHz at each IF, flagging out the frequencies were the line emission was detected. Final maps were obtained with task IMAGR, using Brigg's weighting of visibilities, with robust parameter equal 0 (which is equivalent to 0.5 in the imaging tasks of CASA, such as tclean). The continuum images were obtained with multi-frequency synthesis. All continuum and line images were deconvolved using the CLEAN algorithm (Clark 1980), implemented in task IMAGR.

The absolute astrometric accuracy of the ATCA has been estimated to be $\simeq 0.4''$ for well-calibrated data and under good weather conditions (e.g., Caswell 1997; Ellingsen et al. 2018). Since we self-calibrated our data and the weather conditions were acceptable but not excellent, our astrometric accuracy is then determined by the positional accuracy of our model for each source (the position of the radio continuum emission at 43 GHz for sample 1 or the peak of the ^{28}SiO (v=1, J=1-0) emission in sample 2). A comparison of the position in final images of the features used for self-calibration, with that of their counterpart sources in the *Gaia* DR3 catalog (Gaia Collaboration et al. 2016, 2023), 2MASS point source catalog (Skrutskie et al. 2006), and *Spitzer* catalogs (Spitzer Science 2009) allows us to estimate that our absolute astrometry is accurate to $< 1.2''$ for sample 1, and $< 0.7''$ for sample 2. Positional information in our data was obtained by fitting elliptical Gaussians to the emission, with task JMFIT. The positions we report in the results of this chapter correspond to the emission used as a self-calibration reference. Therefore, for sources detected in continuum emission, we provide the absolute positions at 43 GHz. In the case of sources with detected maser emission, considering the angular resolution of the observations and the signal-to-noise ratio achieved, the different maser components of all SiO transitions within each source were compatible, within the errors, so we cannot provide information about the spatial distribution of the emission. Therefore, for these maser detections, we only give the estimated position of the strongest maser component for the ^{28}SiO(v = 1, J=1-0) transition as representative of all SiO maser emission, in the results presented in Sect. 4.4.2.

The uncertainty of flux calibration in ATCA observations at 7 mm is estimated to be $\simeq 10\%$. However, we note that we do not include this uncertainty when quoting flux density errors in the tables of this chapter. The flux density errors in this chapter only consider the contribution of thermal noise in the maps, and are given at a 1σ level. These errors provide a good representation of the relative flux uncertainties among the different SiO transitions, and between these and the continuum emission, since they all share the same flux and complex gain calibration, and observations are simultaneous. The errors we quote are thus useful for estimating line ratios and their uncertainties in our data. However, the 10% uncertainty in absolute calibration should be added to the flux density errors quoted in this chapter, when comparing with the emission from other datasets. We also note that the errors quoted in this chapter for all parameters are given at a 1σ level, while upper limits are at 3σ.

4.4 Results

We have not detected any SiO maser emission associated with PNe or PN candidates, in either observed sample. In particular, in the young PNe of sample 1 we detected radio continuum emission but no SiO. In sample 2, we detected SiO emission that corresponds that previously reported in single-dish observations toward these objects, but we could not confirm any association of SiO and radio continuum emission. Instead, our interferometric observations allow us to firmly establish the association of the detected SiO emission with strong, point-like infrared sources. Together with the absence of radio continuum emission, we infer that these SiO-emitting sources are most likely AGB or post-AGB stars.

4.4.1 Sample 1

In the case of the sample of confirmed and candidate PNe that emit maser emission of other molecular species (OH and/or H_2O), we do not detect any SiO emission within the observed fields. We detect the continuum emission associated with all the targets in this sample. A summary of the results is presented in Table 4.3. The continuum emission of all sources, except NGC 6302, is unresolved in our images (with an angular resolution $\simeq 6''$). As mentioned in Sect. 7.2, the position and flux densities reported in Table 4.3 for NGC 6302 were obtained by fitting a model of an elliptical Gaussian source to the visibilities. The full width at half maximum of the fitted Gaussian was $11'' \times 9''$, with position angle $\simeq -53°$.

We note that values of the radio continuum emission at 43 and 45 GHz using this dataset were already presented for IRAS 16372−4808 and OH 341.6811+00.2634 in Chapter 3. Here we present slightly revised values for these sources. The main difference with respect to Chapter 3 is that, in that chapter, the data at each frequency were self-calibrated independently, while in the present chapter we used the same self-calibration solutions (those obtained at 43 GHz), as mentioned in Sect. 7.2. The new values are compatible with the previously reported ones.

We also detected the H53α recombination line in seven of the targets of this sample. These results will be presented in a forthcoming paper.

4.4.2 Sample 2

SiO maser emission was detected in most of the observed fields (Table 4.4). SiO maser emission had been previously reported in those sources via single-dish observations, but we

Table 4.3: Radio continuum emission and representative SiO upper limits in confirmed and candidate PNe with OH and/or H_2O masers (sample 1).

Source	R.A.(J2000)	Dec (J2000)	S_{43} (mJy)	S_{45} (mJy)	S_{v1} (mJy)	S_{v2} (mJy)
IRAS 15103−5754	15:14:18.42	−58:05:21.0	18.41 ± 0.09	19.26 ± 0.15	< 8	< 8
IRAS 16333−4807	16:37:06.55	−48:13:43.9	103.6 ± 0.3	109.9 ± 0.7	< 8	< 8
IRAS 16372−4808	16:40:55.97	−48:13:59.9	57.98 ± 0.08	59.6 ± 0.4	< 7	< 6
OH 341.6811+00.2634	16:51:53.66	−43:47:16.8	16.44 ± 0.08	16.32 ± 0.11	< 7	< 7
NGC 6302	17:13:44.56	−37:06:10.4	1475.2 ± 1.1	1449.2 ± 1.2	< 41	< 43
IRAS 17347−3139	17:38:00.55	−31:40:55.4	320.15 ± 0.15	313.3 ± 2.2	< 7	< 5
JaSt 23	17:40:23.05	−27:49:11.5	21.98 ± 0.05	22.49 ± 0.15	< 7	< 6
IRAS 17393−2727	17:42:33.13	−27:28:25.0	22.41 ± 0.08	23.38 ± 0.14	< 6	< 6
IRAS 18061−2505	18:09:12.44	−25:04:34.1	55.88 ± 0.07	56.7 ± 0.6	< 6	< 5
Vy 2-2	19:24:22.22	+09:53:56.3	253.28 ± 0.14	264.0 ± 1.1	< 7	< 7
K 3-35	19:27:44.01	+21:30:05.1	12.45 ± 0.07	12.38 ± 0.14	< 7	< 8

The positions listed in this table were obtained by fitting elliptical Gaussians to the images at 43 GHz. S_{43} and S_{45} are the flux densities at 43 and 45 GHz, respectively. S_{v1} and S_{v2} correspond to the 3σ upper limits per channel of the $v = 1$ and $v = 2$ transitions of ^{28}SiO, respectively, and are representative of the sensitivity for spectral line detection in our data. Uncertainties are quoted at the 1σ level.
For NGC 6302, for which reliable images could not be obtained, the reported position and continuum flux densities were derived by fitting an elliptical Gaussian model directly to the visibilities. In this case, the quoted uncertainties correspond to the formal errors of the fit and may underestimate the true flux density uncertainty if the emission significantly departs from a Gaussian distribution. The SiO upper limits for NGC 6302 were calculated from spectra extracted directly from the calibrated visibility data.

provide accurate interferometric positions, for the first time in most cases. Based on this, in no case we could confirm that it was associated with a PN. In particular, the position of the SiO emission we obtain in our interferometric maps does not match any of the radio continuum sources reported in their neighborhood or, in some cases, the reported continuum sources may be spurious. Only in the case of IRAS 17390−3014, there is an extended radio continuum source that overlaps the optical/infrared position of the SiO-emitting object. However, as discussed in 4.4.2.1, we think it unlikely that the radio continuum source corresponds to a planetary nebula. Moreover, the large offsets found in some sources between SiO and the previously reported radio continuum emission cannot be due to proper motions, since these are lower than 7 mas in all cases, according to *Gaia* data. We present below the results for each individual source, discussing the relative position of the SiO emission with respect to radio, infrared, and optical sources that could be potential hosts of these masers.

4.4.2.1 IRAS 17239−2812

Emission from the ^{28}SiO transitions $v = 1, 2$, J=1-0 was detected by Hall et al. (1990) in single-dish observations toward the position listed in the IRAS point source catalog, using the Parkes Radio Telescope, with angular resolution of 1.6 arcmin, and peak flux densities 25 and 37 Jy for the $v = 1$ and $v = 2$ lines, respectively. More recent interferometric observations with the Very Large Array (VLA) (Dike et al. 2021) detected emission of the ^{28}SiO $v = 0$, J=1-0 transition. Emission from this transition can have both thermal and maser origin, although Dike et al. (2021) conclude that, in this source, it is mostly of maser

TABLE 4.4: SiO (J=1–0) emission for sources of sample 2.

Source	Transition	R.A. (J2000)	Dec (J2000)	$S_{\rm peak}$ (mJy)	$V_{\rm peak}$ (km s^{-1})	$\int S_\nu dV$ (mJy km s^{-1})	$V_{\rm min}$ (km s^{-1})	$V_{\rm max}$ (km s^{-1})
IRAS 17239−2812	^{28}SiO,$v=0$			146 ± 3	−27.6	377 ± 14	−30.2	−27.2
	^{28}SiO,$v=1$	17:27:05.41	−28:15:29.8	7578 ± 5	−29.6	21436 ± 25	−37.6	−23.0
	^{28}SiO,$v=2$			9627 ± 8	−29.8	28950 ± 30	−38.3	−23.5
	^{28}SiO,$v=3$			1642 ± 5	−28.6	2885 ± 18	−31.7	−26.7
	^{29}SiO,$v=0$			490 ± 4	−24.8	1648 ± 21	−30.3	−23.5
	^{29}SiO,$v=1$			< 18				
IRAS 17390−3014	^{28}SiO,$v=0$			85 ± 6	−23.9	76 ± 9	−24.8	−23.7
	^{28}SiO,$v=1$	17:42:18.86	−30:15:29.0	2128 ± 5	−20.4	5310 ± 30	−27.1	−18.0
	^{28}SiO,$v=2$			4538 ± 8	−20.8	9780 ± 30	−27.3	−17.1
	^{28}SiO,$v=3$			739 ± 5	−20.6	845 ± 12	−22.2	−20.0
	^{29}SiO,$v=0$			< 15				
	^{29}SiO,$v=1$			< 18				
H 2–18	^{28}SiO,$v=0$			< 25				
	^{28}SiO,$v=1$			< 45				
	^{28}SiO,$v=2$			< 25				
	^{28}SiO,$v=3$			< 25				
	^{29}SiO,$v=0$			< 48				
	^{29}SiO,$v=1$			< 15				
IRAS 18052−2016	^{28}SiO,$v=0$			60 ± 6	+52.3	200 ± 30	+50.5	+63.3
	^{28}SiO,$v=1$	18:08:16.39	−20:16:12.2	4424 ± 4	+50.5	30130 ± 70	+17.4	+59.2
	^{28}SiO,$v=2$			3866 ± 6	+49.9	18180 ± 60	+33.3	+61.5
	^{28}SiO,$v=3$			133 ± 5	+54.7	350 ± 25	+49.2	+55.6
	^{29}SiO,$v=0$			317 ± 5	+52.8	928 ± 24	+49.1	+56.1
	^{29}SiO,$v=1$			< 18				
IRAS 19508+2659	^{28}SiO,$v=0$			< 15				
	^{28}SiO,$v=1$	19:52:57.85	+27:07:45.4	927 ± 10	+8.6	3230 ± 30	+2.5	+10.1
	^{28}SiO,$v=2$			897 ± 10	+3.3	3550 ± 30	+2.0	+9.9
	^{28}SiO,$v=3$			< 20				
	^{29}SiO,$v=0$			< 16				
	^{29}SiO,$v=1$			< 25				

For each source, we give the position of the peak emission of the ^{28}SiO ($v = 1$, $J = 1$–0) transition, which was used as reference for self-calibration. The positions of all other velocity components and transitions are compatible with this one within the uncertainties. $S_{\rm peak}$ and $V_{\rm peak}$ are the flux density and velocity of the peak emission, respectively. Flux density upper limits are given at the 3σ level. $\int S_\nu dV$ is the velocity-integrated flux density over the whole spectrum. The velocity range over which emission is detected is defined by $V_{\rm min}$ and $V_{\rm max}$. Uncertainties in the flux density and integrated flux density are quoted at the 1σ level. Velocities are given with respect to the LSR.

nature. No explicit coordinates for the emission is given by these authors, although their identification with a 2MASS source is consistent with ours.

IRAS 17239−2812 can be associated with the infrared source 2MASS J17270541-2815299 and the optical object Gaia DR3 4059869891553026048, which provide a more accurate position. It has infrared colors compatible with those of AGB stars, and its OH spectrum shows the typical double-peak profile of this type of objects (Sivagnanam et al. 1990). There are several reports of radio continuum emission, with catalog positions within the beam of the single-dish SiO observations, such as TXS 1723-282 (Douglas et al. 1996) at 365 MHz, MGPS J172702-281511 (Murphy et al. 2007) at 843 MHz, or NVSS J172702-281525 (Condon et al. 1998) at 1.4 GHz. The formal position in the TXS catalog is only $\simeq 6''$ away from the optical/infrared counterpart of IRAS 17239−2812, a distance which is close to the positional uncertainty quoted for TXS 1723-282 ($4''$ in right ascension and $1.6''$ in declination). However, the positions of the sources reported in the MGPS and NVSS catalogs are significantly offset from the optical/infrared one, considering that their positional errors are better than

$\simeq 1'' - 2''$ (e.g., NVSS J172702-281525 is $34''$ away from Gaia DR3 4059869891553026048 but the position error reported for the radio source is $\simeq 0.09'' \times 1.3''$).

We detected several transitions of SiO. Spectra are shown in Fig. 4.1. In Fig. 4.2 we compare the location of the SiO maser emission with respect to some of the optical, infrared, and radio sources mentioned above. Our interferometric observations clearly show that the SiO emission is associated with IRAS 17239−2812, but we found no radio continuum emission, with 3σ upper limits of 90 and 130 μJy beam^{-1} at 43 and 45 GHz, respectively. Moreover, the position of the SiO masers is not compatible with the radio continuum sources NVSS J172702-281525 nor MGPS J172702-281511. We also checked the radio continuum images at 2.1 GHz from the ATCA follow-up of the SPLASH survey (Qiao et al. 2016a), processed in Chapter 3, and there is extended emission associated with NVSS J172702-281525, but no detection at the optical/infrared position of IRAS 17239−2812. It is also likely that the position listed for TXS 1723-282 has a larger error than the one reported in that catalog, and that the emission found in the TXS, MGPS, and NVSS catalogs actually corresponds to the same object. The possibility of such large positional errors in the TXS catalog is further discussed in Douglas et al. (1996). In any case, at this point we have no evidence that IRAS 17239−2812 is associated with any radio continuum emission.

4.4.2.2 IRAS 17390−3014

^{28}SiO maser emission has been previously detected with the Nobeyama 45-m radio telescope by de Gregorio-Monsalvo et al. (2004) and Fujii et al. (2006). The reported values of peak flux density for the J=1-0, $v = 1$ and $v = 2$ lines are similar in both works. For instance, de Gregorio-Monsalvo et al. (2004) obtain a peak flux density of $\simeq 1.4$ Jy for both transitions, while Fujii et al. (2006) get $\simeq 1.3$ Jy.

IRAS 17390−3014 is associated with the near-IR source 2MASS J17421887-3015288 and the optical one Gaia DR3 4056748416698878592. The OH maser spectrum shows a double-peaked profile typical of AGB stars (Sevenster et al. 1997a; Qiao et al. 2018), with a separation between the peaks of $\simeq 23$ km s^{-1}, and a central LSR velocity of $\simeq -22$ km s^{-1}. There is a radio continuum source at 1.4 GHz, NVSS J174218-301526 (Condon et al. 1998), with a flux density of 10.2 ± 1.4 mJy and a catalog position only $\simeq 6''$ away from that of the 2MASS and *Gaia* sources. Moreover, this radio source was reported to be extended, with estimated deconvolved major and minor axes (full width at half maximum) of $66.2'' \pm 12''$ and $< 46.8''$, respectively, with position angle $6^\circ \pm 9^\circ$. Since the identification and parametrization of sources in the NVSS catalog (Condon et al. 1998) were carried out with an automated algorithm, applied on relatively large fields (size $4^\circ \times 4^\circ$), we downloaded the NVSS image to check the accuracy of the reported position and size estimates for the radio source. We fitted a Gaussian with the image viewer of CASA, using a box that only contained NVSS J174218-301526, and obtained deconvolved major and minor axes of $80'' \pm 12''$ and $34'' \pm 8''$ (position angle $-5^\circ \pm 6^\circ$), respectively, which are compatible with the values listed in the NVSS catalog.

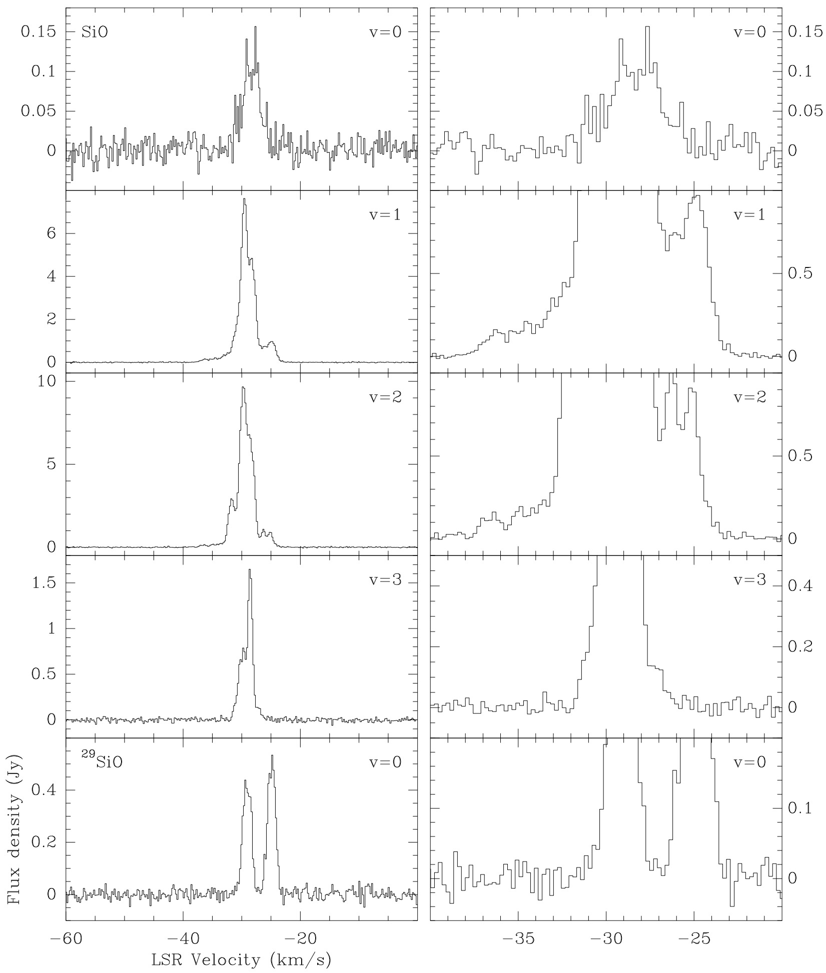

Figure 4.1: SiO(J=1-0) spectra of IRAS 17239−2812. The spectra on the right column are the same as those in the left one (no spectral smoothing applied), but zooming in on the x and/or y axes, to better show the weakest components. The spectra of the other objects presented in this chapter are shown in Appendix 4.A.

We will assume our size estimates in our calculations below. The extended and elongated radio source contains the infrared/optical position of IRAS 17390−3014 so, in principle, it could be associated with this source, tracing, for instance a bipolar ionized nebula, as in many PNe. Moreover, both the infrared/optical and the radio positions are within the beam of the single-dish SiO observations, which makes IRAS 17390−3014 a tantalizing candidate for an SiO-maser-emitting PN.

Ours are the first reported interferometer observations of SiO masers in this region. The SiO spectra are shown in Fig. 4.5. In Fig. 4.3 we plot the relative positions of the SiO maser emission on an infrared image, where we have marked some of the sources mentioned in this section. No radio continuum emission has been detected in our data, with 3σ upper limits of 90 and 80 μJy beam^{-1} at 43 and 45 GHz, respectively. In order to properly compare our limit with the detected radio source at 1.4 GHz (NVSS J174218-301526), we have to consider that the flux density is expected to increase, and the size of the emission to decrease at higher frequencies, in the case of nascent PNe. In quantitative terms, if the radio source

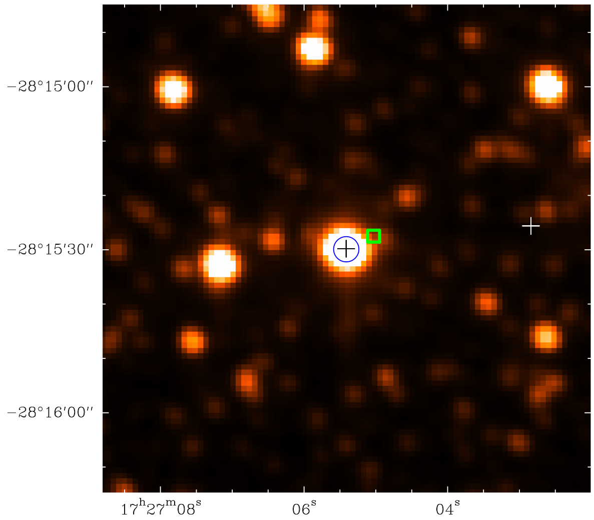

FIGURE 4.2: K-band infrared image from the 2MASS survey, centered at IRAS 17239−2812. The white cross marks the location of the radio source NVSS J172702-281525, the black cross is at the position of the SiO maser emission in our data, and the green square is at the catalog position of TXS 1723-282. The blue circle is centered at the optical source Gaia DR3 4059869891553026048. Coordinates are in the equatorial (equinox J2000) system.

were tracing the free-free emission in a nascent PN, whose photoionized region is expected to have a radial dependency of particle density as $n \propto r^{-2}$, the flux density and linear size of the emission would vary with frequency as $S_\nu \propto \nu^{0.6}$ and $\theta_\nu \propto \nu^{-0.7}$, respectively. These dependencies are valid both for a spherical ionized region (Panagia & Felli 1975) and for a biconical, jet-like distribution with the same radial dependency of density (Reynolds 1986). Therefore a source of 10.2 mJy at 1.4 GHz would emit $\simeq$ 80 mJy at 43 GHz. Regarding its size, assuming an ellipsoidal ionized region with a size dependence of $\theta_\nu \propto \nu^{-0.7}$ in all directions or a biconical distribution with that dependence along the major axis while maintaining the opening angle (Anglada et al. 2018), its size would shrink from $80'' \times 34''$ to $\simeq 7'' \times 3''$. This translates to an expected mean intensity of $\simeq$ 0.5 mJy beam^{-1} at 43 GHz in our observations, which is well above the detection threshold of our continuum data (it should have been detected with a signal-to-noise ratio ≥ 15). Therefore, our non-detection in continuum at 43-45 GHz indicates that the continuum source cannot be tracing an ionized region with a radial dependence of $n \propto r^{-2}$, strongly suggesting that it is not associated with a nascent PN. However, the continuum source could be tracing a more evolved PNe, with an optically thin emission ($\alpha \simeq -0.1$) at least in part of the radio spectrum, and/or with a large size at 43-45 GHz, comparable with that at 1.4 GHz.

To further consider the possibility that the radio emission is tracing a bipolar PN, physically associated with IRAS 17390−3014, we checked publicly available optical and infrared images at different wavelengths. In the images where IRAS 17390−3014 is detected, it shows up as a point source, with no hint of the extended nebulosity that could be expected if the radio continuum emission traces the ionized region of a PN. Therefore, we suggest that the radio continuum emission is not associated with IRAS 17390−3014, but it could be the superposition of several background sources within the $45''$ beam of the NVSS images. It is, however, important to obtain sensitive radio continuum images with a resolution better than those $\simeq 45''$, to find out the sources that may be associated with that type of emission, and to definitely ascertain whether or not some radio continuum emission could be actually related to IRAS 17390−3014. We checked the National Radio Astronomy Observatory Data Archive and the Australia Telescope Observational Archive, to search for publicly available VLA and ATCA observations, but we could not find any data with enough sensitivity for this goal.

4.4.2.3 H 2-18 and IRAS 17403−2107

Our observations were centered at the radio position of the PN H 2-18 (Table 4.1), reported by Gathier et al. (1983), with a positional accuracy of $\simeq 0.2''$. This radio source has a deconvolved size of $1.8'' \pm 0.6''$ and a flux density of 11 mJy at 4.9 GHz. H 2-18 was first cataloged as a possible PN by Haro (1952), and confirmed thereafter (e.g., Acker et al. 1991, 1992). It has a bipolar morphology in the optical, with a size of $\simeq 1.9''$ (Guerrero et al. 2013). Its inclusion in our sample was based on a previous incorrect association of H 2-18 with IRAS 17403-2107 in the SIMBAD database when we built our target list, while these two sources are actually 2.6 arcmin apart. This error was solved in SIMBAD at the time of submission of this chapter. There are several single-dish SiO maser detections toward IRAS 17403-2107 (Izumiura et al. 1995; Deguchi et al. 2007), but no report of radio continuum emission. IRAS 17403-2107 is actually outside the primary beam of our interferometric observations. This source has been classified as a Mira variable (Iwanek et al. 2022).

Even though H 2-18 does not really fulfill our criteria for being included in sample 2 (Sec. 4.2.2) due to this incorrect previous association, we still think that reporting our results on this source is of interest in the context of searching for SiO emission in PNe. In our data, we did not detect any SiO emission associated with the PN H 2-18.

For further evidence of the distinction between H2-18 and IRAS 17403-2107, we point out that the counterparts of IRAS 17403-2107 at optical and near infrared wavelengths are Gaia DR3 4117388024866473088 and 2MASS J17431835-2109031, respectively, whereas H 2-18 is most likely associated with Gaia DR3 4117385040014126592 and 2MASS 17432875-2109515, instead.

4.4.2.4 IRAS 18052−2016 (OH 10.04−0.10)

Emission of different transitions of ^{28}SiO has been reported via single-dish observations, including the $v = 1$, $J = 2 - 1$ transition at 86 GHz (Deacon et al. 2007), $v = 1$ and $v = 2$, $J = 1 - 0$ at 43 GHz (Yoon et al. 2014). Maser emission of other molecular species, such as OH (e.g., Baud et al. 1979a; Sevenster et al. 1997a) and H_2O (Engels et al. 1986; Yoon et al. 2014), has also been found.

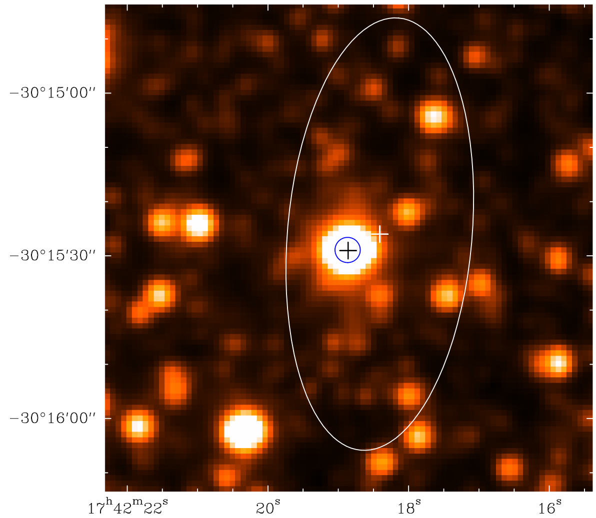

FIGURE 4.3: K-band infrared image from the 2MASS survey, centered at IRAS 17390−3014. The white cross marks the center of the Gaussian fit to the radio source NVSS J174218-301526, while the white ellipse represents the full width at half maximum size of this fit. The black cross is at the position of the SiO maser emission in our data. The blue circle is centered at the optical source Gaia DR3 4056748416698878592. Coordinates are in the equatorial (equinox J2000) system.

IRAS 18052−2016 is associated with the near-IR source 2MASS J18081638-2016115. There is no associated optical source in the *Gaia* DR3 catalog. Radio continuum emission has been reported in this source by Garwood et al. (1988) and Zoonematkermani et al. (1990), from simultaneous observations at 1441.5 and 1611.7 MHz with the VLA, with a flux density of 26 mJy in the combined dataset (central frequency = 1526.6 MHz). However, Becker et al. (1992) pointed out that the detected emission could actually be due to contamination from the OH maser, since it is only present in the band at 1611.7 MHz. The bandpass of the VLA continuum data before 2010 was not sampled in frequency, which would have helped to identify the presence of spectral lines within the band. Later observations by Bains et al. (2009) did not provide any detection of radio continuum emission, with reported 1σ noise values of 0.57 mJy beam^{-1} at 4800 MHz (beam = $6.8'' \times 2.6''$) and 0.11 mJy beam^{-1} at 8640 MHz (beam = $3.7'' \times 1.4''$). In our data, we obtain a 3σ upper limit of 110 μJy beam^{-1} at both 43 and 45 GHz. We thus must conclude that there is no significant amount of ionized gas associated with this source. IRAS 18052−2016 could be a post-AGB star, based on the OH maser spectrum with four components (Qiao et al. 2020), which departs from the usual double-peaked one in AGB objects, and on its infrared colors (Deacon et al. 2004).

In Fig. 4.6, we show the SiO spectra we detected toward this source. We note that the apparent absorption features around 55-60 km s^{-1} in the ^{28}SiO $v = 0$ spectrum smoothed to 0.88 km s^{-1} must be an artifact, since there is no background continuum emission against which line absorption can be produced.

4.4.2.5 IRAS 19508+2659 (OH 63.9−0.2)

Single-dish detections of ^{28}SiO maser emission have been reported in this source by Nakashima & Deguchi (2003b) and Cho et al. (2017). The first single-dish report on OH maser was provided by Baud et al. (1979b), and interferometric confirmation has been subsequently obtained (THOR survey, Beuther et al. 2019). The OH spectrum shows the typical double-peaked profile of AGB stars. H_2O maser emission is also detected in this source (Lewis & Engels 1988; Engels & Lewis 1996).

IRAS 19508+2659 is associated with sources 2MASS J19525786+2707447 and Gaia DR3 2027177220301507072. Radio continuum emission was reported by Garwood et al. (1988) and Zoonematkermani et al. (1990) at 20 cm (mean frequency of 1526.6 MHz), with a flux density of $\simeq$ 13 mJy. However, note that this catalog has the problem (mentioned in Sect. 4.4.2.4 for IRAS 18052−2016) that one of the two bandpasses, centered at 1611.7 MHz and with a bandwidth of 3.125 MHz, includes the frequency of the OH maser line at 1612 MHz, so several sources in these catalogs were not really continuum sources, but were contaminated by OH maser emission. Becker et al. (1992) compiled a list of sources in those data that showed emission at 1611.7 MHz but not at 1441.5 MHz and therefore, they were likely to be OH maser sources. IRAS 19508+2659 was not included in this list of OH maser sources. Using the same data presented by Garwood et al. (1988) and Zoonematkermani et al. (1990), White et al. (2005) reported a value of continuum emission at 20 cm of 8.45 ± 1.48 mJy, at a position R.A.(J2000) = $19^h52^m57.90^s$ (error = $0.7''$), Dec(J2000) = $+27°07'44.7''$ (error = $0.8''$), and with a deconvolved major axis $\simeq 2.34''$. It is possible that these authors assumed that the continuum emission is real, and does not suffer from OH-maser contamination, since it is not in the Becker et al. (1992) catalog. However, we note that such an assumption may not be correct in all cases, since the OH maser list of Becker et al. (1992) included only sources with a flux density $>$ 10 mJy at 1611.7 MHz and undetected at 1441.5 MHz. So the exclusion from this list of the emission associated with IRAS 19508+2659 could just be because it fell below the emission threshold of 10 mJy in the 1611.7 MHz band.

To clarify whether or not IRAS 19508+2659 presents radio continuum emission, we downloaded the 20 cm data mentioned above (observed on 1983 December 30) from the VLA archive, and reprocessed them with the CASA package. In our images, we only detect emission at the position of IRAS 19508+2659 in the band centered at 1611.7 MHz, with a flux density of 10.1 ± 1.2 mJy, and unresolved by the synthesized beam of the images ($6.5'' \times 4.4''$). The 3σ upper limit to the emission at 1441.5 MHz is 3 mJy. Therefore, there is certainly OH maser contamination in these data. OH maser emission ar 1612 MHz has indeed been reported toward this source, in different single-dish observations (e.g., Winnberg et al. 1981; Baud et al. 1981).

For a more complete check on the possible presence of radio continuum emission, we have downloaded the NVSS images at 1.4 GHz, and found no radio source at this position. The NVSS image has a rms noise of $\simeq$ 0.8 mJy beam^{-1} (beam = $45''$), so it is sensitive enough to

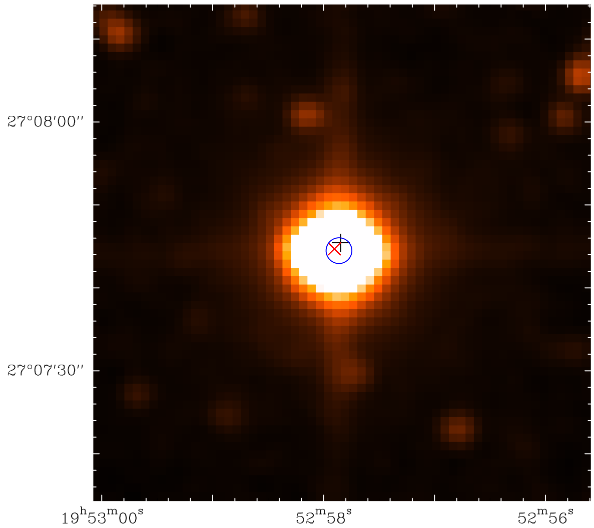

FIGURE 4.4: K-band infrared image from the 2MASS survey, centered at IRAS 19508+2659. The red cross marks the position of the radio continuum source reported by White et al. (2005), but that we argue it actually corresponds to OH maser emission (Sect. 4.4.2.5). The black cross is at the position of the SiO maser emission in our data. The blue circle is centered at the optical source Gaia DR3 4056748416698878592. Coordinates are in the equatorial (J2000) system.

detect a source with the reported values of $8-13$ mJy. Moreover, no source at this position is listed in the catalog of radio continuum emission in the THOR survey (Wang et al. 2018, 2020) at $1-2$ GHz, where they report 7σ upper limits of $\simeq 2-5$ mJy beam^{-1} (beam $\simeq 10''-25''$). This limit should also have been enough to detect the previously reported flux densities. Considering that the free-free emission from ionized gas may be brighter at higher frequencies (unless it is already optically thin at 1.4 GHz, which is rare in planetary nebulae), we also downloaded the Very Large Array Sky Survey (VLASS, Lacy et al. 2020) images at 3 GHz, but we could not see any radio continuum associated with the source, with a 3σ upper limit of 3.6 mJy beam^{-1} (beam $= 3.1'' \times 2.3''$). Moreover, recent VLA observations (Cala et al. in prep) did not provide a detection of the source at 22 GHz, with a 3σ upper limit of $\simeq 70$ μJy beam^{-1} (beam $\simeq 3.5'' \times 2.6''$). In the data presented here, we did not detect any emission at 7 mm, with 3σ upper limits of 140 and 160 μJy beam^{-1} (beam $\simeq 1.13'' \times 0.16''$ at 43 GHz), at 43 and 45 GHz, respectively. Therefore, we must conclude the absence of radio continuum emission from IRAS 19508+2659, with very stringent upper limits at different frequencies.

In Fig. 4.7 we show the SiO spectra toward IRAS 19508+2659. We only detect ^{28}SiO emission of the $v = 1$ and $v = 2$ transitions. The position of the SiO maser emission and the emission at 1611.7 MHz (most likely arising from OH maser emission) are shown on an infrared image, in Fig. 4.4. Since there is no evidence for the presence of radio continuum emission, we then conclude that IRAS 19508+2659 is a regular AGB star.

4.5 Discussion

The lack of confirmed association between SiO maser emission and PNe in this work has different implications, depending on the sample. The negative results in sample 2 (Sect. 4.2.2) are due mainly to the fact that the reported radio continuum emission arises from a nearby, different source from that with SiO maser emission, and therefore, there seems to be no SiO-maser-emitting PN within the beam of the previously reported single-dish maser observations. However, our non-detection of SiO masers in nascent PNe (sample 1, Sect. 4.2.1) posses several interesting questions.

One question is whether the abundance of SiO in gas phase in our targets is not enough to provide the necessary column density of molecules for detectable emission. Moreover, even if SiO is present in the circumstellar environment of PNe, it may be located in regions without the necessary physical conditions for population inversion of the molecular levels, which is a prerequisite to produce maser emission. Of course, it is also possible that SiO masers may be emitted in PNe different from the ones we sampled, specially considering that we targeted PNe harboring masers of other molecular species typical of O-rich stars (OH and H_2O).

The SiO abundance in gas phase tends to drop in circumstellar envelopes as a function of distance from the star, because it is depleted onto dust grains (e.g., Bujarrabal et al. 1986; Verbena et al. 2019). The SiO maser emission during the AGB phase is actually seen within ≤ 5 stellar radii, a distance shorter than the dust formation radius (Diamond et al. 1994). However, SiO may be released again in the presence of shocks. This is the case, for instance, of the "water fountain" sources W43A (probably a late AGB star) and IRAS 16552-3050 (a post-AGB star), objects with clear high-velocity bipolar outflows (Suárez et al. 2008; Tafoya et al. 2020), and which also show SiO maser emission (Nakashima & Deguchi 2003a; Amada et al. 2022). In W43A, this emission seems to trace the base of the bipolar outflow, at distances ≥ 10 au from the central star (Imai et al. 2005), larger than the radius of the SiO maser rings observed in typical AGB stars (< 10 au, Diamond et al. 1994). High-velocity outflows and shocks are also present in PNe (e.g., Hajduk et al. 2024; Miranda et al. 2024), and the detection of water maser emission in some of the objects of our sample 2 is itself a tracer of shocks, since these are thought to be the main pumping mechanism of water masers. Therefore, one should reasonably expect that SiO molecules can be released from dust grains in some PNe.

An additional question for PNe is whether the SiO molecules can survive photoionization close to the hot, central star. Thermal SiO emission at millimeter wavelengths has been reported in the bipolar PN M2-48, using single-dish observations (Edwards & Ziurys 2014). Recent observations with the Atacama Large Millimeter Array of the nascent PN IRAS 15103-5754 (a source included in our sample 1) also show the presence of thermal SiO emission (Gómez et al. 2023). This emission is found at distances ≤ 400 au from the central star. Thus, SiO molecules can indeed be found in gas phase around PNe, but they might not be at close enough distances to the star to produce maser emission.

In the particular case of PNe showing OH and H_2O maser emission, which comprise our sample 1 (Sect. 4.2.1), we note that Cala et al. (2024a) found some evidence that they have dual chemistry, with O-rich external envelopes and C-rich central stars. If the innermost regions of the central envelopes, where one could expect SiO masers to be pumped, are actually C-rich, then this emission will not be produced, due to a lack of SiO molecules. In this case, carbon-bearing molecules may be dominant in the gas phase near the central star.

In summary, the question of the possibility of SiO maser emission around PNe is still open. Our two carefully selected samples comprised what probably were the best candidates to date for such a detection, but none was obtained. Our results clearly indicate that SiO masers, if present at all, are extremely rare. A definite answer about the possibility of finding SiO masers in PNe, and firm constraints for non-detections would require large-scale surveys and mappings of SiO maser emission in the Galactic plane and bulge. A promising example is the Bulge Asymmetries and Dynamical Evolution (BAaDE) survey (Lewis et al. 2020; Sjouwerman et al. 2024), which covers $\simeq 28,000$ sources, although it is still a targeted search, with a sample selected based on infrared colors. The MALT-45 survey (Jordan et al. 2015) includes the SiO lines we studied in this chapter, although its coverage of the galactic plane is limited, with published results only for galactic coordinates $330° < l < 335°$, $|b| < 0.5°$. A larger-scale blind SiO galactic mapping, as carried out for other maser species, like the Methanol Multibeam survey (Green et al. 2008), the Southern Parkes Large-Area Survey in Hydroxyl (SPLASH, Dawson et al. 2022), The HI/OH/Recombination line survey of the inner Milky Way (THOR, Beuther et al. 2016), or the H_2O southern Galactic Plane Survey (HOPS, Walsh et al. 2011) may be necessary to avoid selection biases in the search for SiO-maser-emitting PNe.

4.6 Conclusions

We have carried out a search for SiO maser emission in PNe. A total of 16 objects were observed in two source samples. We find no SiO maser emission associated with any confirmed or candidate PNe. Our non-detections indicate that SiO masers in PNe are extremely rare, if present at all. SiO molecules can be present in the gas phase in the circumstellar material of PNe, but probably not at the locations needed for efficient pumping of SiO masers. Since there is some evidence that PNe with OH and/or H_2O masers have O-rich outer envelopes, but C-rich central stars and inner envelopes, we speculate that C-bearing molecules can be dominant at the inner locations where the physical conditions for SiO maser production may have been met.

Acknowledgments

The Australia Telescope Compact Array is part of the Australia Telescope National Facility (grid.421683.a) which is funded by the Australian Government for operation as a National Facility managed by CSIRO. We acknowledge the Gomeroi people as the traditional owners of the Observatory site. This work is financially supported by grants PID2020-114461GB-I00, PID2023-146295NB-I00, and CEX2021-001131-S, funded by MCIN/AEI /10.13039/ 501100011033, and by grant P20-00880, funded by the Economic Transformation, Industry, Knowledge and Universities Council of the Regional Government of Andalusia and the European Regional Development Fund from the European Union. RC also acknowledges support by the predoctoral grant PRE2018-085518, funded by MCIN/AEI/ 10.13039/501100011033 and by ESF Investing in your Future. We made use of the VLASS QLimage cutout server at URL cutouts.cirada.ca, operated by the Canadian Initiative for Radio Astronomy Data Analysis (CIRADA). CIRADA is funded by a grant from the Canada Foundation for Innovation 2017 Innovation Fund (Project 35999), as well as by the Provinces of Ontario, British Columbia, Alberta, Manitoba and Quebec, in collaboration with the National Research Council of Canada, the US National Radio Astronomy Observatory and Australia's Commonwealth Scientific and Industrial Research Organisation.

4.A Additional figures

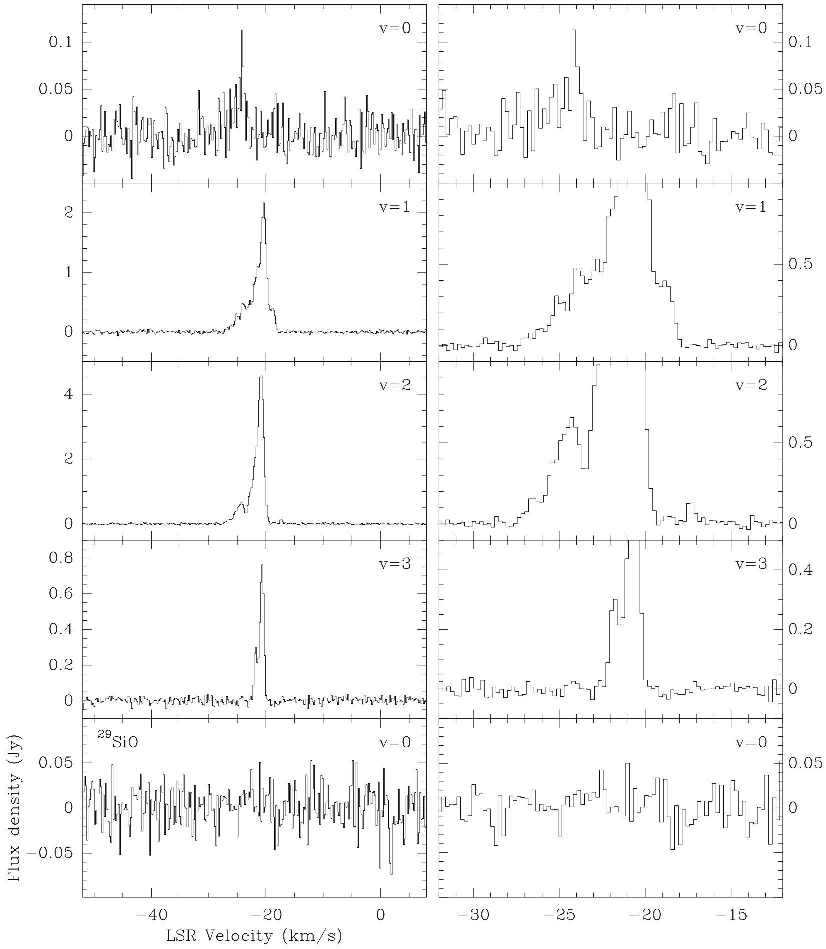

FIGURE 4.5: Same as Fig. 4.1, but for IRAS 17390−3014.

In this appendix we show the SiO(J=1-0) spectra of three of the sources detected in this chapter: IRAS 17390−3014, IRAS 18052−2016, and IRAS 19508+2659. The spectra of IRAS 17239−2812 are presented in Fig. 4.1.

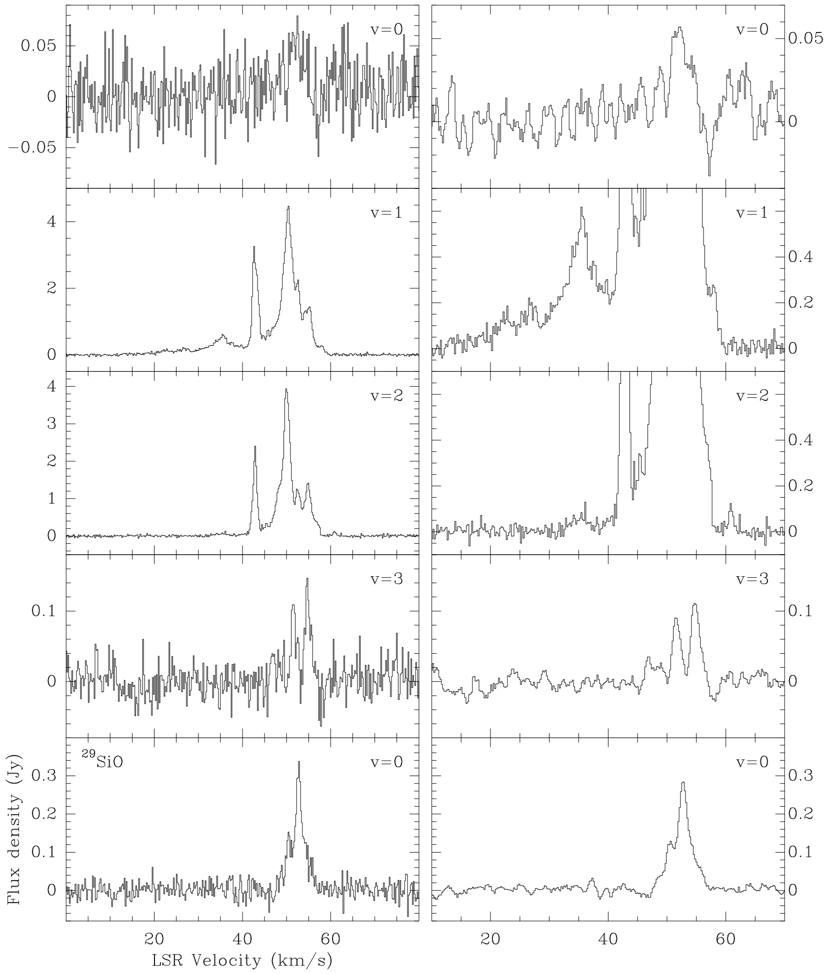

FIGURE 4.6: SiO(J=1-0) spectra of IRAS 18052−2016. The spectra on the right column are the same as those in the left one, but zooming in on the x and/or y axes, to better show the weakest components, except in the case of the $v = 0$ (both isotopologues) and $v = 3$ lines, which have been boxcar-smoothed to a spectral resolution of 0.88 km s^{-1}, to increase the signal to noise ratio.

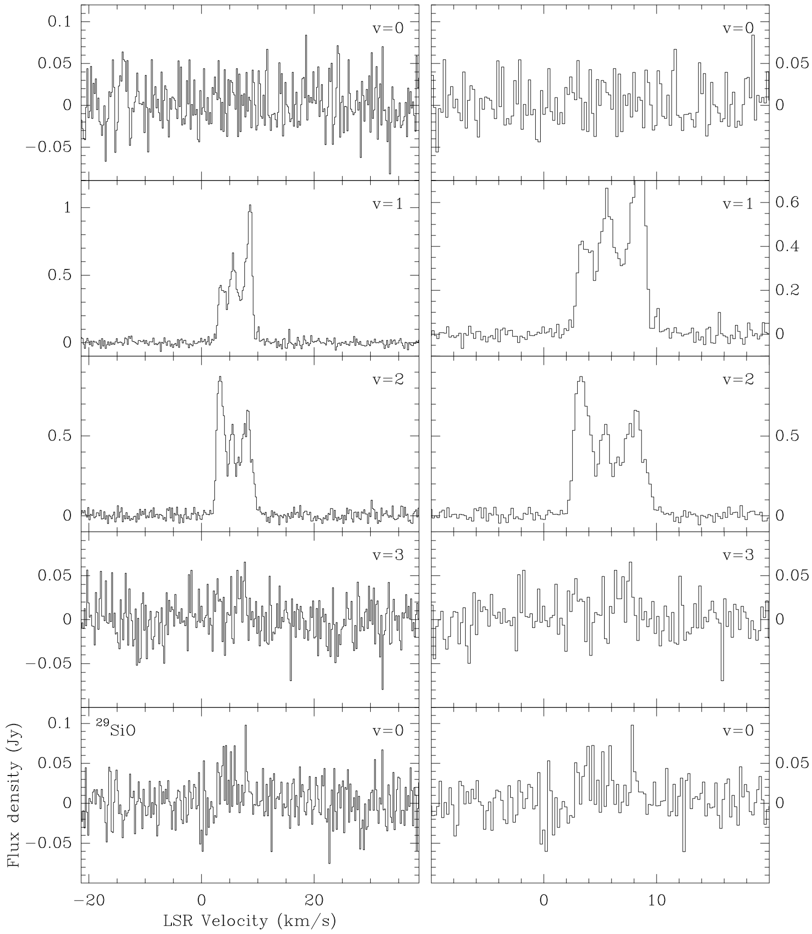

FIGURE 4.7: Same as Fig. 4.1, but for IRAS 19508+2659.

Chapter 5

Long- and short-term variability of the possible nascent planetary nebula IRAS 22568+6141: A late thermal pulse?

5.1 Introduction

Planetary nebulae (PNe) consist of circumstellar matter that is photoionised by hot central stars that evolve towards the cooling white dwarf phase. This ionised gas is the origin of most of the radiation from PNe. The emission at optical and infrared wavelengths is dominated by forbidden and recombination emission lines, while in the radio domain, the main emitting mechanism is bremsstrahlung (or free-free radiation) from free electrons in the plasma. This thermal continuum free-free radiation is characterised by a spectral index (α, where $S_\nu \propto \nu^\alpha$) ranging from +2 (optically thick regime at low frequencies) to −0.1 (optically thin regime at high frequencies; e.g. Aaquist & Kwok 1991) However, Suárez et al. (2015) showed that the young PN IRAS 15103−5754 presents non-thermal radio continuum emission, with $\alpha \simeq -0.54$, compatible with synchrotron radiation. Several other possible PNe also present some evidence of non-thermal emission (Cerrigone et al. 2011, 2017). The detection of non-thermal radio continuum emission in a PN could be an indication that it is in a nascent stage, since the free-free radiation in more evolved PNe would completely veil this non-thermal continuum emission.

IRAS 22568+6141 (PN G110.1+01.9, α(2000) =22h58m51.6s, δ(2000)= +61°57′43.5″; hereafter IRAS22568) could be one such nascent PNe. The optical spectrum presented by (Garcia

This chapter is derived from the following publication:

- Cala et al. (2024c)

Lario et al. 1991, hereafter GL+91) shows emission lines that are compatible with a low-excitation PN, and it is characterised by relatively prominent [N II] and absent [O III] emission lines. The radio continuum emission reported by Cerrigone et al. (2011, 2017) suggests a negative spectral index ($\alpha \simeq -0.35$), which was confirmed by Gómez et al. (in preparation) with quasi-simultaneous observations at different frequencies. Figure 5.1 presents the *Hubble* Space Telescope (HST) image of IRAS22568 in the F606W filter. The nebula is bipolar and extends over $\simeq$8" along the main axis, which is oriented at a position angle P.A.$\simeq -30°$. The bipolar lobes are separated by a dark lane of width $\simeq$0.″25, where no optical emission is observed, and which seems to obscure the central star. Radio continuum observations by Cerrigone et al. (2017) at 8.4 GHz resolved the two lobes and showed emission from a central core between the lobes.

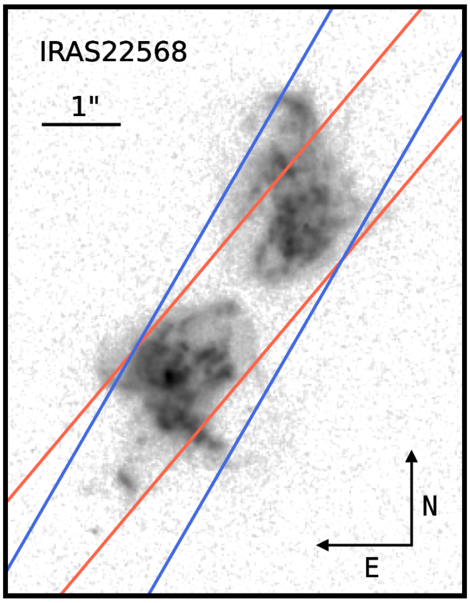

FIGURE 5.1: HST (F606W) image of IRAS 22568+6141 with the long-slit position used for our spectra represented in blue (width = 2″, P.A. −30°), and the spectra used by GL+91 represented in red (width = 1.″5, P.A. −40°).

As part of a project to identify, confirm, and characterise new nascent PNe with non-thermal radio continuum emission, we obtained intermediate- and high-resolution long-slit spectra of IRAS22568 at different epochs. In this chapter, we show that the source presents a peculiar variability on timescales of decades and a few years, as well as an internal kinematics that is not usually seen in PNe. The data presented here are crucial for understanding the nature of this possible nascent PN.

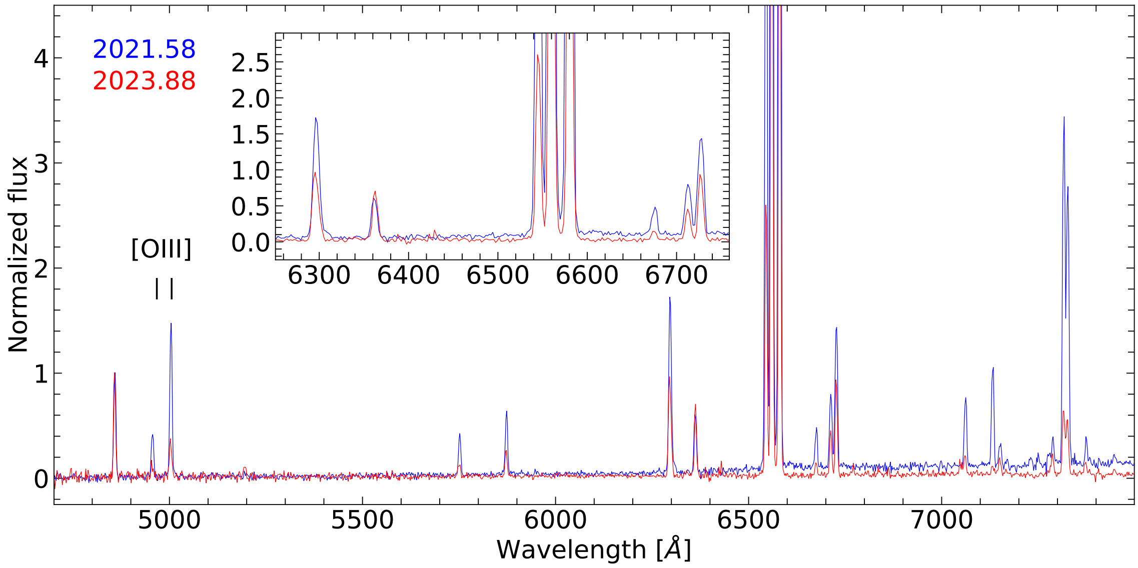

FIGURE 5.2: Intermediate-resolution optical spectra of IRAS 22568+6141 obtained at the Calar Alto Observatory in 2021 (blue) and 2023 (red), normalised to the peak flux of Hβ. The indicated [O III]λ4959,5007 emission lines were not detected in 1988 (see the text).

5.2 Observations and data reduction

5.2.1 Intermediate-resolution long-slit optical spectroscopy

We used the Calar Alto Faint Object Spectrograph (CAFOS) at the 2.2m telescope of the Calar Alto Observatory (Spain) on 2021 August 2 (proposal ID: F21-2.2-0.17; PI: R. A. Cala), and 2023 November 17 (proposal ID: DDT23B.320; PI: R. A. Cala) to obtain intermediate-resolution long-slit spectra on IRAS22568. In Fig. 5.1 we show with blue lines the long slit (width = 2.″0) oriented at a P.A. −30° along the major nebular axis. In both epochs, the sky was photometric during the observations, with a mean seeing of 2.″1, and in both epochs, we observed the standard star BD+28°4211 for the flux calibration. The spectra were recorded in a SITe CCD with 2048×2048 pixel^2. The spatial scale in the detector is 0.53 arcsec pixel^{-1}. In 2021 and 2023, we obtained four and three spectra using grism B-100 (3200-6200 Å) with 1800 s exposure time each, and we combined them into a single spectrum for each epoch. In each epoch, we also obtained one spectrum with grism R-100 (5800-9600 Å) and 1800 s of exposure time. The spectra were calibrated following standard procedures in IRAF. We obtained a dispersion of ∼2 Å pixel^{-1} after the wavelength calibration. PyNeb (version 1.1.19; Luridiana et al. 2015) was used to obtain the physical properties of the ionised gas, and Table 5.5 lists the atomic constants we employed.

5.2.2 High-resolution long-slit optical spectroscopy

High-resolution long-slit spectroscopy of IRAS 22568 was conducted on 2023 August 5–7 using the Manchester Echelle Spectrometer (MES) at the 2.1 m telescope on the San Pedro

Mártir Observatory (Mexico; proposal ID: FM-15; PI: R. Vázquez). The long slit (2" width) was oriented at a P.A. $-30°$ (Fig. 5.1). The spectra were recorded in an E2V-4240 CCD with 1024×1024 pixel^2 and 4×4 binning, resulting in a spatial scale of $0''.704$ pixel^{-1}. Spectra of the Hα, [N II]λ6584, [S II]λ6730, and [O III]λ5007 emission lines (hereafter [N II], [S II], and [O III]) were obtained with exposure times of 1800, 1800, 3600, and 3600 s, respectively. A Th-Ar lamp spectrum was obtained immediately after each source spectrum for the wavelength calibration. The spectra were reduced with IRAF. The average seeing during the observations was $\sim 1''.8$, and the spectral resolution is ~ 11 km s^{-1}, as indicated by the full width at half maximum (FWHM) of the emission lines in the ThAr spectra.

5.3 Results

5.3.1 Spectral variability and physical properties of the ionised gas

Fig. 5.2 shows the intermediate-resolution spectra of IRAS22568 integrated over its two bipolar lobes. Fig. 2 and Fig. 3 in GL+91 immediately reveal significant differences between the 1988, 2021, and 2023 spectra. Although our spectra resolve the two bipolar lobes of the object, we used the observed emission line fluxes in the integrated spectra for the analysis for a better comparison between the spectra at the three epochs. The observed fluxes in 1988 can be found in GL+91 (their Table 2, column 3), and those in 2021 and 2023 are listed in Table 5.6 .

We used the interstellar extinction law of Seaton (1979) to obtain the logarithmic extinction coefficient at Hβ, c(Hβ), and hereby, the intrinsic emission line intensities in the three epochs. The c(Hβ) was derived from the Hα and Hβ emission lines and a theoretical Hα/Hβ line intensity ratio of 2.85. We note that a similar c(Hβ) is obtained from the Paschen 9 (P 9) and Hβ emission lines, and a theoretical P 9/Hβ line intensity ratio of 18.4×10^{-3}. The intrinsic line intensities, Hβ flux, and c(Hβ) at the three epochs are listed in Table 5.1. The differences between the intrinsic line intensities in 1988 obtained by us (listed in our Table 5.1, column 4) and those obtained by GL+91 (listed in their Table 2, column 4) are not significant and are due to the different extinction law employed.

TABLE 5.1: Intrinsic line intensities (I(Hβ)=100) in IRAS22568.

Emission line	I(λ) 1988.58	I(λ) 2021.58	I(λ) 2023.88
4101 Hδ	–[a]	40.71±2.16	–[a]
4340 Hγ	–[a]	57.12±3.72	–[a]
4363 [O III]	–[a]	8.81±2.29	–[a]
4471 He I	–[a]	7.6±0.7	–[a]
4861 Hβ	100±10	100.0±1.6	100.0±2.5

Continued on next page

Table 5.1 continued

Emission line	I(λ) 1988.58	I(λ) 2021.58	I(λ) 2023.88
4959 [O III]	–[a]	40.70±1.15	15.02±1.60
5007 [O III]	–[a]	119.09±1.35	40.58±2.01
5755 [N II]	8.05±0.79	11.00±0.28	7.65±0.30
5876 He I	11.73±1.11	13.83±0.25	12.86±0.40
6300 [O I]	25.89±1.32	22.25±0.19	67.16±0.68
6363 [O I]	10.03±0.49	8.10±0.18	26.88±0.64
6548 [N II]	73.9±1.3	70.04±2.46	80.33±1.67
6563 Hα	285.0±5.1	285.0±2.5	285.0±1.6
6584 [N II]	215.7±4.7	220.0±2.4	235.0±1.6
6678 He I	2.80±0.39	3.69±0.11	4.28±0.26
6716 [S II]	8.86±0.81	7.01±0.12	13.07±0.27
6731 [S II]	17.46±1.32	13.44±0.13	26.00±0.28
7002 O I	–[a]	0.49±0.02	–[a]
7065 He I	4.2±0.4	4.63±0.08	4.69±0.19
7137 [Ar III]	6.1±0.9	6.37±0.08	3.19±0.19
7150 [Fe II]	–[a]	1.49±0.07	4.20±0.19
7230 [Fe II]	–[a]	0.59±0.04	3.53±0.26
7254 O I	–[a]	0.54±0.04	3.24±0.25
7281 He I	–[a]	0.75±0.09	5.90±0.21
7319 [O II]	blended[b]	19.98±0.15	15.16±0.22
7330 [O II]	blended[b]	15.37±0.14	13.95±0.23
7378 [Ni II]	1.73±0.43	1.31±0.14	3.05±0.15
7447 [Fe II]	–[a]	0.55±0.03	1.79±0.18
7751 [Ar III]	–[a]	1.83±0.07	0.67±0.04
8446 O I	blended[c]	3.33±0.06	1.61±0.11
8467 P 17	blended[c]	0.81±0.05	0.71±0.04
8502 P 16	–[a]	0.85±0.06	1.54±0.11
8545 P 15	–[a]	1.09±0.06	1.97±0.14
8578 [Cl II]	–[a]	0.77±0.06	2.26±0.12
8598 P 14	–[a]	0.79±0.06	1.76±0.15
8605 [Fe II]	–[a]	1.31±0.06	4.37±0.12
8665 P 13	–[a]	1.27±0.06	2.26±0.14
8750 P 12	–[a]	0.96±0.05	2.29±0.13
8863 P 11	–[a]	1.53±0.05	2.71±0.11
8890 [Fe II]	–[a]	0.91±0.05	2.29±0.11
9015 P 10	1.57±0.24	1.83±0.07	1.63±0.07
9069 [S III]	9.41±0.86	14.42±0.07	5.15±0.09
9229 P 9	3.45±0.43	3.44±0.08	5.10±0.15

Continued on next page

Table 5.1 continued

Emission line	I(λ) 1988.58	I(λ) 2021.58	I(λ) 2023.88
9535 [S III]	22.34±1.52[d]	32.22±0.19	11.86±0.30
F(Hβ)[e]	1.16±0.12	6.88±0.11	4.11±0.11
c(Hβ)	3.70±0.16	3.05±0.05	1.66±0.04
Av[f] (mag)	7.88±0.34	6.48±0.10	3.53±0.09

[a] Not detected by GL+91 or in 2023.95.
[b] [O II] λ7319,7330 are blended, with I(sum)=32.63±2.26.
[c] O I λ8446 and P 17 λ8467 are blended with I(sum)=6.09±0.61.
[d] Emission line blended with P 8 λ9546.
[e] In units of 10^{-15} erg cm^{-2} s^{-1}.
[f] Nebular extinction, see the text for details.

TABLE 5.2: Electron temperature and electron density of the ionised gas in IRAS 22568+6141 in the three epochs.

	1988.58[a]	2021.58	2023.88
T_e [N II] (K)	13600±1000	17300±600	12400±300
T_e [O III] (K)	–[b]	38400^{+17000}_{-10500}	–[c]
N_e [S II] (cm^{-3})	12100^{+}_{-8500}	10600±2100	12900^{+4500}_{-2900}

[a] No reliable upper limit for the electron density could be obtained.
[b] [O III] emission lines not detected.
[c] [O III] λ4363 not detected.

The most astonishing result is the presence in 2021 of the [O III] λ4363,4959,5007 emission lines in the nebula with I([O III])/I(Hβ)≃1.7, which were absent in 1988 (GL+91). Based on the intensity of the weakest emission line detected in the spectrum from 1988 (I(P 10)/I(Hβ)≃0.016; Table 5.1) as an upper limit to the detection of the [O III] lines, they have emerged between 1988 and 2021 or, at least, their intensity has increased by more than two orders of magnitude in that time span. The subsequent variability of the [O III] λ4959,5007 emission lines is also impressive. Their intensity relative to Hβ has decreased by a factor of ≃3 between 2021 and 2023, while the [O III]λ4363 line is not detected in the last epoch.

Other emission properties of the ionised gas have also substantially changed in IRAS22568. Table 5.1 shows that the Hβ flux increased by a factor ≃6 between 1988 and 2021. This value should be taken with some caution because the long slits used in 1988 and 2021 do not cover exactly the same regions of the object (Fig. 5.1), and extinction (see below) and sensitivity of the observations were different. However, the strong increase in the Hβ flux between 1988 and 2021 should be considered real. Between 2021 and 2023, the Hβ flux decreased by a factor of ≃1.7, and we note that these two spectra were obtained under almost identical conditions (Sect. 9.3.3).

The value of c(Hβ) (Table 5.1) decreased by factors of ≃1.06 between 1988 and 2021, and by factors of ≃1.8 between 2021 and 2023. Given that the nebular reddening E (B–V) and the nebular extinction Av are related by $c(\text{H}\beta)$=1.45×E (B–V), and $c(\text{H}\beta)$=0.47×Av (using the Seaton 1979, extinction law), we obtain Av(1988)=7.88±0.34 mag, Av(2021)=6.48±0.10 mag, and Av(2023)=3.53±0.10 mag. Therefore, the nebular extinction of IRAS22568 decreased 1.40±0.35 mag between 1988 and 2021, and 2.95±0.10 mag between 2021 and 2023.

Other emission lines present a variable intensity relative to Hβ between 1988 and 2023. For the very weak emission lines (e.g., Hγ, Hδ, [Cl II], and [Fe II]) that were not present in the 1988 spectrum, their detection in 2021 and/or 2023 may be due to a combination of an increased nebular flux and better sensitivity in our spectra. The variability in the [S II], [O I], [O II], and He I emission lines can be considered real because these lines are relatively strong and were detected in all three epochs. Moreover, an inspection of the 2021 and 2023 line intensities reveals that IRAS22568 has recombined in this time span. This is directly recognizable in (a) the decrease in the O^{2+}, O^{+}, and S^{2+} line intensities (relative to Hβ) in favour of those of O^{+}, O^{0}, and S^{+}, respectively, (b) the decreasing intensity in the Ar^{2+} emission lines, (c) the increasing intensity in the Fe^{+} and Ni^{+} lines, and (d) the decrease in the Balmer emission intensities. The [N II] λ6548,6583 emission lines increased slightly in their relative intensities between 2021 and 2023, probably due to recombination from N^{2+}, which proceeds faster than recombination from N^{+} to N^{0}. In contrast to the line intensity observed in the nebular [N II] lines, the auroral [N II] λ5755 line intensity clearly decreased between 2021 and 2023, implying that the nebula also cooled.

To calculate the electron temperature (T_e), we used the [N II](6584+6548)/5755 and [O II](4959+5007)/4363 emission lines ratios, while the electron density (N_e) was obtained from the [S II](6716/6731) line intensity ratio. These values were obtained making use of CROSSTEMDEN in PyNeb. The results are listed in Table 5.2. The values of T_e([N II]) are consistent with an increase in the excitation between 1988 and 2021, and with cooling between 2021 and 2023. In 2021, when the [O II] λ4363 was detected, we obtained T_e([O III]) $\simeq$ 38400 K and T_e([N II]) $\simeq$ 17300 K. T_e([O III]) is anomalously high and very much higher than T_e([N II]). These values can hardly be explained with photoionisation, but clearly indicate shock excitation. This is discussed in detail in Sect. 5.4.1. In 2023, we obtained an upper limit for the [O III] λ4363 line intensity (Table 5.6) that prevented us from deriving T_e([O III]), while the [O III] lines were not detected in 1988.

As for the electron density (Table 5.2), the uncertainties in the line intensities in 1988 do not allow us to obtain an upper limit of N_e, suggesting that the nebula could have been in a high-density regime (see GL+91). On the other hand, the nominal values of N_e agree with each other within the errors. We note that the values of N_e are averaged values that were integrated along the line of sight. The knotty structure of IRAS2258 suggests that N_e may present a relatively wide range of values throughout the nebula (see e.g. Lee et al. 2022; Hyung et al. 2023).

With the values obtained for N_e (Table 5.2), we can estimate the recombination timescales, assuming a recombination rate per ion $R_i \simeq 10^5\,\text{yr} / (Z^2\, N_e)$, where Z is the ionic charge (Osterbrock 1989). The recombination timescales of single- and double-ionised species are

TABLE 5.3: Multi-epoch broadband r-filter photometry on IRAS22568.

Epoch	Survey	r (mag)	Reference
1953.8	POSS-I	16.16±0.25	Monet et al. (2003)
1990.5	–	16.7±0.3	GL+91
1991.7	POSS-II	15.15±0.25	Monet et al. (2003)
2003.7	SDSS	15.92±0.02	Abazajian et al. (2009)
2012.7	PanSTARRS	16.40±0.01	Chambers et al. (2016)
2019.5	ZTF	16.15±0.03	Masci et al. (2019)

8–12 and 2–3 yr, respectively, which are consistent with the fact that the [O III] emission lines have almost vanished between 2021 and 2023, while the Balmer lines show a more moderate decrease in intensity between these two epochs.

5.3.2 Light curve

In order to further investigate the optical variability of IRAS22568, we searched for available photometric broadband r-filter observations in the literature and public surveys. We found six photometric values for the r magnitude from 1953 to 2020, which are reported in Table 5.3. However, the characteristics of the filters are not the same in the six epochs. The Panoramic Survey Telescope and Rapid Response System (PanSTARRS) filter is similar to that of GL+91, and we therefore transformed the magnitudes of the Sloan Digital Sky Survey (SDSS) to the PanSTARRS system magnitude (see Chambers et al. 2016). The filter of the Zwicky Transient Facility (ZTF) is broader and its transmission is higher than the other filters, thus the magnitude from 2019.5 should be seen as a lower limit to the r magnitude measured in PanSTARRS. Finally, the Palomar Observatory Sky Survey first (POSS-I) and second (POSS-II) filters are narrower than the other filters, and their r magnitudes should be considered as upper limits to the r magnitude obtained in PanSTARRS.

Figure 5.3 shows the r light curve of IRAS22568. Despite the limited temporal sampling and the lower and upper limits at some epochs, some trends emerge. The r magnitude seems to have decreased $\geq$0.54 mag between 1953 and 1990.5, suddenly rose $\geq$1.5 mag between 1990.5 and 1991.7, and it steadily decreased by $\geq$1 mag between 1991.7 and 2019.5. Our 2021 and 2023 spectra are consistent with this decrease (Table 5.1). Moreover, the flux density of the radio continuum emission also faded between 2005 and 2012 (Cerrigone et al. 2017).

5.3.3 Internal kinematics

Fig. 5.4 displays position-velocity (PV) maps of the Hα, [N II], [S II], and [O III] emission lines derived from the high-resolution long-slit MES spectra obtained in 2023.68, which are close in time to the intermediate-resolution spectra from 2023.88. The MES spectra spatially resolve the north-west (NW) and south-east (SE) lobes of IRAS22568. The emission lines

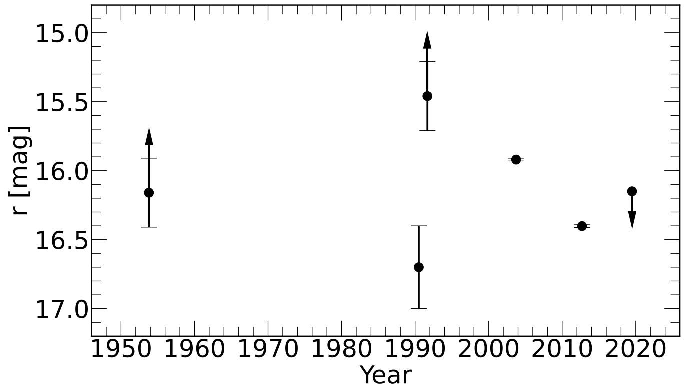

FIGURE 5.3: Light curve of IRAS22568 in the r filter. The arrows represent lower or upper limits. See the text for details.

TABLE 5.4: Properties of the Hα, [N II], [S II], and [O III] emission lines in the high-resolution spectra.

	NW lobe[a]			SE lobe[a]					
Emission line	V_{peak}[b] km s^{-1}	V_{min}[c] km s^{-1}	V_{max}[c] km s^{-1}	V_{peak}[b] km s^{-1}	V_{min}[c] km s^{-1}	V_{max}[c] km s^{-1}	δR[d] arcsec	V_{sys}[e] km s^{-1}	I_{NW}/I_{SE}[f]
Hα	-74 ± 1	-161 ± 2	36 ± 2	-112 ± 1	-216 ± 2	-43 ± 2	3.67 ± 0.04	-93 ± 1	~ 0.44
[N II]	-75 ± 1	-165 ± 2	27 ± 2	-112 ± 1	-212 ± 2	-49 ± 2	3.98 ± 0.04	-94 ± 1	~ 0.49
[S II]	-73 ± 2	-157 ± 2	13 ± 4	-107 ± 2	-222 ± 6	-46 ± 2	3.71 ± 0.11	-90 ± 1	~ 0.82
[O III]	-74 ± 2	-120 ± 2	28 ± 3	-113 ± 2	-200 ± 13	-54 ± 11	3.79 ± 0.12	-93 ± 1	~ 1.19

[a] NW lobe and SE lobe, as indicated in Fig. 5.4. Velocities are reported with respect to the LSR.
[b] Velocity at the emission peak.
[c] Minimum (V_{min}) and maximum (V_{max}) radial velocity at 10% $\pm 1\sigma$ of the peak.
[d] Relative distance between the emission peaks of the two bow shocks.
[e] Systemic velocity, mean of the two peak velocities.
[f] Relative intensity between NW and SE lobes.

arise in two relatively compact regions and are characterised by a large velocity width that reaches up to 450 and 380 km s^{-1} in Hα and [N II], respectively, as measured at the 3σ level above the background (white contours in Fig. 5.4). The [S II] and [O III] emissions are much fainter than those of Hα and [N II], although they seem to present a similar profile. Figure 5.5 presents the emission line profiles as obtained by integrating the emission of each lobe in a region of ≃2" centred on the emission peaks. Despite the differences in S/N, the [S II] and [O III] emission lines also exhibit large velocity widths that seem to be comparable to those observed in Hα and [N II].

In Table 5.4 we list the spectral, spatial, and emission properties of the NW and SE lobes derived from the PV maps (Fig. 5.4). We measured the radial velocity of the emission peaks (V_{peak}), the observed minimum (V_{min}) and maximum (V_{max}) radial velocities in the integrated spectra (see above) at the 10% level of the intensity peak (FW0.1; which avoided the insertion of noise in the [S II] and [O III] emission lines and allowed us to obtain a coherent value from the four emission lines), the angular separation between the emission peaks of the two lobes as obtained from Gaussian line fits to the spatial intensity distribution at the

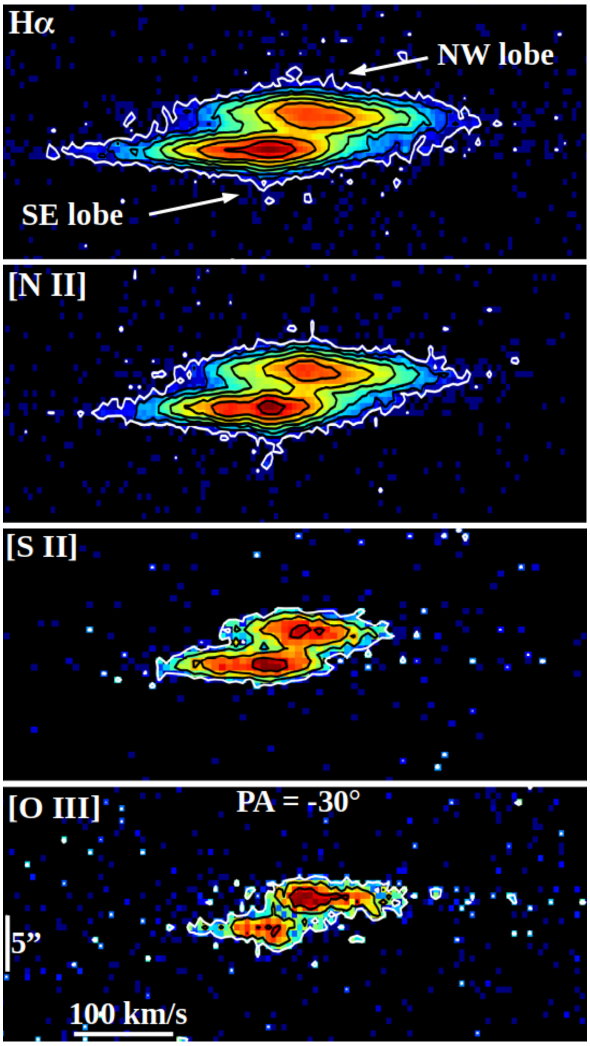

FIGURE 5.4: Position-velocity maps of the Hα, [N II], [S II], and [O III] emission lines obtained at a position angle P.A. -30 in 2023.68. The increment step of the contours is $3\sigma \times 2^n$, starting from $n = 0$ (white). The SE lobe and NW lobe are indicated.

position of the intensity peaks, and the relative intensity of the emission peaks. Throughout this chapter, radial velocities are quoted with respect to the local standard of rest (LSR).

The emission peaks are separated by $\simeq$37 km s^{-1}, and the NW lobe is redshifted with respect to the SE lobe (Table 5.4). The centroid radial velocity of the two emission peaks is very similar in the four emission lines, and the peak values are included in Table 5.4; their mean value is -93 ± 1 km s^{-1}, which we considered the systemic velocity of the optical nebula. It is similar to but somewhat higher than the value of -85 ± 2 km s^{-1} obtained by Sánchez Contreras & Sahai (2012) from the CO emission and also higher than the value of -80 km s^{-1} obtained by GL+91, perhaps because of the different spectral resolution. Secondary peaks are observed in the emission features, but they are more clearly detected in the SW than in the NW lobe.

The FW0.1 in Hα and [N II] is about 200 km s^{-1} in the NW lobe and about 170 km s^{-1} in the SE lobe. In [S II] and [O III], the values of FW0.1 are similar in both lobes and are $\simeq$173

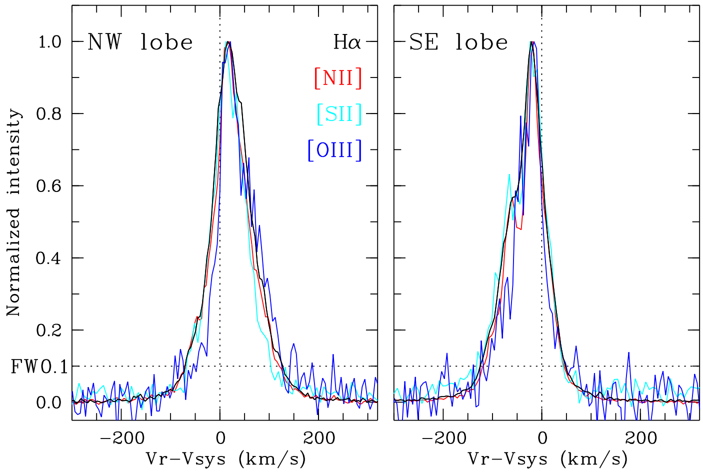

FIGURE 5.5: ,
[S II], and [O III] emission lines of the NW and SE lobes.]Normalised line profiles of the Hα, [N II], [S II], and [O III] emission lines of the NW and SE lobes. The full width at 10% of the peak intensity (FW0.1) is shown as a horizontal dotted line.

and $\simeq$147 km s^{-1}, respectively. It should be noted that the observed differences in FW0.1 are probably due to the different S/N ratio in the four emission lines.

The angular separation between the intensity peaks (Table 5.4) is different in each emission line. However, given the errors in the [S II] and [O III] emission lines and that the line profiles of Hα and [N II] are very well defined, the only conclusion is that the angular separation between Hα and [N II] is different, while the separation in [S II] and [O III] seems to be similar to that of Hα. Finally, the SE lobe is stronger than the NW lobe in Hα and [N II], the opposite is observed in [O III], and both lobes present a similar intensity in [S II] (Table 5.4).

5.4 Discussion

5.4.1 Shock-excited emission from IRAS22568

As described above, the electron temperatures obtained in 2021 are incompatible with photoionisation and suggest shock excitation. In order to understand the origin of the line emission, we made use of the Mexican Million Models Database (3MdB; Morisset et al. 2015), which allowed us to analyse whether the line intensities are consistent with shocks or photoionisation. In Appendix 6.D we explain the setup for the shock and photoionisation models employed below.

In Fig. 5.6 we show the location of shock and photoionisation models in a T_e– T_e diagram (namely, an [O III]4363/5007 vs. [N II]5755/6584 diagram) and the location of IRAS22568 in 2021 (red star). We did not search for the exact models that reproduce the observed line ratio, but used the maximum number of models to define the whole region in which they are located in the T_e (O III)–T_e(N II) diagram relative to the type of ionisation. While the

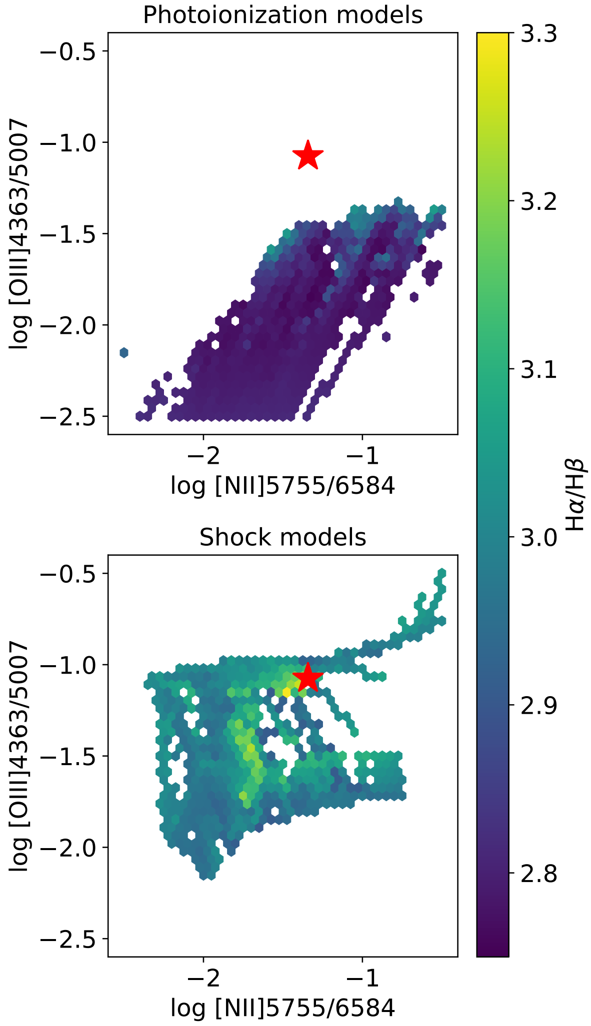

FIGURE 5.6: 4
363/5007 vs. [N II]5755/6584 diagram.]Location of models from the 3MdB database (see text for details) in an [O III]4363/5007 vs. [N II]5755/6584 diagram. The top panel shows models of the PNe, and the bottom panel shows shock and shock+precursor models. The colour code for the models corresponds to the Hα/Hβ line intensity ratio. The red star shows the location of the 2021 observations of IRAS22568.

[N II]5755/6584 line intensity ratio can easily be reproduced by photoionisation and shock models, the high value of the [O III]4363/5007 line intensity ratio can only be reproduced by shock models. The highest ratio obtained by photoionisation models is still 0.25 dex below the observed value.

If shocks were present in 2021, T_e could not be determined in the classical manner, and the values listed in Table 5.1 should be considered with caution. The determination of T_e requires detailed models involving shocks (see e.g., Montoro-Molina et al. 2022), and we defer this to a future paper. We also note that if shock excitation exists, the Hα/Hβ theoretical ratio for determining c(Hβ) could be higher than the assumed value of 2.85. Thus, we calculated

$c(\mathrm{H}\beta)$ and intrinsic emission line intensities for an Hα/Hβ ratio of 3.1, but we obtained values that are very similar to and within the errors of those in Table 5.1.

The shocks observed in 2021 are most probably the mechanism that causes the large velocity widths observed in the PV maps from 2023 (Fig. 5.4). Emission lines with large velocity widths are well known in Herbig-Haro objects that are associated with young stars (e.g. Strom et al. 1974; Dopita 1978; Raga & Bohm 1986; Hartigan et al. 1987). It is well established today that these types of emission features trace bow shocks that are associated with high-velocity jets or bullets and their interaction with the surrounding medium.

Based on the radiative bow-shock models by Hartigan et al. (1987), the shock velocity and viewing angle of the NW and SE lobes (Fig. 5.4) can be determined in a very simple way. We concentrated on the Hα and [N II] data, which have a better quality, and we note that the [S II], and [O III] data provide compatible results. The shock velocity is the difference between the observed V_{min} and V_{max} in Table 3. In the NW lobe, the bow-shock velocity and viewing angle with respect to the observer are $\simeq$195 km s^{-1} and $\simeq$106$\pm$2° with respect to the line of sight, respectively; in the SE lobe, the corresponding values are $\simeq$170 km s^{-1} and $\simeq$64$\pm$3°. Using the radial velocity of the intensity peaks (with respect to the systemic velocity) as representative of the velocity of the bow shocks, we obtained velocities of $\simeq$70 and $\simeq$45 km s^{-1} in the NW and SE lobe, respectively.

We tried to identify the nebular features in the HST image (Fig. 5.1) that might be associated with the bow shocks, but IRAS22568 shows many knots and curved filaments, and, given the small angular size of the lobes, which is comparable to the spatial resolution of the MES spectra, it is difficult to clearly determine an association. On the other hand, we cannot rule out that the spectral features are an overlapping of several bow shocks that are associated with different knots and filaments in the bipolar lobes. If this were so, the viewing angle and expansion velocities obtained above might represent averaged values for each lobe, weighted by the contribution of each individual bow shock. This may explain the differences in expansion velocity and tilt angle of each lobe, without implying that the lobes have a different orientation.

The comparison of the Hα and [N II] PV maps shown in Fig. 5.4 with those by GL+91 (their Fig. 4) is revealing. Despite the differences in spatial and velocity resolution between the two sets of PV maps, those by GL+91 show the emission peaks of each lobe, a secondary peak in the SE lobe, and a velocity width of $\simeq$350–380 km s^{-1} at the spatial position of the intensity peaks, as measured at the weakest contour level. These results agree very well with ours, suggesting that bow-shock excitation might have been present in 1988. Moreover, our high-resolution spectra include a recombination (Hα), a high-excitation ([O III]), and two low-excitation ([N II] and [S II]) emission lines, and in all four cases, the emission features are compatible with bow-shock excitation. Therefore, it is possible that the optical spectrum of IRAS22568 in the three epochs is dominated by shocks. This casts doubt on the classification of IRAS22568 as a low-ionisation PN. Nevertheless, it might be premature to conclude that IRAS22568 is a post-AGB nebula because photoionised gas could be masked by shocks,

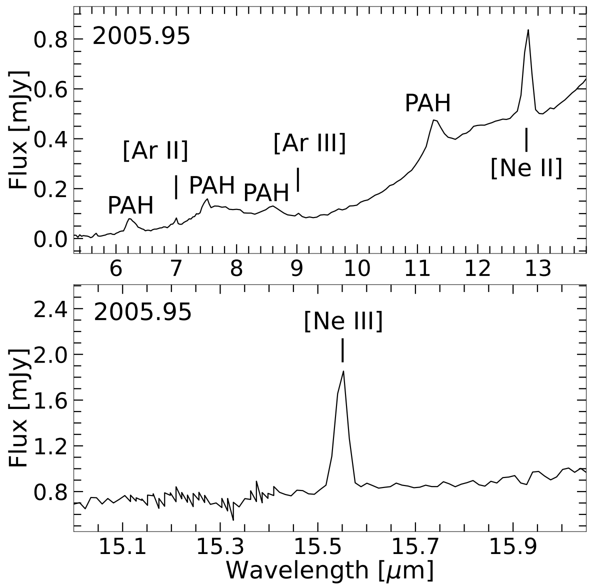

FIGURE 5.7: *Spitzer* spectra of IRAS22568 obtained on 2005.95. The forbidden emission lines of ionised gas ([Ar II]λ7.0μm, [Ar III]λ9.0μm, [Ne II]λ12.8μm, and [Ne III]λ15.55μm) and broad emission of PAHs (6.4, 7.7, 8.6 and 11.3 μm) are indicated.

which are the dominant excitation mechanism. Furthermore, as an additional result, the existence of shocks might be intimately related with the non-thermal radio continuum emission from IRAS22568. Finally, it is worth to emphasize that in addition to the T_e-sensitive line ratios in 2021 (Fig. 5.6), high-resolution spatially resolved spectroscopy has been crucial to determining the excitation mechanism in 2023: without this type of data, post-AGB nebula with shock-excited emission lines could be confused with low-ionisation young PNe when observed at low or intermediate spectral resolution.

IRAS22568 belongs to a small group of post-AGB nebulae and PNe that present emission features with large velocity widths (typically $\geq$150 km s^{-1}) that are characteristic of bow-shock excitation. By means of high-resolution optical spectroscopy, large velocity widths have been detected in the PNe Hen 2-111 (Meaburn & Walsh 1989), M 1-16 (Schwarz 1992; Gómez et al. 2023), KjPn 8 (Lopez et al. 1995), M 2-48 (Vázquez et al. 2000; López-Martín et al. 2002), and IRAS 18061$-$2505 (Miranda et al. 2021). Other PNe present bow-shaped structures that were successfully reproduced using bow-shock models, although in these cases, the structures did not exhibit such large velocity widths (typically 40–90 km s^{-1}), and they were irradiated by the central star; examples include K 4-47, IC 4634, and Hu 1-2 (Gonçalves et al. 2004; Guerrero et al. 2008; Miranda et al. 2012; Fang et al. 2015, see also Mari et al. 2023 for more similar PNe). Similar emission features were observed in the post-AGB nebulae M 1-92 (Solf 1994), OH 231.8+04.2 (Sánchez Contreras et al. 2000), Hen 3-1475 (Riera et al. 2003), M 2-56 (Sánchez Contreras et al. 2010). The reason for the scarcity of large velocity widths associated with jets in PNe in unclear, although it could be related to photoionisation being the dominant excitation mechanism, which (partially) hides the shock-excited emission, and/or to a weakness of the shock contribution with time.

5.4.2 Origin of the variability

The r light curve (Fig. 5.3) shows that IRAS22568 underwent an energetic event in around 1990, which increased its brightness. The consequences of this event are perceptible until today. The radio continuum emission from the nebula has been fading since at least 2005 (Cerrigone et al. 2017), and according to our spectra, IRAS22568 recombined and cooled between 2021 and 2023. Moreover, we consulted the *Spitzer* Heritage Archive and found spectra of IRAS22568 from 2005.95, which are shown in Fig. 6.6. These spectra display, among others, the [Ne III]15.6μm emission line, which indicates that the nebular excitation was higher in 2006 than in later epochs (2021 and 2023), when the [O III] emission lines were relatively weak. Consequently, it is quite possible that the [O III] lines were stronger in 2006 than in 2021, and that IRAS22568 recombined and cooled since 2006 and even earlier. Finally, the spectral and kinematical properties provide clear evidence that the nebular emission was dominated by shocks in 2021 and 2023 and, perhaps, in 1988.

The variability of IRAS22568 could be due to changes of the physical conditions in the shocks. New ejections could have reached and interacted with the lobes by 1990. Similarly, already ejected material could encounter high-density regions in the lobes and be decelerated by that date. In both cases, a rapid increase in T_e and N_e is expected, resulting in an increase in the emission line fluxes and excitation. After the interaction weakens or ceases, recombination and cooling in the post-shock region would lead to a decrease in the excitation and brightness of the nebula, as observed since 2005-2006. Numerical simulations are necessary to confirm whether this scenario can account for the detailed observed variability and the involved timescales and if the physical conditions required for it to occur are reasonable for PNe. We note that if the variability is only due to changes in the shocks, IRAS22568 would be a post-AGB nebula or proto-PN similar to M 1-92, for example, rather than a PN.

Alternatively, a nova-like eruption might have caused the sudden increase in the brightness of IRAS22568. This type of event is typical of binary systems hosting an AGB star and an accreting white dwarf. These symbiotic binaries are in a different evolutionary phase than post-AGB stars and PNe. To determine whether IRAS22568 might be related to this type of binaries, we built its spectral energy distribution (SED; see Appendix 6.5.1), which is shown in Fig. 6.3. The SED presents an emission peak at $\lambda \simeq 30\,\mu$m, which is typical of optically obscured post-AGB stars and young PNe (e.g. Ramos-Larios et al. 2009, 2012), but different from that of symbiotic binaries, where the peak of the SED usually lies at $\lambda \simeq 1\,\mu$m (e.g. Rodríguez-Flores et al. 2014). Although more observations are necessary, the SED of IRAS22568 does not seem to favour a nova scenario as the cause of its variability.

Finally, a third possibility is that a late thermal pulse (LTP) occurred around 1990, as is suggested by the remarkable similarities between the properties and temporal evolution of IRAS22568 and those of the Stingray nebula (Hen 3-1357), whose central star, SAO 244567, was proposed to undergo an LTP (Reindl et al. 2014, 2017). The light curves of IRAS22568 (Fig. 5.3) and Hen 3-1357 (Schaefer & Edwards 2015) are similar. In both objects, the spectral variability of the optical emission lines is consistent with cooling and recombination during decades (see Sec. 5.3.1 and Arkhipova et al. 2013; Peña et al. 2022; Balick et al. 2021). Their radio continuum emission was characterised by a fading of the flux density in the past decades and by negative spectral indices indicating non-thermal emission (Cerrigone et al. 2017; Harvey-Smith et al. 2018). As described above, non-thermal emission and shocks appear to be related to each other in IRAS22568 (Sec. 5.4.1). The same may hold for Hen 3-1357, where shocks were suggested to occur along the nebular perimeter (Balick et al. 2021). Similarly, a relation between shocks and non-thermal radio continuum emission was observed after the (very late) thermal pulse occurred in Sakurai's object (Hajduk et al. 2024). Moreover, if an LTP in IRAS22568 generated a shock wave that propagated into the previous material, all the knots and filaments would be shocked, increasing the nebular brightness, excitation, and the subsequent recombination and cooling. Nevertheless, in the LTP scenario, the situation may be more complicated. The increase in the effective temperature of the central star after the LTP (Lawlor 2023, and references therein) would provide an additional source of ionising photons, and the emission line spectra of IRAS22568 would be produced in a combination of shocks and photoionisation, each presenting its own timescale of variability, depending on the evolution of the central star and nebula. It is interesting to note that the *Spitzer* spectra (Fig. 6.6) display broad emission features that were attributed to dust made of polycyclic aromatic hydrocarbons (PAHs), which might be fresh byproducts of the LTP and indicate carbon-rich material in the nebula. Finally, if the LTP scenario is correct, IRAS22568 would indeed be a nascent PN.

In contrast with SAO 244567, which is visible and whose properties and evolution have been studied for decades (Henize 1967; Parthasarathy et al. 1993, 1995; Reindl et al. 2014, 2017), the central star of IRAS22568 has never been observed, and its current evolutionary stage is unknown. In particular, within the LTP scenario, we cannot assert whether the central star of IRAS22568 increases its effective temperature or returns to the AGB (see Hajduk et al. 2020). Millimeter observations might elucidate whether the molecular abundances of IRAS22568 are similar to those in other sources in which an LTP seems to have occurred (e.g., Schmidt et al. 2018). In addition, a photometric and spectroscopic monitoring in the coming years and modelling of the data are key to trace the evolution of IRAS22568 and confirm the origin of the variability.

5.5 Conclusions

IRAS22568 has been classified as a low-ionisation PN and shows non-thermal radio continuum emission, suggesting that it is a nascent PN. We performed intermediate-resolution optical spectroscopy in 2021 and 2023 for this source and high-resolution spectroscopy in 2023, and we gathered a discrete r-filter light curve from 1953 to 2020.

It is clear that an energetic event occurred in IRAS22568 around 1990 that manifested itself as a sudden and rapid increase in the nebular brightness. Afterwards, the brightness decreased much more slowly. Compared with a published spectrum from 1988, our spectrum of 2021 shows a noticeable increase in the emission line fluxes and the [O III] emission lines, which were not detected in 1988. Two years later, in 2023, the emission line fluxes decreased and the [O III] emission lines almost vanished. The observed spectral variability between 2021 and 2023 shows that IRAS22568 is recombining and cooling, and this phenomenon has probably occurred since at least 2005, as indicated by the reported fading of the radio continuum emission and archival mid-IR spectra around that epoch.

Some emission line ratios in 2021 reveal that the spectrum is excited by shocks. Moreover, the large velocity widths ($\sim$400 km s^{-1}) observed in the high-resolution 2023 spectra are compatible with bow-shock excitation, which may also have been present in 1988. Our data suggest a connection between shock excitation and non-thermal radio continuum emission. Nevertheless, we cannot exclude that photoionisation has contributed to the spectra at least since 2006.

Changes in the physical conditions in the shocks might explain the observed variability, but modelling is necessary to confirm this scenario. A nova-like eruption is another possibility, although this is not favoured by the SED of IRAS22568. Finally, a late thermal pulse in the central star of IRAS22568 provides a simple and consistent explanation for the energetic event in 1990 and for the subsequent photometric and spectral evolution of the object. We found noticeable similarities between the variability of IRAS22568 and that of the Stingray nebula, for which the variability was interpreted as caused by a late thermal pulse.

Acknowledgments

We are very grateful to our anonymous referee for his/her constructive comments that have improved the chapter. We thank Calar Alto Observatory for allocation of director's discretionary time to this programme. This research is based on observations collected at the Centro Astronómico Hispano en Andalucía (CAHA) at Calar Alto, operated jointly by Junta de Andalucía and Consejo Superior de Investigaciones Científicas (IAA-CSIC); upon observations at the Observatorio Astronómico Nacional on the Sierra San Pedro Mártir (OAN-SPM), Baja Califormia, México; on data from the program 9463 of the NASA/ESA *Hubble* Space Telescope obtained from the Space Telescope Science Institute, which is operated by the Association of Universities for Research in Astronomy, Inc., under NASA contract NAS 5-26555; on data from the VLA and the National Radio Astronomy Observatory is a facility of the National Science Foundation operated under cooperative agreement by Associated Universities, Inc. IRAF used here is distributed by the National Optical Astronomy Observatories, which is operated by the Association of Universities for Research in Astronomy, Inc., under contract to the National Science Foundation. The POSS-II were produced at the Space Telescope Science Institute under U.S. Government grant NAG W-2166. The images of these surveys are based on photographic data obtained using the Oschin Schmidt Telescope on Palomar Mountain and the UK Schmidt Telescope. The plates were processed into the present compressed digital form with the permission of these institutions.The Guide Star Catalogue-II is a joint project of the Space Telescope Science Institute and the Osservatorio Astronomico di Torino. Space Telescope Science Institute is operated by the Association of Universities for Research in Astronomy, for the National Aeronautics and Space Administration under contract NAS5-26555. The participation of the Osservatorio Astronomico di Torino is supported by the Italian Council for Research in Astronomy. Additional support is provided by European Southern Observatory, Space Telescope European Coordinating Facility, the International GEMINI project and the European Space Agency Astrophysics Division. The PS1 and the PS1 public science archive have been made possible through contributions by the Institute for Astronomy, the University of Hawaii, the Pan-STARRS Project Office, the Max-Planck Society and its participating institutes, the Max Planck Institute for Astronomy, Heidelberg and the Max Planck Institute for Extraterrestrial Physics, Garching, The Johns Hopkins University, Durham University, the University of Edinburgh, the Queen's University Belfast, the Harvard-Smithsonian Center for Astrophysics, the Las Cumbres Observatory Global Telescope Network Incorporated, the National Central University of Taiwan, the Space Telescope Science Institute, the National Aeronautics and Space Administration under Grant No. NNX08AR22G issued through the Planetary Science Division of the NASA Science Mission Directorate, the National Science Foundation Grant No. AST-1238877, the University of Maryland, Eotvos Lorand University (ELTE), the Los Alamos National Laboratory, and the Gordon and Betty Moore Foundation. Based on observations obtained with the Samuel Oschin 48-inch Telescope at the Palomar Observatory as part of the ZTF project. ZTF is supported by the National Science Foundation under Grant No. AST-1440341 and a collaboration including Caltech, IPAC, the Weizmann Institute for Science, the Oskar Klein Center at Stockholm University, the University of Maryland, the University of Washington, Deutsches Elektronen-Synchrotron and Humboldt University, Los Alamos National Laboratories, the TANGO Consortium of Taiwan, the University of Wisconsin at Milwaukee, and Lawrence Berkeley National Laboratories. Operations are conducted by COO, IPAC, and UW. This work is based [in part] on archival data (ID: 20590, PI: R. Sahai) obtained with the Spitzer Space Telescope, which was operated by the Jet Propulsion Laboratory, California Institute of Technology under a contract with NASA. Support for this work was provided by NASA. This work has made use of the SIMBAD database, operated at the CDS, Strasbourg, France, and the NASA/IPAC Infrared Science Archive, which is operated by the Jet Propulsion Laboratory, California Institute of Technology, under contract with the National Aeronautics and Space Administration. It also makes use of data products from 2MASS (a joint project of the University of Massachusetts and the Infrared Processing and Analysis Center/California Institute of Technology, funded by NASA and the NSF), AKARI (a JAXA project with the participation of ESA), HERSCHEL (Herschel is an ESA space observatory with science instruments provided by European-led Principal Investigator consortia and with important participation from NASA), IRAS (was a joint project of the US, UK and the Netherlands), MSX (funded by the Ballistic Missile Defense Organization with additional support from NASA Office of Space Science), and

WISE (a joint project of the University of California, Los Angeles, and the Jet Propulsion Laboratory/California Institute of Technology, funded by the NASA). RAC, LFM, JFG are supported by grants PID2020-114461GB-I00, PID2023-146295NB-I00, and CEX2021-001131-S, funded by MCIN/AEI /10.13039/501100011033, and by grant P20-00880, funded by the Economic Transformation, Industry, Knowledge and Universities Council of the Regional Government of Andalusia and the European Regional Development Fund from the European Union. RC also acknowledges support by the predoctoral grant PRE2018-085518, funded by MCIN/AEI/ 10.13039/501100011033 and by ESF Investing in your Future. CM acknowledges the support of UNAM/DGAPA/PAPIIT grants IN101220 and IG101223.

Table 5.5: Atomic datasets used for collisionally excited lines in the PyNeb calculations.

Ion	Transition Probabilities[a]	Collision Strengths[b]
N^{+}	1	1
O^{2+}	1, 2	2, 3
S^{+}	3	4

[a] 1. Froese Fischer & Tachiev (2004); 2. Storey & Zeippen (2000); 3. Rynkun et al. (2019).
[b] 1. Tayal (2011); 2. Froese Fischer & Tachiev (2004); 3. Storey et al. (2014); 4. Tayal & Zatsarinny (2010).

5.A Atomic datasets used in PyNeb

Table 5.5 shows the atomic datasets used for collisionally excited lines in the PyNeb calculations presented in this chapter.

5.B Emission line fluxes of IRAS22568 in the three epochs

In Table 5.6 we report the emission line fluxes in 1988, 2021, and 2023. The emission line fluxes in 1988 are taken from GL+91 (their Table 2, column 4).

5.C Parameters of the shock and photoionisation models in the 3MdB

5.C.1 Shock models

The shock models are taken from the work of Alarie & Morisset (2019) who computed models using Mappings V (Sutherland & Dopita 2017) and store them in the 3MdB (Alarie & Morisset 2019). These models use the same grid definition as Allen et al. (2008). We consider here the 15968 models that correspond to the "shock" and the "shock+precursor" results from the "Allen08" shock family, the precursor being the region photoionised by the photons emitted by the shock itself, for velocities higher than 100 $\mathrm{km\,s^{-1}}$ (at lower velocities no ionising photons are produced by the shock). This preionisation is treated by Mappings in a fully consistent way and is described in detail by Sutherland & Dopita (2017). The free parameters of the grid are the metallicities, the pre-shock density, the shock velocity and the magnetic field. The details of the parameter distribution are given in Alarie & Morisset (2019).

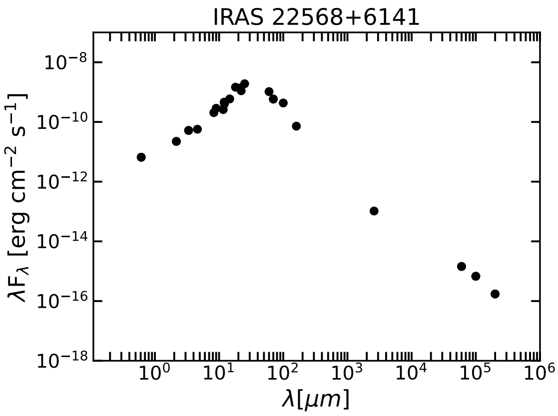

FIGURE 5.8: SED of IRAS22568. The size of the circles is larger than the errors.

5.C.2 Photoionisation models

The PN photoionisation models have been computed by Delgado-Inglada et al. (2014) using the multi-purpose transfer code CLOUDY v17 (Ferland et al. 2017). These models are taken from the 3MdB database, using the reference `ref LIKE "PNe_202_"`. We filter the models using the `com6=1 AND MassFrac > 0.7` commands. The first one is to only consider the realistic PNe models as defined in Sec. 2.1 of Delgado-Inglada et al. (2014) and in the grid model webpage[1]. The second filter is used to only select the radiation-bonded models, as well as the matter-bounded models in which the mass of the nebula is greater than 70% of the corresponding radiation-bounded case. The input parameters of the grid are: the nebular density and metallicity, the luminosity and effective temperature of the ionising spectral energy distribution (which can be a Planck function or a stellar atmosphere model), the presence or absence of dust, the distance between the central ionising source and the inner radius of the nebula. This leads to 68041 models.

5.D Spectral energy distribution of IRAS22568

We have gathered available archival optical, infrared, millimeter, and centimeter data ($\sim$0.5 - 2×10^5 μm), and have built the SED of IRAS22568 (Fig. 6.3). Infrared data were obtained from the Two Micron All Sky Survey (2MASS), AKARI, *Herschel* Space Observatory, Infrared Astronomical Satellite (IRAS), Midcourse Space Experiment (MSX), and Wide-field Infrared Survey Explorer (all-WISE survey). The flux density at 0.1 and 2.6 mm were taken from Marton et al. (2024) and Sánchez Contreras & Sahai (2012), respectively. The flux density of the optical r-magnitude corresponds to the average value of those presented in the Table 5.3. Similarly, the radio flux density values are the average values reported by Cerrigone et al. (2017) at 4.8 and 8.6 GHz, while the value at 1.4 GHz was reported by Condon et al. (1998).

[1]https://sites.google.com/site/mexicanmillionmodels

TABLE 5.6: Absolute emission line fluxes F(λ) in units of 10^{-15} erg cm^{-2} s^{-1} for IRAS22568 in the three epochs.

Emission line	1988.58 F(λ)[a]	2021.58 F(λ)[a]	2023.88 F(λ)[a]
4101 Hδ	–	2.80±0.14	–
4340 Hγ	–	3.93±0.24	–
4363 [O III]	–	0.61±0.13	<34.4
4471 He I	–	0.52±0.04	–
4861 Hβ	1.16±0.11	6.88±0.11	4.11±0.11
4959 [O III]	–	2.80±0.08	0.62±0.06
5007 [O III]	–	8.19±0.09	1.67±0.08
5755 [N II]	0.48±0.04	0.757±0.019	0.314±0.012
5876 He I	0.86±0.07	0.952±0.017	0.529±0.016
6300 [O I]	3.41±0.17	1.531±0.013	2.760±0.028
6363 [O I]	1.43±0.07	0.557±0.012	1.105±0.026
6548 [N II]	13.22±0.23	4.82±0.16	3.30±0.07
6563 Hα	51.9±0.9	19.61±0.17	11.71±0.07
6584 [N II]	40.3±0.9	15.14±0.16	9.66±0.07
6678 He I	0.58±0.07	0.254±0.007	0.176±0.010
6716 [S II]	1.91±0.16	0.482±0.008	0.537±0.011
6731 [S II]	3.84±0.27	0.925±0.009	1.069±0.011
7002 O II	–	0.034±0.0011	–
7065 He I	1.28±0.11	0.319±0.005	0.193±0.008
7137 [Ar III]	1.97±0.25	0.438±0.005	0.131±0.007
7150 [Fe II]	–	0.103±0.005	0.173±0.007
7230 [Fe II]	–	0.041±0.003	0.145±0.010
7254 O I	–	0.037±0.003	0.133±0.010
7281 He I	–	0.052±0.006	0.242±0.008
7319 [O II]	blended[b]	1.375±0.010	0.623±0.009
7330 [O II]	blended[b]	1.057±0.010	0.573±0.009
7378 [Ni II]	0.70±0.14	0.090±0.009	0.125±0.006
7447 [Fe II]	–	0.0383±0.0021	0.074±0.007
7751 [Ar III]	–	0.126±0.005	0.0280±0.0020
8446 O I	blended[c]	0.229±0.004	0.066±0.004
8467 P17	blended[c]	0.056±0.003	0.0294±0.0021
8502 P16	–	0.058±0.004	0.063±0.004
8545 P15	–	0.075±0.004	0.081±0.005
8578 [Cl II]	–	0.053±0.004	0.093±0.005
8598 P14	–	0.054±0.004	0.072±0.006
8605 [Fe II]	–	0.090±0.004	0.180±0.005
8665 P13	–	0.087±0.004	0.093±0.005
8750 P12	–	0.066±0.003	0.094±0.005
8863 P11	–	0.105±0.003	0.111±0.004
8890 [Fe II]	–	0.063±0.003	0.094±0.004
9015 P10	3.0±0.4	0.126±0.005	0.067±0.003
9069 [S III]	19.1±1.6	0.992±0.005	0.212±0.004
9229 P9	7.4±0.8	0.237±0.005	0.210±0.006
9535 [S III]	51.04±3.26[d]	2.217±0.013	0.487±0.012

[a] '–' stands for not detected.
[b] [O II] λ7319,7330 are blended with F(sum)=12.6±0.8.
[c] O I λ8446 and P 17 λ8467 are blended with F(sum)=5.8±0.5.
[d] Blended with P 8 λ9546.

Chapter 6

Identification and characterization of nascent planetary nebulae with OH and H_2O masers

6.1 Introduction

The morphology of low- and intermediate-mass stars with initial masses (M_i) up to $8\,\mathrm{M}_\odot$ changes at the end of their life, when the spherical envelopes created during the asymptotic giant branch (AGB) phase somehow transform into the elliptical, bipolar, multipolar, and, in general, non-spherical forms of planetary nebulae (PNe; Manchado et al. 1996a), which are nebulae photoionized by a hot central star that evolves towards a cooling white dwarf. Consequently, these hot central stars are expected to contain essential information for understanding the complete evolution of PNe. For example, the formation of circumstellar envelopes that are rich in oxygen (O) around central stars rich in carbon (C) (Zijlstra et al. 1991; Miranda et al. 2021) would be better understood by studying sources at the onset of this evolutionary phase.

Maser emission has been considered as a tracer of nascent PNe (Zijlstra et al. 1989). In fact, masers of circumstellar nature are widespread in the AGB phase, but they seem to be extremely rare among PNe. During the AGB phase, the circumstellar envelope grows as the star loses mass at a rate of up to $\simeq 10^{-5}\ \mathrm{M}_\odot\,\mathrm{yr}^{-1}$, depending on the initial mass of the star (Decin et al. 2019). If the envelope is O-rich, special physical conditions can pump maser emission from molecules of SiO, H_2O, and OH (e.g. Reid & Moran 1981b), but if it is C-rich, HCN and SiS masers are observed (e.g. Menten et al. 2018). Spatially resolved observations show that O-bearing masers in spherically symmetric AGB envelopes are stratified, with SiO,

This chapter is derived from the following publication:

- Cala et al. (2025a)

H_2O, and OH masers typically located at approximately 10, 100 and 1000 au, respectively (e.g. Reid & Moran 1981b; Elitzur 1992; Diamond et al. 1994).

The intense mass-loss during the AGB removes a significant part of the mass of the star until the beginning of the post-AGB phase. During this post-AGB phase, the mass-loss rate drops to 10^{-8} $M_{\odot}$ yr^{-1} (Bloecker 1995), the envelope gets detached from the star (Vassiliadis & Wood 1994; Miller Bertolami 2016) and then cools and expands. Favorable conditions for maser emission start to disappear, persisting up to 10, 10^2, and 10^3 yr after the beginning of the post-AGB phase for SiO, H_2O, and OH molecules, respectively (Lewis 1989; Gómez et al. 1990). The central star shrinks and increases its effective temperature ($T_{\rm eff}$), until it reaches approximately $\simeq$ 25000-30000 K, at which point it can photoionize the previously detached envelope and form a PN, 10^2-10^4 yr after the beginning of the post-AGB phase, depending on the initial mass of the star (Vassiliadis & Wood 1994; Miller Bertolami 2016). These timescales make circumstellar masers valuable signposts of nascent PNe. Moreover, soon after the beginning of the PN phase, the increasing number of ionizing photons from the hot central star starts to destroy these molecules, which may prevent the detection of maser emission in evolved PNe. On the other hand, dense molecular clumps, or an unknown special shielding mechanism, have been proposed to explain the presence of molecular masers after the onset of photoionization (Tafoya et al. 2007). Furthermore, the presence of thermal emission from some of these molecules in PNe, possibly due to dense condensations of material (e.g., Cox et al. 1998; Marquez-Lugo et al. 2013; Manchado et al. 2015), also indicates that they may survive on longer timescales (Schmidt & Ziurys 2019; Gold et al. 2024; Ouyang et al. 2024).

Therefore, the identification of maser-emitting PNe is extremely important because they could be a key to characterizing the beginning of the PN phase. So far, no PN has been found to host SiO masers (Cala et al. 2024a), and only in eight cases has H_2O and/or OH maser emission been confirmed to spatially coincide with the position of sources spectroscopically classified as PNe. These PNe associated with H_2O (H_2OPNe) or OH maser emission (OHPNe) may be among the youngest objects in this evolutionary phase. Most of them are bipolar nebulae, and the spatial distribution of the masers trace equatorial rings or toroidal structures close to the central star, although with two important exceptions. In K 3-35, the H_2O masers also trace the tip of bipolar jets (Miranda et al. 2001). In IRAS 15103−5754, the H_2O maser emission shows high-velocity components tracing a jet-like structure (Gómez et al. 2015a), which indicates that it is a 'water fountain' (WF). Similarly, OH masers have been observed tracing bipolar outflows of post-AGB stars (e.g., Zijlstra et al. 2001). The presence of masers in bipolar outflows of post-AGB stars and PNe means that this type of emission can arise not only from the remnants of maser-emitting regions from the AGB phase, but also that they can trace non-spherical mass-loss episodes.

The jet traced by H_2O masers in IRAS 15103−5754 mentioned above deserves further attention, since most WFs seem to be binary or multiple systems hosting a post-AGB star (Gómez et al. 2017; Khouri et al. 2021), whereas this source is the only WF that seems to host a PN (Gómez et al. 2015a). WFs can be defined, in general terms, as evolved stars whose H_2O maser emission traces collimated ejections. They have been classically identified by their large velocity range covered by the emission (up to hundreds of km s^{-1}; e.g., Imai et al. 2002; Gómez et al. 2011; Uscanga et al. 2023; Imai et al. 2023), larger than the $\sim$ 50 km s^{-1} ranges expected by the spherical mass-loss, which builds up large-scale ($\geq 10^4$ au) slowly expanding envelopes (expansion velocities $\lesssim$25 km s^{-1}, typically traced by OH masers) during the AGB phase (te Lintel Hekkert et al. 1991). The spatial distribution and proper motions of the maser emission clearly show the presence of jets (e.g. Suárez et al. 2009; Orosz et al. 2019). In addition to these 'classical' WFs, there are other objects in which the velocity range of the H_2O maser spectra is relatively narrow $\lesssim$ 50 km s^{-1}, but some components fall outside the range covered by the OH maser emission, suggesting the presence of non-spherical mass loss (Gómez et al. 1994; Engels 2002). When observed with high angular resolution, the H_2O maser emission in these objects seem also to trace jets (e.g., Boboltz & Marvel 2005), so they can be considered as 'low-velocity' WFs. While the difference between classical and low-velocity WFs has been sometimes interpreted as a projection effect (Boboltz & Marvel 2005; Vlemmings et al. 2014), there is some evidence of evolution in the jet velocities of WFs, with slower ones being present closer to the beginning to the post-AGB phase (Yung et al. 2013). This possible evolutionary effect make WFs relevant also in the context of nascent PNe. Considering that the kinematical ages of WFs ($\sim 10^2$ yr; e.g., Day et al. 2010; Yung et al. 2011; Orosz et al. 2019) are similar to the timescales of disappearance of H_2O maser emission after the AGB phase, a potential group of PNe with WF characteristics should be extremely rare and probably at the onset of photoionization.

The central stars of H_2OPNe and OHPNe are heavily obscured at optical wavelengths, and only in two cases has a stellar classification been proposed. In IRAS 18061−2505, the central star shows broad carbon emission lines and has been classified as [WC8] (see Miranda et al. 2021, and references therein), implying that it is C-rich. Similarly, a [WC11] classification has been suggested for the central star of Vo 1 (see Zijlstra et al. 1991, and references therein). In Vy 2-2, Arkhipova et al. (2017) suggested the presence of weak stellar emission lines (*wels*) similar to those observed in other central stars (see Tylenda et al. 1993; Marcolino & de Araújo 2003; Weidmann et al. 2020), although *wels* may not be a real spectral type (see Parthasarathy et al. 1998; Weidmann et al. 2015). With these few cases, it is impossible to assert whether maser-emitting PNe are associated with a particular type of central star or whether they are a common phase of different types of central stars at the beginning of the PN phase. Therefore, it is essential to identify more H_2OPNe and OHPNe to understand the nature and evolution of these objects.

6.2 Procedure to search for new maser-emitting PNe

In order to find new maser-emitting PNe, there are two different aspects to tackle. The first is to ensure that the maser emission is actually associated with a prospective PN. This is the main focus of this chapter. The second is to determine whether the maser-emitting source is actually a PN, rather than another type of object.

Regarding the spatial location of the maser emission, many searches for maser emission toward evolved stars are carried out with single-dish telescopes, which typically have beam sizes of several arcminutes. For example, the Green Bank Telescope, one of the largest radio telescopes in the world (100 m diameter), has a half-power beam size of $\simeq 30''$ at 22 GHz (for H_2O masers) and $\simeq 8'$ at 1.6 GHz (for OH masers). When the spectrum is obtained with a single-dish antenna only at the catalog position of the source, the detected maser emission can arise from any source within that beam and, if the contaminant maser is strong enough, the emission can even spill through the antenna sidelobes (cf. the case of IRAS 19071+0857 in Gómez et al. 2015b), significantly farther away than the nominal beam width at half maximum. It is possible to improve the positional accuracy of a single-dish observation, by taking several spectra offset from the nominal position of the source and fitting the decrease of emission assuming that the beam has a Gaussian profile. The astrometric error in this case is determined by the antenna rms pointing accuracy (which is typically several arcseconds) and the Gaussian profile fitting error (1σ error $\simeq \theta/(2 \times \mathrm{snr})$, where θ is the telescope beam, and snr is the signal-to-noise ratio of the maser spectrum), which can also amount to several arcseconds, even with a good signal-to-noise ratio. The resulting theoretical astrometric accuracy of tens of arcseconds in single-dish observations may not even be enough to ascertain whether the emission arises from our target of interest, especially in crowded fields, such as the Galactic Bulge. Moreover, observing a maser source with different angular offsets is rarely done in maser surveys, since it is very time-consuming and, therefore, the positional uncertainty for detections in these surveys is of the order of arcminutes. Hence, single-dish reports of maser emission are usually not accurate enough to determine the location of the emitting source. In some particular cases, the probability that the emission seen with a single-dish telescope arises from a contaminant source within the beam may be low, specially when observing at high galactic latitudes, or if the velocity of the maser emission is close to the central velocity of the target source obtained with line observations at other frequencies. In the case of OH masers, a strong infrared source is required for their excitation. While H_2O masers do not necessarily require a strong infrared source, H_2OPNe often exhibit significant infrared excess due to their thick circumstellar envelopes. Therefore, if there is only a single strong infrared source within a single-dish beam, and the maser velocity is consistent with that of the star, there is little doubt on the identification of the maser-emitting source, especially in the case of OH emission. However, in general, radio interferometric observations with much higher positional accuracy are necessary for a definitive confirmation of the association of the maser emission with a PN (e.g. Miranda et al. 2001; Cala et al. 2024a).

In practice, our general strategy for finding new candidate maser-emitting PNe is to match the position of H_2O and OH masers and radio continuum emission, considering the latter as a tracer of the photoionized gas that characterizes PNe. Both maser and radio continuum emission can be observed with radio interferometers, which provide much improved positional accuracy over single-dish telescopes. The absolute astrometric accuracy in interferometers is determined by different factors, such as phase errors during the observations or how accurately the position of the antennas and the coordinates of the calibrators used for phase reference are known. The astrometric errors due to these factors amount to a fraction (roughly 10%) of the size of synthesized beam of the interferometers, so, in principle, it is relatively easy to achieve accuracies better than one arcsecond.

The best results can be achieved if the continuum observations are close in frequency to the maser lines, so they can be carried out simultaneously with the same telescope, sharing the same amplitude and phase calibration. In this case, the absolute astrometry is not so important for a spatial match between maser and continuum, but rather the relative positional errors between them, which is only determined by the signal-to-noise ratio of the emission (uncertainty $\simeq \theta/(2 \times \mathrm{snr})$). These relative positional errors can reach values much smaller than the absolute astrometric precision for images with a high signal-to-noise ratio, and it is possible to spatially match maser and radio continuum emission with relative accuracies of a few milliarcseconds using interferometers with synthesized beams of $\simeq 1''$.

These extremely high relative accuracies between maser and continuum emission can provide further valuable information, such as the location of masers close to the central star, or on the nebular lobes (e.g., Miranda et al. 2001). Moreover, these accuracies also apply to the individual maser components, so it is possible to determine their spatial distribution, tracing structures such as toroids or jets.

After identifying prospective PN candidates by spatially matching radio continuum and maser emission, our second task is to confirm their nature as true PNe, since maser and radio continuum emission can both be present in objects that are not PNe, such as compact and ultracompact H II regions, post-AGB stars, galaxies, young stellar objects, symbiotic stars, supernova remnants and red nova remnants (e.g. Hofner & Churchwell 1996; Deguchi et al. 2005; Cho & Kim 2010; Qiao et al. 2016a, 2018, 2020; Ortiz-León et al. 2020, and references therein). The confirmation of an object as a PN requires additional observations, such as multiwavelength imaging and spectroscopy.

For this chapter, we started by carrying out an extensive literature search, to identify new H_2O and OH maser-emitting PN candidates. To this end, we cross-matched sources in radio continuum surveys (e.g. Zoonematkermani et al. 1990; Helfand et al. 1992; Becker et al. 1994; Condon et al. 1998; White et al. 2005; Urquhart et al. 2009; Murphy et al. 2010; Purcell et al. 2013; Wang et al. 2018; Irabor et al. 2018; Medina et al. 2019; Gordon et al. 2021; Hale et al. 2021; Irabor et al. 2023; Dzib et al. 2023) with maser databases (e.g. Forster & Caswell 1989b; Benson et al. 1990; Engels & Bunzel 2015; Ladeyschikov et al. 2019). We also matched the same maser databases with objects labeled as true, possible, and likely PNe in the Hong Kong/AAO/Strasbourg Hα (HASH) PN database (Parker et al. 2016).

The initial source list compiled after this search was subsequently purged, first by getting rid of bona fide PNe and PN candidates that have already been interferometrically confirmed

TABLE 6.1: Initial sample of confirmed or possible maser-emitting PNe

Name	Alt. name	Coordinates[a]		Maser emission[b]		Status[c]	References[d]		
		R.A(J2000)	DEC(J2000)	H_2O	OH		H_2O	OH	Nature
IRAS 07027−7934	Vo 1	06:59:26.41	−79:38:47.0	ND	D	SP	1	2	3, 4
IRAS 14079−6402	WRAY 16-146	14:11:46.27	−64:16:24.0	–	D	SP	–	5	6
IRAS 14086−6907		14:12:50.43	−69:21:09.0	–	D	SC	–	5	7
IRAS 15559−5546	WRAY 16-198	15:59:57.63	−55:55:33.0	–	D	SP	–	5	8
IRAS 16029−5055	SCHD 68	16:06:40.63	−51:03:57.2	–	D	IC	–	9	10
IRAS 16280−4008	NGC 6153	16:31:30.57	−40:15:13.1	–	D	SP	–	11	12
IRAS 17180−2708	PN M 3-39	17:21:11.49	−27:11:37.9	–	D	SP	–	11	8
IRAS 17253−2824		17:28:30.68	−28:26:54.0	–	D	SC	–	5	13
IRAS 17374−2700		17:40:33.15	−27:02:25.3	–	D	SC	–	5	13
IRAS 17385−2211	PN M 3-13	17:41:36.60	−22:13:02.9	–	D	SP	–	5	13
PN H 2-18		17:43:28.75	−21:09:52.0	–	D	SP	–	5	14
IRAS 17487−1922	OH 008.9+03.7	17:51:44.92	−19:23:43.8	ND	D	SC	15	5	16
IRAS 18213−1245A		18:24:10.40	−12:43:22.8	D	D	IC	17	18	19
IRAS 18243−1048		18:27:08.24	−10:46:09.6	–	D	SC	–	5	20
IRAS 18271−1014		18:29:56.09	−10:12:12.9	–	D	SC	–	21	22
IRAS 18295−2510	NGC 6644	18:32:34.70	−25:07:45.7	–	D	SP	–	5	23
OH 25.646−0.003		18:38:06.14	−06:28:51.2	–	D	IC	–	18	24
IRAS 18464−0140	OH 31.21−0.18	18:48:56.66	−01:36:42.9	D	D	IC	25	25	19
IRAS 18443−0231	RFS 505	18:47:00.41	−02:27:55.12	D	–	SP	26	–	27, 28
IRAS 18480+0008		18:50:36.65	+00:12:29.8	–	D	IC	–	18	19
IRAS 18508+0047	GPSR5 33.906−0.044	18:53:22.10	+00:50:49.2	–	D	IC	–	18	19
IRAS 19035+0801	PM 1−279	19:05:56.40	+08:05:57.9	–	D	SC	–	29	30
IRAS 19123+1139		19:14:40.87	+11:44:49.3	–	D	SC	–	31	22
IRAS 19127+1717	SS 438	19:14:59.72	+17:22:46.0	ND	D	SP	32	33	34
IRAS 19176+1251	GLMP 898	19:19:55.77	+12:57:37.6	ND	D	IC	15	18	19
IRAS 19194+1548		19:21:40.46	+15:53:54.6	–	D	IC	–	18	19, 35
IRAS 19200+1035		19:22:26.80	+10:41:21.2	ND	D	SC	36	37	38
IRAS 19508+2659		19:52:57.86	+27:07:44.7	D	D	SC	39	40	41
IRAS 20266+3856		20:28:30.67	+39:07:01.2	ND	D	SC	31	42	41

Notes.[a] Position of the radio continuum emission reported in the literature, used as the phase center of our observations (Table 6.3). [b] D: detected. ND: not detected. –: no observations available. [c] Source status, as defined in Section 6.2. [d] Reference for the maser emission (columns H_2O, OH). The last column (nature) indicates references that spectroscopically confirmed the sources with SP status as PNe. For PN candidates (SC, IC), that column reports the radio continuum detection: 1. Suárez et al. (2009). 2. Zijlstra et al. (1991). 3. Menzies & Wolstencroft (1990). 4. Surendiranath (2002). 5. te Lintel Hekkert et al. (1991). 6. Suárez et al. (2006). 7. Hale et al. (2021). 8. Frew et al. (2013). 9. Sevenster et al. (1997a). 10. Irabor et al. (2023). 11. te Lintel Hekkert & Chapman (1996). 12. Pottasch et al. (1986). 13. Kimeswenger (2001) 14. Gesicki et al. (2024). 15. Gómez et al. (2015b). 16. Kohoutek (2001). 17. Walsh et al. (2014). 18. Beuther et al. (2019). 19. Wang et al. (2018). 20. Helfand et al. (1992). 21. David et al. (1993). 22. Urquhart et al. (2009). 23. Hsia et al. (2010). 24. White et al. (2005). 25. Forster & Caswell (1989b). 26. Urquhart et al. (2011). 27. Cooper et al. (2013). 28. Kanarek et al. (2015). 29. Yung et al. (2013). 30. van de Steene & Pottasch (1995). 31. Yung et al. (2014). 32. Yoon et al. (2014). 33. Likkel (1989). 34. Whitelock & Menzies (1986). 35. Sabin et al. (2014) 36. Benson & Little-Marenin (1996). 37. Benson et al. (1990). 38. Zijlstra et al. (1989). 39. Cesaroni et al. (1988). 40. Eder et al. (1988). 41. Zoonematkermani et al. (1990). 42. te Lintel Hekkert et al. (1989).

in the literature as maser emitters (see Chapter 3), and of sources whose radio continuum emission is known to be associated with objects that are not evolved stars. In Table 6.1 we present the final sample of 29 confirmed or candidate PNe that may be associated with maser emission, resulting from our catalog matching and search of the literature.

Our list of sources can be classified, based on whether the association between maser and continuum emission has been confirmed with the high positional accuracy of interferometric observations (sources labeled as "I"), or if only single-dish maser observations have been reported (labeled as "S"), and whether the target has been previously confirmed as a PN (label "P"), or the nature of the radio continuum source is still unknown, and therefore, it is only a PN candidate (label "C"). Therefore, we can define four different categories of sources, with the following labels used in the seventh column of Table 6.1 (status):

1. SC: radio continuum sources of unknown nature within the beam of a single-dish maser detection.
2. SP: Planetary nebulae within the beam of a single-dish maser detection.
3. IC: radio continuum sources whose association with maser emission has been confirmed interferometrically. In the following, we will refer to these sources as candidate maser-emitting PNe (candidate OHPNe and/or candidate H_2OPNe).
4. IP: planetary nebulae with interferometrically confirmed association with maser emission. We will refer to them as confirmed maser-emitting PNe (confirmed OHPNe and/or confirmed H_2OPNe).

Our initial search resulted in 11 SC, 10 SP, and eight IC.

In this chapter, we have carried out interferometric observations of maser and radio continuum emission of sources labeled as SC and SP in Table 6.1, to confirm whether both types of emission are spatially associated, so that we could update their status to IC or IP. We also observed the H_2O maser emission in the IC IRAS 19194+1548, to find out whether it is associated with this emission, in addition to OH maser one. We did not pursue observations of two ICs (IRAS 18213−1245A and IRAS 18464−0140), since that spatial association was already confirmed from interferometric data in the literature. However, these two sources are discussed in Appendix 6.C, together with the sources for which our interferometric observations allow us to update them as either IP or IC.

Determining the evolutionary stage of an evolved star, particularly in the transition from the AGB to the PN phase, remains a complex and widely debated issue, especially in the absence of optical and infrared imaging and spectroscopy. In this context, establishing whether the sources presented in this chapter as candidate PNe are genuine PNe (that is, an update from C to P status) is beyond the scope of this work. However we discuss in Appendix 6.C some of the available evidence that suggests a possible PN nature for some of our targets.

6.3 Observations and data processing

We observed 27 of the 29 sources (see above) of the initial sample listed in Table 1. Additionally, we observed the previously identified OHPNe candidates IRAS 17494−2645 and IRAS 18019−2216 (Chapter 3) to search for H_2O maser emission. The observations were carried out with the Australia Telescope Compact Array (ATCA) of the Australia Telescope

National Facility (ATNF) and the Karl G. Jansky Very Large Array (VLA) of the National Radio Astronomy Observatory (NRAO). Table 6.3 shows the final list of observed targets, as well as the main parameters of our radio interferometric observations.

6.3.1 ATCA

ATCA observations (ID: C3390, P.I.: R. A. Cala) were carried out in two 12-hour sessions performed on 2020 October 19 and 20 using the 6A configuration of the telescope. The CFB 1M-0.5k mode of the Compact Array Broadband Backend (CABB) was configured to observe the ground level OH transitions at L band, with the rest frequencies 1612.2309, 1665.4018, 1667.3590, and 1720.5299 MHz, with a total bandwidth of 1 MHz each, sampled over 6146 channels of 0.5 kHz (total velocity coverage of 557 $\mathrm{km\,s^{-1}}$ and velocity resolution of $\sim$90 $\mathrm{m\,s^{-1}}$ for each line) and full linear polarization products. The velocity coverage is enough to detect the range of $\sim$120 $\mathrm{km\,s^{-1}}$, which is the maximum range detected in OH in any of our target sources from single-dish observations. Also, the channel width is narrower than the reported linewidths. In both sessions, we observed continuum emission at an intermediate frequency centered at 2.1 GHz, with full linear polarization and a bandwidth of 2 GHz sampled into 2048 broadband channels. A second intermediate frequency replicates the same frequency configuration. The flux and bandpass calibrator in both observing sessions was PKS 1934-638. Variations in phase and amplitude were tracked by interleaving observations of our targets with nearby phase calibrators (Table 6.3).

Manual flagging of bad data, as well as calibration of visibilities were performed with the MIRIAD software following standard data reduction procedures. For the continuum data, further flagging of the channels containing the frequencies of the ground-state OH maser transitions, as well as imaging of the calibrated visibilities, were done with the Common Astronomy Software Applications (CASA; CASA Team et al. 2022) using tasks *plotms* and *tclean*, respectively. For the line data, spectral data cubes were obtained with the Astronomical Image Processing System (AIPS), since it proved to be significantly faster than CASA. First, we corrected the Doppler shift in the spectral line data due to the observatory motion to align the observations of each source with the same kinematical local standard rest (LSR) velocity (V_{LSR}), using task *cvel* of AIPS. Imaging was performed using task *imagr*. Self-calibration was attempted on the channel with brightest OH maser emission, but we did not obtain a significant improvement in the signal-to-noise ratio (S/N) of any of the sources. We present data without applying self-calibration. In the detected sources we also tried to split the band of 2 GHz width into several subbands, to better sample the frequency dependence of flux density. However, the resulting emission either was not detected or had a very low S/N ratio. Thus, we report their continuum emission over the full bandwidth.

6.3.2 VLA

VLA observations (ID: 21A-138, PI: R. A. Cala) were carried out in the D configuration of the array, in four observing blocks (OBs) performed in 2021 March and April (see Table 6.3). Two OBs were dedicated to L-Band (1–2 GHz) observations and the other two OBs to K-Band (20–24 GHz) observations. For the L band, the VLA correlator was configured with 8-bit samplers. This allowed us to observe the 1612.2309 MHz OH transition within a 4 MHz subband, sampled over 4098 channels (velocity coverage and resolution of $\sim$743 and $\sim$0.18 km s^{-1}, respectively), and the 1665.4018, 1667.3590, and 1720.5299 MHz OH lines, each with a 2-MHz wide subband sampled over 2048 channels (velocity coverage and resolution of $\sim$360 and $\sim$0.18 km s^{-1}, respectively). Sixteen additional subbands were set up to cover the whole 1 GHz provided by the 8-bit sampler, for continuum detection. For K band, the 8-bit and 3-bit samplers were mixed, in order to efficiently observe spectral line and radio continuum emission simultaneously. The 8-bit sampler was used to observe the 22235.08 GHz H_2O maser transition using a 32 MHz subband, sampled over 2048 channels (velocity coverage and resolution of $\sim$421 and $\sim$0.21 km s^{-1}, respectively). The velocity coverage is enough to detect the range of $\sim$68 km s^{-1}, which is the maximum velocity range detected of H_2O masers in any of our target sources from single-dish observations. The spectral resolution is finer than the reported linewidths. Moreover, 4 subbands of 128 MHz each (512 MHz in total) of the 8-bit sampler and the whole 4 GHz bandwidth of the 3-bit sampler pairs were dedicated for detection of continuum emission. The absolute flux calibrator was 3C286. The quasar J1733−1304 (QSO B1730−130) was used as a bandpass calibrator. Sources close to our targets in the sky were chosen as phase calibrators (Table 6.3), to correct for phase and amplitude variations.

The continuum and line emission data of each OB was calibrated independently using the VLA pipeline implemented in CASA. After initial imaging with CASA, we tested self-calibration using the channels with brightest maser emission in each detected source. We were only successful in improving the S/N of the H_2O maser data of IRAS 18443−0231 and IRAS 18480+0008. Moreover, comparing our self-calibration results with CASA and AIPS, we noticed that the latter provided S/N ratio a factor of $\sim$1.4 times better than CASA in the channel with the most intense maser emission. Hence, we kept the successful self-calibration solutions obtained in AIPS for this channel, and applied them to the rest of the spectral line data and to all continuum spectral windows at K band for these two sources. Self-calibration of the continuum data of IRAS 17494−2645 and IRAS 19194+1548 also significantly improved the S/N of this emission. After self-calibration, subsequent imaging of both continuum and line emission was performed in CASA using the task *tclean*. As in the case of the ATCA data, to better sample the frequency dependence of flux density, we tried to split the data into different frequency ranges. We started with IRAS 18443−0231, which was the strongest source detected and, therefore, the one with the highest S/N. We split the bandwidth of band L and band K data in two different frequency ranges each. These values will be presented below in the discussion of spectral indices in Section 6.5.5. In the remaining sources, we noticed that the S/N of the resulting emission in the L band was very low and, in addition, the small relative frequency coverage of the K band around 22 GHz would not result in a significant improvement of their spectral indices reported in Section 6.5.5, at the expense of lowering an already limited S/N. Thus, for all sources except IRAS 18443−0231, we present only one value of flux density per observed band.

For sources IRAS 18443−0231, IRAS 18464−0140, and IRAS 18508+0047, we found and processed archival VLA data of continuum emission. For IRAS 18443−0231 we found VLA B configuration data from observations performed on January 10 2014 (ID: 13A-334, P.I.: K. Menten) which allowed us to create a continuum map of the emission at 5.7 GHz. For IRAS 18464−0140 and IRAS 18508+0047 we found archival VLA data from observations performed in the A configuration on March 08 2022 (ID: 22A-297, PI: A. Yang) which allowed us to create continuum emission maps at 10 GHz. All of these continuum data were processed with the VLA CASA pipeline, successfully self-calibrated, and imaged in CASA. Moreover, for IRAS 18464−0140 we reprocessed archival VLA H_2O maser data from observations performed with the C configuration on 21 June 1984 (ID: AF80, PI: J. R. Forster). The initial calibration of these data was carried out with CASA. Self-calibration was successfully applied with AIPS using the channel with the brightest maser emission.

6.4 Results

The initial criterion we have used to assess the interferometric association between the maser and the continuum emission is that the distance between the maser and the peak of the continuum emission is smaller than the FWHM synthesized beam of the continuum map, in the case of unresolved sources. This match criterion is the same as that used in previous searches of nascent PNe (e.g. Payne et al. 1988; Zijlstra et al. 1989; de Gregorio-Monsalvo et al. 2004; Uscanga et al. 2012). If the continuum emission of the target is resolved, then the criterion is that the maser emission falls within a four-sigma contour level of this resolved emission. We then carefully examined the sources with and without a positional match following these criteria, to minimize false positives and negatives.

In the case of identified possible matches, we have to rule out the possibility that the continuum and the maser emission may arise from different sources lying close in the sky. Most distances between the maser and continuum emission are less than 2", which makes the chance of alignment highly unlikely. However, we inspected optical and infrared images to make sure that there is no obvious contaminant source near the main infrared source from which maser emission is most likely to arise. In some cases where we could determine the distribution of maser emission, this shows a morphology that aligns well with the elongation of the nebula traced by radio continuum emission, which further reinforces their mutual association. We therefore conclude that in all matches we found, the same object is the source of maser and radio continuum radiation.

In Table 6.4 we show the interferometric positions of the radio continuum and maser emission of the matches we found, as well as the angular distance between the two types of emission (δ). In some cases, these spatial matches were obtained from the positions reported in literature data. Moreover, our interferometric ATCA/VLA observations allowed us to upgrade the status of several of the sources labeled SC or SP in Table 6.1 to either IC or IP. This updated status is also presented in Table 6.4, with a different nomenclature that reflects the particular maser species involved. Details of these sources are presented in the Appendix 6.C.

Spectra of the detected maser emission in our data are presented in Fig. 6.1. Our criterion for claiming a positive detection of a maser spot is that the emission is present above 3 sigma in at least three consecutive velocity channels and at a compatible position, which makes the probability of a false positive virtually negligible. In three objects, our positional accuracy was enough to determine the spatial distribution of the individual H_2O maser components. The parameters of these spectral components are listed in Appendix 6.B.2. Maps of their spatial distributions are presented in Fig. 6.2. As mentioned in Appendix 6.B.2, the positional uncertainties are those obtained with a fit of an elliptical Gaussian to the channel with the peak emission of each maser component. The radio continuum emission appears unresolved in all cases, except for IRAS 18443−0231 (Appendix 6.C.2.3), where we can see some extended emission.

To minimize the possibility of false negatives, we also inspected images at different wavelengths of the sources for which the maser emission falls outside the beam of the continuum observations (for unresolved sources) or the total extent of the emission (for resolved sources). Our goal was to discard the fact that, despite their apparent misalignment, the maser and continuum emission may arise from different locations from the same source (e.g., the central star or the lobes in a PNe). After this analysis, we could discard as possible maser-emitting PNe several of the objects labeled as SC and SP in Table 6.1, since the maser and continuum emission appear associated with different sources. These are presented in Table 6.12 and details of individual sources are given in appendices 6.B.3.1 to 6.B.3.6. In the case of sources in which either maser or continuum emission was not detected in our data (Table 6.13), we cannot confirm or discard a putative association, since variability could bring either emission below our sensitivity threshold.

6.5 Source characterization

After confirmation of the association between maser and radio continuum emission, we investigated whether the identified objects are consistent with being PNe. Although some of the sources in which we found an interferometric match between maser and continuum emission have been classified spectroscopically as PNe in the literature, no such classification is available for the ones we termed candidate maser-emitting PNe. In this section, we present some further characterization of all sources in Table 6.4, which shows that all candidate sources

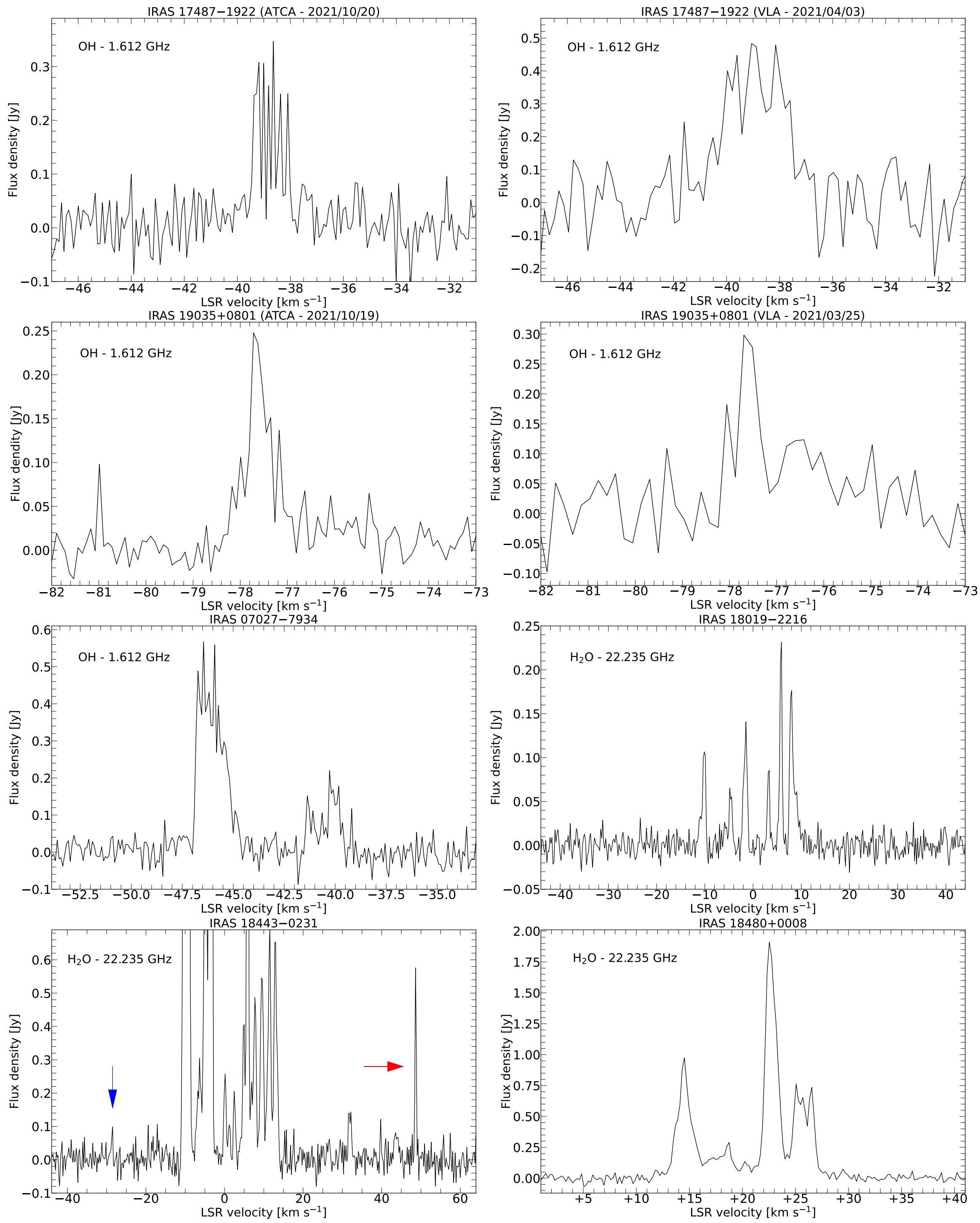

FIGURE 6.1: Spectra of OH and H_2O emission detected in our observations. In IRAS 18443−0231 we show an enlarged view to clearly show the most blueshifted and redshifted H_2O masers, which are indicated by a blue and red arrow, respectively.

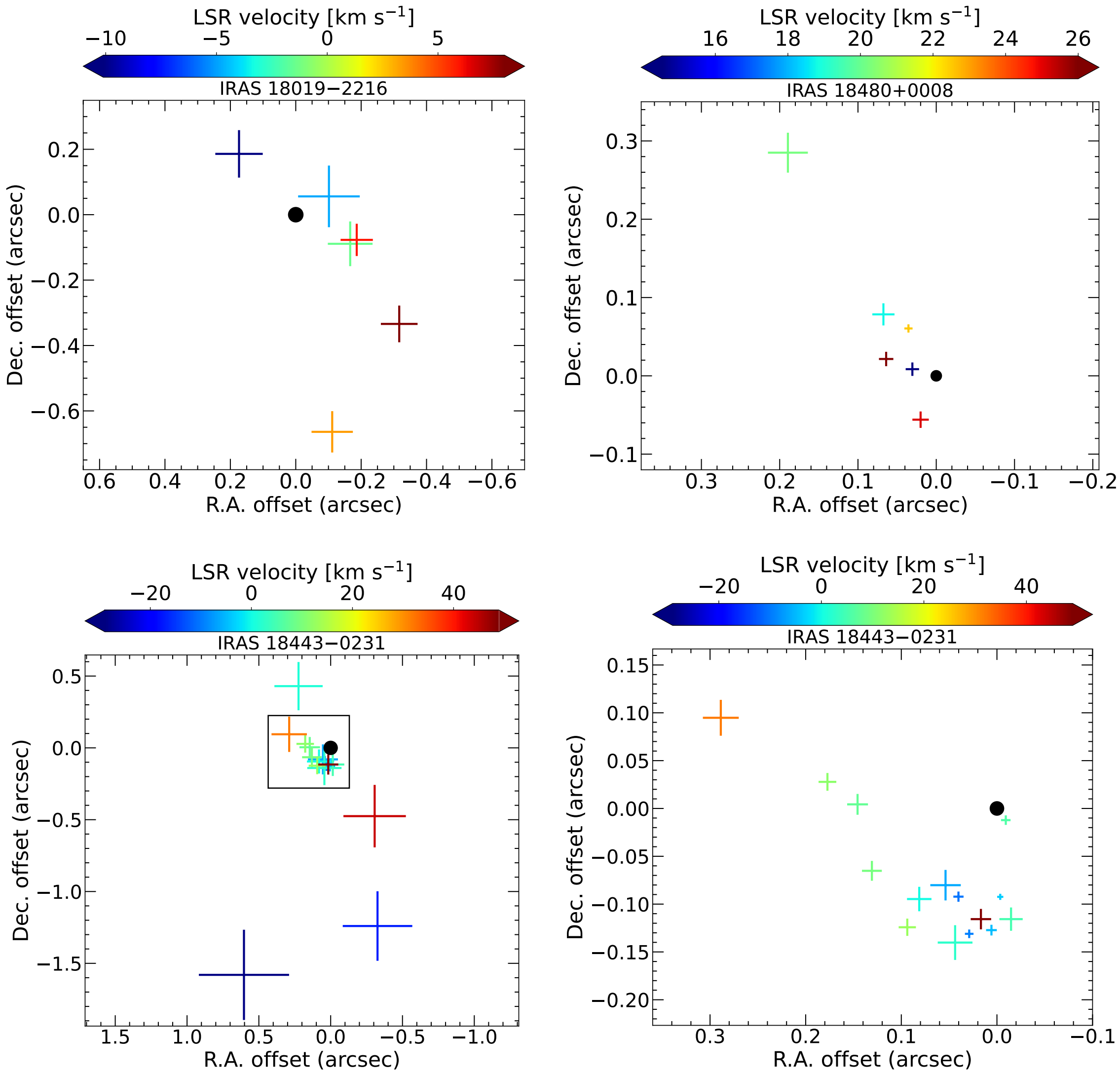

FIGURE 6.2: Spatial distribution of the H_2O maser components (crosses) with respect to the position of the radio continuum emission peak (filled circle) at 22.22 GHz. The colorbar represents the LSR velocity of the masers and the symbol sizes are their positional uncertainties. The bottom right panel is a close-up of H_2O maser components in the central area of IRAS 18443−0231 (marked by a black dashed rectangle in the left panel), close to the continuum emission peak.

seem to be evolved objects, rather than extragalactic sources or YSOs, source types which could also show maser and continuum emission. Therefore, all our candidate sources are compatible with being PNe, although in several cases further observations are necessary to determine whether the radio continuum emission arises from a photoionized region or from shock-ionized gas, as seen in post-AGB stars (e.g., Pérez-Sánchez et al. 2017).

6.5.1 Spectral energy distribution (SED)

We have collected all available archival optical, infrared, and millimeter data, together with the radio data presented in Section 6.5.5, to build their SED between ∼0.5 μm and 40 cm.

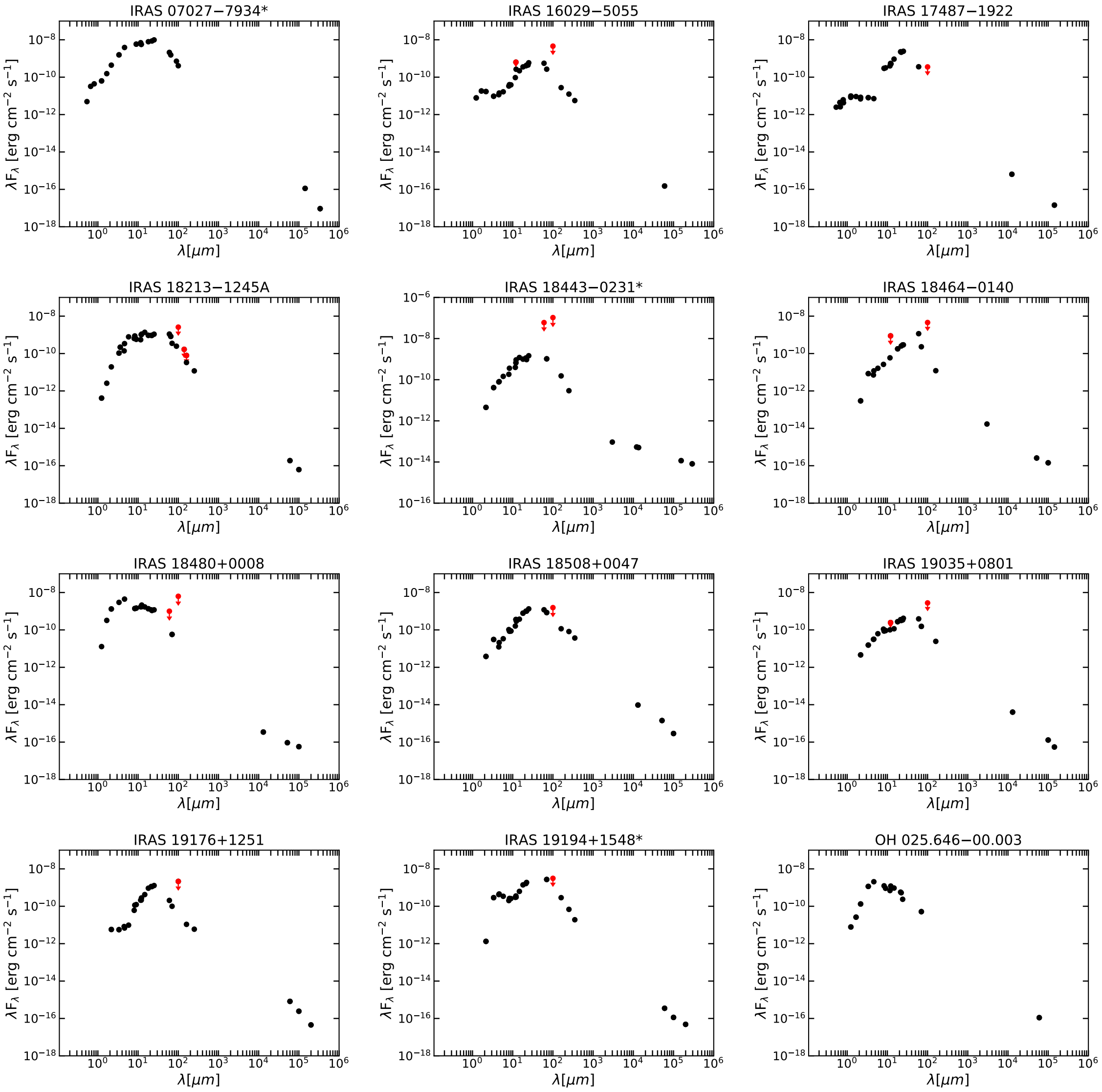

FIGURE 6.3: SED of the new maser-emitting PN (indicated with an asterisk next to its name) and candidates (rest of the panels). The circles are the photometric values found for each of the new identified sources. The size of the circles is larger than the errors. Red color stands for upper limits.

Optical and infrared data were obtained from the Two Micron All Sky Survey (2MASS), AKARI, Deep Near Infrared Survey of the Southern Sky (DENIS), Gaia, *Herschel* Space Observatory, Infrared Astronomical Satellite (IRAS), Midcourse Space Experiment (*MSX*), Panoramic Survey Telescope and Rapid Response System (Pan-STARRS), Spitzer Space Telescope, United Kingdom Infrared Telescope (UKIRT), United States Naval Observatory (USNO)-B catalog, Visible and Infrared Survey Telescope for Astronomy variable survey (VVV), and Wide-field Infrared Survey Explorer (all-*WISE* survey). Flux densities at 3 mm were obtained from Ginsburg et al. (2020). These SEDs are presented in Fig. 6.3, with the exception of IRAS 17494−2645 and IRAS 18019−2216, which were already shown in Chapter 3.

Although SEDs alone are not sufficient to unambiguously determine the nature of these objects, there are some useful trends that can give support to a prospective classification. The SEDs of all sources in this chapter show significant similarities and, in particular, they present their emission peak at $\lambda<60\,\mu$m. This feature is also observed in the SEDs of confirmed and candidate H_2OPNe and OHPNe previously reported (Uscanga et al. 2012, and Chapter 3) and, in general, it is also the case of compact PNe (Zhang & Kwok 1991), and optically obscured post-AGB stars and PNe (e.g. Ramos-Larios et al. 2009, 2012). Moreover, the shape of the SED and the wavelength of the peak is significantly different from other types of objects that present both maser and radio continuum emission, such as YSOs or galaxies and therefore, could contaminate our group of candidates. For instance, the SED of YSOs usually peaks at wavelengths around $1\,\mu$m or longer than $70\,\mu$m (e.g. Robitaille et al. 2007). In the particular case of low-mass YSOs, radio continuum emission from shock-ionized jets is more prominent in the earlier stages (class 0 and class I sources), when the SED peaks at long wavelengths ($> 100\,\mu$m; Dunham et al. 2008, 2013). In the case of high-mass YSOs, the peak of the SED for H II regions (including ultracompact ones) usually lies at wavelengths longer than $70\,\mu$m (Wood & Churchwell 1989; Anderson et al. 2012).

In galaxies with active galactic nuclei, the peak of the SED seems to be at wavelengths shorter than $1\,\mu$m or longer than $100\,\mu$m (e.g. Dale et al. 2005; Popescu et al. 2011; Brown et al. 2014; Lyu & Rieke 2022). Thus, the differences between the SEDs in Fig. 6.3 and those of typical YSOs and galaxies indicate that our targets are more likely to be evolved objects. Moreover, among these, symbiotic stars (SySts) can also present maser emission (e.g., Cho & Kim 2010), although OH ones are extremely rare (e.g., Morris 1987; Seaquist et al. 1995). The SED peak of SySts usually lies at $\lambda \leq 10\ \ \mu$m (Akras et al. 2019). This only happens in two of the objects in Fig. 6.3, which will be discussed below. Therefore, the SED of most of the newly identified objects in this chapter seems more consistent with post-AGB stars and PNe hosting maser emission.

6.5.2 Infrared morphologies

We inspected the available mid- and near-infrared images of the new IC sources reported in this work. All seem to be compact sources in the mid-infrared, with the exception of IRAS 19194+1548, which is compact but marginally resolved. Furthermore, this source (Sec. 6.C.2.6) shows a point-symmetric morphology in near-infrared images that is typical of evolved stars, rather than YSOs. The compact and isolated morphology of the sources classified as IC in this chapter supports their identification as evolved stars rather than YSOs, which are usually surrounded by diffuse and extended structures from their parental clouds.

6.5.3 Mid-infrared colors

To further elucidate if the emission properties of the identified sources are more compatible with circumstellar envelopes of evolved stars, Fig. 6.4 shows an *MSX* color-color diagram

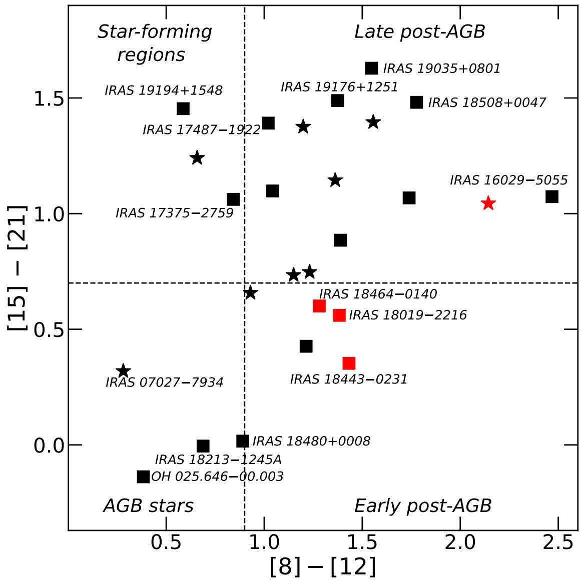

FIGURE 6.4: *MSX* color-color diagram, as defined by Sevenster (2002), including all known and new maser-emitting PNe and candidates, and adopted from Chapter 3. The vertical and horizontal dashed lines separate the diagram into four quadrants, where different types of sources tend to cluster. The filled star and square symbols without source names represent the previously reported maser-emitting PNe and candidates, respectively. These same symbols with source names are the new maser-emitting PNe and candidates, respectively. IRAS 16029−5055, IRAS 17375−2759 and IRAS 19176+1251 are included as PNe (see Section 6.5.4). Symbols with red color represent sources with WF characteristics.

of all known maser-emitting PNe and candidates (collecting the sources presented in this chapter, and those previously reported in the literature). This color-color diagram, where each color is defined as $[a]-[b]{=}2.5\,log(S_a/S_b)$, was presented by Sevenster (2002) to help identify post-AGB stars among evolved stars with OH maser emission, and later used by Uscanga et al. (2012) and Chapter 3 in the characterization of maser-emitting PNe. We note that this diagram does not provide a clear-cut diagnosis of the nature of each source, but it shows quadrants where it is more likely to find sources of a particular type. The confirmed and candidate maser-emitting PNe cluster mainly in the quadrant of late post-AGB stars, as expected if they are all bona fide PNe. However, some interesting cases are identified in this chapter, clearly located in the quadrant of AGB stars (the confirmed PN IRAS 07027-7934 and the candidate PNe IRAS 18123-1245A and OH 025.646-00.003), which deserve further attention. These objects may be rapidly evolving to the PN phase, while still retaining an envelope with AGB characteristics.

In Fig. 6.5 we show a *WISE* color-color diagram of all known and new maser-emitting PNe and candidates, adopted from Chapter 3. The diagram was presented in Gómez et al. (2017) for a comparison between the colors of WFs and the optically obscured post-AGB stars. Chapter 3 suggested that the colors $10.5\leq[3.4]-[22]\leq13.5$, and $4.0\leq[4.6]-[12]\leq7.0$ could identify new nascent PNe and candidates. Adding to this diagram the new confirmed and candidate maser-emitting PN found in this chapter, we can see that these objects tend to cluster in the area delimited by the colors mentioned above. However, these limits are not

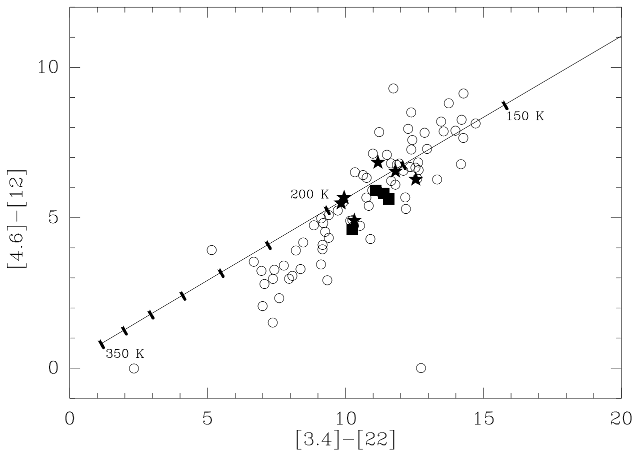

Figure 6.5: *WISE* color–color diagram, similar to the one presented in Gómez et al. (2017), including all known and new maser-emitting PNe and candidates, and adopted from Chapter 3. The stars and squares represents the confirmed maser-emitting PNe and candidates, respectively, as presented in Fig. 6.4. The red color stands for WF nature of the source. The open circles represent obscured post-AGB candidates (Ramos-Larios et al. 2009, 2012). The solid line represents the loci of the colors for blackbody brightness distributions. The tick marks in the blackbody line go from 150 to 350 K at increment steps of 25 K.

strict, since some sources lie clearly outside of them. In particular, there are two candidates with $[3.4]-[22] \simeq 5$ (IRAS 18480+0008 and OH 25.646−00.003), which seem to correspond to objects within or close to the quadrant of AGB stars in Fig. 6.4, suggesting that they may be different from the rest of confirmed or candidate maser-emitting PNe.

6.5.4 Mid-infrared spectra and diagnostic diagram

We have searched for *Spitzer* spectra of objects observed with the Infrared Spectrograph (IRS; Houck et al. 2004) and enhanced data products in the *Spitzer* Heritage Archive. We found spectra, obtained with the Short-Low (SL) and Short-High (SH) modules covering the range 5.13-14.29 μm and 9.9-19.6 μm, respectively, for two of the new OHPN candidates identified in this work, IRAS 16029−5055 (Program ID: 50652; PI: D. Engels) and IRAS 19176+1251 (Program ID: 30258; PI: P. Garcia-Lario), which we show in Fig. 6.6. We also found *Spitzer* spectra from one previously reported OHPN, IRAS 17393−2727 (Program ID: 3633; PI: M. Bobrowsky) (Pottasch et al. 1987; García-Hernández et al. 2007), and one previously reported OHPN candidate, IRAS 17375−2759 (Program ID: 3235; PI: M. Waelkens) (Uscanga et al. 2012), which are also shown in those figures, for comparison purposes. In addition, we found two highly processed archive spectra (2-45 μm) in the Infrared Space Observatory (ISO) data center[1] of IRAS 17347−3139 and K 3-35, two previously reported

[1]The spectra presented by Uscanga et al. (2012) are available at the ISO data center and the technical report is available at https://nida.esac.esa.int/hpdp/technical_reports/technote52.pdf

OHPN and H_2OPN (Miranda et al. 2001; de Gregorio-Monsalvo et al. 2004; Tafoya et al. 2009), which were shown in Uscanga et al. (2012), and we analyze them below, also for comparison purposes.

The *Spitzer* spectra shown in Fig. 6.6 display narrow and wide emission features commonly associated with ionized gas and dust grains, respectively. Usual ionized gas tracers are the fine-structure spectral lines of [Ar II], [Ar III], [Ne II], [Ne III], [Ne V], and [S IV] at 6.98, 8.98, 12.81, 15.55, 14.32, and 10.51 μm, respectively, while the broad features at 6.3, 8.6, and 11.6 μm are commonly associated with emission from polycyclic aromatic hydrocarbons (PAHs). In addition, there is spectrally resolved emission of PAHs at 7.4 μm. The spectra of galaxies, H II regions, and YSOs with low and high masses usually display an absorption feature at 9.8 μm (e.g., Peeters et al. 2004; Simpson et al. 2012), which is absent in the spectra shown here. Moreover, the lines of the ionized gas in this wavelength range are characteristic of PNe, and not of post-AGB stars (see also Matsuura et al. 2014, for *Spitzer* spectra of post-AGB stars and PNe in the Milky Way and Large Magellanic Cloud), so IRAS 16029−5055, IRAS 17375−2759, and IRAS 19176+1251 are likely to be PNe.

In order to better determine if these spectral lines tracing ionized gas in the mid-infrared actually identify these objects as PNe, we used the Mexican Million Models Database (3MdB; Morisset et al. 2015; Alarie & Morisset 2019), which allowed us to analyze whether the line intensities are consistent with shocks or photoionization. We have used the shock models of Sutherland & Dopita (2017) and the photoionization models of Ferland et al. (2017) stored in the 3MdB to create line-ratio diagnostic diagrams. We did not search for exact models to match the observed line ratios. Instead, we used the maximum number of models to define the entire region within these diagrams that is compatible to either origin of ionization. More details on the grid parameters are provided in the Appendix 6.D. The final diagnostic diagram is shown in Fig. 6.7, displaying line ratios compatible with shock ionization and photoionization, which we compared with our data.

In this comparison, we have not corrected the spectra by extinction. This extinction is relatively low in the mid-infrared, and we have used ratios of lines that are close in wavelength ([Ne II], [Ne III] and [Ne V] seen at 12.81, 15.55, and 14.32 μm, respectively) so their line intensity ratios are practically insensitive to extinction (e.g., Genzel et al. 1998; Martín-Hernández et al. 2002; Pereira-Santaella et al. 2010; Weaver et al. 2010). In addition, each spectrum has been continuum-subtracted using a polynomial curve fitting, and then each emission line was measured with an individual Gaussian fitting using Astropy (Astropy Collaboration et al. 2013, 2018, 2022).

Although we can reasonably expect that the origin of ionization in nascent PNe is a combination of both shocks and photoionization, the location of the sources in the line-ratio diagnostic diagrams that separate either process is revealing. The intensity ratios fall outside the region covered by the shock ionization models in all cases, specially in the [Ne III]/[Ne II] ratio, whereas they can be consistent with the photoionization models. The incompatibility with shocks alone indicates that these fine-structure spectral lines must have a significant

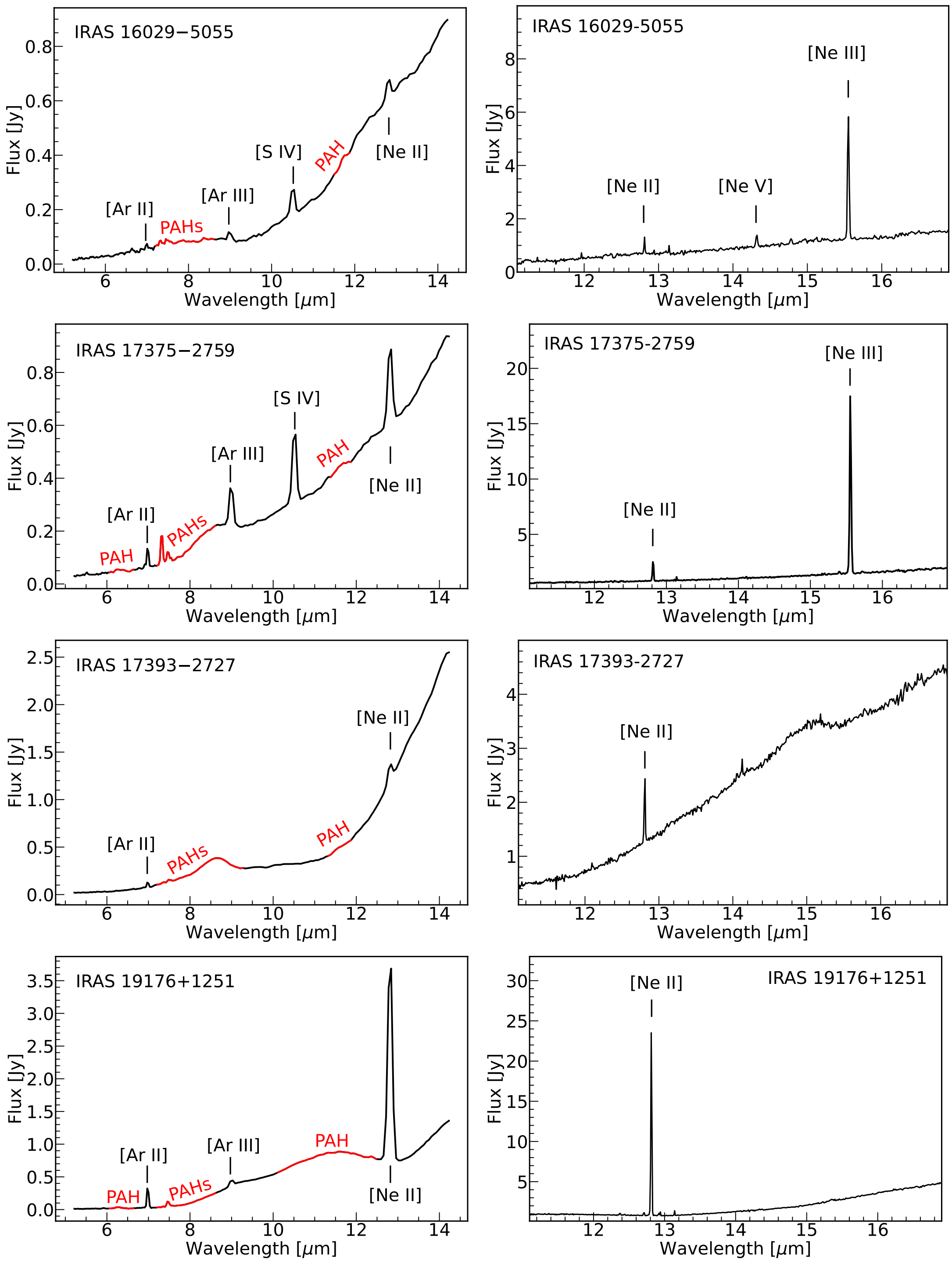

FIGURE 6.6: Mid-infrared spectra of IRAS 16029−5055, IRAS 17375−2759, IRAS 17393−2727, and IRAS 19176+1251, as seen by the IRS SL (left) and SH (right) modules of *Spitzer*. Narrow and broad emission lines (red color) from ionized gas and dust grains, respectively, are present in their spectra. The narrow emission lines of [Ar II], [Ar III], [S IV], [Ne II], [Ne III], and [Ne V] are observed at around 6.98, 8.98, 10.51, 12.84 μm, 15.55, and 14.32 μm, respectively. The broad emission lines are usually attributed to emission from PAHs, which present a different chemistry (C-rich) from that of the O-rich maser-emitting regions.

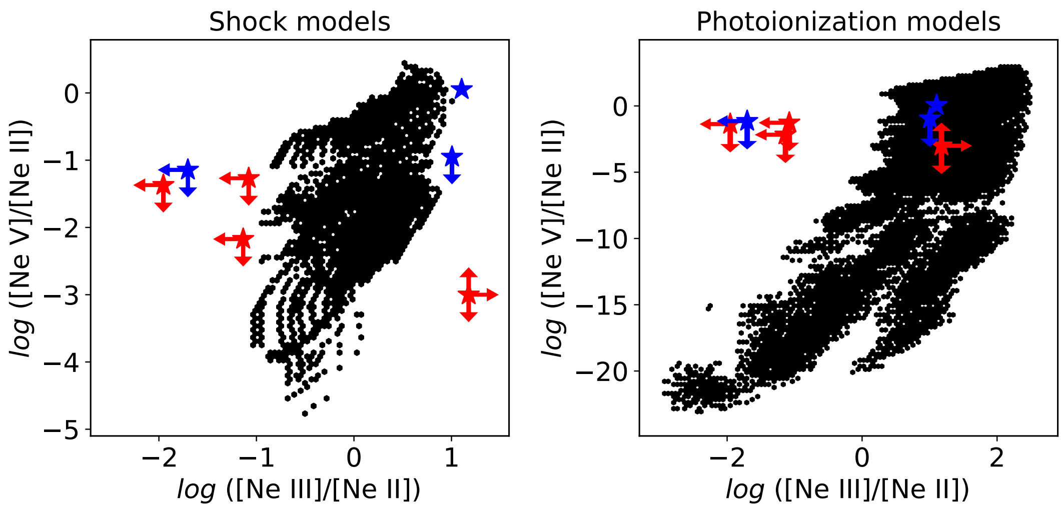

FIGURE 6.7: Line ratio diagnostic diagram for the mid-infrared emission lines of [Ne II], [Ne III], and [Ne V] at 12.81, 15.55, and 14.32 μm, respectively. The left panel shows shock models, and the right panel shows photoionization models. The blue stars mark the new objects in which the presence of photoionized gas is favored by these diagrams (IRAS 16029−5055, IRAS 17375−2759, and IRAS 19176+1251). The red stars mark previously reported maser-emitting PNe (IRAS 17347−3139, IRAS 17393−2727, and K 3-35). The sizes of the symbols are larger than their errors. The arrows indicate values of line ratios that are either upper or lower limits, derived from the upper limits for the lines not detected in each case (see Fig. 6.6). In one case (K 3-35, red star with three arrows) the value *log* ([Ne V]/[Ne II]) is undetermined, and it could be located anywhere in the vertical direction. See Appendix 6.D for more details on the grid parameters.

photoionization contribution. Therefore, these models favor the presence of photoionized gas in IRAS 16029−5055, IRAS 17375−2759, and IRAS 19176+1259. For comparison, previously reported maser-emitting PNe IRAS 17347−3139, IRAS 17393−2727, and K 3-35 also fall outside the region of shock models in Fig. 6.7 (left).

6.5.5 Spectral indices and variability of the radio continuum emission

The dependence of the flux density (S_ν) of the radio continuum emission with frequency (ν) can give useful hints on the emission processes and therefore on the nature of the sources. Spectral indices (α, with $S_\nu \propto \nu^\alpha$) of thermal (free-free) emission of the photoionized gas in PNe must be in the range from +2 at low frequencies (optically thick regime) and −0.1 at high frequencies (optically thin regime). The observed radio spectra usually show two different ranges (e.g., Taylor et al. 1987; Aaquist & Kwok 1991; Gruenwald & Aleman 2007). At low frequencies, α ranges from $\simeq +0.6$ to +2, indicating (partially) optically thick emission, while at high frequencies the slope flattens to values $\alpha \simeq -0.1$. The turn-over frequency separating both regimes can be used to estimate the emission measure (EM) of the nebulae that, in its turn, is thought to be related with age, with younger PN having higher EM (Kwok et al. 1981). Thus, the turn-over frequencies would tend to decrease with time. In the particular case of a nascent PN, while the ionization front advances at supersonic velocities (R-type ionization front, Kahn 1954; Franco et al. 1990), the plasma still briefly maintains the density distribution of the circumstellar envelope created by mass-loss in the AGB phase, with a radial dependence of the electron density to be $n_e \propto r^{-2}$. In this case, the radio spectral index must be around +0.6 (partially optically thick) in most of the centimeter domain (see e.g., Olnon 1975; Panagia & Felli 1975). Spectral indices on this order, and high turn-over frequencies (> 20 GHz) are indeed observed in nascent PNe (e.g., Gómez et al. 2005, and Chapter 3). However, we note that the same spectral index is also expected in the case of shock-ionized winds, including biconical jets (Reynolds 1986), which could be present before the PN phase. In this case, considerations of the required mass-loss rate to produce the observed flux densities can help us to discern if the emission is compatible with shock ionization or photoionization (see Tafoya et al. 2009; Uscanga et al. 2014). One of such cases is IRAS 17347−3139, which was reported before as PN because the required mass-loss rates are incompatible with shock ionization alone (Tafoya et al. 2009), and in this work (Sec. 6.5.4) we spectroscopically confirmed the presence of photoionized gas in this object and, therefore, corroborated that it is a PN.

Together with the radio continuum emission in our data, we collected publicly available measurements of flux densities in our targets at different frequencies. Recent observational efforts have aimed at updating and creating new all-sky radio continuum surveys such as, for instance, the VLA Sky Survey (VLASS; Gordon et al. 2021), Co-Ordinated Radio 'N' Infrared Survey for High-mass star formation (CORNISH; Irabor et al. 2018, 2023), GLObal view on Star formation in the Milky Way (GLOSTAR; Medina et al. 2019; Dzib et al. 2023), Rapid Australian SKA Pathfinder (RASKAP; Hale et al. 2021), or The HI/OH/Recombination line survey of the inner Milky Way (THOR; Wang et al. 2018).

Maser-emitting PNe and candidates show increasing flux densities in timescales of years and decades (Gómez et al. 2005; Tafoya et al. 2009, and Chapter 3), with the exception of IRAS 15103−5754, which shows a decrease non-thermal radio continuum emission in timescales of a few months (Suárez et al. 2015). Hence, simultaneous observations across a large part of the centimeter domain are crucial to obtain a precise determination of the radio spectral indices. Using data at different frequencies taken at different epochs can result in unrealistic slopes in the radio spectrum, so special care should be taken in these cases. Obtaining spectral indices from different catalogs or observational projects can provide a useful first approximation, but a definite confirmation of the actual radio spectrum can only be obtained with (quasi-)simultaneous observations. In our case, while flux densities reported in the surveys mentioned above can be used to obtain preliminary radio spectra of the new identified maser-emitting sources, we can obtain even more solid confirmation of the spectral indices by focusing only on the measured flux density values at different frequencies in our own observations for several targets, which were taken within less than eight days for each individual source (Table 6.3).

Fig. 6.8 shows the flux densities and determined spectral indices of the new maser-emitting PNe and candidates, using the data from our observations (black symbols) and from the

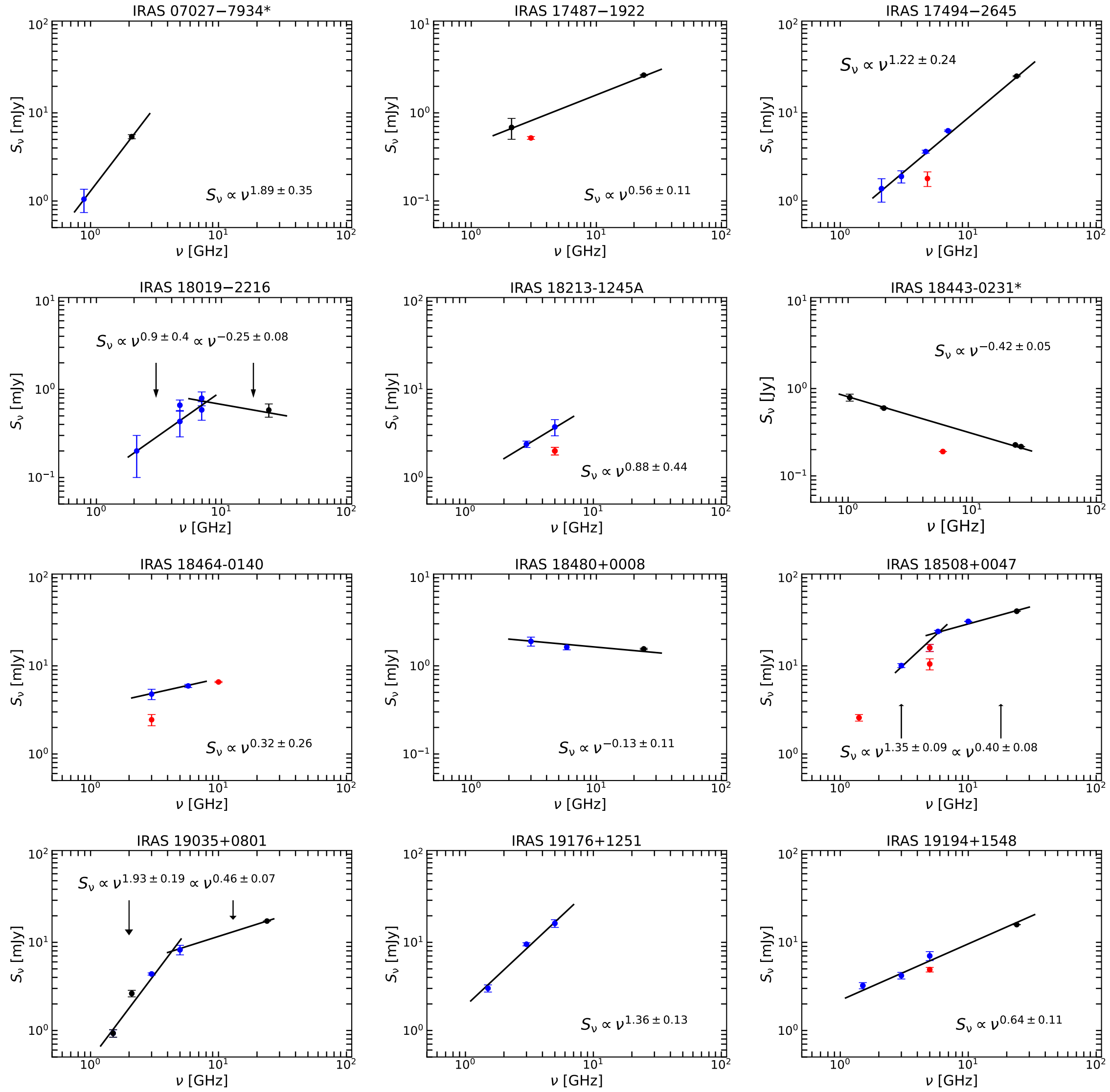

FIGURE 6.8: Radio continuum emission of the new maser-emitting PN (indicated with an asterisk next to its name) and candidates (rest of the panels), including the new flux density values at 24.5 GHz from our VLA observations in the previously reported OHPN candidates IRAS 17494−2645 and IRAS 18019−2216 (Chapter 3). The source names and obtained spectral indices (α) are indicated in each panel. Black circles are data from our ATCA/VLA observations. Blue circles are data from the literature which, together with the black circles, were employed to fit the spectral indices. Red circles correspond to values from epochs earlier than the blue and black ones, except for IRAS 18464−0140, where the point at 10 GHz is from a more recent epoch. Thus, these red points were not used in the spectral index fits, since they were obtained at a significantly different epoch. See the text for more details.

surveys mentioned above (red and blue symbols). The black and blue symbols were used in the fits to estimate spectral indices. In the case of the red points, most of them were obtained from an earlier epoch than the blue ones and/or our data. In particular, the red point of IRAS 17487−1922 was reported by VLASS from observations performed on 30/06/2019, which significantly deviates from the observed tendency from the data points of our own VLA observations; the one of IRAS 17494−2645 was discussed by Chapter 3 the one in IRAS 18213−1245A was reported by White et al. (2005); in IRAS 18464−0140 the red point at 5 GHz was reported by White et al. (2005), and that at 10 GHz is from 08/03/2022 (see Section 9.4.1), which is the only one that is from a more recent epoch; in IRAS 18508+0047, the red point at 1.4 GHz was reported by Becker et al. (1994), while those at 5 GHz were reported by White et al. (2005) and Urquhart et al. (2009); the red point in IRAS 19194+1548 was reported by Urquhart et al. (2009). These red points were not used in the spectral index fit, since they consistently show lower flux densities and where obtained at a significantly different time than other data, but are useful to illustrate the variability of the objects. The new OHPN candidates IRAS 16029−5055 and OH 025.646−00.003 are not presented in this figure, since we found only one flux density value available in the literature with no other data in the ATCA and VLA archives, and thus we cannot obtain the spectral index values of these sources.

The radio spectrum of most of the sources identified here seems compatible with free-free emission and, therefore, these sources could be PNe. These indices would further suggest that they are not background galaxies or pulsars, which tend to show negative spectral indices, due to the non-thermal nature of their emission (e.g. Maron et al. 2000). The most noticeable exception is IRAS 18443−0231, for which the obtained α=−0.42±0.05 from our VLA observations between 1-24 GHz is consistent with non-thermal radio continuum emission. This result is robust, since it was obtained from our observations and taken close in time. This source is described in detail in Section 6.C.2.3, providing strong arguments that it is an evolved star, despite its non-thermal radio continuum spectrum.

For some sources, there are indications of a spectral index change along the spectrum, although we cannot always confirm this due to the lack of quasi-simultaneous observations at different frequencies. The study of the turnover frequencies is interesting, since they may reveal some additional information. For example, the turnover between $\alpha\simeq+0.6$ and −0.1 in a nascent PN could indicate that the electron density in the innermost regions falls well below the $n_e \propto r^{-2}$ law. This could happen if there is an inner, non-ionized hole close to the central star (Anglada et al. 2018). Such a central hole is expected, since the PN is the result of ionizing a circumstellar envelope ejected in previous evolutionary phases. The size of such a hole will increase as the PN evolves, causing this turnover frequency to decrease with time. A possible example of such a turnover to optically thin emission ($\alpha\simeq-0.1$) at high frequencies is IRAS 18019−2216. Assuming a turnover frequency of 8 GHz, the radius of this hole would be of $\simeq$12 au $\times$ d for a spherical ionized region surrounding that hole, where d is the distance in kpc from the object (see Eq. 10 of Anglada et al. 2018), a small size that would be consistent with a young PN. On the other hand, a turnover between the optically thick regime ($\alpha\simeq+2$) and the standard $\alpha\simeq+0.6$ expected in nascent PNe may trace the existence of a sharp outer boundary in the ionized nebula. As the ionization front advances in a nascent PN, one could also expect this turnover frequency to decrease over time. Possible sources with this turnover frequency from $\alpha\simeq+2$ to +0.6 are IRAS 18508+0047 and IRAS 19035+0801. However, only in the latter case can our own data, obtained close in time, give more solid support to this change of spectral index.

As mentioned above, the points marked in red in Fig. 6.8 are data from the literature that were not used in the fit of spectral indices because they were obtained at a significantly different epoch than the blue or black ones. In several cases, they clearly depart from the fit. This shows a clear trend of flux density increase with time. This has been found in other confirmed and candidate maser-emitting PNe (e.g. Gómez et al. 2005, and Chapter 3), and has been interpreted as tracking the growth of pristine ionizing regions at the beginning of the PN phase.

Therefore, the combined evidence provided by the spectral indices and variability of the radio continuum emission provides further support that the sources identified in this work are compatible with being nascent PNe.

6.6 Discussion

As a summary after our results in this chapter, in Table 6.2 we report the total number of maser-emitting PNe and candidates identified in this work, together with those previously reported in other works. We have increased the number of confirmed maser-emitting PNe known to nine, while the number of candidates has increased to 16. In addition, we have increased the number of WFs to 18 (Table 6.14), including the first two 'low-velocity' WFs radio continuum emitters.

This increase in candidate maser-emitting PNe is an important step forward, although eventually confirming their nature as bona-fide PNe would be crucial to better understand the nature and properties of this category of sources.

To confirm the identified PN candidates as bona fide maser-emitting PNe, it is first necessary to ascertain the presence of photoionized gas. Considering that these candidates are, in general, optically obscured objects, we suggest that this confirmation can be achieved by means of near- and mid-infrared spectroscopic observations, complemented with a comparison of the observed emission line ratios with diagnostic diagrams that represent photoionization and shock ionization models. A first attempt has been made for some sources in Section 6.5.4. Using several diagnostic diagrams involving different line rations would strongly support whether or not photoionized gas is present in our objects. Furthermore, high-resolution imaging of the emission lines that are used to create diagnostic diagrams, such as those of [Ne II] and [Ne III] shown in Fig. 6.7, should be obtained in order to create spatially resolved maps of emission line ratios across the ionized circumstellar nebula, pinpointing the distribution of the photoionized gas from the PN. In addition, high-resolution imaging of radio and millimeter/submillimeter recombination lines can also reveal whether their kinematics is more consistent with an ionized wind, or with the expansion of a photoionized nebula.

Even if we could confirm as PNe a significant number of the identified candidates, their numbers may still be scarce to draw firm conclusions about important issues such as their

TABLE 6.2: List of all known maser-emitting PNe and candidates.

			Maser emission[a]				References[b]			
Name	Alt. name	Galactic Coordinates	SiO	H_2O	OH	Status[c]	SiO	H_2O	OH	Nature
IRAS 07027−7934	Vo 1	291.375−26.294	–	No	Yes	IP	–	1	TW	2, 3
IRAS 15103−5754	GLMP 405	320.907−00.293	No	Yes	–	IP	4	5	–	5, 6
IRAS 16029−5055	SCHD 68	331.158+00.781	–	–	Yes	IC	–	–	7	TW
IRAS 16333−4807		336.644−00.696	No	Yes	Yes	IP	4	8	9	8, 9
IRAS 16372−4808	SCHD 117	337.064−01.173	No	No	Yes	IC	4	10	11	12
IRAS 17150−3754	PBZ 1	349.351−00.211	–	No	Yes	IC	–	–	13	13
IRAS 17347−3139	RPZM 28	356.801−00.055	No	Yes	Yes	IP	4	14	15	14, 16, 15, TW
IRAS 17371−2747	JaSt 23	000.340+01.574	No	–	Yes	IP	4	–	17	18, 19
IRAS 17375−2759	PBOZ 26	000.208+01.412	–	–	Yes	IC	–	–	20	19, TW
IRAS 17393−2727	OH 0.9+1.3	000.892+01.341	No	–	Yes	IP	4	–	13	13, 21, TW
IRAS 17487−1922	OH 008.9+03.7	008.905+03.712	–	No	Yes	IC	–	TW	TW	TW
IRAS 17494−2645	SCHB 220	002.640−00.191	–	No	Yes	IC	–	TW	22	12, TW
IRAS 18019−2216	SCHB 281	007.958−00.393	–	Yes	Yes	IC	–	TW	23	12, TW
IRAS 18061−2505	MaC 1-10	005.974−02.611	No	Yes	No	IP	4	24	24	24, 25
IRAS 18213−1245A		018.526+00.150	–	Yes	Yes	IC	–	26	27	TW
IRAS 18443−0231	RFS 505	030.234−00.138	–	Yes	No	IC	–	TW	TW	TW
IRAS 18464−0140	OH 31.21−0.18	031.213−00.180	–	Yes	Yes	IC	–	28	28	TW
IRAS 18480+0008		033.023+00.279	–	Yes	Yes	IC	–	TW	27	TW
IRAS 18508+0047	GPSR5 33.906-0.044	033.906−00.043	–	No	Yes	IC	–	TW	27	TW
IRAS 19035+0801	PM 1-279	041.787+00.488	–	No	Yes	IC	–	TW	TW	TW
IRAS 19176+1251	GLMP 898	047.688−00.302	–	No	Yes	IC	–	29	27	TW
IRAS 19194+1548		050.480+00.705	–	No	Yes	IC	–	TW	27	30, TW
IRAS 19219+0947	Vy 2-2	045.498−02.703	No	No	Yes	IP	4	31	32	33, 32
IRAS 19255+2123	K 3-35	056.096+02.094	No	Yes	Yes	IP	4	34	34	35, 34, TW
OH 25.646−0.003		025.646−00.003	–	No	Yes	IC	–	27	TW	TW
OH 341.681+00.264		341.681+00.263	No	–	Yes	IC	4	–	11	12

Notes. [a] –: no interferometric observations available. [b] Reference for the interferometric maser emission detected. In the Nature column, we provide references that have contributed to classifying the source as a PN candidate or confirmed PN. TW: This work. 1. Suárez et al. (2009). 2. Menzies & Wolstencroft (1990). 3. Surendiranath (2002). 4. Cala et al. (2024a). 5. Gómez et al. (2015a). 6. Suárez et al. (2015). 7. Sevenster et al. (1997a). 8. Uscanga et al. (2014). 9. Qiao et al. (2016a). 10. Deacon et al. (2007). 11. Qiao et al. (2016b). 12. Cala et al. (2022). 13. Pottasch et al. (1987). 14. de Gregorio-Monsalvo et al. (2004). 15. Tafoya et al. (2009). 16. Gómez et al. (2005). 17. Sevenster (2002). 18. Jacoby & Van de Steene (2004). 19. Uscanga et al. (2012). 20. Zijlstra et al. (1989). 21. García-Hernández et al. (2007). 22. Qiao et al. (2018). 23. Qiao et al. (2020). 24. Gómez et al. (2008). 25. Miranda et al. (2021). 26. Walsh et al. (2014). 27. Beuther et al. (2019). 28. Forster & Caswell (1999b). 29. Gómez et al. (2015b). 30. Sabin et al. (2014). 31. Gómez et al. (1990). 32. Seaquist & Davis (1983). 33. Vyssotsky et al. (1945). 34. Miranda et al. (2001). 35. Miranda et al. (2000). [c] As defined in Table 6.1. IC: interferometrically confirmed maser-emitting PN candidate. IP: interferometrically confirmed maser-emitting PN.

evolutionary status, or whether they all evolve from stars with similar characteristics (e.g., initial masses, metallicity). It is then important to continue working on increasing the number of known members of this type of sources, for instance, confirming the nature of the identified candidates as PNe (by means of optical and infrared spectroscopy) or undergoing new sensitive mappings of masers in our Galaxy, such as the future Galactic Australian Square Kilometre Array Pathfinder (GASKAP)-OH project (Dawson et al. 2024).

In addition to the scarcity of known maser-emitting PNe, observational biases are also a potential problem to understand properties such as the nature, timescales, or prevalence of maser emission in PNe. Many searches for masers in evolved stars have selected their target samples based on particular infrared properties (e.g. David et al. 1993; te Lintel Hekkert & Chapman 1996), which may leave out many PNe. These biases are being mitigated by the increasing number of published maser surveys, which performed a complete mapping of wide regions throughout the Galactic center and plane (e.g. Walsh et al. 2014; Beuther et al. 2019;

Qiao et al. 2016b, 2018, 2020). Keeping in mind these caveats, the current list of sources can start to provide some interesting patterns, although they will have to be taken with care.

The infrared properties of these maser-emitting sources, as shown in the *MSX* (Fig. 6.4) and *WISE* (Fig. 6.5) color-color diagrams, seem very diverse, as they populate all regions of those diagrams. In principle, this suggests that they do not constitute a homogeneous group and that different types of PNe can give rise to maser emission. However, there are hints of a higher density of sources in certain regions of the color-color diagrams, such as the top right quadrant in Fig. 6.4 and $9 \leq [3.4]-[22] \leq 13$ in Fig. 6.5, probably indicating that PNe with particular properties have a higher tendency to pump masers.

In line with the suggestion of Cala et al. (2024a), we found, apart from the known case of IRAS 17347−3139, one more OHPN (IRAS 17393−2727) and three more OHPN candidates (IRAS 16029−5055, IRAS 17375−2759, and IRAS 19176+1251) that could have mixed chemistry, with O-rich outer envelopes (where OH and H_2O masers are emitted), but with C-rich inner nebulae and/or central stars (see Sect. 6.5.4). Thus, they could potentially be similar to IRAS 07027−7934 and IRAS 18061−2505, which harbor C-rich central stars of the type [WC] (see Zijlstra et al. 1989; Miranda et al. 2021, and Sec. 6.C.1). In general, PNe harboring [WC] have been found surrounded by both O- and C-rich dust (e.g., De Marco & Soker 2002), but only in these PNe does the presence of masers link the [WC] with an O-rich star progenitor in the AGB phase. Hence, these PNe are potentially key in characterizing the formation mechanisms of [WC], which may involve a recent thermal pulse and/or a common envelope (see Ivanova et al. 2013; Zou et al. 2020, and references therein). A common envelope has previously been suggested in the formation and evolution of other maser-emitting PNe (Gómez et al. 2018b; Miranda et al. 2021). In any case, the formation mechanisms of [WC] are still not completely understood (e.g. De Marco & Soker 2002; García-Segura et al. 2018; Hajduk et al. 2020).

In this chapter we have also identified two objects (IRAS 18019−2216 and IRAS 18464−0140) which could be classified as 'low-velocity' WFs because they show bipolar H_2O maser distributions, a velocity coverage of the H_2O masers larger or in a range different from that of the OH masers, but a H_2O maser velocity coverage of only tens of $\mathrm{km\,s^{-1}}$ (Yung et al. 2013; Fan et al. 2024), in contrast to the usual velocity spreads of hundreds of $\mathrm{km\,s^{-1}}$ of classical WFs (Table 6.14). Yung et al. (2013) found that WFs with low velocity masers showed infrared colors suggesting that they are in the late AGB or early post-AGB phases. If this is correct, IRAS 18019−2216 and IRAS 18464−0140 would probably not be PNe, and their radio continuum emission would arise from shock-ionized gas.

6.7 Conclusions

We have undergone an extensive search for new maser-emitting PNe. Our main conclusions are as follows.

- We have increased the number of confirmed maser-emitting PNe known to nine and increased the number of candidates to 16. Furthermore, we have increased the number of known WFs to 18, and reported the first two 'low-velocity' WFs emitters of radio continuum.

- The wide distribution of maser-emitting PNe in the *MSX* and *WISE* color-color diagrams suggests that they do not constitute a homogeneous group and that PNe of different properties may host maser emission during its evolution. However, there is some evidence that PNe with particular infrared properties may have a higher tendency to pump maser emission.

- In addition to the OHPN IRAS 07027−7934 and the H_2OPN IRAS 18061−2505, which had already been shown to host a [WC] central star with an O-rich envelope, we report the presence of PAH emission in one more OHPN (IRAS 17393−2727) and three more OHPN candidates (IRAS 16029−5055, IRAS 17375−2759, and IRAS 19176+1251), suggesting that they may also show mixed chemistry, with C-rich central star or inner circumstellar regions. Together with the OHPN and H_2OPN IRAS 17347−3139, previously reported with PAHs, they could represent an emergent group of PNe that underwent a recent thermal pulse and/or common envelope evolution.

- The new interferometrically confirmed WF IRAS 18443−0231 shows strong and variable non-thermal radio continuum emission, as in magnetized outflows, and near infrared spectroscopy indicates ionized emission compatible with both shocks and photoionization. More research is needed on this object to confirm it as a PN.

Acknowledgments

The Australia Telescope Compact Array is part of the Australia Telescope National Facility (grid.421683.a) which is funded by the Australian Government for operation as a National Facility managed by CSIRO. We acknowledge the Gomeroi people as the traditional owners of the Observatory site. The National Radio Astronomy Observatory is a facility of the National Science Foundation operated under cooperative agreement by Associated Universities, Inc. We used continuum images from the VLA Sky Survey, downloaded from the Canadian Initiative for Radio Astronomy Data Analysis (CIRADA), which is funded by a grant from the Canada Foundation for Innovation 2017 Innovation Fund (Project 35999), as well as by the Provinces of Ontario, British Columbia, Alberta, Manitoba and Quebec. This work has made use of the SIMBAD database, operated at the CDS, Strasbourg, France, and the NASA/IPAC Infrared Science Archive, which is operated by the Jet Propulsion Laboratory, California Institute of Technology, under contract with the National Aeronautics and Space Administration. It also makes use of data products from 2MASS (a joint project of the University of Massachusetts and the Infrared Processing and Analysis Center/California Institute of Technology, funded by NASA and the NSF), AKARI (a JAXA project with the participation of ESA), DENIS (partly funded by the SCIENCE and the HCM plans of the European Commission under grants CT920791 and CT940627), HERSCHEL (Herschel is an ESA space observatory with science instruments provided by European-led Principal Investigator consortia and with important participation from NASA), IRAS (was a joint project of the US, UK and the Netherlands), Pan-STARRS (have been made possible through contributions by the Institute for Astronomy, the University of Hawaii, the Pan-STARRS Project Office, the Max-Planck Society and its participating institutes), *Spitzer* Space Telescope (operated by the Jet Propulsion Laboratory, California Institute of Technology under a contract with NASA), MSX (funded by the Ballistic Missile Defense Organization with additional support from NASA Office of Space Science), UKIDSS (The project is defined in Lawrence et al. (2007) and uses the UKIRT Wide Field Camera (WFCAM; Casali et al. 2007) and a photometric system described in Hewett et al. (2006). The pipeline processing and science archive are described in Hambly et al. (2008)), USNO-B catalog (the construction and contents of the catalog can be found in Monet et al. 2003), VVV survey (is supported by the European Southern Observatory, by BASAL Center for Astrophysics and Associated Technologies PFB-06, by FONDAP Center for Astrophysics 15010003, by the Chilean Ministry for the Economy, Development, and Tourism's Programa Iniciativa Científica Milenio through grant P07-021-F, awarded to The Milky Way Millennium Nucleus), and WISE (a joint project of the University of California, Los Angeles, and the Jet Propulsion Laboratory/California Institute of Technology, funded by the NASA). We also used the VLASS QLimage cutout server at URL cutouts.cirada.ca, operated by the Canadian Initiative for Radio Astronomy Data Analysis (CIRADA). CIRADA is funded by a grant from the Canada Foundation for Innovation 2017 Innovation Fund (Project 35999), as well as by the Provinces of Ontario, British Columbia, Alberta, Manitoba and Quebec, in collaboration with the National Research Council of Canada, the US National Radio Astronomy Observatory and Australia's Commonwealth Scientific and Industrial Research Organisation. This work made use of Astropy:[2] a community-developed core Python package and an ecosystem of tools and resources for astronomy (Astropy Collaboration et al. 2013, 2018, 2022). RAC, JFG, LFM, GA are financially supported by grants PID2020-114461GB-I00, PID2023-146295NB-I00, and CEX2021-001131-S, funded by MCIN/AEI /10.13039/501100011033. RAC also acknowledges support by the predoctoral grant PRE2018-085518, funded by MCIN/AEI/ 10.13039/501100011033 and by ESF Investing in your Future. K.O. acknowledges the support of the Agencia Nacional de Investigación Científica y Desarrollo (ANID) through the FONDECYT Regular grant 1240301.

[2]http://www.astropy.org

6.A Parameters of the ATCA and VLA observations

Table 6.3 shows the final list of observed targets, as well as the main parameters of our radio interferometric observations.

TABLE 6.3: Parameters of the ATCA/VLA observations.

Target name	Date	Band	Phase calibrator	Synthesized beam[a] (arcsec)	(deg)	rms[b] (mJy beam^{-1})	Telescope
IRAS 07027−7934	2020/10/19	L	PKS 0606-796	5.2 × 3.3	+72	13	ATCA
IRAS 14079−6402	2020/10/19	L	PMN J1355-6326	6.1 × 3.0	−22	42	ATCA
IRAS 14086−6907	2020/10/19	L	PMN J1355-6326	5.9 × 3.0	−22	45	ATCA
IRAS 15559−5546	2020/10/19	L	PMN J1650-5044	6.1 × 3.3	−40	34	ATCA
IRAS 16280−4008	2020/10/19	L	PMN J1650-5044	8.5 × 3.5	−42	29	ATCA
IRAS 17180−2708	2020/10/20	L	PKS 1657-261	8.0 × 3.6	−5	59	ATCA
	2021/04/03	L	J1700-2610	107 × 32	−21	39	VLA
	2021/04/01	K	J1700-2610	6.2 × 2.2	−23	9	VLA
IRAS 17221−3038	2020/10/20	L	PMN J1733-3722	7.9 × 3.4	−4	38	ATCA
IRAS 17253−2824	2020/10/20	L	PKS 1657-261	7.5 × 3.7	+5	33	ATCA
	2021/04/03	L	J1700-2610	110 × 31	−18	23	VLA
	2021/04/01	K	J1700-2610	6.4 × 2.1	−21	7	VLA
IRAS 17374−2700	2020/10/20	L	PKS 1657-261	8.6 × 3.4	−8	33	ATCA
	2021/04/03	L	J1700-2610	118 × 30	−22	24	VLA
	2021/04/01	K	J1700−2610	6.0 × 2.1	−20	8	VLA
IRAS 17385−2211	2020/10/20	L	1808-209	9.0 × 3.4	−1	16	ATCA
	2021/04/03	L	J1700-2610	89 × 32	−20	23	VLA
	2021/04/01	K	J1733-1304	4.9 × 2.5	−13	13	VLA
IRAS 17403−2107	2020/10/20	L	1808-209	9.6 × 3.3	−2	40	ATCA
	2021/04/03	L	J1700-2610	83 × 33	−14	38	VLA
	2021/04/01	K	J1733-1304	4.6 × 2.2	−13	11	VLA
IRAS 17487−1922	2020/10/20	L	1808-209	12.6 × 3.3	−2	80	ATCA
	2021/04/03	L	J1700-2610	79 × 39	−15	10	VLA
	2021/04/01	K	J1733-1304	4.3 × 2.2	−12	12	VLA
IRAS 17494−2645	2021/04/01	K	J1820-2528	5.8 × 2.2	−20	8	VLA
IRAS 18019−2216	2021/04/01	K	J1820-2528	5.1 × 2.2	−20	10	VLA
IRAS 18243−1048	2020/10/19	L	1819-096	18.8 × 3.7	−1	12	ATCA
IRAS 18271−1014	2020/10/19	L	1819-096	20.3 × 3.5	0	11	ATCA
	2021/04/03	L	J1700-2610	63 × 33	−18	20	VLA
	2021/04/01	K	J1832-1035	3.9 × 2.4	−17	9	VLA
IRAS 18295−2510	2020/10/20	L	1808-209	9.6 × 3.4	−7	39	ATCA
	2021/04/03	L	J1700-2610	99 × 31	−19	60	VLA
	2021/04/01	K	J1820-2528	5.2 × 2.2	−15	14	VLA
OH 25.646−0.003	2021/03/25	K	J1832-1035	3.7 × 2.4	−26	12	VLA
IRAS 18443−0231	2021/04/03	L	J1822-0938	52 × 35	0	75	VLA
	2021/03/25	K	J1851+0035	4.2 × 3.3	−14	8	VLA
IRAS 18480+0008	2021/03/25	K	J1851+0035	3.4 × 2.4	−23	7	VLA
IRAS 18508+0047	2021/03/25	K	J1851+0035	3.4 × 2.4	−21	12	VLA
IRAS 18551+0159	2021/04/03	L	J1822-0938	51 × 33	−11	70	VLA
	2021/03/25	K	J1851+0035	3.3 × 2.4	−21	14	VLA
IRAS 19035+0801	2020/10/19	L	1910+052	30.2 × 3.4	0	10	ATCA
	2021/03/25	L	J1925+2106	49 × 35	−6	27	VLA
	2021/03/25	K	J1851+0035	3.1 × 2.4	−21	13	VLA
IRAS 19123+1139	2020/10/19	L	1910+052	30.2 × 3.4	0	29	ATCA
	2021/03/25	L	J1925+2106	47 × 35	−6	75	VLA
	2021/03/25	K	J1924+1540	2.9 × 2.4	−17	12	VLA
IRAS 19127+1717	2020/10/19	L	1910+052	25.8 × 3.2	+2	20	ATCA
	2021/03/25	L	J1925+2106	46 × 36	−3	30	VLA
	2021/03/25	K	J1924+1540	2.8 × 2.4	−13	11	VLA
IRAS 19194+1548	2021/03/25	K	J1924+1540	2.8 × 2.4	−14	11	VLA
IRAS 19200+1035	2020/10/19	L	1910+052	22.7 × 3.4	0	30	ATCA
	2021/03/25	L	J1925+2106	48 × 35	−7	30	VLA
	2021/03/25	K	J1924+1540	3.0 × 2.4	−15	12	VLA
IRAS 19508+2659	2021/03/25	K	J2023+3153	3.5 × 2.6	−71	12	VLA
IRAS 20266+3856	2021/04/03	L	J2025+3343	43 × 33	+27	70	VLA
	2021/03/25	K	J2015+3710	3.7 × 2.5	−83	15	VLA

Notes. [a] Major and minor axes and position angle of the synthesized beam of continuum images. [b] Noise level, measured at the channel map with the weakest maser. If there is no detection, measured at the position and channel map with the V_{LSR} of the reported OH maser from single-dish observations.

6.B Further details of our results

6.B.1 Targets with positional association between maser and radio continuum in our ATCA/VLA observations

In Table 6.4 we show the interferometric positions of the radio continuum and maser emission of the matches we found, as well as the angular distance between the two types of emission (δ). In some cases, these spatial matches were obtained from the positions reported in literature data. Moreover, our interferometric ATCA/VLA observations allowed us to upgrade the status of several of the sources labeled SC or SP in Table 6.1 to either IC or IP. In order to report the specific maser species involved, IP sources (confirmed maser-emitting PNe) are shown in Table 6.4 as OHPNe and/or H_2OPNe in the "nature" column. For IC sources (candidate maser-emitting PNe) we use the same labels, but enclosed by parentheses. Similarly, we label water fountain sources as WF, and WF candidates as WF, but enclosed by parenthesis.

6.B.2 Details of individual maser components

In Tables 6.5 to 6.11 we present the parameters of the spectral components of masers, in the sources where there is more than one such component. In sources with a single maser component, relevant information is already given in Table 6.4. For each maser component, we indicate its position (right ascension and declination), their positional uncertainties ($\delta_{\rm R.A.}$, $\delta_{\rm dec}$), the observed transition (H_2O at 22235 MHz, or OH at 1612, 1665, 1667, and 1720 MHz), LSR velocity ($V_{\rm LSR}$) in $\rm km\,s^{-1}$, and peak flux density (S_ν) in Jy. In most cases, the masers components in these tables were obtained from the observations reported in this chapter, but we have also added values from the literature, when relevant.

We note that the reported positional uncertainties are those obtained with a fit of an elliptical Gaussian to the image of the channel with the peak emission of each component. These are to be understood as relative errors among the components of an individual maser transition and observational epoch. To compare positions between different epochs and transitions, one should consider the uncertainties in absolute astrometry, which are typically on the order of 10% of the synthesized beam.

6.B.3 Targets without positional association between maser and radio continuum in our ATCA/VLA observations

In Table 6.12 we report the cases for which maser and continuum emission were both detected in our field of view, but their position did not match, and a careful analysis indicates that the emission of each type arises from different sources, and thus we can discard them as

TABLE 6.4: Characteristics of the radio continuum, H_2O and OH maser emission of the new maser-emitting PNe and candidates studied in this Chapter.

Source	Radio continuum emission Position RA, DEC (J2000)	Frequency (GHz)	Flux density (mJy)	Maser emission Position RA, DEC (J2000)	Transition	δ^a ($''$)	Flux density (Jy)	Nature[b]
From our observations								
IRAS 07027−7934	06:59:26.327 −79:38:47.02	2.1	5.37±0.28	06:59:26.273 −79:38:46.99	OH 1612 MHz	0.15±0.04	0.602±0.016	OHPN
IRAS 17487−1922	17:51:44.868 −19:23:42.26	2.1	0.68±0.18	17:51:44.981 −19:23:40.21	OH 1612 MHz	2.6±1.8	0.44±0.07	(OHPN)
		1.5	<1.45	17:51:44.645 −19:23:38.67	OH 1612 MHz	5±9	0.52±0.05	
IRAS 18443−0231	18:47:00.4017 −02:27:52.573	22.2	226.3±0.4	18:47:00.4012 −02:27:52.552	H_2O 22 GHz	0.022±0.009	9.80±0.03	(H_2OPN), WF
IRAS 19035+0801	19:05:56.436 +08:06:56.88	2.1	2.63±0.22	19:05:56.413 +08:06:57.86	OH 1612 MHz	1.0±0.4	0.364±0.019	(OHPN)
		1.5	0.93±0.09	19:05:56.289 +08:06:56.17	OH 1612 MHz	2.3±5.9	0.857±0.019	
From our observations and the literature								
IRAS 18019−2216[c]	18:04:57.359 −22:15:50.84	22.2	0.583±0.018	18:04:57.347 −22:15:50.91	H_2O 22 GHz	0.18±0.26	0.332±0.010	(H_2OPN), WF
IRAS 18480+0008[d]	18:50:36.659 +00:12:28.25	3.0	1.90±0.22	18:50:36.685 +00:12:28.34	OH 1665 MHz	0.4±1.9	0.116±0.009	(OHPN)
	18:50:36.659 +00:12:28.13	22.2	2.020±0.013	18:50:36.6614 +00:12:28.191	H_2O 22 GHz	0.071±0.020	1.957±0.014	(H_2OPN), (WF)
From the literature								
IRAS 16029−5055	16:06:40.60 −51:03:57.2	5.5	3.02±0.15	16:06:40.637 −51:03:55.73	OH 1612 MHz	1.5±0.9	1.31±0.13	(OHPN)
IRAS 18213−1245A	18:24:09.722 −12:43:22.84	4.8	3.6±0.8	18:24:09.727 −12:43:23.90	OH 1665 MHz	1.1±1.0	0.139±0.005	(OHPN)
				18:24:09.706 −12:43:24.04	H_2O 22 GHz	1.22±1.41	3.70±0.04	(H_2OPN)
IRAS 18464−0140	18:48:56.647 −01:36:42.98	3.0	4.8±0.4	18:48:56.523 −01:36:43.32	OH 1612 MHz	1.9±1.9	1.749±0.021	(OHPN)
				18:48:56.62 −01:36:44.3	OH 1665 MHz	1.4±1.7	0.500±0.010	
				18:48:56.523 −01:36:42.99	OH 1667 MHz	1.9±1.5	1.90±0.010	
				18:48:56.65 −01:36:43.04	H_2O 22 GHz	0.1±0.4	16.11±0.14	(H_2OPN), WF
IRAS 18508+0047	18:53:22.196 +00:50:49.03	1.4	2.58±0.22	18:53:22.29 +00:50:48.46	OH 1612 MHz	1.5±1.9	0.529±0.005	(OHPN)
IRAS 19176+1251	19:19:55.744 +12:57:37.70	1.5	3.01±0.28	19:19:55.850 +12:57:37.80	OH 1720 MHz	1.6±0.4	0.115±0.003	(OHPN)
IRAS 19194+1548	19:21:40.374 +15:53:55.16	1.5	3.23±0.26	19:21:40.514 +15:53:54.74	OH 1612 MHz	2.1±1.2	0.917±0.008	OHPN
				19:21:40.286 +15:53:46.39	OH 6035 MHz	8.86±1.12	4.80±0.11	
OH 25.646−0.003	18:38:06.242 −06:28:51.22	5.0	2.21±0.04	18:38:06.165 −06:28:54.10	OH 1612 MHz	3.1±1.9	0.254±0.005	(OHPN)

Notes. [a] Relative distance between the radio continuum emission peak and the maser spot. [b] In parenthesis sources candidates to PN or candidate to WF. WF: water fountain characteristics. [c] This source is a previously reported OHPN candidate (Chapter 3) [d] The flux density at 3 GHz was reported in VLASS (Gordon et al. 2021), and the 1665 MHz emission was reported in THOR (Beuther et al. 2019).

Table 6.5: OH maser emission in our ATCA observations of IRAS 07027−7934.

Maser coordinates R.A.(J2000)	Dec(J2000)	$\delta_{\mathrm{R.A.}}$ (arcsec)	δ_{dec} (arcsec)	Transition (MHz)	V_{LSR} (km s^{-1})	S_ν (Jy)
06:59:26.273	−79:38:46.99	0.04	0.05	1612	−46.45	0.646±0.027
06:59:26.780	−79:38:47.54	0.22	0.21	1612	−40.28	0.30±0.04
06:59:25.218	−79:38:49.04	0.24	0.24	1612	−41.37	0.173±0.031

Table 6.6: OH maser emission in our ATCA and VLA observations of IRAS 17487−1922

Maser coordinates R.A.(J2000)	Dec(J2000)	$\delta_{\mathrm{R.A.}}$ (arcsec)	δ_{dec} (arcsec)	Transition (MHz)	V_{LSR} (km s^{-1})	S_ν (Jy)
17:51:44.89120	−19:23:46.8	0.0020	0.4	1612	−39.18	0.39±0.07
17:51:44.79420	−19:23:46.66	0.0013	0.20	1612	−39.00	0.41±0.04
17:51:44.9810	−19:23:41.91	0.015	0.24	1612	−38.82	0.44±0.05
17:51:44.91960	−19:23:40.9	0.0019	0.4	1612	−38.64	0.44±0.09
17:51:44.8501	−19:23:46.8	0.004	0.6	1612	−38.37	0.345±0.011
17:51:44.98140	−19:23:40.21	0.0020	0.31	1612	−38.10	0.44±0.07
17:51:45.12	−19:23:42.9	0.4	0.4	**1612**	−38.15	0.58±0.05
17:51:44.711	−19:23:43.41	0.21	0.21	**1612**	−39.06	0.48±0.08
17:41:45.36	−19:23:42.0	0.3	0.4	**1612**	−39.60	0.38±0.04

The VLA observations are marked with the frequency of the transition in boldface. The ones with normal font represent the ATCA observations.

Table 6.7: H_2O maser emission in our VLA observations of IRAS 18019−2216.

Maser coordinates R.A.(J2000)	Dec(J2000)	$\delta_{\mathrm{R.A.}}$ (arcsec)	δ_{dec} (arcsec)	Transition (MHz)	V_{LSR} (km s^{-1})	S_ν (Jy)
18:34:57.3719	−22:15:50.65	0.005	0.24	22235	−10.11	0.194±0.017
18:34:57.3520	−22:15:50.8	0.013	0.4	22235	−4.63	0.111±0.020
18:34:57.3472	−22:15:50.92	0.006	0.21	22235	−1.47	0.222±0.013
18:34:57.3511	−22:15:50.23	0.005	0.18	22235	+3.37	0.167±0.013
18:34:57.3468	−22:15:50.91	0.003	0.11	22235	+5.90	0.332±0.010
18:34:57.3365	−22:15:51.17	0.004	0.14	22235	+8.01	0.247±0.008

Table 6.8: H_2O maser emission (our VLA observations) and OH (from the literature) maser emission of IRAS 18480+0008.

Maser coordinates R.A.(J2000)	Dec(J2000)	$\delta_{\mathrm{R.A.}}$ (arcsec)	δ_{dec} (arcsec)	Transition (MHz)	V_{LSR} (km s^{-1})	S_ν (Jy)
18:50:36.685	+00:12:28.34	0.10	0.10	1665	+12.00	0.345±0.009
18:50:36.66107	+00:12:28.140	0.0009	0.020	22235	+14.53	1.026±0.011
18:50:36.6635	+00:12:28.21	0.003	0.05	22235	+18.75	0.244±0.007
18:50:36.6720	+00:12:28.41	0.017	0.17	22235	+20.22	0.110±0.012
18:50:36.66141	+00:12:28.191	0.0004	0.007	22235	+22.54	1.9844±0.0008
18:50:36.66040	+00:12:28.07	0.0013	0.03	22235	+25.07	0.690±0.010
18:50:36.66330	+00:12:28.147	0.0010	0.020	22235	+26.54	0.782±0.009

The parameters of the OH maser transition at 1665 MHz were reported by Beuther et al. (2019).

Table 6.9: H_2O maser emission in our VLA observations of IRAS 18443−0231.

Maser coordinates R.A.(J2000)	Dec(J2000)	$\delta_{R.A.}$ (arcsec)	δ_{dec} (arcsec)	Transition (MHz)	V_{LSR} (km s^{-1})	S_ν (Jy)
18:47:00.4421	−02:27:54.0	0.014	0.8	22235	−28.49	0.048±0.009
18:47:00.380	−02:27:53.7	0.03	0.5	22235	−17.11	0.055±0.012
18:47:00.40411	−02:27:52.552	0.0005	0.010	22235	−10.37	2.458±0.013
18:47:00.40336	−02:27:52.591	0.0003	0.007	22235	−9.32	3.875±0.014
18:47:00.4049	−02:27:52.54	0.005	0.09	22235	−6.37	0.234±0.012
18:47:00.40182	−02:27:52.587	0.0005	0.011	22235	−4.90	1.796±0.010
18:47:00.40120	−02:27:52.552	0.00016	0.004	22235	−3.42	9.826±0.018
18:47:00.4069	−02:27:52.56	0.003	0.06	22235	+0.16	0.315±0.009
18:47:00.4165	−02:27:52.03	0.009	0.23	22235	+1.42	0.098±0.012
18:47:00.4044	−02:27:52.60	0.006	0.12	22235	+2.47	0.14±0.08
18:47:00.4004	−02:27:52.56	0.003	0.05	22235	+5.05	0.390±0.012
18:47:00.40080	−02:27:52.472	0.0004	0.009	22235	+5.84	2.370±0.011
18:47:00.41120	−02:27:52.46	0.0017	0.04	22235	+7.74	0.543±0.011
18:47:00.41020	−02:27:52.53	0.0018	0.04	22235	+9.64	0.572±0.011
18:47:00.41332	−02:27:52.43	0.0015	0.03	22235	+11.54	0.653±0.010
18:47:00.40773	−02:27:52.58	0.0013	0.03	22235	+12.80	0.681±0.010
18:47:00.4208	−02:27:52.37	0.007	0.12	22235	+31.76	0.144±0.010
18:47:00.3810	−02:27:52.9	0.011	0.4	22235	+43.98	0.103±0.011
18:47:00.40251	−02:27:52.58	0.0017	0.04	22235	+48.61	0.488±0.010

Table 6.10: H_2O and OH maser emission of IRAS 18213−1245A (from the literature).

Maser coordinates R.A.(J2000)	Dec(J2000)	$\delta_{R.A.}$ (arcsec)	δ_{dec} (arcsec)	Transition (MHz)	V_{LSR} (km s^{-1})	S_ν (Jy)
18:24:09.73	−12:43:23.727	0.20	0.10	1665	+27.00	0.139±0.005
18:24:09.71	−12:43:23.96	8.7	1.36	22235	+23.60	3.70±0.05
18:24:09.71	−12:43:24.04	9.6	1.36	22235	+21.70	0.75±0.05

The H_2O masers were reported in HOPS (Walsh et al. 2014), and the OH masers in THOR (Beuther et al. 2019).

Table 6.11: H_2O and OH masers in IRAS 18464−0140.

Maser coordinates R.A.(J2000)	Dec(J2000)	$\delta_{R.A.}$ (arcsec)	δ_{dec} (arcsec)	Transition (MHz)	V_{LSR} (km s^{-1})	S_ν (Jy)
18:48:56.523	−01:36:43.32	0.20	0.20	1612	−28.10	1.749±0.021
18:48:58.62	−01:36:44.3	0.1	0.1	1665	−28.90	0.350±0.020
18:48:52.72	−01:36:44.3	0.1	0.1	1665	−29.45	0.500±0.010
18:48:56.52	−01:36:43.0	0.4	0.4	1667	−29.00	0.377±0.010
18:48:56.680580	−01:36:42.6796	0.00020	0.0025	22235	−37.89	34.85±0.17
18:48:56.6914	−01:36:42.72	0.014	0.13	22235	−28.68	1.01±0.20
18:48:56.65030	−01:36:43.040	0.0013	0.013	22235	−11.56	5.71±0.22
18:48:56.6462	−01:36:43.04	0.004	0.03	22235	−6.29	2.56±0.21

The 1612 and 1667 MHz OH maser emission were reported in THOR (Beuther et al. 2019). The 1665 MHz OH maser positions are taken from Forster & Caswell (1999b) and are given in B1950 coordinates. The H_2O maser emission was initially reported by Forster & Caswell (1999b), but we reprocessed it completely, including normal calibration and self-calibration. The values given in this table correspond to those we obtained after this reprocessing.

possible maser-emitting PNe. Each of these sources are described in the subsections 6.B.3.1 to 6.B.3.6 of this appendix.

Table 6.13 shows the sources in which continuum and/or maser emission was not detected. Given the possible variability of the sources, in those cases we cannot discard nor confirm that the previously reported emission of these types was actually associated, but one or both of them fell below our sensitivity threshold. We note that we also included the source OH 25.646−0.003 in that table, although it is a confirmed OHPN candidate, but we show there our non-detection of H_2O masers at 22 GHz, and of continuum emission around that frequency.

6.B.3.1 The field of IRAS 14086−6907

OH maser emission was first reported toward IRAS 14086−6907 from single-dish observations by te Lintel Hekkert et al. (1991). Radio continuum emission (source RACS-DR1 J141249.8-692104) was detected with the ASKAP interferometer near this object (Hale et al. 2021). The radio continuum position is $\sim 7''$ away from the source 2MASS J14125041-6921092, which is the near-infrared counterpart of IRAS 14086−6907. We have detected both OH masers and radio continuum emission in our interferometer observations. We confirm that the OH maser emission is associated with the AGB star IRAS 14086−6907 (Lebzelter et al. 2023), and is indeed separated from the continuum emission by $\sim 7''$. The parallax of the Gaia source associated with IRAS 14086−6907 (Gaia DR3 5846602400091413632) indicates it is at a distance of $\simeq$ 1 kpc. The separation of the radio continuum emission would correspond to 7000 au at this distance. We can confidently discard that the presence of this radio continuum emission could indicate that IRAS 14086−6907 is a PN, since we would not expect unresolved radio continuum emission that far away from the central star without any hint of emission closer to it. The nature of the radio continuum emission is unknown, but it is probably associated to an extragalactic object, since it is brighter at 887.5 MHz (Hale et al. 2021) than at 1367.5 MHz (Duchesne et al. 2024), suggesting non-thermal emission. A possible optical counterpart for the radio continuum source is Gaia DR3 5846602404392109312.

6.B.3.2 The field of IRAS 15559−5546

IRAS 15559−5546 (Hen 2-142) has been spectroscopically classified as a PN (Frew et al. 2013). OH maser emission with a double-peaked spectral profile has been reported in its neighborhood with single-dish observations (te Lintel Hekkert et al. 1991). We have detected both radio continuum and OH maser emission within the observed field, with a separation between them of ∼2.4 arcmin. The radio continuum emission is clearly associated with the PN IRAS 15559−5546, while the OH masers are emitted by IRAS 15557−5546 (Sevenster et al. 1997a), which has been previously classified as an AGB star (Sevenster 2002). We did not detect any radio continuum emission from IRAS 15557−5546.

6.B.3.3 The field of IRAS 17385−2211

IRAS 17385−2211 has been spectroscopically classified as PN (Frew et al. 2013). Double-peaked 1612 MHz OH maser emission was reported in its neighborhood based on single-dish observations (te Lintel Hekkert et al. 1991). We have detected the radio continuum emission from the PN. However, the position of the OH maser emission coincides with that of IRAS 17388−2203, which has been spectroscopically classified as a post-AGB star (Suárez et al. 2006), and it is ∼8.3 arcmin away from IRAS 17385−2211. We confirm the association of OH maser emission from this post-AGB star for the first time. The maser spectrum displays multiple emission features, whose velocities coincide with those seen in the single-dish spectrum reported by te Lintel Hekkert et al. (1991). We did not detect any radio continuum emission at 2.1 GHz from IRAS 17388−2203.

6.B.3.4 The field of IRAS 18243−1048

Double-peaked 1612 MHz OH maser emission was reported by single-dish observations towards IRAS 18243−1048 (te Lintel Hekkert et al. 1991). There is a radio continuum source located ∼ 20" away from this infrared source, whose emission has been reported at different frequencies (e.g., Condon et al. 1998; Purcell et al. 2013), and that lies within the beam of the OH single-dish observations. Our interferometric observations detect both the OH maser and radio continuum emission in the field, and we can confirm that the OH maser emission is indeed associated with IRAS 18243−1048 (2MASS J18270824-1046099), ∼ 20" away from the radio continuum source. The position of the latter is located next (∼ 2" away) to a different infrared source in 2MASS (source 2MASS J18270688-1046087) and Spitzer (source SSTGLMC G020.5893+00.4247) images, with no extended emission connecting it with IRAS 18243−1048.

6.B.3.5 The field of IRAS 18295−2510

IRAS 18295−2510 (NGC 6644) is a spectroscopically classified PN (e.g., Frew et al. 2013). The possible association of this PN with OH maser emission at 1612 MHz had been previously suggested by Zijlstra et al. (1989), based on single-dish observations. We have detected the radio continuum emission from the the PN. We also found double-peaked OH maser emission in the field, but it arises from a different source, IRC 20491, located $\simeq 2'$ away from NGC 6644.

6.B.3.6 The field of IRAS 19200+1035

Double-peaked 1612 MHz OH maser-emission has been reported towards IRAS 19200+1035 based on single-dish observations (Eder et al. 1988). The position of this source (associated to 2MASS 19222483+1040506) lies $\sim 41''$ away from the spectroscopically confirmed PN K 3-33, so both objects fall within the beam of the OH maser observations. In our data, we have detected the radio continuum emission from the PN. We have also detected OH maser emission in the field, but it is not associated with either PN K 3-33 or IRAS 19200+1035, but with the source IRAS 19201+1040 (2MASS J19222916+1046200) instead, an object which is ∼5 arcmin away from PN K 3-33. This same double-peaked OH maser emission has also been reported in IRAS 19201+1040 (e.g., Lewis 1994), and ours is the first interferometric detection of this emission, which allows us to properly associate it to IRAS 19201+1040, rather than to IRAS 19200+1035. We have not detected any radio continuum emission from IRAS 19201+1040.

6.C Details on individual sources with association between maser and continuum emission

6.C.1 The OHPN IRAS 07027−7934: interferometric determination of maser positions in our observations

This source is the spectroscopically confirmed PN Vo 1 (Menzies & Wolstencroft 1990; Surendiranath 2002). OH observations with the 26-m Hartebeeshoek (beam=0.5°; Zijlstra et al. 1991) and the 64-m Parkes antennas (beam=13′; te Lintel Hekkert et al. 1991) show a symmetric double peak at 1612 MHz, with flux densities of $S_\nu \simeq 10$ Jy beam^{-1} and $V_{\rm LSR}\simeq -40$ and -47 km s^{-1}, as well as a single-peaked spectrum at 1667 MHz ($S_\nu \simeq 2$ Jy beam^{-1}, $V_{\rm LSR}\simeq -51$ km s^{-1}). Suárez et al. (2009) did not detect any H_2O maser emission in this source in spectra taken with the Parkes antenna (rms=0.22 Jy beam^{-1}). Despite the reported OH detections were carried out with single-dish antenna, Zijlstra et al. (1991) indicated that the Parkes beam was sufficiently small (13′) that the chance of confusion with other sources is negligible, given the high galactic latitude of IRAS 07027−7934. The LSR velocities of the reported OH maser components, ranging between −51 and −40 km s^{-1}, are blueshifted with respect to the systemic velocity of the source, traced by the CO peak (with $V_{\rm LSR} \simeq -27$ and -22 km s^{-1}; Loup et al. 1990; Zijlstra et al. 1991), and they are actually close to the blueshifted edge of the observed CO spectrum ($\simeq -40$ km s^{-1}). While double-peaked OH spectra in AGB stars have mean velocities coinciding with the stellar one, the blueshifted bias of maser emission seen in this source is a commonly observed trend in maser-emitting PNe (Uscanga et al. 2012).

In our interferometric ATCA observations, we detected maser emission at 1612 MHz (Fig. 6.2), but not at 1667 MHz (rms=13 mJy beam^{-1}). The LSR velocities of the observed maser components (Fig. 6.1; Table 6.5) are similar to the 1612 MHz OH masers previously reported. However, the symmetric double peak spectrum of the 1612 MHz line has changed and is now clearly asymmetric, and has faded by a factor of $\simeq 20$. This fading correlates with the one of the maser at 1667 MHz, whose non-detection indicates a weakening of at least a factor of 50. The positional accuracy of our ATCA data does not allow us to determine the spatial distribution of the OH masers.

TABLE 6.12: Sources with discarded association in our ATCA/VLA observations.

Radio continuum emission				Maser emission			
Source name	Position RA, DEC (J2000)	Flux density[a] (mJy)	Frequency (GHz)	Source name	Position RA, DEC (J2000)	Flux density[b] (Jy)	Transition
RACS-DR1 J141249.8−69210	14:12:50.756 −69:21:03.56	48.6±0.7	2.1	IRAS 14086−6907	14:12:50.393 −69:21:09.75	5.61±0.04	OH 1612 MHz
IRAS 15559−5546	15:59:57.644 −55:55:33.24	69.3±1.8	2.1	IRAS 15557−5546	15:59:41.667 −55:54:51.21	1.49±0.06	OH 1612 MHz
IRAS 17385−2211	17:41:36.590 −22:13:03.90	0.68±0.09	2.1	IRAS 17388−2203	17:41:48.979 −22:05:17.03	2.56±0.05	OH 1612 MHz
		<1.0	1.5		17:41:48.963 −22:05:15.27	2.53±0.03	OH 1612 MHz
	17:41:36.610 −22:13:03.37	0.70±0.05	24			<42	H_2O 22 GHz
GPSR 020.590+0.425	18:27:07.018 −10:46:08.70	20.2±1.0	2.1	IRAS 18243−1048	18:27:08.273 −10:46:06.93	0.92±0.04	OH 1612 MHz
NGC 6644	18:32:34.682 −25:07:44.15	13.0±0.3	2.1	IRC −20491	18:32:07.675 −24:57:18.95	3.084±0.05	OH 1612 MHz
	18:32:34.687 −25:07:44.27	79.2±1.6	1.5		18:32:07.675 −24:57:18.85	3.09±0.04	OH 1612 MHz
	18:32:34.689 −25:07:44.18	78.0±0.4	24			<42	H_2O 22 GHz
K 3-33	19:22:26.694 +10:41:23.19	13.0±0.3	2.1	IRAS 19201+1040	19:22:29.168 +10:46:21.62	1.23±0.05	OH 1612 MHz
	19:22:26.669 +10:41:21.06	10.7±0.5	1.5		19:22:29.172 +10:46:21.00	2.56±0.05	OH 1612 MHz
	19:22:26.645 +10:41:20.30	15.34±0.08	24			<36	H_2O 22 GHz

Notes. [a] For sources in which radio continuum emission is not detected, we report the $3\,\sigma$ upper limit to the intensity (in mJy beam^{-1}). [b] For sources in which maser emission is not detected, we also report the $3\,\sigma$ upper limit, using the noise level (in mJy beam^{-1}), measured at the position and channel map with the $V_{\rm LSR}$ of the reported OH maser from single-dish observations.

Table 6.13: Sources with undetected continuum and/or maser emission in our ATCA/VLA observations.

Target name	Date	Continuum[a]		Maser[b]	Telescope	Association[c]
		Frequency (GHz)	Flux density (mJy)	Flux density (mJy)		
IRAS 14079−6402	2021/10/19	2.1	1.81±0.16	<39	ATCA	UM
IRAS 16280−4008	2021/10/19	2.1	615.3±1.5	<87	ATCA	UM
IRAS 17180−2708	2021/10/20	2.1	265.0±0.3	<177	ATCA	UM
	2021/04/03	1.5	268.6±1.8	<117	VLA	UM
	2021/04/01	24	174.9±1.6	<27	VLA	UM
IRAS 17221−3038	2021/10/20	2.1	8.60±0.13	<114	ATCA	UM
IRAS 17253−2824	2021/10/20	2.1	<0.19	171±20	ATCA	UC
	2021/04/03	1.5	<2.0	224±14	VLA	UC
	2021/04/01	24	<0.04	<20.1	VLA	UC, UM
IRAS 17374−2700	2021/10/20	2.1	<0.18	<99	ATCA	UC, UM
	2021/04/03	1.5	<1.12	<72	VLA	UC, UM
	2021/04/01	24	<0.04	<24	VLA	UC, UM
IRAS 17403−2107	2021/10/20	2.1	11.26±0.16	<120	ATCA	UM
	2021/04/03	1.5	11.8±0.5	<114	VLA	UM
	2021/04/01	24	7.79±0.09	<33	VLA	UM
IRAS 18271−1014	2021/10/19	2.1	1.5±0.4	<33	ATCA	UM
	2021/04/03	1.5	<3	<60	VLA	UM
	2021/04/01	24	1.95±0.09	<18	VLA	UM
OH 25.646−0.003[d]	2021/03/25	24	<0.08	<36	VLA	UC, UM
IRAS 18551+0159	2021/04/03	1.5	143±5	<210	VLA	UM
	2021/03/25	24	189.6±0.4	<42	VLA	UM
IRAS 19123+1139	2021/10/19	2.1	29.5±1.0	<87	ATCA	UM
	2021/03/25	1.5	33±3	<237	VLA	UM
	2021/03/25	24	17.09±0.11	<36	VLA	UM
IRAS 19127+1717	2021/10/19	2.1	0.79±0.16	<60	ATCA	UM
	2021/03/25	1.5	2.2±0.4	<90	VLA	UM
	2021/03/25	24	5.94±0.05	<33	VLA	UM
IRAS 19508+2659	2021/03/25	24	<0.06	565±11	VLA	UC
IRAS 20266+3856	2021/04/03	1.5	<4	1336±180	VLA	UC
	2021/03/25	24	<0.06	<45	VLA	UC, UM

Notes. [a] For sources in which radio continuum emission is not detected, we report the $3\,\sigma$ upper limit to the intensity (in mJy beam^{-1}). [b] For sources in which maser emission is not detected, we also report the $3\,\sigma$ upper limit, using the noise level (in mJy beam^{-1}), measured at the position and channel map with the $V_{\rm LSR}$ of the reported OH maser from single-dish observations. [c] UC: undetected continuum emission. UM: undetected maser emission. [d] This object is a new OHPN candidate, but we have included it in this table because we did not detect any H_2O maser nor radio continuum emission in our VLA observations (see Appendix 6.C.3.6).

Our map of radio continuum emission at 2.1 GHz shows an unresolved source. Furthermore, the OH maser emission is located only at $0\farcs15 \pm 0\farcs04$ from the peak of the radio continuum, well within the beam of our ATCA observations ($5\farcs3 \times 3\farcs3$). The positional accuracy in this match between maser and continuum emission improves by four orders of magnitude the one provided by previous single dish observations, which was determined by the size of the Parkes beam (13′). This positional coincidence further reinforces the classification of this source as an OHPN, previously proposed by Zijlstra et al. (1991) based on single-dish OH observations. Moreover, the masers arise from regions relatively close to the central star, as previously seen in other OHPNe (Christianto & Seaquist 1998; Miranda et al. 2001; Tafoya et al. 2009; Qiao et al. 2016a), and not from the faint extended structure observed in the Hα image, with an angular diameter of $\sim 15''$ (Zijlstra et al. 1991).

Vo 1 has been proposed to be a link between OH/IR stars and C-rich central stars (Zijlstra et al. 1991) since the observed OH masers could have been emitted only by an O-rich star at the AGB phase, and now Vo 1 harbors a [WC11] central star (Menzies & Wolstencroft 1990). Hence, this OH maser emission, the crystalline silicates and water ice (Cohen et al. 2002), suggest that Vo 1 is, in general, an O-rich nebula, while PAH emission arises from an elliptical shell surrounding the [WC11] central star over a region of $\sim 1\farcs0 \times 0\farcs8$ (García-Hernández et al. 2006).

6.C.2 New candidate maser-emitting PNe in our observations

6.C.2.1 IRAS 17487−1922

This source has been classified as a post-AGB star (Szczerba et al. 2007; Ramos-Larios et al. 2009). Single-peaked OH maser emission at 1612 MHz was reported at $V_{\rm LSR}$=−37.7 km s^{-1} based on 64-m Parkes observations (te Lintel Hekkert et al. 1991). We have detected this OH maser emission in our interferometric VLA and ATCA observations, and resolved it into several individual spectral features. In particular, in our ATCA observations, which have a better spectral resolution, we identified six emission features (Fig. 6.1, Table 6.6). The positional accuracy of our ATCA/VLA data does not allow us to determine the spatial distribution of the OH masers. No H_2O masers were detected in previous observations with the 100-m Green Bank antenna (Gómez et al. 2015b), nor in our own VLA observations. The radio continuum emission is unresolved, and is reported here for the first time, as well as its association with OH masers. Hence, IRAS 17487−1922 is a new OHPN candidate.

6.C.2.2 IRAS 18019−2216

This source has been classified as an OHPN candidate by means of radio interferometric observations Chapter 3. Emission of H_2O masers was not detected in observations made in 2010 (rms=36 mJy beam^{-1}; Walsh et al. 2014). However, in our observations, made in

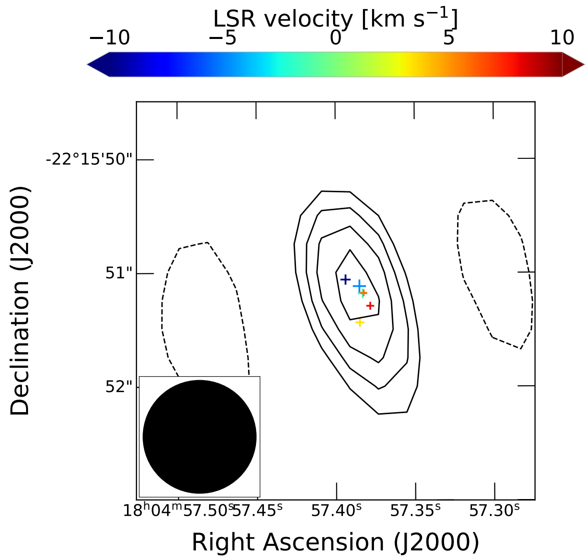

FIGURE 6.9: Radio continuum emission at 5.7 GHz of IRAS 18019−2216 from GLOSTAR. The contours are −3, 3, 4, 5, and $6\times1\sigma$ (where $\sigma=90$ μJy beam^{-1} is the rms of the map). The crosses are the positions of the H_2O masers, as shown in Fig. 6.2 (top left panel), assuming that the peak emission of the radio continuum emission at 22.22 GHz from our VLA observations lies at the same position as that of this map at 5.7 GHz. The color of the crosses represent the LSR velocity of the masers as indicated in the colorbar. The size of the crosses is proportional to the positional uncertainty of the masers. The beam is shown at the bottom left corner.

2021, we detected 22.235 GHz H_2O maser emission, where the brightest maser feature shows a S_ν=332 mJy beam^{-1} (Fig. 6.1 and Table 6.7). Thus the H_2O masers seem to have emerged or presented significant variability between 2010 and 2021. Moreover, in IRAS 18019−2216, the OH and H_2O maser-emitting material are kinematically different, since the velocity range of the H_2O maser emission (from −10 to +8 km s^{-1}) falls outside that of the OH (from −38 to −29 km s^{-1}), as seen in other WFs (e.g., Boboltz & Marvel 2005; Yung et al. 2013; Vlemmings et al. 2014). Therefore, apart from being a H_2OPN and OHPN candidate, and taking into account this small spread of its H_2O maser emission, IRAS 18019−2216 is also a new 'low-velocity' WF (see Yung et al. 2013, for this classification).

The spatial distribution of the H_2O masers in IRAS 18019−2216 (Fig. 6.2, top left) shows that the blueshifted and redshifted maser components occupy two different regions, (to the NE and SW, respectively), as expected in a bipolar jet. Fig. 6.9 (left) shows the radio continuum map of IRAS 18019−2216 at 5.7 GHz obtained by GLOSTAR (Dzib et al. 2023) with the B configuration of the VLA. An elliptical Gaussian fit to the continuum emission indicates a deconvolved size of ($\simeq$3.″0±0.″53) × (0.″90±0.″03), and position angle ∼18±3°. This orientation is similar to the direction of the bipolar jet traced by the H_2O masers, as it can be seen in Fig. 6.9, where we have assume that the peak emission of the radio continuum emission at 22.22 GHz from our VLA observations lies at the same position as that of this map at 5.7 GHz. This radio continuum emission at 22.22 GHz only shows an unresolved source.

6.C.2.3 IRAS 18443−0231

This optically obscured object has been classified as a PN by Cooper et al. (2013)[3] and Kanarek et al. (2015), based on its near-infrared spectrum with prominent emission lines and weak continuum emission, which can distinguish it from objects with similar infrared colors, such as H II regions or Wolf-Rayet stars. Although these works do not give any specific information that may allow us to discern whether the source is a late post-AGB star or a young PN, its SED (Fig. 6.3), peaking at $\simeq 25$ μm, strongly support that it is an evolved star.

An interesting feature in the infrared spectrum is that the ionized emission shows the recombination line of He I at 2.058 μm stronger than the Br γ emission (Cooper et al. 2013; Kanarek et al. 2015). This is consistent with the photoionized gas of young PNe that host a central star with $T_{\rm eff} \leq 40000$ K and present nebular electron densities larger than $\sim 10^4$ cm^{-3} (Depoy & Shields 1994; Lumsden et al. 2001a,b). However, using the 3MdB, we have checked that this emission line ratio can also be reproduced by shock-induced ionization (Cala et al., in preparation), and it is also seen in post-AGB stars showing shock-excited H_2 emission (Gledhill & Forde 2015). Hence, IRAS 18443−0231 seems to be a post-AGB star for which more research is needed to confirm its possible nature as a PN.

A spectrum of H_2O maser emission obtained with the 100 m Green Bank Telescope (Urquhart et al. 2011) shows a total velocity spread of maser components of 68 km s^{-1}, from $V_{\rm LSR} = -28$ to $+40$ km s^{-1}, indicating that this source could be a WF, as suggested by Ortega et al. (2024). However, given the presence of several H II regions in its neighborhood (Ortega et al. 2024), interferometric observations were necessary to discern whether all these maser components actually arise from IRAS 18443−0231. Actually, our VLA observations do interferometrically confirm the association between H_2O masers and the radio continuum. Moreover, our data also show H_2O maser components covering a wider velocity range than detected by Urquhart et al. (2011), with components between $V_{\rm LSR} = -28.5$ and $+48.6$ km s^{-1} (Fig. 6.1 and Table 6.9). All these components, covering a total velocity spread of 77 km s^{-1} are spatially associated with the source, finally confirming IRAS 18443−0231 as a WF. We detected no OH maser emission in this source (rms $\simeq 75$ mJy beam^{-1}).

All H_2O maser components in this source are blueshifted with respect of the reported central velocity of the system, $V_{\rm LSR} = +110.3$ km s^{-1} (Urquhart et al. 2008). Thus, the detected maser emission would be tracing outflow motions of $\simeq -60$ to -138 km s^{-1} along the line of sight. The systemic LSR velocity was estimated from a single-dish spectrum of the ^{13}CO(1-0) rotational line (Urquhart et al. 2008). We note, however, that those spectra show multiple spectral components, ranging from $V_{\rm LSR} = +50.4$ to $+110.3$ km s^{-1}. There is obvious interstellar confusion in this spectrum, which is normal for single-dish observations of molecular lines at the low galactic latitude of this source. The criterion used by Urquhart et al. (2008) to select the ^{13}CO component associated with the source was to choose the

[3]Further characteristics of this object are available in http://rms.leeds.ac.uk/

brightest one in the spectrum. This criterion seems reasonable for high-mass star-forming regions, which were the main targets for these authors, within the RMS survey. However, this criterion is not necessarily applicable to evolved objects, such as WFs. As an illustration, the CO(1-0) single-dish observations of ten WFs carried out by Rizzo et al. (2013) show contamination from multiple interstellar components in most of the spectra, and in no case the most intense component corresponds to the velocity of the source. The emission associated with these WFs, when detectable, is extremely weak. Anderson et al. (2011) also reported radio recombination line emission at 9 cm toward IRAS 18443−0231, at $V_{\rm LSR} = +63.4$ and $+98.5$ km s^{-1}, from observations with the Green Bank Telescope (beam size $\simeq 82''$). These lines most likely arise from the neighboring H II regions. Thus, we can conclude that there is no solid estimate of the systemic velocity of the source so far, and we tentatively assume the intermediate LSR velocity between the two most extreme H_2O maser components ($\simeq +10$ km s^{-1}) in the graphical representation of the maser velocities. If the systemic velocity of the source is confirmed to be close to this assumed one, then the weak CO emission around $+120$ km s^{-1} that Ortega et al. (2024) interpreted as tracing the redshifted lobe of molecular outflow from IRAS 18443−0231 is unlikely to be associated with the source.

Fig. 6.2 (bottom left) shows the spatial distribution of all the H_2O masers we identified, with respect to the radio continuum emission peak at 22.22 GHz, from our VLA observations. The H_2O masers trace a jet-like structure with an S-shaped morphology with a general north-south orientation on a larger scale. The maser components farther away from the center are the weakest ones, and they do not show a clear velocity distribution as expected in a jet (a trend of red- and blueshifted components separated on either side of the central source). However, the strongest innermost components (Fig. 6.2, bottom right) are arranged in a linear structure in the northeast (NE) to southwest (SW) direction, with a rough trend of more blueshifted components to the SW. The brightest maser components are blueshifted, and are located closer to this radio continuum emission peak. They seem to form a relatively dense cluster with a roughly circular or arc shape, suggesting the existence of bow-shocks (as seen in, e.g., IRAS 18113−2503; Orosz et al. 2019), or the origin of a molecular jet as it emerges from the surrounding circumstellar material (as seen in, e.g., W43A; Tafoya et al. 2020).

Another outstanding characteristic of IRAS 18443−0231 is its spectral index, as mentioned in Section 6.5.5. Clearly negative spectral indices, characteristic of non-thermal radio emission, have been reported before in this source, with observations that indicate values $\alpha \simeq -1.15$ to $\alpha \simeq -0.36$ (e.g., Xu et al. 2006; Dzib et al. 2023). Some of these estimates should be taken with care, as the available information at radio frequencies of the source shows variability of a factor > 2 (Becker et al. 1994; Xu et al. 2006; Purcell et al. 2013; Medina et al. 2019; Dzib et al. 2023; Ortega et al. 2024). In this sense, the result of Xu et al. (2006) is more robust, as it was obtained with observations taken close in time.

Negative spectral indices, such as the one seen in IRAS 18443−0231, are characteristic of jets in which free electrons move in a magnetized environment. These jets are traced by

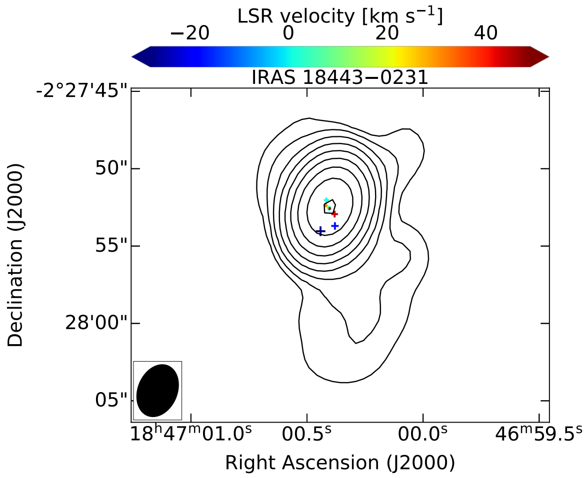

FIGURE 6.10: Contour map of the radio continuum emission of IRAS 18443−0231 at 24 GHz. The contours increment in steps of $3\sigma\times2^n$ starting from n=0 (σ= 0.23 mJy beam^{-1} is the rms of the map). The crosses are the positions of the H_2O masers, as shown in Fig. 6.2 (bottom panels). The color of the crosses represent the LSR velocity of the masers as indicated in the colorbar. The size of the crosses is proportional to the positional uncertainty of the masers. The beam is shown in the bottom left corner.

the WF, and the derived spectral index $\alpha\simeq-0.42$ is similar to the spectral index of synchrotron jets of active galactic nuclei. Moreover, it has also been suggested that the powerful jets in this object can produce X- and γ-ray emission (Ortega et al. 2024), although the association of these high-energy emission with the source is still uncertain. Negative spectral index values have been reported in some WFs, such as the post-AGBs IRAS 15445−5449 and IRAS 18043−2116 (Pérez-Sánchez et al. 2013a; Pérez-Sánchez et al. 2017), and the nascent PN IRAS 15103−5754 (Suárez et al. 2015), as well as other post-AGB stars and PNe (Cerrigone et al. 2011, 2017). This group of non-thermal radio continuum emitters may be ideal sources for investigating the role of magnetic shaping of circumstellar structures in these evolutionary phases (e.g. García-Segura et al. 2020).

Figure 6.10 shows the radio continuum emission of IRAS 18443−0231 at 24 GHz. It shows a compact, bright central component, plus some extended structure, with low-level extensions to the southwest, which are also observed in images at 3 and 5 GHz from VLASS and CORNISH, respectively (see Fig. 10 of Ortega et al. 2024). Archival VLA continuum map at 5.7 GHz shows an unresolved source at a beam size of $1\farcs2\times0\farcs9$. Similarly, Xu et al. (2006) reported an unresolved source (beam size $0\farcs9$) at 15 GHz. We also show in Fig. 6.10 the location of the H_2O masers, as presented in Fig. 6.2 (bottom panels). The central linear structure of masers is located near the bright central non-thermal component of the ionized gas, although the weakest masers extend over a larger region and could be related with mass-loss along the direction of the extended continuum emission.

6.C.2.4 IRAS 18480+0008

The VLA THOR survey reported a single peak 1665 MHz maser feature at $V_{\rm LSR}$=+12.0 km s^{-1} from this source (Beuther et al. 2019). VLA surveys of radio continuum have also reported this source with emission at 3 and 5 GHz (Medina et al. 2019; Gordon et al. 2021; Dzib et al. 2023). From these observations we report here for the first time this source as a OHPN candidate. Furthermore, our VLA observations show a match between H_2O masers and radio continuum emission at 22.22 GHz. The latter is unresolved in our data (beam $\simeq 3''$). Moreover, archival continuum data performed with the VLA in the B configuration at 5.7 GHz (beam $\simeq 1''$) also shows unresolved emission. The H_2O maser spectrum displays multiple spectral features emitted between $V_{\rm LSR}$=+14 km s^{-1} and $V_{\rm LSR}$=+28 km s^{-1} (Fig. 6.1 and Table 6.8). The positions of the H_2O masers (Fig. 6.2, top right) trace a linear distribution from the northeast to the southwest direction, which is expected from either a collimated mass-loss event or a toroidal structure. Hence, IRAS 18480+0008 is a new H_2OPN and OHPN candidate, and could be a new WF. A confirmation of its nature as a WF would require further studies to determine the orientation of the nebula with respect to the water masers, or proper motion studies of the latter, to determine whether this maser emission actually traces a jet.

6.C.2.5 IRAS 19035+0801

This source has been classified as a candidate for PN based on its infrared colors and radio continuum emission (van de Steene & Pottasch 1995; Irabor et al. 2018). Based on single-dish observations, Eder et al. (1988) reported single-peaked 1612 MHz OH maser emission at $V_{\rm LSR}$=−80.2 km s^{-1}. We have also detected this maser emission at around −78 km s^{-1} in both ATCA and VLA observations and confirm that it has a positive positional coincidence with the source of radio continuum previously reported (see Fig. 6.1 and Table 6.4). The positional accuracy of our data is not enough to determine the spatial distribution of the OH masers. We have not detected any H_2O maser emission. Hence, IRAS 19035+0801 is a new candidate for OHPN.

6.C.2.6 IRAS 19194+1548

This source was spectroscopically classified as a likely PN G50.4802+0.7058 (Sabin et al. 2014). OH maser emission at 6035 MHz has also been reported in this source, using ATCA interferometric observations (Avison et al. 2016). The 6035 MHz spectrum shows an asymmetric double peak at $V_{\rm LSR}$ of +48.12 and +48.22 km s^{-1} (see Table 6.4). Data from the THOR survey report the presence of both OH maser emission at 1612 MHz (Beuther et al. 2019) and 1.5 GHz continuum emission (Wang et al. 2018) at the source position. These maser and continuum detections were reported separately, although they were obtained in

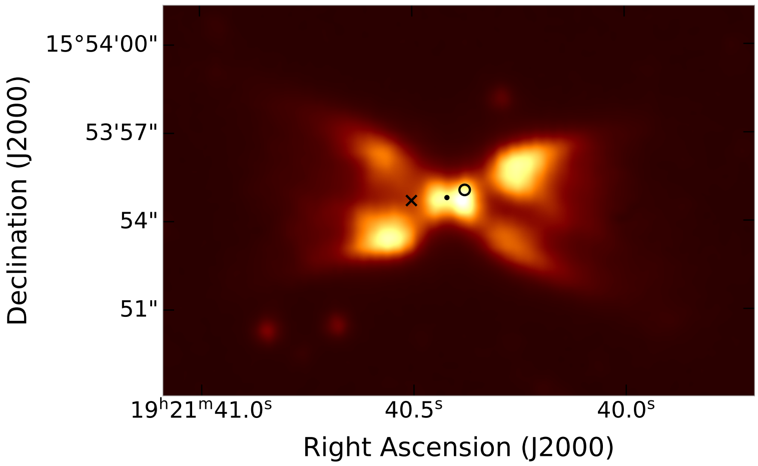

FIGURE 6.11: Near-infrared broadband emission at 2.1 μm of IRAS 19194+1548 by the UKIRT in logarithmic scale. The black empty circle and 'x' lie at the reported positions of the continuum emission peak at 1.5 GHz and 1612 MHz OH maser, respectively. The sizes are proportional to their relative positional accuracy. The black point lies at the position of the continuum emission peak at 24 GHz from our VLA observations. Its size is proportional to its positional uncertainty.

simultaneous observations. The 1612 MHz OH maser emission shows only one emission feature at $V_{\rm LSR}$=+43.5 km s^{-1}. The match between OH maser and radio continuum emission, as well as their association with this likely PN are reported here for the first time. In our VLA observations, we did not detect any 22.235 GHz H_2O maser emission.

In Figure 6.11 we present an archival infrared image of IRAS 19194+1548 at 2.1 μm taken from the archive of the United Kingdom Infrared Telescope (UKIRT), which shows a point-symmetric bipolar nebula with a narrow waist. The position of the radio continuum emission (Wang et al. 2018) is near the center of the nebula, while the OH emission may be associated with the eastern lobe (relative positional accuracy of 0.″5). A Gaussian fit to our radio continuum map at 24 GHz indicates that the emission peak [RA(J2000)=19h21m40.421, DEC(J2000) +15d53m54.83s] lies at a position closer to the waist than to the lobes (see black point in Fig. 6.11).

It should be noted that Akras et al. (2019) classified this object as a possible SySt, based on its SED, whose peak they reported to be at $\simeq$ 4 μm. However, as shown in Fig. 6.3, our updated SED, including additional data, shows a peak between 30 and 70 μm, which is compatible with an obscured PN, rather than a SySt, as discussed in Sec. 6.5.1. In addition, an inspection of the spectrum shown by Sabin et al. (2014), suggests the presence of an emission line at 6830 Å that may be associated with the O VI Ramman-scattered line. However, this emission feature line is observed in both SySt and young PNe or may be a blending of several emission lines (see Akras et al. 2019, and references therein). On the other hand, the near-infrared spectrum obtained from the RMS survey[4] shows CO(3–1) emission at 2.31 μm (Cooper et al. 2013), which is observed in stars that have already entered the post-AGB phase (e.g. Hrivnak et al. 1994; Oudmaijer et al. 1995; Gledhill et al. 2011; Gledhill

[4]The spectra and further characteristics of this object are available at http://rms.leeds.ac.uk/

& Forde 2012). This emission is not expected in a SySt, where the main component is a red giant which only show CO absorption lines (Rayner et al. 2009). We also point out that, as mentioned before, this source has OH emission both at 1612 and 6032 MHz. The former is extremely rare in SySts (e.g., Norris et al. 1984; Seaquist et al. 1995), since the companion white dwarf ionizes the outer envelopes where these masers are produced, dissociating the OH molecules. Moreover, the 6035 MHz OH line has only been detected in nascent PNe (in Vy 2-2 and K 3-35; Jewell et al. 1985; Desmurs et al. 2002, 2010), but not in SySts.

In summary, there are some pieces of indirect evidence suggesting that this object could be a PN. However, here we report IRAS 19194+1548 as a new OHPN candidate (see also Marton et al. 2024), for which more research is needed to definitely confirm its nature as a PN.

6.C.3 New candidate maser-emitting PNe from the literature search

6.C.3.1 IRAS 16029−5055

This source, also called OH 331.158+00.781, has been classified as a post-AGB star due to its infrared colors and single peak OH spectrum at 1612 MHz, with $V_{\rm LSR} = -89.1$ km s^{-1} (Sevenster et al. 1997a). In the CORNISH South Survey, a weak radio continuum source has been reported, with a flux density of 3.20±0.39 mJy at 5.5 GHz (Irabor et al. 2023). No other radio continuum nor maser line emission has been reported on this source. We reported for the first time the match between the interferometric positions of this single-peak OH maser and the radio continuum emission. Moreover, the analysis presented in Sec. 6.5.4 of the archival *Spitzer* spectrum shown in Fig. 6.6 (top panel) allows us to strongly suggest the presence of photoionized gas. Hence, we report IRAS 16029−5055 as a new OHPN candidate, for which more observations are necessary before a final confirmation as bona fide OHPN (see Section 6.6).

6.C.3.2 IRAS 18213−1245A

Based on its infrared and radio continuum emission, this source has been classified as the PN candidate G018.5242+00.1519 (Urquhart et al. 2009; Irabor et al. 2018). Based on ATCA observations, Walsh et al. (2014) reported two H_2O maser features at $V_{\rm LSR}$ of $\simeq$+21.7 km s^{-1} and $\simeq$+23.6 km s^{-1} on this source. In addition, a wide 1665 MHz OH single peaked feature at $V_{\rm LSR}$=27 km s^{-1} covering a range of velocities of $\sim$15 km s^{-1} was reported by Beuther et al. (2019) in THOR, based on VLA observations. Although these maser and continuum data were not obtained simultaneously, their spatial locations are sufficiently close (distance $\simeq 1''$), and therefore, here we report the match between the interferometric positions of the PN candidate and these masers. Hence, IRAS 18213−1245A is a new H_2OPN and OHPN candidate.

6.C.3.3 IRAS 18464−0140

Based on its infrared and radio continuum emission, this source has been classified as the PN candidate G031.2131−00.1803 (Irabor et al. 2018; Medina et al. 2019). This classification as PN is supported by the non-detection of thermal ammonia emission (Anglada et al. 1996), which is more commonly detected in star-forming regions than in evolved stars (see Anglada et al. 1996; Wong et al. 2018). VLA observations in 1984 detected H_2O maser emission spread between $V_{\rm LSR}$ of −6.3 and −39.2 km s^{-1} and a peak emission of 20.2 Jy beam^{-1} at $V_{\rm LSR}$=−37.1 km s^{-1} (Forster & Caswell 1989b, 1999b). In addition, single emission peaks of OH maser emission at 1612, 1665, and 1667 MHz have been detected at $V_{\rm LSR}$ of −26.6 to −30.2 km s^{-1} based on VLA observations (Forster & Caswell 1989b, 1999b; Beuther et al. 2019). The 1665 MHz OH emission presents significant variability, with flux densities of $\simeq$ 0.50 and 0.35 Jy (Table 6.10) reported by reported by Forster & Caswell (1989b), but it was not detected in THOR (rms=0.01 Jy beam^{-1}; Beuther et al. 2019). Based on the spatial coincidence of maser and continuum emission, we report IRAS 18464−0140 as a new H_2OPN and OHPN candidate.

Fig. 6.12 shows a radio continuum map at 10 GHz of IRAS 18464−0140, which shows an elongated source with a deconvolved size of (344±14) × (53±36) mas^2 elongated at position angle 56±2°. We also show the location of the H_2O maser components from observations performed on 1984, and initially reported by Forster & Caswell (1999b), which we reprocessed completely, including calibration and self-calibration. The increased signal-to-noise ratio, of a factor ∼2 in the maser emission, due to the self-calibration process, allowed us to detect two new components (at −28.68 and −6.29 km s^{-1}) not reported by Forster & Caswell (1999b). The parameters of the detected maser components are shown in Table 6.11. The blueshifted and redshifted maser clusters are separated ∼0.″7, and distributed along the same direction as the elongated continuum emission. This suggests that the masers are tracing a jet, which is characteristic of WFs (e.g. Suárez et al. 2008; Gómez et al. 2017). Hence, in addition to being a new H_2OPN and OHPN candidate, and considering this small spread of velocities of its H_2O maser emission, IRAS 18464−0140 is also a new ‘low-velocity’ WF (for this classification see Yung et al. 2013). We note that, while the association of maser and continuum emission, and their similar orientations are clear, it is not possible to exactly determine an accurate positional alignment between these two types of emission, since those data were not obtained simultaneously. It is likely that the masers actually lie at the tips of the bipolar structure traced by the continuum emission. Thus, new simultaneous H_2O maser and continuum observations are needed to accurately determine the location of the maser emission with respect to the nebula.

6.C.3.4 IRAS 18508+0047

Based on its infrared and radio continuum emission, this source has been classified as the PN candidate G033.9059−00.0436 (Urquhart et al. 2009; Irabor et al. 2018). A single 1612

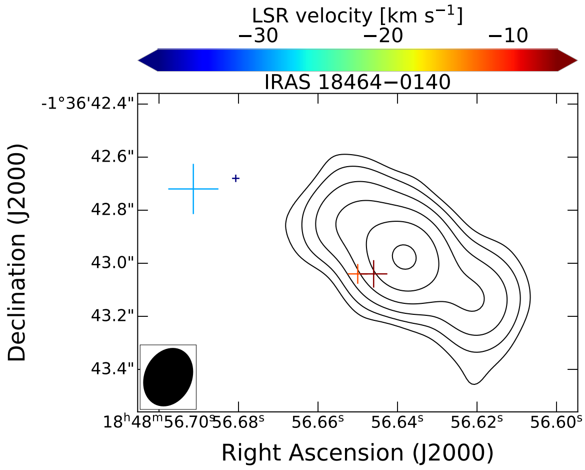

FIGURE 6.12: Contours of the radio continuum emission at 10 GHz of IRAS 18464−0140 from archival VLA data from observations performed on 2022. The contours increment in steps of $3\sigma\times 2^n$ starting from n=0 ($\sigma = 31\,\mu$Jy beam^{-1}). The crosses are the positions of the H_2O masers obtained from our reprocessing of archival VLA data from observations performed on 1984. The color of the crosses represent the LSR velocity of the masers as indicated in the colorbar. The size of the crosses is proportional to the positional uncertainty of the masers.

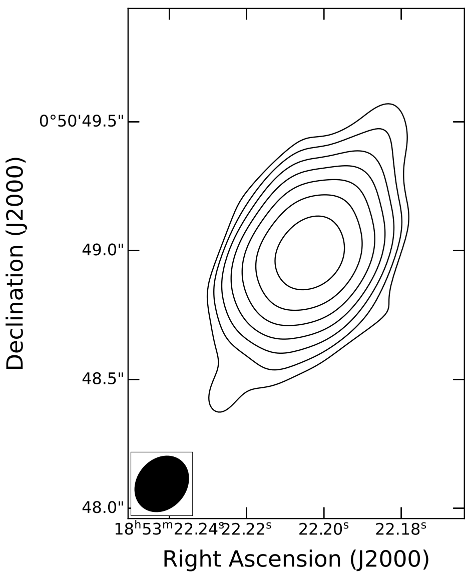

FIGURE 6.13: Contours of the radio continuum emission at 10 GHz of IRAS 18508+0047. The contours increment in steps of $3\sigma\times 2^n$ starting from n=0 (where $\sigma = 44\ \mu$Jy beam^{-1} is the rms of the map). The filled ellipse is the synthesized beam of the radio continuum emission map.

MHz OH maser feature at +76.5 km s^{-1} was reported at galactic position 33.906−0.044 by the THOR survey (Beuther et al. 2019). In this work, we report the match between the interferometric positions of the PN candidate and the OH maser emission (Table 6.4). Hence, IRAS 18508+0047 is a new OHPN candidate. Fig. 6.13 shows archival VLA continuum data from this source at 10 GHz. It originates from a strong compact source and weak extended emission in the northwest-southeast direction. A Gaussian fit indicates a deconvolved size of $284\pm3\times200\pm2$ mas^2, pa $147.9\pm1.2°$.

6.C.3.5 IRAS 19176+1251

This source has been classified as the PN candidate G047.6884−00.3024, based on its infrared and radio continuum emission (Preite-Martinez 1988; van de Steene & Pottasch 1995; Szczerba et al. 2007; Ramos-Larios et al. 2012; Irabor et al. 2018). Observations of H_2O masers have not detected emission on the source (rms=0.08 Jy beam^{-1}; Gómez et al. 2015b). Simultaneous observations of continuum and line emission detected both the 1.5 GHz radio continuum and the single peak 1720 MHz OH maser emission at −39.0 km s^{-1} (see Table 6.4). These findings have been independently reported in the THOR survey for continuum and OH line emissions at the position of source G47.688−0.302 (Wang et al. 2018; Beuther et al. 2019). The analysis presented in Sec. 6.5.4 of the archival *Spitzer* spectrum shown in Fig. 6.6 (bottom right panel) is consistent with the presence of photoionized gas. Hence, we report IRAS 19176+1251 as a new OHPN candidate, for which more observational data are necessary before a final confirmation as bona fide OHPN (see Section 6.6).

To our knowledge, IRAS 19176+1251 is the first evolved low- to intermediate-mass star known to have detected OH maser emission at 1720 MHz, and without any association with other OH and H_2O maser, providing an excellent opportunity for investigation of the physical conditions for this OH maser transition in evolved stars. Although OH emission at 1720 MHz has been reported in other PNe (Miranda et al. 2001; Qiao et al. 2016a; Gómez et al. 2016), it was always found together with other OH maser transitions. The exclusive presence of OH masers at 1720 MHz is typical of shock waves of supernova remnants encountering interstellar molecular clouds (see Wardle & Yusef-Zadeh 2002), some star forming regions (Ogbodo et al. 2020), and in FU Ori-type outbursts (see Szabó et al. 2025, and references therein).

6.C.3.6 OH 025.646−00.003

A symmetric double-peaked maser spectrum at 1612 MHz has been reported from OH 025.646−00.003 in the THOR survey (Beuther et al. 2019). Radio continuum emission at 4.8 GHz has also been reported at this position (White et al. 2005). Here, the match between radio continuum and OH masers is reported for the first time. We did not detect H_2O maser nor radio continuum emission at 24 GHz from the source. Hence OH 025.646−00.003 is a new OHPN candidate.

6.D Parameters of the shock and photoionization models

Taking into account the mid-infrared spectra of newly and previously identified objects (Fig. 6.6), we have used the fine-structure spectral lines of [Ne II], [Ne III], and [Ne V] seen at 12.81, 15.55, and 14.32 μm, respectively, to create diagnostic plots in the 3MdB (Morisset et al. 2015; Alarie & Morisset 2019) that represent shock ionization and photoionization models, which we describe below.

6.D.1 Shock models

We have used the 3MdB (Morisset et al. 2015; Alarie & Morisset 2019) to obtain the shock models of Sutherland & Dopita (2017), which follow the same grid definition as Allen et al. (2008), for a total of 15968 models. These models were then applied to generate the diagnostic diagram shown in Fig. 6.7 (left). The same models and parameters were used in Chapter 5, where a more detailed explanation can be found.

6.D.2 Photoionization models

We have used the 3MdB (Morisset et al. 2015; Alarie & Morisset 2019) to obtain the PN photoionization models of Delgado-Inglada et al. (2014). These models were computed using Cloudy v.17 (Ferland et al. 2017), resulting in a total of 68041 models. These models were then applied to generate the diagnostic diagram shown in Fig. 6.7 (right). The same models and parameters were used in Chapter 5, where a more detailed explanation can be found.

6.E List of all confirmed water fountains

Table 6.14 presents the list of all confirmed water fountain sources reported in the literature and newly identified in this work. For each object, its name, alternative designation, and velocity range of the H_2O masers are provided.

Table 6.14: List of all confirmed water fountains.

Name	Alt. name	V_{range}[a] km s^{-1}	Reference[b]
IRAS 15103−5754	GLMP 405	70	1
IRAS 15445−5449	OH 326.5−0.4	90	2
IRAS 16342−3814	OH 344.1+5.8	260	3
IRAS 16552−3050	GLMP 498	170	4
IRAS 17291−2147	GLMP 498	70	5
IRAS 18019−2216	SCHB 281	20	This work
IRAS 18043−2116	OH 9.1−0.4	800	6, 7
IRAS 18113−2503	PM 1−221	500	8
IRAS 18139−1816	OH 12.8−0.9	50	9
IRAS 18286−0959	OH 21.80−0.13	200	10
IRAS 18443−0231	RFS 505	80	This work
IRAS 18450−0148	W43A	180	11
IRAS 18455+0448		40	12
IRAS 18460−0151	OH 31.0−0.2	310	13
IRAS 18464−0140	OH 31.21−0.18	30	This work
IRAS 18596+0315	OH 37.1−0.8	60	5
IRAS 19134+2131		100	14
IRAS 19190+1102	PM 1−298	100	15

Notes. [a] Velocity range of the H_2O masers to date. [b] Interferometric confirmation as WF and velocity range: 1. Gómez et al. (2015a). 2. Pérez-Sánchez et al. (2011). 3. Claussen et al. (2009). 4. Suárez et al. (2008). 5. Gómez et al. (2017). 6. Walsh et al. (2009) 7. Uscanga et al. (2023). 8. Gómez et al. (2011). 9. Boboltz & Marvel (2005). 10. Yung et al. (2011). 11. Imai et al. (2002). 12. Vlemmings et al. (2014). 13. Imai et al. (2013). 14. Imai et al. (2004). 15. Day et al. (2010).

Chapter 7

Low- and high-velocity "water fountains": Different evolutionary stages

7.1 Introduction

"Water fountains" (WFs) are evolved stars with H_2O maser emission tracing collimated mass loss. Most WFs are believed to be in the post-asymptotic giant branch (post-AGB) phase. High-resolution observations of the H_2O masers have shown incipient small-scale ($\sim$$10^2$-$10^3$ au) bipolar jets that can reach velocities of hundreds of kilometers per second (e.g., Imai et al. 2002; Boboltz & Marvel 2005; Gómez et al. 2011; Uscanga et al. 2023). The short kinematical ages estimated for WF jets ($\lessapprox$ 100 yr; e.g., Day et al. 2010; Yung et al. 2011; Orosz et al. 2019; Tafoya et al. 2020) suggest that these small-scale jets could be one of the initial manifestations of non-spherical mass loss that occur in evolved low- and intermediate-mass stars (e.g., Imai et al. 2002). So far, 18 objects have been confirmed as WFs (Gómez et al. 2017, and Chapter 6). Among these, only one (W43A) has been classified as an AGB star (Imai et al. 2002, 2005), while another (IRAS 15103−5754) has been classified as a planetary nebula (PN), and it could be one of the youngest PNe known (Gómez et al. 2015b).

Recently, four additional interesting objects were identified: three new confirmed WFs (IRAS 18019−2216, IRAS 18443−0231, and IRAS 18464−0140) and a new WF candidate, IRAS 18480+0008 (Chapter 6). Remarkably, these four objects present radio continuum emission indicating the presence of an ionized region that characterizes PNe. Thus, they could be new WF PNe. However, definitive classification as PNe requires further spectroscopic

This chapter is derived from the following publication:

- Cala et al. (2025b)

confirmation since shock-ionized gas around post-AGB stars can also produce radio continuum emission (e.g., Cerrigone et al. 2017; Pérez-Sánchez et al. 2017). We note that, in addition to these four objects and the WF PN IRAS 15103−5754, only one additional object, WF IRAS 15445−5449, presents radio continuum emission, and its evolutionary stage is unknown (Pérez-Sánchez et al. 2013a). Interestingly, the radio continuum emission in IRAS 15445−5449, IRAS 15103−5754, and IRAS 18443−0231 is not mainly due to free-free processes. Instead, it is mostly due to a non-thermal nature (Pérez-Sánchez et al. 2013a; Suárez et al. 2015, and Chapter 6).

Most WFs are optically obscured (e.g., Suárez et al. 2008; Gómez et al. 2017; Pérez-Sánchez et al. 2017) because they are surrounded by thick circumstellar envelopes, probably as a result of a common-envelope episode in a close binary system (Khouri et al. 2021). Therefore, their characterization requires observations at infrared (or longer) wavelengths.

In this chapter, we present near-infrared spectra of the four radio continuum emitting WFs (IRAS 15445−5449, IRAS 18019−2216, IRAS 18443−0231, and IRAS 18464−0140) and the WF candidate (IRAS 18480+0008) and aim to clarify their nature. We also observed the WF PN IRAS 15103−5754 for comparison purposes.

7.2 Observations and data processing

We performed long-slit intermediate resolution K-band near-infrared spectroscopy with the New Technology Telescope (NTT) of the European Southern Observatory (ESO) located at the La Silla Observatory in Chile on 11 and 12 June, 2023 (Project ID: 111.24T1.001; P.I.: R. A. Cala). Photometric conditions, average temperatures of +10°C, and a seeing of 2″ were experienced on both nights. To obtain and record the spectra, we used the infrared spectrograph Son of ISAAC (SOFI), a slit of 1″ width, 1.4′ length, the third-order HR grism (resolution of R≃2200 for a 0.″6 slit width and wavelength range 2.00-2.30 μm), and the 1024×1024 Hawaii HgCdTe array. The position angle of the slit was 0° in all cases except for IRAS 15103−5754, where the slit was oriented along the jet traced by the H_2O masers (+56°; Gómez et al. 2015b). In order to cancel out the telluric lines, we observed B main-sequence stars after or before each target, making use of the same instrumental setup (see Appendix 7.A).

The spectra of the telluric standard stars and of our targets were processed using the ESO's SOFI pipeline in *esorex*, which performed dark-current correction, flat fielding, slit curvature distortion, combination of frames, and wavelength calibration. The dispersion obtained was ∼5Å pixel^{-1}. The wavelength accuracy is ∼0.004 μm in most of the spectral range and ∼0.01 μm when longer than 2.25 μm. We used IRAF to extract the spectra and clean the bad pixels. We then removed the Brγ absorption line from the telluric standards by interpolating across that part of the spectrum. We then divided the target spectra by the spectra of their corresponding telluric standard in order to cancel out atmospheric absorption features. The absolute flux calibration was carried out by multiplying by a normalized blackbody spectrum at the temperature of the telluric standard, and the result was re-scaled to fit the K-band magnitudes of our targets reported in the Two Micron All Sky Survey (2MASS) and United Kingdom Infrared Deep Sky Survey (UKIDSS). Assuming that the telluric standards are not variable in the infrared, uncertainties of ±5-10% in absolute flux calibration are expected from this method, although taking into account that the slit width could be narrower than the angular size of the observed targets, some emission could be filtered out, and thus larger uncertainties are possible.

7.3 Results and discussion

Figure 7.1 shows the spectra of the six observed WFs, and it allowed us to classify the objects into two groups. The sources in the top panels of Fig. 7.1 (IRAS 18019−2216, IRAS 18464−0140, and IRAS 18480+0008; hereafter Group A) show no emission lines but only absorption features due to the first overtone bandhead of CO ($\nu = 2$–0) at 2.29 μm and CO ($\nu = 3$–1) at 2.31 μm, although the last absorption feature is not detected in IRAS 18019−2216. Weak absorption lines of Na I, Ca I, and Si I at ∼2.20, ∼2.25, and ∼2.26 μm, respectively, are detected in IRAS 18480+0008 and apparently also in IRAS 18464−0140.

In the sources shown in the bottom panels of Fig. 7.1 (IRAS 15103−5754, IRAS 15445−5449, and IRAS 18443−0231; hereafter Group B), the spectra are rich in emission lines, and there is no obvious CO absorption. In IRAS 15445−5449, there is emission of the CO ($\nu = 2$–0) bandhead and of the doublet of Na I at 2.206 and 2.209 μm observed around 2.210 μm. In Appendix 7.B and Table 7.2, we report fluxes of the emission lines detected in Group B. We note that the spectrum of the WF IRAS 18443−0231 (Fig. 7.1, bottom-left panel) is consistent with the spectra of this source previously reported in near-infrared surveys (Cooper et al. 2013; Kanarek et al. 2015).

7.3.1 Evolutionary stage of the objects

The most noticeable spectral features in the spectra of the sources in Group A are the absorption of the CO bands near 2.29 and 2.31 μm. These bands are characteristic of cool ($T_{\rm eff} \simeq 2100$-5700 K) main-sequence, giant, and supergiant stars of spectral types G, K, and M (Rayner et al. 2009). They are ubiquitous in the spectra of AGB stars and have been detected in some early post-AGB stars (e.g., Hrivnak et al. 1994; Oudmaijer et al. 1995; Kanarek et al. 2015). We also noticed a rising continuum towards longer wavelengths in IRAS 18464−0140 and IRAS 18480+0008.

By comparing the spectra of our Group A sources with those in the atlas of infrared spectra by Rayner et al. (2009), these objects should be M-type giants or supergiants. This is consistent with an AGB or early post-AGB nature. Thus, although the radio continuum

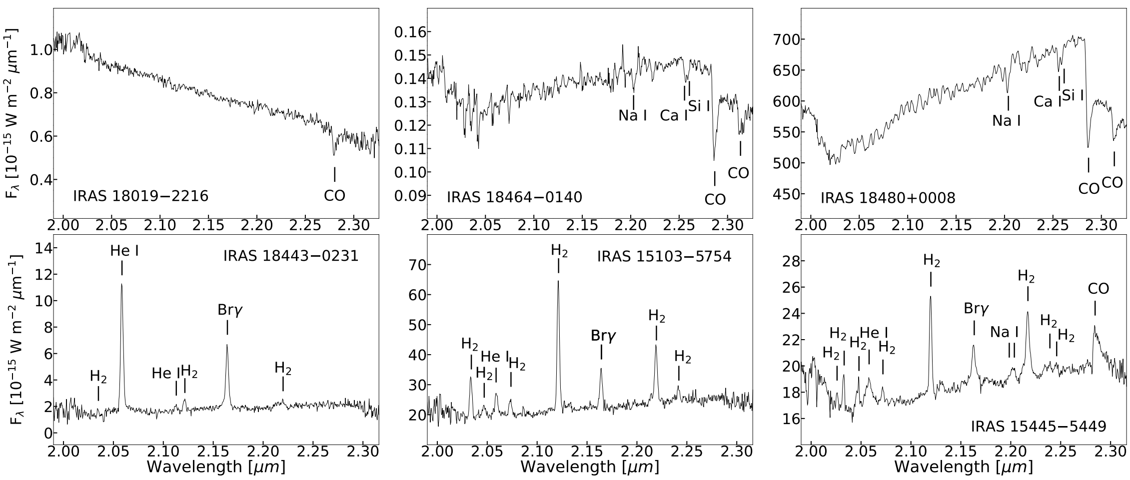

FIGURE 7.1: *K*-band near-infrared spectra of our targets. The top panels contain the objects without emission lines (Group A), and the bottom panels present the objects with emission lines (Group B). Other possible emission lines are are difficult to identify due to the low resolution of the spectra.

emission in the Group A sources indicates the presence of ionized gas, we do not expect this ionization to be due to ultraviolet radiation, as in the case of PNe, but to shocks, as has been previously reported in post-AGB stars (e.g., Cerrigone et al. 2017; Pérez-Sánchez et al. 2017).

The spectra of sources in Group B are dominated by recombination lines of hydrogen (Br γ) and He I as well as H_2 emission lines. These lines can be produced both in photoionized nebulae and as a consequence of shocks (Black & van Dishoeck 1987; Depoy & Shields 1994; Sutherland & Dopita 2017). Thus, these objects could either be post-AGB stars with shocks or nascent PNe. In any case, they seem more evolved than the sources in Group A, whose spectra indicate cool giant stars.

To investigate whether the observed emission lines trace photoionized gas typical of PNe or shock-excited gas, we used the Mexican Million Models Database (3MdB; Morisset et al. 2015; Alarie & Morisset 2019) and the shock models by Sutherland & Dopita (2017) stored in the 3MdB (for more details see Cala et al. 2024a). The diagnostic diagram is shown in Fig. 7.2 and displays line intensity ratios compatible with shock ionization. Unfortunately, the 3MdB has not yet incorporated the response of the He I 2.120 μm line to photoionization models, and therefore, the corresponding diagram cannot be constructed in this case.

The diagram in Fig. 7.2 does not provide any constraints to the nature of the emission in IRAS 15103−5754 and IRAS 15445−5445, where the He I at 2.120 μm is not detected in our data. However, we note that the shock-ionization models are distributed along a relatively narrow strip in the diagram, providing a useful prediction of the expected intensity of the He I 2.120 μm emission line. Thus, new, deeper spectra of these sources could shed light on these objects by investigating whether the 2.120μm He I/Brγ ratio is consistent with shocks.

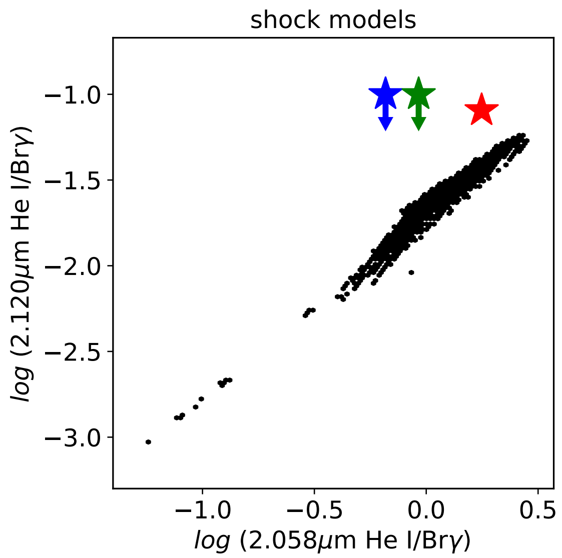

FIGURE 7.2: Emission-line ratio diagnostic diagram for recombination lines of Brγ at 2.166 μm and He I lines at 2.058 and 2.120 μm. The region occupied by the black points corresponds to the values expected from the shock models of Sutherland & Dopita (2017). The filled stars are IRAS 15103−5754 (blue), IRAS 15445−5445 (green), and IRAS 18443−0231 (red). The sizes of the symbols are larger than their errors. The arrows indicate upper limits for the flux of the He I 2.120 μm emission line (see Fig. 7.1 and Table 7.2).

However, in the case of IRAS 18443−0231, this line ratio seems to be incompatible with shocks alone. This strongly suggests that there should be a significant contribution of photoionization in the observed spectrum of this source. Moreover, the He I emission at 2.058 μm is a factor of $\simeq 2$ stronger than the Brγ one, which would be consistent with a photoionized region with $\log T_{\rm eff}[\rm K] \leq 4.6$ and $\log n_e[\rm cm^{-3}] \geq 4$, according to Figure 2 of Depoy & Shields (1994). In summary, the 2.120 μm He I/Brγ ratio suggests that IRAS 18443−0231 could be a nascent PN whose radio continuum emission is dominated by non-thermal processes, as in IRAS 15103−5754 (Suárez et al. 2015).

7.3.2 The slow and fast jets in WFs

Water fountains are usually identified in single-dish spectra of H_2O maser emission when they show components spread over a velocity range larger than that expected from the expansion of the AGB envelope ($\simeq 50\,\rm km\,s^{-1}$, assuming maximum expansion velocity $\simeq 25\,\rm km\,s^{-1}$; e.g., te Lintel Hekkert et al. 1991). However, another criterion commonly used for WF identification is that the H_2O maser components fall outside the velocity range covered by OH masers (Yung et al. 2013; Fan et al. 2024) since this is considered to be an indication of the presence of non-spherical mass loss. This is based on the fact that in the case of maser emission in spherical AGB envelopes, H_2O masers are pumped at distances closer to the star than OH masers. Therefore, their velocities must be lower, with OH masers tracing the terminal velocities of the outer envelope. Similarly, the comparison of the velocity ranges of other lines, such as the OH main lines (1665 and 1667 MHz) with respect to the satellite line (1612 MHz) have been used to infer the presence of non-spherical mass loss (Xie et al. 2025). In the case of WFs, sources with H_2O maser emission that have low-velocity spreads ($< 50\,\mathrm{km\,s^{-1}}$) but fall outside the range of OH velocities have been classified as low-velocity WFs (Yung et al. 2013). Moreover, independent of the characteristics of OH emission, one could also classify as low-velocity WFs sources whose H_2O maser emission shows low-velocity spreads, but it has been seen to trace bipolar jets when observed with radio interferometers (e.g., Boboltz & Marvel 2005). These slow jets traced by H_2O masers have been interpreted in some cases as a projection effect, occurring when the jet axis is close to the plane of the sky (Boboltz & Marvel 2005; Vlemmings et al. 2014). However, Yung et al. (2013) found four candidate low-velocity WFs whose infrared colors resemble those of AGB stars and are clearly different from classical high-velocity WFs, whose colors are typical of post-AGB stars. Based on that finding, Yung et al. (2013) suggested that these low-velocity WFs are transitional objects in the late AGB or early post-AGB phase and that their jets are intrinsically slower than those of high-velocity WFs.

Chapter 6 presented maps of the H_2O maser distribution of the three evolved stars of Group A in this chapter: IRAS 18019−2216, IRAS 18464−0140, and IRAS 18480+0008. The first two objects clearly present a linear distribution of the H_2O maser emission, indicating the presence of jets with radial velocity spreads of only $\leq$30 $\mathrm{km\,s^{-1}}$. Thus, the authors classified them as low-velocity WFs. The H_2O maser distribution in IRAS 18480+0008 also suggests a jet, but higher-resolution observations are necessary for confirmation, so we can consider it a candidate low-velocity WF. However, the sources in Group B are classical high-velocity WFs, since the reported velocity spreads of the H_2O maser emission in Group B (IRAS 15103−5754, IRAS 15445−5449, and IRAS 18443−0231) has been reported to be 70, 90, and 80 $\mathrm{km\,s^{-1}}$, respectively (Pérez-Sánchez et al. 2013a; Gómez et al. 2015b, and Chapter 6).

The clear differences in the infrared spectra of the Group A sources with respect to the classical high-velocity WFs of Group B (Fig. 7.1) strongly suggest that the difference between low- and high-velocity WFs is not necessarily due to a projection effect (although it could be possible in particular cases). Instead, they are intrinsically different objects in different evolutionary phases. This aligns with the suggestion put forward by Yung et al. (2013, see above), but we provide a stronger support based on spectroscopy. Moreover, our results may indicate a possible evolution of the ejection velocity of jets in evolved stars, which increases as the post-AGB evolution proceeds.

We note, however, that there is a potential bias in our sample since all three sources in our Group B present non-thermal radio continuum emission and evidence of the presence of ionized gas (due to the detection of infrared recombination lines). These properties might not be shared by all known high-velocity WFs. Extending our spectroscopic study to a larger sample of WFs would help confirm the evolutionary trends suggested in this work.

7.3.3 Origin of the CO and Na I emission in IRAS 15445−5449

Notably, IRAS 15445−5449 is the only source in our sample that shows the CO band and Na I doublet in emission. The CO band emission has been found in several post-AGB stars, which has been interpreted in some cases as tracing ongoing mass loss (e.g., Hrivnak et al. 1994). In the WF IRAS 16342−3814 (Claussen et al. 2009), the CO band and Na I doublet are both observed in emission (Gledhill & Forde 2012), as in IRAS 15445−5449. These features originate from an unresolved region around the central star of IRAS 16342−3814 and seem to be scattered toward our line of sight by dust in the nebula. Gledhill & Forde (2012) suggested that this emission may also arise from a circumstellar disk, which is analogous to what has been observed in young stellar objects (e.g., Martin 1997; Fedriani et al. 2020). The maser jet in IRAS 15445−5449 (Pérez-Sánchez et al. 2013a) suggests the presence of both a circumstellar accretion disk and active mass loss, which could be the origin of the CO band and Na I doublet. Further high-resolution observations can help unravel the spatial location and nature of this emission in IRAS 15445−5449.

7.4 Conclusions

We have presented near-infrared spectra of six objects with WF characteristics and radio continuum emission. The aim of our observations was to unveil their evolutionary stage. The main conclusions of this chapter are outlined as follows:

- The objects IRAS 18019−2216, IRAS 18464−0140, and IRAS 18480+0008 exhibit CO absorption bands characteristic of cool ($T_{\rm eff}\simeq$2100-5700 K) giant stars, while IRAS 15103−5754, IRAS 15445−5449, and IRAS 18443−0231 show H_2, Brγ, and He I emission lines consistent with shocks around post-AGB stars or photoionization from PNe. In particular, the emission line ratios in IRAS 18443−0231 indicate that it may have entered the photoionization phase and may be a nascent PN.
- The three WFs classified as giant stars are low-velocity WFs, while the other three are classical high-velocity WFs, which strongly suggests that the difference between low- and high- velocity WFs reflects intrinsically different evolutionary stages. Moreover, the combined spectral characteristics and maser kinematics support the idea that the ejection velocity of jets is higher for more evolved post-AGB stars than for younger ones.
- The spectrum of IRAS 15445−5449 shows the CO band in emission and Na I emission lines, suggesting the presence of a circumstellar disk and/or active mass loss.

These findings provide new spectroscopic evidence linking the velocity of WF jets to the evolutionary stages of their central stars. Future studies should extend the spectroscopic analysis to a larger sample of WFs, ideally complemented by high angular resolution imaging and maser monitoring, to confirm the proposed evolutionary sequence.

Acknowledgments

We are very grateful to our anonymous referee for their constructive comments that have improved the chapter. Based on observations collected at the European Organisation for Astronomical Research in the Southern Hemisphere under ESO programme(s) 111.24T1.001. This publication makes use of data products from the 2MASS, which is a joint project of the University of Massachusetts and the Infrared Processing and Analysis Center/California Institute of Technology, funded by the National Aeronautics and Space Administration and the National Science Foundation, and UKIDSS. RAC, LFM, JFG are supported by grants PID2023-146295NB-I00 and CEX2021-001131-S, funded by MCIN/AEI /10.13039/501100011033. RAC also acknowledges support by the predoctoral grant PRE2018-085518, funded by MCIN/AEI/ 10.13039/501100011033 and by ESF Investing in your Future. K.O. acknowledges the support of the Agencia Nacional de Investigación Científica y Desarrollo (ANID) through the FONDECYT Regular grant 1240301.

TABLE 7.1: Parameters of the near-infrared K-band spectroscopic observations.

Name	K (mag)	RA(J2000)	DEC(J2000)	DIT (s)	NDIT	Time (min)
I 15103	10.64	15:14:18.54	−58:05:20.38	360	2	48
I 15445	10.89	15:48:19.42	−54:58:20.15	360	2	48
I 18019	14.35	18:34:57.36	−22:15:50.84	300	3	60
I 18443	13.33	18:47:00.40	−02:27:52.47	360	2	48
I 18464	16.24	18:48:56.52	−01:36:43.32	800	2	106
I 18480	7.12	18:50:36.69	+00:12:28.34	30	4	11

[a] I15103 = IRAS 15013−5754, I15445 = IRAS 15445−5449, I18019 = IRAS 18019−2219, I18443 = IRAS 18443−0231, I18464 = IRAS 18464−0140, I18480 = IRAS 18480+0008.
[b] Broadband K magnitudes were taken from 2MASS, except for IRAS 18019−2216, which was taken from UKIDSS.
[c] Coordinates of the radio continuum emission reported in Suárez et al. (2015) and CHapter 3 and Chapter 6.
[d] Detector integration time.
[e] Number of frames.
[f] Total integration time.

7.A Parameters of the observations

The K-broadband magnitudes of the targets were taken from the Two Micron All Sky Survey (2MASS) and the United Kingdom Infrared Deep Sky Survey (UKIDSS [1]). The targets and parameters of the performed observations are shown in Table 7.1.

The small angular size of the targets allowed the creation of sky and target frames simultaneously by jittering (20″ randomly) and nodding (80″ along the slit) the NTT around the target position, without the need of further offset observations of the sky.

In order to favor the detection of weak emission lines, the Hawaii array was configured in non-destructive mode to take 30 readings per exposure and 4 samples per reading. The detector integration time (DIT) and the number of frames (NDIT) per jittered position were chosen depending on the broadband K magnitude of the target, night-time conditions, and field crowding. All targets were observed at least 2 NDIT per jittered position to enhance the signal-to-noise ratio of the emission.

7.B Emission line fluxes of Group B sources

In Table 7.2 we report the emission line fluxes in the spectra of Group B: IRAS 15103−5754, IRAS 15445−5445, and IRAS 18443−0231 (Fig. 7.1). These values have been obtained by

[1]The project is defined in Lawrence et al. (2007) and uses the UKIRT Wide Field Camera (Casali et al. 2007) and a photometric system described in Hewett et al. (2006). The pipeline processing and science archive are described in Hambly et al. (2008))

TABLE 7.2: Emission line fluxes, F(λ), in units of F(Brγ)=100 in the spectra of Group B sources.

Emission line	I 15103[a] F(λ)[d]	I 15445[b] F(λ)[d]	I 18443[c] F(λ)[d]
2.025 H_2	–	12.9±2.3	–
2.034 H_2	89.0±5.5	32.6±3.6	5.7±1.2
2.046 H_2	38.9±3.5	46.3±4.4	–
2.058 He I	65.8±4.9	92.5±6.6	176.9±6.9
2.074 H_2	43.7±3.5	17.0±2.6	–
2.120 He I	–	–	8.1±2.2
2.122 H_2	264.5±8.9	117.0±7.2	19.9±2.3
2.166 Brγ	100±7	100±9	100±3
2.210 Na I	–	26.4±3.1	–
2.223 H_2	150.1±6.4	137.5±7.6	2.73±0.29
2.240 H_2	–	17.1±2.6	–
2.248 H_2	25.3±2.7	22.4±3.0	–
2.294 CO	–	89.5±5.9	–
F(Brγ)	4.80±0.32	2.00±0.19	1.730±0.044

[a] IRAS 15103−5754.
[b] IRAS 15445−4559.
[c] IRAS 18443−0231.
[d] '–' stands for not detected.
[e] In units of 10^{-18} W m^{-2}.

fitting gaussians following standard procedures in the software IRAF[2].

[2]IRAF is distributed by the National Optical Astronomy Observatories, which is operated the Association of Universities for Research in Astronomy, Inc., under contract to the National Science Foundation.

Chapter 8

Near-infrared and optical spectroscopy on the nascent planetary nebula Vy 2-2: Evidence of binary-star evolution

8.1 Introduction

The evolution of stars with initial masses (M_i) up to 8 $M_\odot$ (e.g., the Sun) from the asymptotic giant branch (AGB) into the planetary nebula (PN) phase is one of the fastest and most astonishing processes in stellar evolution, resulting in the transformation of a roughly spherical envelope into a plethora of non-spherical morphologies (Manchado et al. 1996a) ionized by central stars of different spectral types (Weidmann et al. 2020). The identification of nascent PNe is thus crucial to investigate the first stages of the PN formation. In particular, OH maser-emitting PNe (OHPNe) are considered to be nascent PNe (Uscanga et al. 2012) because OH masers tend to disappear in timescales of $\sim 10^3$ yr after the AGB (Lewis 1989; Uscanga et al. 2012; Uno et al. 2021), while, in comparison, the PN phase starts 10^3-10^4 yr after the AGB, depending on M_i (Blöcker 1995; Miller Bertolami 2016). To date, only eight OHPNe have been identified: Vy 2-2, IRAS 17393–2727, K 3–35, IRAS 17347–3139, JaSt 23, IRAS 16333–4807, and Vo 1 (Seaquist & Davis 1983; Miranda et al. 2001; Uscanga et al. 2012; Qiao et al. 2016a, and see Chapter 6).

Vy 2-2 (PN G045−02.7; Vyssotsky et al. 1945) is the first PN in which maser emission was detected. Davis et al. (1979) reported the detection of the OH maser line at 1612 MHz towards this PN, based on Arecibo observations. Seaquist & Davis (1983) confirmed the association of the radio continuum and 1612 MHz emission from Vy 2-2 using accurate interferometric positions. Afterwards, Gómez et al. (2016) reported the presence of shock-excited OH maser transition at 1720 MHz. Water and silicon monoxide masers have not been detected to date in this PN (Gómez et al. 1990; de Gregorio-Monsalvo et al. 2004; Cala et al. 2024a).

Vy 2-2 is also peculiar because the ionic abundances obtained from optical recombination lines (ORLs) are unusually higher than those obtained from collisionally excited lines (CELs). The difference of ionic abundances obtained with these two types of lines is usually quantify with the abundance discrepancy factor (*adf*), defined as the $O^{2+}_{ORL}/O^{2+}_{CEL}$ abundance ratio, and has a typical value of *adf*(O^{+2})$\lesssim$5 among PNe (Wesson et al. 2005, 2018). For Vy 2-2, an initial value of *adf*(O^{+2})$\simeq$11.8 has been reported by Wesson et al. (2005). Such a high *adf* tends to favor the inclusion of H-deficient ejecta (Wesson et al. 2003) and/or the interaction between the central star and a companion as found in PNe hosting a binary central star (Wesson et al. 2018; Jacoby et al. 2020). However, a new value of *adf*(O^{+2})$\simeq$4.3 has recently been reported for this OHPN by Ruiz-Escobedo & Peña (2022), which is usual for PNe. It is obvious that a new independent determination of the *adf* in Vy 2-2 is required to solve this discrepancy and to properly interpret the object.

The radio continuum emission of Vy 2-2 is consistent with thermal (free-free) emission from photoionized gas. The flux density (S_ν) dependence at radio frequencies ν<14 GHz has a spectral index (α, where $S_\nu \propto \nu^\alpha$) α=1.30$\pm$0.07, which indicates a partially optically thick regime for the free-free emission (Seaquist & Davis 1983; Christianto & Seaquist 1998). Figure 8.1 (left) shows the radio continuum map of Vy 2-2 at 4.9 GHz adapted from Seaquist & Davis (1983) (see their Fig. 1). It shows that this OHPN is composed of a very bright and compact central core surrounded by a weak bipolar formation with the major axis at position angle (pa) $\simeq$34º (Seaquist & Davis 1983). At frequencies ν>14 GHz the radio continuum spectrum of Vy 2-2 flattens to a value of $\alpha\simeq-0.1$, which is more consistent with optically thin emission (Seaquist & Davis 1983). Furthermore, the very bright core is resolved into a circular shell with a radius of $\simeq$0.″24 at 15 and 22 GHz (Christianto & Seaquist 1998).

Figure 8.1 (right) also presents the Hα image of Vy 2-2 obtained from the legacy archive of the Hubble Space Telescope (*HST*). As in the radio images, it clearly shows a bright central core, and faint emission extending up to $\simeq$2.″3 from the center tracing a circular or slightly elliptical shell. Miranda & Solf (1991) (hereafter MS91) identified a bright, slowly expanding compact central core and a bipolar formation in Vy 2-2 with the main axis at position angle PA$\simeq$34 by means of spatially resolved high-resolution optical long-slit spectroscopy. These structures probably correspond to those observed at 4.9 GHz (Fig. 1, left). The analysis by MS91 was based on the [N II]λ6583 emission line only, but it would be interesting to extend it to other emission lines to obtain a more complete picture of the internal kinematics and ionization structure of the object. Finally, Ramos-Larios et al. (2016) found in the *HST* images at least four concentric rings spaced by $\sim$0.″55 around the bipolar nebula. Moreover, Kaplan et al. (2026) recently found a pair of high-velocity jets or bullets along the North-South direction, indicating that collimated outflows are also present in Vy 2-2.

Other observations indicate the presence of carbon monoxide (CO; Huggins et al. 1996), molecular hydrogen (H_2; Hora et al. 1999), a photodissociation region (PDR; Liu et al.

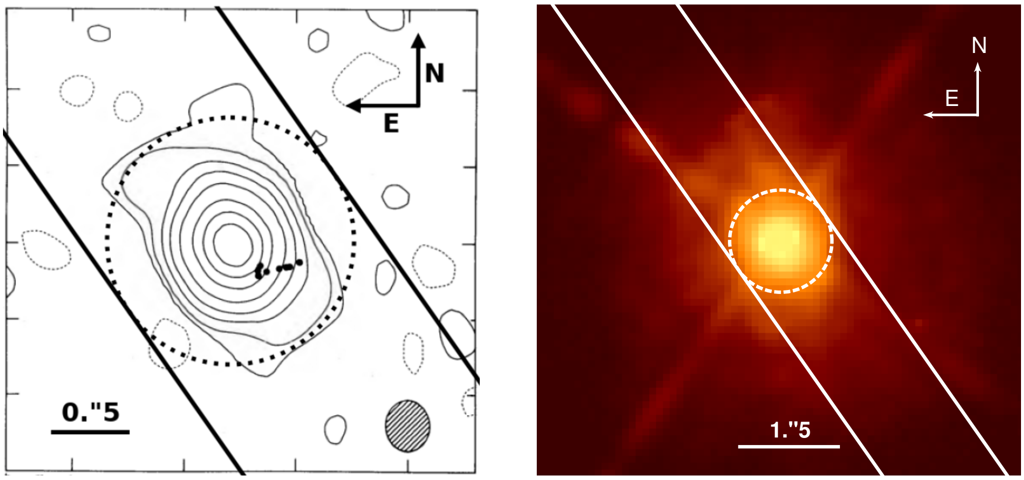

FIGURE 8.1: *Left.* Contour map of Vy 2-2 at 4.9 GHz adapted from Seaquist & Davis (1983). The hatched ellipse at the bottom right represents the beamsize of the VLA interferometer. The black dots mark the positions of the 1612 OH masers. The black solid lines and dashed circle represent the long-slit of CAFOS (width = 1.″5) and the CARMENES fiber FOV (diameter = 1.″5), respectively. *Right.* Hα image of Vy 2-2 obtained with the *HST*. The white solid lines and dashed circle represent the same as in the left panel.

2001), silicate dust and H_2O ice (Molster et al. 2002), as well as dredge up material (Sterling et al. 2015). Silicon carbonide (SiC) and polycyclic aromatic hydrocarbons (PAHs) have not been detected (Rinehart et al. 2002; Cohen & Barlow 2005). Therefore, the circumstellar environment of Vy 2-2 is O-rich.

In this chapter we present and analyze new intermediate- and high-resolution spectroscopic observations on the OHPN Vy 2-2. The intermediate-resolution spectra are used to derive the physical conditions and chemical abundances from both CELs and ORL, aiming at a redetermination of the *adf*. The high-resolution spectra are used to analyze the internal kinematics of the nebula in emission lines of different excitation and ionization potential, aiming at obtaining a more detailed description of the morphokinematic and ionization structure of this object. With our results we provide relevant hints in our understanding of formation and evolution of the nascent PN Vy 2-2.

8.2 Observations and data reduction

8.2.1 Intermediate-resolution optical spectroscopy

Intermediate-resolution, long-slit spectra were obtained on Calar Alto Observatory (Almería, Spain) with the Calar Alto Faint Object Spectrograph (CAFOS) at the 2.2 m telescope on 2016 August 24 (proposal ID: H16-2.2-024, P.I: L.F. Miranda). The detector was a SITe CCD with 2048×2048 pixels. We used grisms B-100 and R-100 to cover the spectral ranges 3200-6200 Å and 5800-9600 Å, respectively, at a dispersion of $\sim$2.0 Å px^{-1}. The spatial scale in the detector is 0.″53 pixel^{-1}. In Fig. 8.1 we show the position and orientation of the used long-slit (width of 1.″5). It was centered on the object, and oriented at position angle PA = 35°, hence covering the bright core and the weak bipolar emission. The spectra were taken with exposure times of 1200, 300, 120, and 60 s using the grism B-100, and of 1200, 300, 60, 30, and 20 s using the grism R-100. The spectrophotometric standard star BD+28°4211 was also observed for flux calibration. Sky was photometric during the observations and the seeing was ∼1.″5.

Each individual spectrum was reduced following standard procedures in IRAF[1] package. We note that the flux calibration failed at the very red edge of the CCD, coinciding with the [S III]λ9532 emission line; therefore the fluxes of this emission line are unreliable and will be not considered further in this chapter. The use of very different exposure times allow us an optimal measurement of the strongest emission lines in the short exposure spectra, of very faint emission lines in deepest ones, and several measurements of emission lines with intermediate intensity. A gaussian or multi-gaussian (in the case of blended lines) line fit was used to measured the emission line fluxes. The individual flux measurements of each emission line in each spectrum were finally combined into a single mean value, weighted by the exposure time. The physical conditions and ionic abundances were derived using Pyneb (Luridiana et al. 2015).

8.2.2 High-resolution optical and near-infrared spectroscopy

High-resolution optical and near-infrared échelle spectra were obtained on Calar Alto Observatory on 2016 July 12 with the Calar Alto high-Resolution search for M dwarfs with Exoearths making use of the Near-infrared and optical Échelle Spectrographs (CARMENES) (proposal ID: H16-3.5-0.36; PI: L.F. Miranda). The detectors for the optical and near-infrared spectra were an e2v CCD with 4096×4096 pixels, and two Teledyne Hawaii arrays with 2048×2048 pixels, respectively. CARMENES is coupled to the 3.5 m telescope with two optical fibers (diameter=1.″5), one for the target, and one for sky. The wavelength coverage of the spectra is 5200-9600 Å and 9600-17100 Å for the optical and near-infrared ranges, respectively. The spectral resolution (FWHM) is ≃2.4–3.2 $\mathrm{km\,s^{-1}}$ in the visible channel and ≃4.3–5.4 $\mathrm{km\,s^{-1}}$ in the infrared one. The CARMENES fiber for the object was centered on Vy 2-2 and covers the bright central region and the bipolar lobes (Fig 1). Seeing was ≃1.″5 and no flux calibration was carried out because we are interested in the internal kinematics of the object.

Five optical and near-infrared spectra were taken with an exposure time of 300 s each. The spectra were reduced with the pipeline CARACAL (Caballero et al. 2016). The five individual visible and five near-infrared spectra were combined into one final spectra at either wavelength range, making use of a statistical median, to increase the signal-to-noise ratio and to remove cosmic rays. The analysis of these final spectra was done using IRAF

[1]IRAF is distributed by the National Optical Astronomy Observatories, which is operated the Association of Universities for Research in Astronomy, Inc., under contract to the National Science Foundation.

and the final errors were obtained propagating errors from each individual spectrum. We have also inspected the sky fiber to confirm that relevant sky emission lines do not exist when compared with those from Vy 2-2. It should be noted that CARMENES uses vacuum wavelengths to carry out the wavelength calibration; consequently, to extract the information from the emission lines (e.g., radial velocity) we used the vacuum rest wavelengths as obtained from NIST[2] database. Nevertheless, in the figures and tables of this chapter we will use the more common air wavelengths.

8.3 Results

TABLE 8.1: Intrinsic emission line intensities in Vy 2-2 in units of $I(\mathrm{H}\beta)$=100.

Emission line	$f(\lambda)$	$I(\lambda)$	Emission line	$f(\lambda)$	$I(\lambda)$
3705 He I+H 16	0.26	0.95 ± 0.21	5812 C IV	−0.203	0.231 ± 0.011
3712 H 15	0.255	1.05 ± 0.18	5874 He I	−0.216	25.76 ± 0.44
3727 [O II]	0.25	12.06 ± 0.55	5958 Si II	−0.229	0.14 ± 0.01
3750 H 12	0.247	2.23 ± 0.31	5978 Si II	−0.231	0.095 ± 0.008
3770 H 11	0.244	2.60 ± 0.24	6045 O I	−0.245	0.134 ± 0.019
3798 H 10	0.245	3.65 ± 0.25	6300 [O I]	−0.285	1.215 ± 0.044
3818 He I	0.234	0.61 ± 0.08	6312 [S III]	−0.287	2.976 ± 0.041
3835 H 9	0.236	4.43 ± 0.24	6347 S III	−0.292	0.153 ± 0.011
3868 [Ne III]	0.228	46.85 ± 1.43	6363 [O I]	−0.294	0.420 ± 0.011
3889 He I+H 8	0.223	9.91 ± 1.35	6548 [N II]	−0.321	6.77 ± 0.18
3967 Hϵ+[Ne III]	0.203	42.59 ± 0.67	6563 Hα	−0.323	285.0 ± 9.3
3997 [F IV] + N II	0.195	0.141 ± 0.007	6583 [N II]	−0.326	18.28 ± 0.62
4024 He I	0.189	2.19 ± 0.20	6678 He I	−0.338	4.86 ± 0.07
4040 N II	0.189	0.105 ± 0.008	6716 [S II]	−0.343	0.305 ± 0.012
4045 N II	0.189	0.061 ± 0.008	6731 [S II]	−0.345	0.563 ± 0.012
4060 [F IV]	0.179	0.350 ± 0.024	7000 O I	−0.376	0.127 ± 0.004
4068 [S II]	0.18	2.64 ± 0.13	7065 He I	−0.383	11.51 ± 0.30
4069 [O II] + [O II]	0.178	1.110 ± 0.033	7135 [Ar III]	−0.39	22.46 ± 1.60
4077 [O II] + [O II]	0.178	0.59 ± 0.05	7155 [Fe II]	−0.393	0.309 ± 0.012
4089 O II	0.177	0.290 ± 0.024	7231 [C II]	−0.401	0.191 ± 0.007
4102 Hδ	0.172	19.23 ± 0.33	7254 O I	−0.403	0.169 ± 0.007
4144 He I	0.163	0.527 ± 0.037	7281 He I	−0.406	1.057 ± 0.020
4266 C II	0.141	0.269 ± 0.021	7298 He I	−0.407	0.072 ± 0.004
4340 Hγ	0.129	39.24 ± 0.52	7319 [O II]	−0.41	10.31 ± 0.21
4363 [O III]	0.124	7.85 ± 0.49	7330 [O II]	−0.411	9.73 ± 0.20
4388 He I	0.117	0.76 ± 0.19	7378 [Ni II]	−0.416	0.164 ± 0.003

[2] https://www.nist.gov/pml/atomic-spectra-database

Emission line	$f(\lambda)$	$I(\lambda)$	Emission line	$f(\lambda)$	$I(\lambda)$
4471 He I	0.095	6.20 ± 0.05	7387 Fe II	−0.416	0.079 ± 0.003
4591 O II	0.065	0.085 ± 0.003	7410 Si II	−0.42	0.078 ± 0.004
4596 O II	0.065	0.077 ± 0.003	7452 [Fe II]	−0.423	0.052 ± 0.002
4631 N II	0.052	0.270 ± 0.018	7466 N I	−0.424	0.0350 ± 0.0021
4640 O II + O II + N II	0.052	0.718 ± 0.019	7498 He I	−0.427	0.073 ± 0.002
4649 O II + O II + C III	0.052	0.985 ± 0.019	7751 [Ar III]	−0.451	4.95 ± 0.11
4658 C IV + Fe III	0.052	1.415 ± 0.026	7816 He I	−0.457	0.174 ± 0.007
4686 He II	0.033	1.736 ± 0.031	7888 Fe I	−0.463	0.0461 ± 0.0019
4701 Fe III	0.034	0.744 ± 0.030	7998 Fe I	−0.475	0.0210 ± 0.0019
4712 [Ar IV]	0.036	1.239 ± 0.025	8045 C II	−0.477	0.072 ± 0.0021
4733 [Fe III]	0.031	0.247 ± 0.028	8392 P 20	−0.509	0.53 ± 0.05
4740 [Ar IV]	0.029	0.25 ± 0.05	8413 P 19	−0.512	0.57 ± 0.05
4753 [Fe III]	0.027	0.276 ± 0.036	8438 P 18	−0.516	0.67 ± 0.05
4768 [Fe III]	0.024	0.172 ± 0.007	8446 O I	−0.517	1.62 ± 0.05
4813 [Fe III]	0.012	0.072 ± 0.003	8467 P 17	−0.521	0.74 ± 0.05
4861 Hβ	0	100.0 ± 2.54	8502 P 16	−0.526	0.92 ± 0.05
4880 [Fe III]	−0.005	0.41 ± 0.07	8528 He I	−0.53	0.062 ± 0.030
4922 He I	−0.014	1.65± 0.04	8545 P 15	−0.532	0.93 ± 0.05
4959 [O III]	−0.023	219.7 ± 18.0	8579 Cl II	−0.537	0.19 ± 0.06
5007 [O III]	−0.034	635.3 ± 8.5	8598 P1 4	−0.54	1.06 ± 0.05
5159 Fe I + C I	−0.064	0.199 ± 0.042	8617 [Fe II]	−0.543	0.185 ± 0.027
5192 [Ar III]	−0.073	0.195 ± 0.019	8647 He I	−0.547	0.090 ± 0.029
5199 N I	−0.074	0.113 ± 0.017	8665 P 13	−0.55	1.19 ± 0.05
5270 [Fe III]	−0.089	0.85 ± 0.05	8750 P 12	−0.562	1.38 ± 0.05
5411 He II	−0.118	0.170 ± 0.022	8863 P 11	−0.578	1.674 ± 0.030
5517 [Cl III]	−0.139	0.119 ± 0.014	8995 He I	−0.596	0.125 ± 0.017
5537 [Cl III]	−0.143	0.298 ± 0.024	9015 P 10	−0.599	2.26 ± 0.17
5666 N II	−0.147	0.069 ± 0.002	9069 [S III]	−0.606	44.60 ± 1.44
5676 N II + 5679 N II	−0.147	0.150 ± 0.002	9209 He I	−0.612	0.563 ± 0.049
5755 [N II]	−0.191	2.872 ± 0.037	9229 P 9	−0.612	7.975 ± 0.102
5801 C IV	−0.201	0.253 ± 0.006	9462 He I	−0.618	5.89 ± 0.14
log $F_{H\beta}$ (erg cm^{-2} s^{-1})		−11.649 ± 0.003			
c(Hβ)		1.66 ± 0.03			

8.3.1 Nebular emission lines

Table 8.1 lists the nebular emission lines identified in the intermediate-resolution spectra of Vy 2-2. From the Hα and Hβ emission line fluxes, a theoretical Hα/Hβ=2.85 intensity ratio, and the interstellar extinction law of (Seaton 1979), we obtain a logarithmic extinction

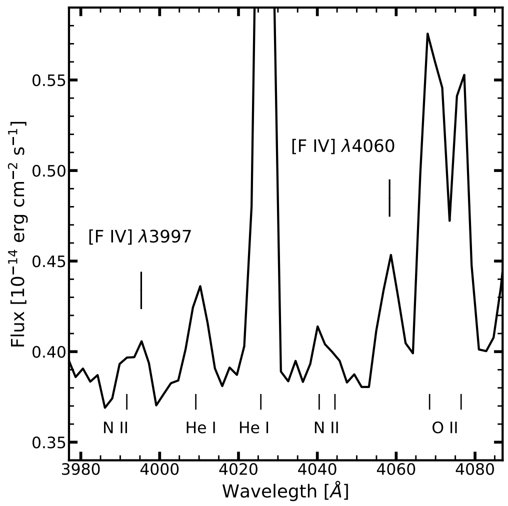

FIGURE 8.2: The 3980-4885 Å region of deepest spectrum of Vy 2-2. The possible [F IV] λ3997,4060 emission lines as well as other recombination emission lines are marked.

coefficient at Hβ, cH(β)=1.66±0.03. This value agrees with those reported by Wesson et al. (2005) and Arkhipova et al. (2017) but is very different from 0.66±0.06 reported by Ruiz-Escobedo & Peña (2022).

Table 8.1 also shows the intrinsic emission line intensities using the interstellar extinction law of Seaton (1979), and the observed Hβ flux. In this chapter we do not show the nebular spectrum of Vy 2-2 because similar ones have already been published elsewhere (e.g. Arkhipova et al. 2017). However, a detailed inspection of our spectra allowed us to identified for the first time ORLs and CELs many of which are key to determine some physical conditions in Vy 2-2. These lines will be individually mentioned, and parts of the spectra shown later in this section.

8.3.2 Fluorine in Vy 2-2?

In Fig. 8.2 we show the 3980-4085 Å region of the deepest blue spectrum of Vy 2-2, where we have identified two emission lines which may be the forbidden ones of the triply ionized doublet of fluorine, namely, [F IV]λ3997,4060. They are clearly identified only in this spectrum. In Table 8.1 we include their dereddened emission line intensities and we note that the λ3997 line is blended with the N II λ3991 one (Fig. 8.2. Using a two-gaussian line fit to separate these two emission lines we obtained $I(\lambda4060/\lambda3997)$ ≃2.5, which is similar to the theoretical value of ≃2.8 (Zhang & Liu 2005; Otsuka et al. 2008). Moreover, we do not detect the [F II]λ4789 emission line in our spectra, as it happens in other PNe where λ3997,4060 are detected (Zhang & Liu 2005; Otsuka et al. 2008). If our identifications are correct, they would be the first report of F in Vy 2-2.

TABLE 8.2: Elemental abundances (12+log[X/H] scale) in Vy 2-2 derived from CELs obtained in this work, by Wesson et al. (2005) (WLB05) and Ruiz-Escobedo & Peña (2022) (REP22), and in the Sun (Asplund et al. 2009).

	WLB05	REP22	This work	The Sun
He	11.03	11.06±0.01	$11.07^{+0.08}_{-0.06}$	10.93±0.01
O	7.98	$8.46^{+0.12}_{-0.05}$	$8.09^{+0.07}_{-0.09}$	8.69±0.05
N	7.83	$7.74^{+0.13}_{-0.09}$	$7.70^{+0.03}_{-0.06}$	7.83±0.05
Ne	7.24	$7.58^{+0.11}_{-0.05}$	$7.36^{+0.24}_{-0.21}$	7.93±0.10
S	6.65	7.31±0.05	$6.71^{+0.04}_{-0.03}$	7.12±0.03
Ar	5.88	6.48±0.03	$6.24^{+0.06}_{-0.07}$	6.40±0.13
Cl	-	$4.97^{+0.23}_{-0.11}$	$4.26^{+0.19}_{-0.12}$	5.50±0.30
Fe	-	$6.35^{+0.08}_{-0.06}$		7.50±0.04

8.3.3 Physical conditions, chemical abundances, and adf

We used the line intensity ratios between the CELs [O III]λ(4959+5007)/4363, [O II]λ(3726 +3729)/(7320+7330), and [Ar III]λ(7136+7751)/5192 to derive values of electron temperature (T_e), and those of [S II]λ6716/6731 and [Cl III]λ5517/5537 to derive values of electron density (N_e). We did not use the [N II]λ(6548+6584)/5755 line intensity ratio to obtain T_e because this ratio presents a high value ($\simeq$0.11, see Table 8.1), indicating collisional deexcitation. We found that the ionized gas seems to be composed by several zones with different physical conditions (T_e, N_e). In Table 8.7 we report these zones as Zone 1, 2, and 3, together with their corresponding values of T_e and N_e. Ruiz-Escobedo & Peña (2022) also identified three different zones in the ionized gas of Vy 2-2 with different physical conditions, although their zones present some differences with respect to ours. Nevertheless, we agree with Ruiz-Escobedo & Peña (2022) in the existence of a zone (Zone 3) in which Vy 2-2 clearly presents significantly higher T_e and N_e than in Zones 1 and 2.

Table 8.7 also shows the ionic abundances. These values were calculated taken into account the particular excitation conditions and ionization potential of each ion, as listed in Table 8.7. In general, our ionic abundances are similar to (or in between of) those reported by Wesson et al. (2005) and Ruiz-Escobedo & Peña (2022). We note that the ionic abundance of F has not been obtained because it requires knowing of Ne^{3+}, which is not available. For the elemental abundances, we use the ionization correction factors by Kingsburgh & Barlow (1994) and they are reported in Table 8.2, where we compare our values with those by Wesson et al. (2005), Ruiz-Escobedo & Peña (2022), and in the Sun (Asplund et al. 2009). Our results are compatible with (or in between of) those reported by Wesson et al. (2005) and Ruiz-Escobedo & Peña (2022), and we note that the abundances of Vy 2-2 are subsolar.

Physical conditions have been also obtained from ORLs (see Appendix 8.B for details about line identification). From the O II λ4649.13/4661.63 and λ4075.86/4070 line intensity ratios we obtain T_e(O II)=6309^{+769}_{-686} K, and N_e(O II)=4467^{+781}_{-664} cm^{-3}, respectively. We use Pyneb to determine the individual line abundances based on these physical conditions. The obtained values are listed in Table 8.3 and are in general agreement with those reported

TABLE 8.3: Ionic abundances relative to H^+ from ORLs.

Line	Ion	$[\times 10^{-4}]^a$
	O^{++}/H^+	
λ4638.86		18.07±4.90
λ4641.81		12.65±3.42
λ4649.13		10.01±0.36
λ4650.84		17.33±1.03
		15.23±1.27[b]
	C^{++}/H^+	
λ4267.0		**2.34±0.25**[b]
	N^{++}/H^+	
λ5666.63		3.74±0.12
λ5676.02		3.28±0.23
λ5679.56		3.36±0.05
		3.46±0.27[b]

[a] The errors are the upper and lower values obtained using the maximum and minimum values of each of the variables involved (N_e, T_e, and $I(\lambda)$).

[b] Final adopted ionic abundances. For O II and N II, the adopted values are the average of the individual line abundances.

by Wesson et al. (2005). In particular, they reported $O^{++}_{ORL}/H^+ \simeq 10.86$, which is comparable to ≃15.23 obtained by us. Ruiz-Escobedo & Peña (2022) found a different value of $O^{++}_{ORL}/H^+ \simeq 5.50$, most probably due to the different values of N_e(O II) obtained by them and by us (see the Appendix 8.B for more details).

To determine the N/O abundance ratio from ORLs, we used the expression N/O = ICF(N^{++}/O^{++})×($N^{++}_{ORL}/O^{++}_{ORL}$) as proposed by Delgado-Inglada et al. (2014) and their equations 14, 15, and 16. We obtained ICF(N^{++}/O^{++})=$0.99^{+0.30}_{-0.15}$ and, hence, N/O=$0.23^{+0.07}_{-0.09}$. This value is somewhat lower than that of 0.41±0.09 derived from CELs (Table 8.2). However, our values are even more discrepant from N/O≃0.66 obtained by Wesson et al. (2005), which was based on ORLs. The difference could be due to the fact that Wesson et al. (2005) used N^{++} lines that may be of stellar origin (see Sec. 8.3.4 for more details) while we used nebular N^+ recombination lines reported here for the first time (see Table 8.3).

The C/O abundance ratio was calculated with the expression C/O = ICF(C^{++}/O^{++}) × ($C^{++}_{ORL}/O^{++}_{ORL}$) as proposed by Delgado-Inglada et al. (2014). From Fig. 14 in Delgado-Inglada et al. (2014), we obtained $\log_{10}$ICF(C^{++}/O^{++})=$0.0^{+0.2}_{-0.1}$ and, hence, C/O=$0.15^{+0.09}_{-0.04}$. This is a lower value than that of ≃0.26 obtained by Wesson et al. (2005), but these would be compatible within the errors.

The ionic abundance reported in Tables 8.7 and 8.3 yield an *adf*(O^{2+})=13.60±2.57. This value is similar to ≃11.8 reported by Wesson et al. (2005), but is significantly different from $4.30^{+1.00}_{-1.16}$ reported by Ruiz-Escobedo & Peña (2022), providing support to the idea of an unusually high *adf*(O^{2+}) in Vy 2-2. Finally, we could not obtain *adf*(C^{2+}) and *adf*(N^{2+}) because C^{++}/H^+ and N^{++}/H^+ were obtained only for ORLs, and not for CELs.

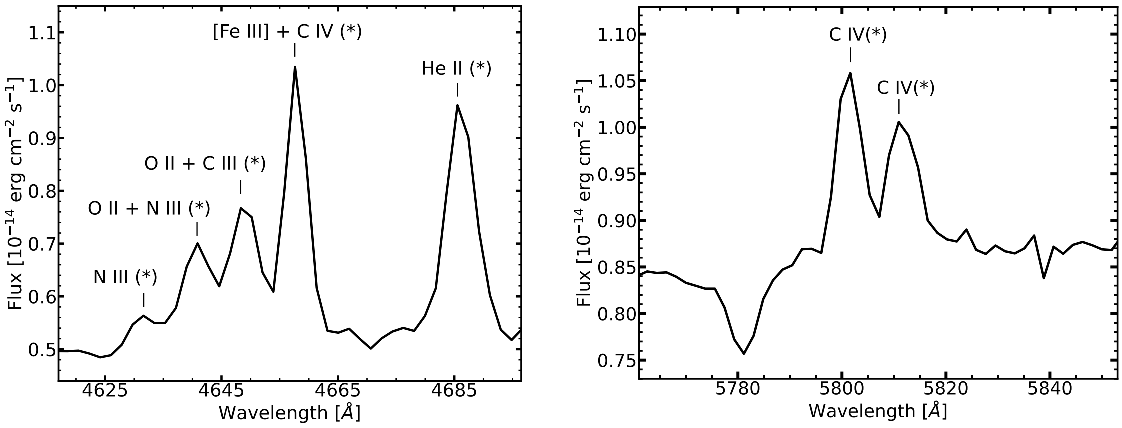

FIGURE 8.3: Weak emission lines (*wels*) (*) in the optical blue spectrum of Vy 2-2.

8.3.4 Stellar emission lines

The possible presence of stellar emission lines in Vy 2-2 was already suggested by Arkhipova et al. (2017), and Ruiz-Escobedo & Peña (2022) associated the recombination line He IIλ4686 to the central star of Vy 2-2. Fig. 8.3 presents our deepest blue spectrum in which stellar weak emission lines (*wels*) are clearly identified. Table 8.4 lists the intrinsic line intensities of these lines obtained with the same $c(\mathrm{H}\beta)$ as deduced for the nebula (Table 8.1).

The observed stellar *wels* in Vy 2-2 are similar to those observed in other PNe (Marcolino & de Araújo 2003). The detection of the doublet of C IV$\lambda\lambda$5801,5812 emission lines in our spectra is clear (Fig. 8.3). Moreover, the value of $I(\lambda5801)/I(\lambda5812)$ is $\simeq 4/3$, in agreement with the theoretical ratio (Moore 1945). Besides, if we assume the theoretical intensity ratio between the emission lines of $I(\lambda4658)/I(\lambda5812)$=5/4 (Moore 1945), the intensity of C IVλ4658 would be 0.316±0.008, indicating that this stellar C emission line is blended with nebular [Fe III]λ4658 emission line. The rest of the lines in Fig. 8.3 have been identified according to the spectra presented in Marcolino & de Araújo (2003), and taking into account the nebular emission lines observed in the high-resolution spectrum of Vy 2-2 presented by Ruiz-Escobedo & Peña (2022). Also, the intensity of the emission line at λ4649 (Table 4) includes a contribution from the stellar recombination line C IIIλ4650 of 0.385±0.026 (see Appendix 8.B). In principle, the presence of these C emission lines suggests that the central star of Vy 2-2 is C-rich, which strongly contrasts with the O-rich nature of the nebula (Sec. 8.3.3). Nevertheless, other possibilities will be discussed below (Sec. 8.4.2).

8.3.5 Internal kinematics of the nebula

In Figure 8.4 we show a representative set of emission line profiles observed in the final CARMENES spectrum, including recombination and forbidden emission lines of different ionization potential and state. The high spectral resolution achieved by CARMENES (Sec. 8.2.2) allows us to identify asymmetries and emission peaks in the line profiles, which are indicative

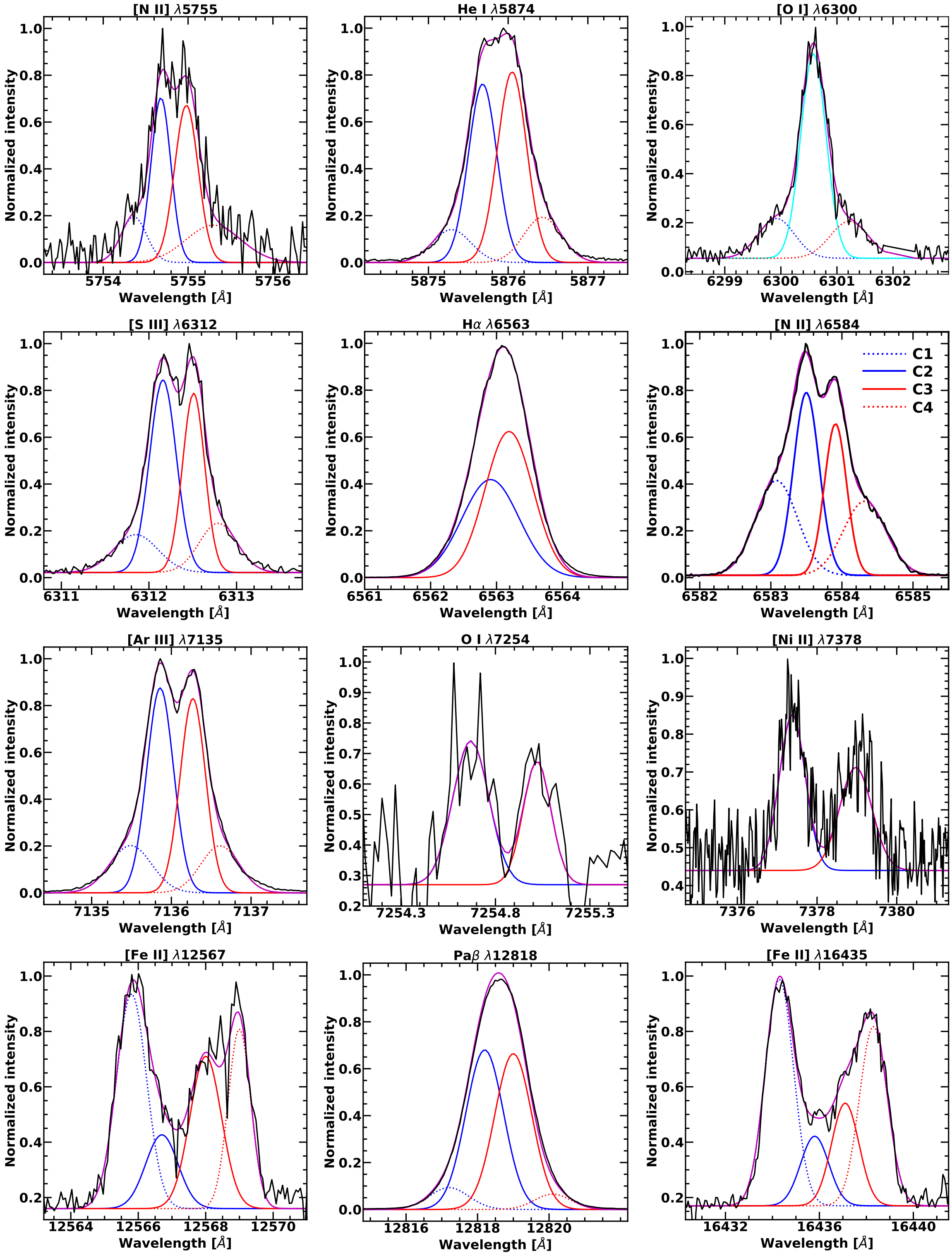

FIGURE 8.4: Profiles of selected emission lines in the optical and near-infrared high-resolution CARMENES spectra of Vy 2-2. Each emission line is identified at the top of its individual panel. The black line is the observed spectrum. The solid and dotted lines represent the central region (components C2–C3) and bipolar lobes (C1–C4), respectively (see the panel of the [N II]λ6585 emission line). Red and blue colors are used for blueshifted and redshifted emission, respectively, with respect to the systemic velocity of Vy 2-2 ($\upsilon_{\rm sys}(LSR)$ = $-50.7\,{\rm km\,s^{-1}}$). In the [O I] spectra, the cyan line represents the blended C2 and C3 components.

TABLE 8.4: Intrinsic intensities of the identified stellar emission lines or blends in units of $I(\mathrm{H}\beta)$=100.

Emission line[a]	$f(\lambda)$	$I(\lambda)$
N III (*) λ4631	0.052	0.270±0.018
O II + N III (*) λ4640	0.052	0.718±0.019
O II + C III (*) λ4649	0.052	0.985±0.019
[Fe III] + C IV (*) λ4658	0.052	1.415±0.026
He II (*) λ4686	0.033	1.736±0.031
C IV (*) λ5801	-0.201	0.253±0.006
C IV (*) λ5812	-0.203	0.231±0.011

[a] Stellar emission lines are marked with (*), other emission lines are nebular.

of the existence of different kinematical components in the nebula. In particular, two or four different kinematical components can be recognized, depending on the emission line.

To analyze and characterize the kinematical components we have performed a multi-gaussian line fit to the emission line profiles assuming two or four gausssians. We will use the wavelength at the intensity peak and the FWHM of each gaussian as representative of the radial velocity [υ_{r}(LSR)] and the velocity width ($\Delta\upsilon$) of each component, respectively. The results are listed in Table 8.8. An inspection of Table 8.8 reveals that the radial velocity defines four different kinematical components, hereafter refereed to as C1, C2, C3, and C4, with radial velocities around −80, −60, −40, and −20 km s^{-1}, respectively. These components are also indicated in Table 8.8. Moreover, the pairs C1–C4 and C2–C3 appear symmetric with respect to the radial velocity centroid of the emission profiles. The velocity width of C1 and C4 typically ranges from ∼15 to ∼30 km s^{-1}, which are values somewhat smaller than for C2 and C3. Components C1 to C3 were already identified by Miranda & Solf (1991) in the [N II]λ6584 emission line profile, but they did not identify C4 probably due to the lower spectral resolution in their spectra (FWHM≃6 km s^{-1}) than in the CARMENES ones (Sec. 8.2.2).

Only C2 and C3 could be unambiguously identified in the Hα emission line. This is most probably because Hα shows broad emission wings that extend up to ∼1500 km s^{-1} (not show here) and hid the weaker C1 and C4 components. Extended Hα wings in Vy 2-2 were already reported by Arrieta & Torres-Peimbert (2003) who found a velocity extent similar to ours and attributed them to Rayleigh-Raman scattering. The Paschen lines are not affected by this scattering and the four components are recognized. We have not included the [S II]λ6716,6731 lines (not shown here) in our analysis because they are extremely weak and have a very low signal-to-noise ratio. We have not included them in our analysis. The [O I]λ6300,6363 lines present a peculiar profile (Fig. 4): C1 and C4 are clearly present but a single emission peak is observed where the two central emission peaks due to C2 and C3 would be expected. We tried to fit these lines using two Gaussian profiles at their center, but no reasonable result was obtained. In Table 8.8 we assign the measurements to C2-C3. In the O Iλ7256 line only C2 and C3 can be identified while in the [Ni II]λ7380 line only C1 and C4 can be recognized.

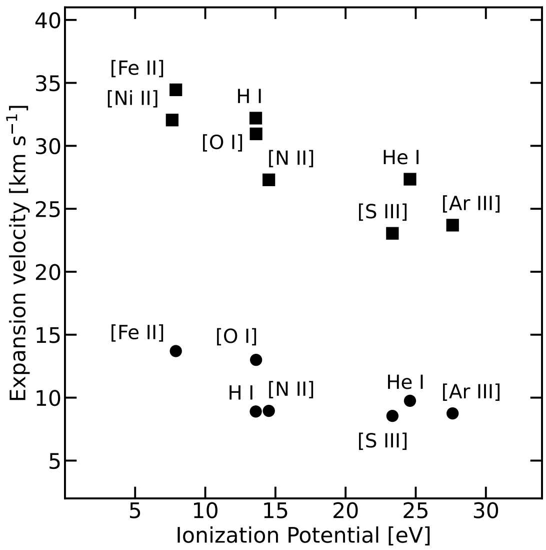

FIGURE 8.5: Expansion velocity versus ionization potential in the bipolar lobes (filled squares) and bright central region (filled circles) of Vy 2-2 (see Table 8.5).

The intensity of the He I and H I emission lines is largely dominated by C2–C3, and a similar situation is observed in the relatively high excitation emission lines of [Ar III] and [S III] (Fig. 4). In [N II] the intensity difference between C2–C3 and C1–C4 is not so marked, while C1–C4 clearly dominate the low-excitation lines of [Ni II] and [Fe II]. It is evident that C2–C3 are related to regions with higher excitation than those where C1–C4 arise.

Finally, in order to obtain the systemic velocity ($\upsilon_{\rm sys}$) of Vy 2-2, we firstly compute the mean value of the radial velocities of the components identified in all emission lines. Afterwards, we determined two different values for $\upsilon_{\rm sys}$: the first one using C1 and C4, and the second one using C2 and C3. These three values of $\upsilon_{\rm sys}$ were found to be virtually identical to each other, indicating a noticeable symmetry in the internal kinematics of Vy 2-2. We finally report $\upsilon_{\rm sys}({\rm LSR}) = -50.7 \pm 0.1$ km s^{-1}.

8.4 Discussion

8.4.1 The morphokinematical structure of Vy 2-2

MS91 detected three components in the line profile of [N II] spectra, and proposed a simple model for the 3D structure of Vy 2-2, namely, a slowly expanding central region and two wide bipolar lobes. The high resolution of the CARMENES spectra allowed us to detect four components and to refine the model. A comparison of the [N II] line profile in Fig. 8.4 with the position-velocity maps of the [N II] emission line in MS91 (e.g., their Fig. 3) shows that C2–C3 are located at the center of the emission line and should correspond to the central region, C1 is located towards the NE, and C4 towards the SW, consequently, C1–C4 trace the bipolar lobes. Remarkably, while the existing images of Vy 2-2 do not provide information

TABLE 8.5: Mean ionic expansion velocities (υ_e) of each spectral component of the ionized gas shown in Table 8.8, with respect to the systemic velocity $\upsilon_{sys} \simeq -50.7$ km s^{-1}.

Ion	Component	υ_e [km s^{-1}]
H^+	1	−31.5
	2	−8.8
	3	+9.0
	4	+32.9
He^+	1	−29.3
	2	−10.1
	3	+9.4
	4	+25.4
N^+	1	−28.0
	2	−9.5
	3	+8.4
	4	+26.6
O^0	1	−31.0
	2	−13.0[a]
	3	+13.0[a]
	4	+30.9
S^{2+}	1	−22.9
	2	−8.2
	3	+8.4
	4	+21.7
Ar^{2+}	1	−25.7
	2	−9.8
	3	+7.7
	4	+21.7
Fe^+	1	−33.5
	2	−10.1
	3	+17.3
	4	+35.4
Ni^+	1	−30.1
	4	+34.0

[a] Obtained from $\Delta\upsilon$ of component 2–3 of the [O I]λ6300 in Table 8.8 (see text for details).

about properties of the nebular components, our CARMENES spectra allow us to state that the central region presents a higher excitation than the bipolar lobes where a very low excitation should exist in their outermost regions, as suggested by the presence of [Fe II] and [Ni II] emission lines with the highest expansion velocities (see also next paragraph).

Assuming this morphological structure we can obtain the expansion velocity of each kinematic component in each ion. Table 5 shows the results where we have averaged the values from emission lines of the same ion. To further analyze these results, we have plotted the expansion velocity versus the ionization potential of each ion in the central region and bipolar lobes. The results are presented in Fig. 8.5 and show the well-known Wilson effect in both structures, with the expansion velocity increasing for decreasing ionization potential (Wilson 1950). This strongly suggests a stratification in the nebula such that the low/high

TABLE 8.6: Estimated mass of the main nebular components in Vy 2-2 and mass ratios between some of them.

$\mathrm{Mass}_{component}$	Mass [$M_\odot$]
$M_{\rm ion}$ [a]	$1.6\times10^{-4}\times D^{2.5}$
$M_{\rm PDR}$ [b]	$1.6\times10^{-2}\times D^{2}$
$M_{\rm m}$ [c]	$7.0\times10^{-4}\times D^{2}$
$M_{\rm dust}$ [a]	$1.4\times10^{-6}\times D^{2}$
$M_{\rm CSE}$ [d]	4.8×10^{-2}
$M_{\rm RGB}$ [e]	0.2
$M_{\rm lost}$ [f]	0.25

[a] Ionized ($M_{\rm ion}$) and dust ($M_{\rm dust}$) mass reported by Davis et al. (1979).
[b] Mass of the PDR ($M_{\rm PDR}$) obtained from the [C II]λ158 μm flux (Liu et al. 2001), C/H=4.661×10^{-4} (Wesson et al. 2005), and the expression in Liu et al. (2001).
[c] Molecular mass ($M_{\rm m}$) determined by Huggins et al. (1996).
[d] Total circumstellar mass ($M_{\rm CSE}$) as the sum of the previous values, adopting $D = 1.68\pm0.02$ kpc (see Sec. 8.4.1).
[e] Typical mass lost in the red giant branch phase ($M_{\rm RGB}$) (Dorman et al. 1993).
[f] Total mass lost $M_{\rm lost}=M_{\rm CSE}+M_{\rm RGB}$.

excitation lines arise in the outer/inner nebular regions. These results are typical of a photoionized nebula. In fact, we have not found any evidence in our optical spectra for shock excitation in the main nebula, which is also indicated by the near-infrared spectra by Kaplan et al. (2026) who found shock excitation only in the bipolar jets/bullets. In particular, we note that the intensities of the [Fe II]λ8761 and [Ni II]λ7378 emission line place Vy 2-2 in the photoionized region of the log([Ni II]λ7378/Hα) versus log([Fe II]λ8761/Hα) obtained by Bouvis et al. (2025, their Figure 15). Moreover, the intensities of the near-infrared Brγ, He I 2.058μm, and He I 2.120μm recombination lines obtained by Hora et al. (1999) in Vy 2-2 place it in a position incompatible with shock-ionization models, according to the diagnostic diagram presented in Chapter 7. Corroborating that shock excitation does not dominate or is not relevant in our spectrum of the main ionized shell of Vy 2-2 (and in any other PN or structure) is a crucial step to confirm whether the classical method to obtain chemical abundances is applicable. If shocks play an important role in the observed spectrum, this classical method may provide unrealistic results (See Chapter 5).

Assuming a spherical shell of radius $\simeq0''.24$, as suggested by the 14.965 and 22.485 GHz radio continuum emission maps, and an expansion velocity of 9 km s^{-1} in H$^+$ for the central region, we obtain a kinematical age of $\simeq125\times D$ [kpc] yr where D is the distance to the nebula. For Vy 2-2, Christianto & Seaquist (1998) obtained a value of 1.13 ± 0.12 mas yr^{-1} for the angular expansion of the central region as observed in radio continuum. Combining this value with the expansion velocity of the central region in H$^+$, and assuming spherical geometry, we derive a distance of $\simeq1.68\pm0.02$ kpc, implying a kinematical age of 210 ± 3 yr, which further corroborates the general idea that Vy 2-2 is an extremely young PN.

8.4.2 The formation of Vy 2-2 and its central star

The central star of Vy 2-2 had never been identified before. The detection stellar emission lines would be the first direct detection of this central star and its *wels* spectral type.

However, Parthasarathy et al. (1998) and Weidmann et al. (2015) already showed that *wels* may not be of real spectral type of central stars because absorption lines are detected in some *wels* when observed at enough spectral resolution, indicating different classifications. Actually, observations of several PNe have shown that stellar emission lines, as those observed in Vy 2-2 (Fig. 3), arise from main-sequence companions irradiated by the central stars in post-common envelope binary systems (e.g., Miszalski et al. 2011a,b; Jones & Boffin 2017; Munday et al. 2020). Therefore, the possibility is open that Vy 2-2 hosts a post-common envelope binary.

Interestingly, more properties of Vy 2-2 also point to a close binary. The unusually high $adf(O^{2+})$ of ≃13.6 in Vy 2-2 has also been found by Wesson et al. (2018) in close binary systems (period around 1 day) with values of $adf(O^{2+}) \geq 10$. Concentric rings around the main nebula, bipolar morphologies and collimated outflows are signatures of binary central stars (Ivanova et al. 2013; Zou et al. 2020) and these structures are observed in Vy 2-2 (Ramos-Larios et al. 2016; Kaplan et al. 2026, Fig. 1 and Sect. 4.1). Fluorine production may also be related to binary star evolution (Otsuka et al. 2008). Finally, the Rayleigh−Raman scattering traced by the large Hα wings requires the existence of a very high density ($\geq 10^9$ cm^{-3}) region located very close to the central star, which could probably be better explained by invoking a companion (Miranda et al. 2022, and references therein).

If the observed stellar emission lines are associated to a companion, the central star of this PN remains unidentified. Fortunately, estimates for its M_i may be obtained from observed abundance ratios and other observational data. The value of $C/O=0.15^{+0.09}_{-0.04}$ in Vy 2-2 (Sec. 8.3.3) is extremely low and, to the best of our knowledge, the lowest one ever found in PNe. According to Miller Bertolami (2016) (see his Table 2), only stellar models with $M_i \lessapprox 0.85\,M_\odot$ and metallicities Z=1-10$\times 10^{-3}$ will end up in the AGB phase with such a low value of C/O surface abundance ratio. The subsolar metallicity found in Vy 2-2 is compatible with stellar models while the low M_i is compatible with the O-rich nature of the nebula and very low N/O abundance ratio which rules out hot bottom burning and, consequently, $M_i \geq 3$–4,$M_\odot$. Nevertheless, we note that the C/O abundance ratio of O-rich AGB stars increases after each thermal pulse and that a low C/O abundance ratio could also be caused if the AGB evolution of the progenitor of the central star is interrupted due to interaction with a companion (e.g. De Marco 2009; Karakas & Lattanzio 2014; Miller Bertolami 2016).

The M_i of the central star can also be estimated by calculating the mass of the main components of the nebula, namely, the ionized gas, the molecular gas, the photodissociation region (PDR), and dust. Table 8.6 lists the estimated mass of these components by using already reported values and/or available data. We note that the PDR is the heaviest component, followed by the molecular and ionized gas, while dust is the lightest one. With the distance to Vy 2-2 determined in Section 8.4.1, the total mass of the circumstellar nebula ($M_{\rm CSE}$) is $4.79{\pm}0.11 \times 10^{-2}\,{\rm M}_{\odot}$. In addition, assuming that the mass lost by the star during the red giant branch phase ($M_{\rm RGB}$) is $0.2{\pm}0.1\,{\rm M}_{\odot}$ (Dorman et al. 1993), the mass lost by the star $M_{\rm lost}$=$M_{\rm CSE}$+$M_{\rm RGB}$ during the previous evolutionary phases would be $0.25{\pm}0.10\,{\rm M}_{\odot}$. This value would be consistent with stellar models for $M_{\rm i}{\lesssim}0.9\,{\rm M}_{\odot}$ (Miller Bertolami 2016).

The results obtained above suggest an initial mass for the progenitor star of Vy 2-2 of $\lesssim$0.9 $\rm M_{\odot}$, implying a central star mass of $\simeq$0.5–0.6 $\rm M_{\odot}$ (Miller Bertolami 2016). If the stellar emission lines detected in Vy 2-2 indeed arise from an irradiated companion with a mass of 0.1–0.6 $\rm M_{\odot}$, as found in other *wels* binaries (Miszalski et al. 2011a,b; Jones & Boffin 2017; Wesson et al. 2018), orbital periods of 0.3–3.0 d and orbital separations of $\simeq$1.5–9.5 $\rm R_{\odot}$ could be expected (Wesson et al. 2018). Time-resolved spectroscopy of the stellar emission lines to look for periodic radial velocity modulations is crucial to confirm the binary nature of the central star of Vy 2-2 and to constrain some of its properties.

8.5 Conclusions

We have analyzed new intermediate- and échelle high-resolution spectra of the OHPN Vy 2-2 with the idea of obtaining a new value for the *adf* for this object, investigating the internal kinematics and structure of the nebula, and inferring its possible formation processes. The main conclusions of this work can be summarized as follows.

Our intermediate-resolution spectra have revealed many previously unreported nebular recombination (e.g., N^{+}) and forbidden (e.g., [Ni II] and, possibly, [F IV]) emission lines, as well as stellar recombination emission lines of C^{3+}, C^{4+}, and N^{3+}. Some of the newly detected nebular recombination emission lines are crucial in determining abundances from ORLs.

The analysis of the intermediate-resolution spectra corroborates that Vy 2-2 is composed by several regions characterized by their own $T_{\rm e}$ and $N_{\rm e}$, with an inner region where the electron density is very high ($\simeq$65000 cm^{-3}). Additionally, the broad Rayleigh–Raman scattering Hα wings observed in the high-resolution spectrum strongly suggest the existence of an extremely dense region ($\geq$10^{9} cm^{-3}) in the immediate vicinity of the central star.

The abundances determined from CELs are subsolar and similar to those obtained previously by other authors. The new value of the *adf*(O^{2+}) obtained from our intermediate-resolution spectra is 13.6±2.6 which favors including Vy 2-2 among the PNe with unusually high *adf*(O^{2+}).

The high-resolution spectra allow us to analyze the emission lines with different ionization degree and ionization potential. We identify four kinematical components in the nebula: two components related to the relatively high-excitation central region and two components tracing the relatively low-excitation bipolar lobes of the object. The kinematics observed in emission lines with different ionization potential, our optical and published near-infrared spectra indicate that shock excitation is not present in the main ionized shell of Vy 2-2. This provides support to apply to Vy 2-2 the usual method for calculating chemical abundances.

By combining the expansion velocity of the central region in H^+ with the angular expansion of the same region obtained from radio continuum observations, we obtain a distance of 1.68 ± 0.02 kpc to Vy 2-2, which implies a kinematical age of 210±3 yr, further supporting the extreme youth of this PN.

Although the stellar emission lines detected in Vy 2-2 suggest a *wels* type central star, they may be related to an irradiated close companion. This possibility is favored by the unusually high *adf*, the concentric rings, bipolar morphology, collimated outflows, the origin of the Rayleigh–Raman scattering Hα wings, and presence of fluorine. In fact, all these properties suggest that Vy 2-2 may host a post-common-envelope binary.

Finally, abundance ratios and an estimate for the mass lost by the star progenitor of Vy 2-2 during its life suggest a relatively low main-sequence initial mass of $\lesssim$0.9 $M_\odot$. If the stellar emission lines indeed arise in an irradiated companion, a comparison with similar systems suggests a secondary mass of 0.1–0.6 $M_\odot$, resulting in a binary system with an orbital period of $\simeq$0.3–3.0 d and an orbital separation of $\simeq$1.5–9.5 $R_\odot$.

Acknowledgments

CARMENES is an instrument for the Centro Astronómico Hispano-Alemán de Calar Alto (CAHA, Almería, Spain). CARMENES was funded by the Max-Planck-Gesellschaft (MPG), the Consejo Superior de Investigaciones Científicas (CSIC), the Ministerio de Economía y Competitividad (MINECO) and the European Regional Development Fund (ERDF) through projects FICTS-2011-02, ICTS-2017-07-CAHA-4, and CAHA16-CE-3978, and the members of the CARMENES Consortium (Max-Planck-Institut für Astronomie, Instituto de Astrofísica de Andalucía, Landessternwarte Königstuhl, Institut de Ciències de l'Espai, Institut für Astrophysik Göttingen, Universidad Complutense de Madrid, Thüringer Landessternwarte Tautenburg, Instituto de Astrofísica de Canarias, Hamburger Sternwarte, Centro de Astrobiología and Centro Astronómico Hispano-Alemán), with additional contributions by the MINECO, the Deutsche Forschungsgemeinschaft (DFG) through the Major Research Instrumentation Programme and Research Unit FOR2544 "Blue Planets around Red Stars", the Klaus Tschira Stiftung, the states of Baden-Württemberg and Niedersachsen, and by the Junta de Andalucía. This research is based on observations collected at the Centro Astronómico Hispano en Andalucía (CAHA) at Calar Alto, operated jointly by Junta de Andalucía and Consejo Superior de Investigaciones Científicas (IAA-CSIC). Also, it is based on observations made with the NASA/ESA Hubble Space Telescope obtained from the Space Telescope Science Institute, which is operated by the Association of Universities for Research in Astronomy, Inc., under NASA contract NAS 5-26555. These observations are associated with program 6353. RAC, LFM, JFG are supported by grants PID2023-146295NB-I00 and CEX2021-001131-S, funded by MCIN/AEI/10.13039/501100011033. RC also acknowledges support by the predoctoral grant PRE2018-085518, funded by MCIN/AEI/10.13039/501100011033 and by ESF Investing in your Future. We thank Pedro J. Amado for helping with the data reduction and data handling.

TABLE 8.7: Zones in Vy 2-2, their T_e and N_e, and mean ionic abundances relative to H^+ obtained from CELs.

Zone	T_e [K]	N_e [cm^{-3}]	Ion	Ionic abundance
1	[Ar III] 10700^{+700}_{-650}	[S II] 7250^{+3900}_{-2050}		
			S^+	$3.83^{+1.15}_{-0.61} \times 10^{-8}$
			O^0	$1.87^{+0.52}_{-0.40} \times 10^{-6}$
			N^0	$5.86^{+2.38}_{-1.27} \times 10^{-7}$
			N^+	$3.26^{+0.56}_{-0.47} \times 10^{-6}$
			Ar^{++}	$1.74 \pm 0.26 \times 10^{-6}$
2	[O III] 12400^{+450}_{-450}	[S II] 7250^{+3900}_{-2050}		
			O^{++}	$1.12 \pm 0.19 \times 10^{-4}$
			S^{++}	$2.96^{+0.41}_{-0.35} \times 10^{-6}$
3	[O II] 16800^{+1600}_{-1300}	[Cl III] 63400^{+}_{-38600} [a]		
			O^+	$8.50^{+2.52}_{-3.27} \times 10^{-6}$
			Ar^{+++}	$1.20^{+0.24}_{-0.24} \times 10^{-8}$
			Ne^{++}	$8.59^{+2.03}_{-1.78} \times 10^{-6}$
			Cl^{++}	$1.82^{+0.98}_{-0.44} \times 10^{-8}$
			Cl^{+++}	$1.88^{+0.26}_{-0.26} \times 10^{-9}$
			He^{+} [b]	$11.69^{+2.50}_{-1.59} \times 10^{-2}$
			He^{++} [b]	$1.47 \pm 0.04 \times 10^{-3}$

[a] The upper limit for the ionic abundances in Zone 3 used the mean value of N_e and the error of the dereddened emission line. This is because the [Cl III] diagnostic ratio is temperature-sensitive and gets unstable at the upper limit of T_e([O II]).

[b] Averaged value from the three zones. For Zone 3, a maximum value of N_e= 63400 cm^{-3} was used.

8.A Physical conditions and ionic abundances in Vy 2-2.

Table A1 shows the zones in the ionized gas of Vy 2-2, which have been identified by their values of T_e and N_e. We also show the ions associated to each zone, and the ionic abundances.

8.B Physical conditions from optical recombination lines

N II recombination lines help determine physical conditions using the λ5679.56/λ5666.63 and λ5679.56/λ4041.31 line intensity ratios (Fang et al. 2011; Fang & Liu 2013). In our spectra, the N II λ5679.56 emission line is blended with the N II λ5676.02 one, and theoretically $I(\lambda5679.56)/I(\lambda5676.02) \simeq 4.65$, so it is obtained $I(\lambda5679.56) = 0.1177 \pm 0.0016$. Therefore, the line ratios would be λ5679.56/λ5666.63$\simeq$1.71 and λ5679.56/λ4041.31$\simeq$1.12. While the former ratio indicates a range for N_e(N II)=1000-3200 cm^{-3}, the ratio falls outside the region that allow us the determination of the T_e (see Fig. 8 of Fang et al. 2011). This inconsistency makes this range of N_e(N II) unsuitable to determine ionic abundances, even if used in combination with a T_e determined with a different ion. Furthermore, as previously noted for the case of the CELs of [N II], the intensity of these lines may be affected by high-density zones (Zone 3) in the ionized gas, which could also affect the intensities of the N II ORLs, making these lines not suitable for determining physical conditions for both ORLs and CELs.

The relative intensity ratio $I(\lambda4649.13)/I(\lambda4591.63)$ from O II recombination lines is insensitive to electron density and has been used to determine the electron temperature (Fang & Liu 2013). The O IIλ4591 emission line is clearly detected in Vy 2-2 in our spectra. However, the λ4649 emission line is a blend of O IIλ4649.13, O IIλ4650.84, and possibly, C III recombination lines. To ascertain the true contribution of $I(\lambda4649.13)$, we proceed as follows: Firstly, in our spectra, $I(\lambda4640)$ is a mix of O IIλ4638.86, O IIλ4641.81, and N IIλ4640.64 intensities. Utilizing the relative intensities from these ORLs reported in a recent high-resolution optical spectrum of Vy 2-2 (Ruiz-Escobedo & Peña 2022), we determine that $I(\lambda4638.86)+I(\lambda4641.81)=0.564\pm0.015$. Theoretically, $I(\lambda4641.81)/I(\lambda4638.86)\simeq1.5$. Thus, $I(\lambda4638.86)=0.226\pm$ 0.06 and $I(\lambda4641.81)=0.338\pm0.09$. Additionally, $I(\lambda4649.13)$ $/I(\lambda4641.81)\simeq1.1$ and $I(\lambda4649.13)/I(\lambda4650.84)\simeq1.5$. Consequently, $I(\lambda4649.13)=0.375\pm$ 0.013 and $I(\lambda4650.81)=0.225\pm0.013$. The total emission measured is $I(\lambda4649)=0.985$ ±0.019, including a $I(\lambda4650)=0.385\pm0.026$ component, likely originating from C III recombination lines of stellar origin (Sec. 8.3.4). Lastly, from the O II recombination line intensity ratio $I(\lambda4649.13)/I(\lambda4591.63)$, we deduce T_e (O II) $=6309^{+769}_{-686}$ K. Ruiz-Escobedo & Peña (2022) found $T_e=8300\pm300$ K via a different method, consistent with our results.

The relative intensity ratio between $I(\lambda4075.86)/I(\lambda4070)$ of O II recombination lines is largely unaffected by electron temperature, making it useful for electron density determination (Fang & Liu 2013). Specifically, $I(\lambda4070)$ is defined as $I(\lambda4069.89)+I(\lambda4069.62)$. In our measurements, this encompasses $I(\lambda4069.89)+I(\lambda4069.62)+I(\lambda4072.16)$. The theoretical intensity ratio $I(\lambda4069.89)+I(\lambda4069.62)/I(\lambda4072.16)$ is approximately 1.19. From our spectra, we find $I(\lambda4069)$ to be 1.100 ± 0.033, leading to $I(\lambda4070)$ as 0.592 ± 0.018. Conversely, $I(\lambda4077)=I(\lambda4075.85)+I(\lambda4078.84)$ gives a value of 0.59 ± 0.05, while theoretically, $I(\lambda4075.86)/I(\lambda4078.84)$ is about 7.09, allowing us to deduce $I(\lambda4075.86)$ as 0.51 ± 0.05. Consequently, utilizing the O II recombination intensity ratio $I(\lambda4075.86)/I(\lambda4070)$, we derive an electron density N_e(O II) $=4467^{+781}_{-664}$ cm^{-3}. This differs substantially from the prior report by Ruiz-Escobedo & Peña (2022), which gave N_e(O II) $=19900\pm4300$ cm^{-3} based on the $I(\lambda4649.13)/I(\lambda4661)$ ratio. This discrepancy most probably arises due to the fact that stellar C III emission lines are contaminating the nebular $I(\lambda4649.13)$ in Vy 2-2, as analyzed in Sec. 8.3.4.

From the analysis of O II recombination lines, the relative intensities between $I(\lambda4649.13)/$ $I(\lambda4661.63)$ and $I(\lambda4649.13)/I(\lambda4089.29)$ both can be use to determine physical conditions (McNabb et al. 2013; Fang & Liu 2013). However, our CAFOS spectra are limited in spectral resolution and the $I(\lambda4661.63)$ is not detected or is blended with a much more intense λ4658 emission line. Therefore we cannot estimate $I(\lambda4661.63)$. Furthermore, the line ratio $I(\lambda4649.13)/I(\lambda4089.29)\simeq1.29$ is outside the area covered by the calculations presented in McNabb et al. (2013).

We were not able to estimate an electron temperature from the Balmer jump. It lies at the very blue end of our spectra and even in the deepest spectrum the measurement can become extremely inaccurate.

TABLE 8.8: Radial velocity of the intensity peak [v_r (LSR)] and velocity width [Δv (FWHM)] of the kinematical components identified in the CARMENES spectra of Vy 2-2 for selected emission lines. The line identification includes the usual air wavelength and we also provide the vacuum wavelength used for the calculations (see Sect. 2.2 for details).

Line+λ(air) λ(vacuum)($\AA$)	Kinematical component[1]	v_r (LSR) (km s^{-1})	Δv (FWHM) (km s^{-1})	Line+λ(air) λ(vacuum)($\AA$)	Kinematical component[1]	v_r (LSR) (km s^{-1})	Δv (FWHM) (km s^{-1})
[N II] λ5755	C1	−75.8	18.4	[Fe II] λ7155	C1	−81.3	37.4
λ5756.19	C2	−59.2	14.3	λ7157.14	C4	−17.2	48.7
	C3	−43.5	17.0	O I λ7254	C2	−56.9	9.3
	C4	−26.9	40.0	λ7256.44	C3	−39.5	7.2
He I λ5874	C1	−80.4	29.0	He I λ7281	C1	−72.6	32.9
λ5877.25	C2	−60.6	21.5	λ7283.36	C2	−58.6	20.7
	C3	−41.7	22.1		C3	−40.1	13.6
	C4	−22.3	28.4		C4	−29.0	21.9
[O I] λ6300[2]	C1	−81.7	30.5	[Ni II] λ7378	C1	−81.3	31.3
λ6302.05	C2–C3	−50.3	29.0	λ7379.86	C4	−16.7	38.9
	C4	−19.8	28.6	[Ar III] λ7751	C1	−76.8	25.4
[S III] λ6312	C1	−73.6	28.3	λ7753.24	C2	−60.6	16.8
λ6313.81	C2	−58.9	17.1		C3	−42.8	17.3
	C3	−42.3	14.1		C4	−29.2	31.5
	C4	−29.0	24.1	P 5 λ8545	C1	−82.8	30.5
[N II] λ6548	C1	−79.8	34.6	λ8547.31	C2	−59.5	29.0
λ6549.86	C2	−60.2	20.0		C3	−40.8	28.6
	C3	−40.9	16.8		C4	−15.0	27.9
	C4	−21.7	33.4	[Fe II] λ8617	C1	−85.1	38.3
Hα λ6563	C2	−59.2	46.6	λ8619.32	C4	−22.8	57.0
λ6564.63	C3	−46.4	39.3	He I λ11970	C1	−86.2	14.8
[N II] λ6583	C1	−80.2	31.5	λ11972.32	C2	−61.2	19.8
λ6585.27	C2	−61.1	19.3		C3	−38.6	17.9
	C3	−42.4	16.8		C4	−26.1	31.8
	C4	−23.8	32.0	[Fe II] λ12567	C1	−85.6	25.1
He I λ6678	C1	−82.2	26.0	λ12570.20	C2	−64.2	27.0
λ6680.00	C2	−61.6	21.2		C3	−33.2	26.2
	C3	−42.7	21.8		C4	−9.3	18.8
	C4	−23.4	29.1	Pβ λ12818	C1	−81.6	27.4
He I λ7065	C1	−78.9	24.0	λ12821.58	C2	−59.5	28.9
λ7067.14	C2	−61.9	17.8		C3	−42.6	29.1
	C3	−43.2	20.6		C4	−20.5	27.8
	C4	−25.8	29.5	[Fe II] λ16435	C1	−84.8	25.9
[Ar III] λ7135	C1	−75.9	26.1	λ16440.01	C2	−57.4	25.8
λ7137.76	C2	−60.3	16.6		C3	−33.7	25.1
	C3	−43.1	15.8		C4	−11.83	25.6
	C4	−28.8	23.9				

[a] C1 and C4 represent blueshifted and redshifted emission, respectively, from the bipolar lobes; C2 and C3 represent blueshifted and redshifted emission, respectively, from the central region (see the text and Fig. 4 for details).

[b] C2 and C3 are not separated in radial velocity in this emission line (see the text).

8.C Kinematical components in the ionized gas

Table 8.8 shows the kinematical components C1 to C4 detected in our CARMENES spectra (see Sec. 8.3.5) in selected emission lines, for which we report their radial velocity (v_r) with respect to the Local Standard of Rest (LSR), and width FWHM.

Chapter 9

A search for possible planetary nebulae with non-thermal radio continuum emission.

9.1 Introduction

The planetary nebula (PN) phase constitutes one of the final evolutionary stages of stars with initial masses $M_i \leq 8M_\odot$ (e.g., eventually including the Sun). PNe are characterized by a circumstellar envelope photoionized by a central star. The envelope tends to present non-spherical morphologies, including bipolar and multipolar structures, rotating disks, or S-shaped point-symmetry, which contrast with the roughly spherical envelope observed in previous evolutionary phases (Manchado et al. 1996a; Sahai et al. 2011). The ionizing central star, on the other hand, usually has an effective temperature ($T_{\rm eff}$) in the range $T_{\rm eff} \simeq 25000 - 200000\,$K, different chemical compositions and wind properties (Acker & Neiner 2003; Weidmann et al. 2020). Furthermore, it can be part of a binary or multiple stellar system. Such systems have been detected at the nuclei of non-spherical PNe, predominantly with bipolar morphologies and density-enhanced equatorial regions (Miszalski et al. 2009; Jones & Boffin 2017; Boffin & Jones 2019).

In essence, an ionizing photon from the central star absorbed by an atom liberates an electron with kinetic energy equal to the excess photon energy. When free electrons recombine with ions their kinetic energy is emitted as line emission, including recombination lines (e.g., Lyman, Balmer, etc.) and collisionally excited (including forbidden) lines from the ultraviolet to the far-infrared (see Peimbert et al. 2017, and references therein).

Apart from the collisionally excited and recombination lines, free-moving ions and electrons can also cool the photoionized region significantly through electrostatic interactions.

In fact, bremsstrahlung (free-free) radiation is a characteristic emission of PNe. These free-moving electrons do not have quantized energy states, and the changes in their kinetic energy do not result in monochromatic emission lines, but instead in a continuum emission. In the radio continuum, the variation of the flux density (S_ν) with frequency (ν) that characterizes the photoionized regions of PNe tend to show ranges of spectral indices (α, with $S_\nu \propto \nu^\alpha$) for the thermal (free-free) emission from +2 at low frequencies (optically thick regime) and −0.1 at high frequencies (optically thin regime) (Taylor et al. 1987; Aaquist & Kwok 1991; Gruenwald & Aleman 2007; Hajduk et al. 2018).

If energetic electrons propagate through a medium permeated by a strong magnetic field, they follow spiral motions along the magnetic-field lines due to Lorentz forces. This process is called magneto-bremsstrahlung (e.g. synchrotron radiation) and in the radio continuum it is characterized by variable flux densities and negative spectral indices ($\alpha \ll -0.1$). Moreover, this radiation could still be present during the PN phase, but, at the usual observing range of radio telescopes (> 1 GHz), it is, in general, overwhelmed by the more intense thermal (free-free) emission from the photoionized region (Casali et al. 2007). Thus, non-thermal radio continuum emission would be most easily detected in nascent PNe, when the photoionized region is small, and the thermal (free-free) emission is weaker than the non-thermal radiation (Suárez et al. 2015). Nevertheless, the recent report of non-thermal continuum emission at <1 GHz (Hajduk et al. 2025) in relatively more evolved PNe opens a new window of study of the role of magnetic fields in PNe shaping, using observations at low frequencies.

To further investigate the role of non-thermal emission and magnetic shaping during the PN phase, in this chapter we present a search for new (probably nascent) PNe showing non-thermal emission at cm wavelengths. In addition, we present our own near-infrared and optical spectroscopic observations of the newly identified sources.

9.2 Procedure to search for non-thermal PNe

Since the lowest spectral index of thermal radio continuum emission is $\alpha = -0.1$, indices $\alpha \ll -0.1$ indicate the presence of non-thermal radio continuum emission. Hence, our main criterion in this search has been the identification of sources in the available literature with reported spectral indices $\alpha \leq -0.3$.

Intraband radio spectral indices have been reported by The HI/OH/Recombination (THOR) line survey of the inner Milky Way between 1 and 2 GHz (Wang et al. 2018), and by the Global View of Star Formation in the Milky Way (GLOSTAR) between 4 and 8 GHz. Furthermore, GLOSTAR has released two different datasets, first with the Very Large Array (VLA) in the D configuration (hereafter GLOSTAR I; Medina et al. 2019), and then a follow-up also with the VLA but in the B configuration (hereafter GLOSTAR II; Dzib et al. 2023), allowing to robustly corroborate in some cases $\alpha \leq -0.3$ in more than one epoch.

Table 9.1: Non-thermal PNe and candidates.

Source name	RA(J2000)[a]	DEC(J2000)[a]	α, I[b]	α, II[b]	α, III[b]	III/II[c]	Nature[d]	Reference[e]
PHR J1813−1543	18:13:29.12	−15:43:20.12	−0.84±0.51	–	–	–	(PN)	1
StMul 1	18:14:25.94	−15:41:33.72	−0.80±0.35	–	–	–	(PN)	1
PHR J1815−1457	18:15:06.47	−14:57:20.68	−0.46±0.20	–	–	–	(PN)	2
PHR J1821−1353	18:21:43.92	−13:53:13.93	−0.96±0.48	–	–	–	(PN)	2, TW
G19.2356+0.4951	18:24:17.00	−11:56:01.25	−0.75±0.02	–	−1.05±0.04	–	ES?	3
M 3-28	18:32:41.28	−10:05:50.03	−0.45±0.14	–	**−1.66±0.26**	–	PN	4, TW
Pa 112	18:40:49.37	−02:59:51.06	−0.35±0.35	−0.24±0.09	−0.85±0.14	0.56	(PN)	1
Pe 1-14	18:42:08.04	−06:40:55.31	−0.33±0.19	–	–	–	(PN)	4
FBP7	18:42:15.84	−05:00:45.00	−1.37±0.64	–	−0.80±0.15	–	(PN)	5, TW
IRAS 18404−0217	18:43:02.52	−02:14:38.11	–	−0.46±0.15	−1.35±0.46	0.62	(PN)	6, TW
G029.2+00.0	18:44:53.38	−03:20:32.91	+0.52±0.04	−0.06±0.02	−1.73±0.42	0.13	(PN)	7
IRAS 18454+0001	18:48:01.18	+00:04:48.44	–	−0.23±0.07	−0.71±0.09	0.61	(PN)	9
G33.448+00.318	18:51:14.61	+00:36:17.18	–	−0.45±0.12	−0.46±0.10	1.20	Not PN	TW
MPA J1852−0044	18:52:24.18	−00:44:46.62	–	−0.10±0.10	−0.93±0.28	0.41	(PN)	4
IRAS 18551+0159	18:57:37.75	+02:03:39.38	+0.65±0.03	−0.05±0.02	−1.81±0.18	0.24	ES?	3
PHR J1857+0207	18:57:59.39	+02:07:06.13	−0.01±0.05	−0.08±0.03	**−1.04±0.42**	0.08	(PN)	2
HaTr 11	19:02:59.35	+03:02:21.30	−0.52±0.16	–	–	–	(PN)	4, TW
G47.611+1.082	19:14:45.16	+13:32:14.90	−0.39	–	–	–	(PN)	8, TW
Kn 11	19:41:19.08	+24:30:53.28	−0.47	–	–	–	(PN)	10
Kn 7	19:42:26.00	+21:45:21.10	−0.61	–	–	–	(PN)	10
G58.179−0.811	19:43:01.31	+21:54:24.00	−0.78	–	–	–	(PN)	8, TW
IRAS 19447+2445	19:46:53.57	+24:53:23.71	−1.04±0.34	–	–	–	(PN)	11, TW
G62.702+0.006	19:49:40.90	+26:15:21.12	−0.67±0.38	–	–	–	(PN)	8, TW

[a] Position of the radio continuum emission peak. [b] Values of the spectral index (α) reported in epochs I (THOR), II (GLOSTAR-I), and III (GLOSTAR-II). The α without errors are reported for sources with a S/N$\simeq$5–7. The symbol '–' stands for not covered or not detected. In bold, values of sources that were reported as resolved in that survey. [c] When available, the ratio between the flux density reported from epoch III and that from epoch II. [d] Based on spectroscopic observations: PN: confirmed PN. (PN): PN candidate. Not PN: discarded PN. Based on photometric data: ES?: evolved star candidate. [e] References: 1. Parker et al. (2016). 2. Parker et al. (2006). 3. Irabor et al. (2018). 4. Acker et al. (1992). 5. Fragkou et al. (2018). 6. Gaia Collaboration et al. (2018). 7. Thompson et al. (1991). 8. Sabin et al. (2014). 9. Oudmaijer et al. (2022). 10. Hsia & Zhang (2014). 11. Preite-Martinez (1988). TW: This work.

Subsequently, we cross-identified the interferometric positions of the newly identified objects with the Hong Kong/AAO/Strasbourg Hα (HASH) PN (Parker et al. 2016), Gaia (Gaia Collaboration et al. 2018), and SIMBAD databases to check whether their nature as PNe has been reported previously.

Table 9.1 presents the selected non-thermal PNe and candidates, together with their corresponding radio spectral index values reported in the available literature. Note that four sources in THOR (G47.611+1.082, Kn 11, Kn 7, and G58.179−0.811) do not have uncertainties in the spectral index because they are weak continuum emitters between 1-2 GHz, and have been detected with a signal-to-noise ratio of five to seven. Thus, these values should be taken with care. Nonetheless, one of these sources, Kn 7, has been reported with non-thermal emission below 1 GHz, with a spectral index α=–0.33±0.06 (Hajduk et al. 2025). Additionally, when available, the flux density ratio between GLOSTAR II and GLOSTAR I has been included as a quantification of variability, together with the nature of the objects. This classification is discussed in Section 9.5.3.

In total, 23 objects have been found with $\alpha \leq -0.3$ in at least one epoch after this

TABLE 9.2: New optical and near-infrared (K-band) spectroscopic observations performed on non-thermal PNe and candidates.

Target name	Coordinates (RA, DEC J2000)	Spectrum	Exposure[a]	Slit position angle (°)	Date
PHR J1821−1353	18:13:29.12 –15:43:20.12	Red	1 × 2700	0	2021/06/11
IRAS 19447+2445	19:46:53.57 +24:53:23.71	Red	1 × 3600	90	2021/06/12
IRAS 18404−0217	18:43:02.52 –02:14:38.11	Red	1 × 2700	90	2021/06/12
		near-IR	2 × 4 × 200	0	2023/06/12
M 3-28	18:32:41.28 –10:05:50.03	Red	1 × 2700	0	2021/07/05
		Blue	1 × 2700	0	2021/07/05
HaTr 11	9:02:59.35 +03:02:21.30	Red	1 × 2700	90	2021/07/06
		Blue	1 × 2700	90	2021/07/06
FBP7	18:42:15.84 –05:00:45.00	Red	2 × 1800	0	2021/07/13
G58.179−0.811	19:43:01.31 +21:54:24.00	Red	2 × 1800	135	2021/07/13
G47.611+1.082	19:14:45.16 +13:32:14.90	Red	2 × 1800	135	2021/07/14
G62.702+0.006	19:49:40.90 +26:15:21.12	Red	2 × 1800	45	2021/07/14
G019.2356+00.4951	18:24:17.00 –11:56:01.25	near-IR	2 × 4 × 240	0	2023/06/10
G33.448+00.318	18:51:14.61 +00:36:17.18	near-IR	2 × 4 × 220	0	2023/06/11

[a] For optical observations, the first and second numbers indicate the number of spectra and the exposure time, respectively. For near-infrared observations, the last number corresponds to the detector integration time (DIT), the middle one to the number of frames, and the first one to the number of exposures per position.

cross-identification procedure. Including the results shown below, we identified one non-thermal PN (M 3-28), 19 non-thermal PN candidates, and discarded one source as a PN (G33.448+00.318). Additionally, two previously classified evolved star candidates have been selected (G19.2356+0.4951 and IRAS 18551+0159).

9.3 Observations and data processing

To investigate the morphological properties of the sources reported as resolved by GLOSTAR II and shown in bold in Table 9.1, we reprocessed their corresponding continuum data between 4-8 GHz. In addition, we searched these sources for available optical images. Also, we carried out near-infrared and optical spectroscopic observations to examine the spectral characteristics and physical conditions of the ionized emission in sources presented in Table 9.2.

9.3.1 Archival radio continuum data and optical images

GLOSTAR II reported resolved continuum emission in two sources, namely PHR J1857+0207 and M 3-28, highlighted in bold in Table 9.1. In order to investigate their morphological properties, we obtained the relevant archival VLA continuum data between 4 and 8 GHz from GLOSTAR II from observations performed in 04/01/2014 (Project ID: 13A-334; PI: Karl M. Menten) and 19/04/2015 (Project ID: 14A-420; PI: Karl M. Menten), respectively.

We calibrated the visibilities of these data using the VLA pipeline. Imaging was performed with the Common Astronomy Software Applications (CASA; CASA Team et al. 2022). Self-calibration in CASA significantly enhanced the initial signal-to-noise ratio of the emission by up to a factor of five. We also consulted the available radio continuum maps at 4.8 GHz from the CORNISH survey and downloaded that of M 3-28, from observations performed in 2006 (Purcell et al. 2013).

Optical images of these sources have been found in the VST Photometric Hα Survey of the Southern Galactic Plane and Bulge (Drew et al. 2014) stored in HASH and the archive of the Panoramic Survey Telescope and Rapid Response System (PanSTARRS; Chambers et al. 2016) for PHR J1857+0207 and M 3-28, respectively.

9.3.2 Near-infrared spectroscopy

We performed long-slit intermediate resolution near-infrared spectroscopy using the New Technology Telescope (NTT) on June 10-12 2023 (Project ID: 111.24T1.001; P.I.: R. A. Cala), focusing on three targets. The NTT was equipped with the Son OF Isaac (SOFI) infrared spectrograph, a 1" wide and 1.4' long slit, the third-order HR grism for K-band (2.00-2.30 μm) observations, and a 1024×1024 Hawaii HgCdTe array as a detector. The angular size of the targets enabled simultaneous sky and target frame creation through jittering (random 20" shifts) and nodding (80" along the slit) without additional sky offsets. To enhance weak emission line detection, the Hawaii array operated in non-destructive mode for 30 readings per exposure, with 4 samples per reading. Table 9.2 provides details on the NTT-SOFI observations. The detector integration time (DIT) and number of DITs (NDIT) per jittered position were selected based on target K-band magnitude and nighttime conditions, ensuring at least two NDITs per position to boost the signal-to-noise ratio. Observations included nearby main-sequence O- and B-type stars (HD166689, HD171305, HD176158) as telluric standards, recorded before and after each science target using the same instrument setup, with one NDIT per jittered position.

The telluric standard and science target spectra were processed making use of the SOFI pipeline in the software *esorex*, which performed dark current correction, flat fielding, slit curvature distortion, combination of the frames, and wavelength calibration. We made use of IRAF to extract both telluric standard and science target spectra. We noticed that the spectra of O-B stars, which were chosen as telluric standards, present Brγ in absorption. Therefore, we have interpolated before and after this line to remove them from their spectra. Then, we have divided out the science targets by the telluric standards, and flux calibrated the spectra making use of their K-broadband magnitudes reported in Two Micron All Sky Survey (Skrutskie et al. 2006).

9.3.3 Optical spectroscopy

We have employed the Calar Alto Faint Object Spectrograph (CAFOS) mounted on the 2.2m telescope of the Centro Astronómico Hispano en Andalucía (CAHA) on Spain during the nights of June 07-08 2021 and July 11-14 2021 (proposal ID: F21-2.2-0.17; PI: R. A. Cala), to apply intermediate resolution long-slit (width of 2 arcsec) spectroscopy on the targets listed on Table 9.2. The weather conditions were photometric during the observations with an average seeing of 3 arcsec. To calibrate the spectra, we observed standard stars BD+28°4211 and BD+33°2642. The spectra were recorded using a SITe CCD with 2048×2048 pixels and a spatial scale of 0.53 arcsec per pixel. We used B-100 grism (3200-6200 $\AA$) and R-100 grism (5800-9600 $\AA$). More observational data are provided in Table 9.2. The spectra were calibrated using standard procedures in the software IRAF, resulting in an approximate dispersion of $\sim$2 $\AA$ per pixel. This software and PyNeb (Luridiana et al. 2015) were used to analyze the physical conditions of the ionized gas.

9.4 Results

9.4.1 Radio and optical images

Figure 9.1 shows continuum emission maps at 4.8 GHz of PHR J1857+0207 and M 3-28, overlaid on their corresponding optical counterparts. In PHR J1857+0207 (left), the radio continuum emission seems to trace a face-on ring-like structure, similar to the one seen in the Hα image, which could trace a face-on toroid or a nearly spherical shell. In the case of M 3-28 (right), the radio continuum emission at 4.8 GHz detected in both GLOSTAR II (red) and CORNISH (blue) traces a slightly elongated morphology compatible with an edge-on toroidal distribution at the center and perpendicular to the more extended quadrupolar structure reveled by the r-band optical image. Thus, the radio emission is suggestive of a central, ionized toroid. Furthermore, while a bright, unresolved non-thermal core dominates the emission from GLOSTAR II, such non-thermal core is not detected in that of CORNISH. Interestingly, the CORNISH and GLOSTAR II data correspond to observations performed in 2006 and 2015, respectively.

9.4.2 Optical spectra

Figure 9.2 displays the 6350-6800 Å region for seven sources where only the emission lines Hα and [N II] $\lambda\lambda$6548,6584 were detected (PHR J1821–1353, G47.611+1.082, IRAS 19447+2445, FPB7, IRAS 18404-0217, G58.179-0.811, and G29.578-0.268), the entire 3900-9600 Å region of HaTr 11 and M 3-28, and the 5900-9600 Å region of G62.702+0.006, for which the blue spectrum was not obtained.

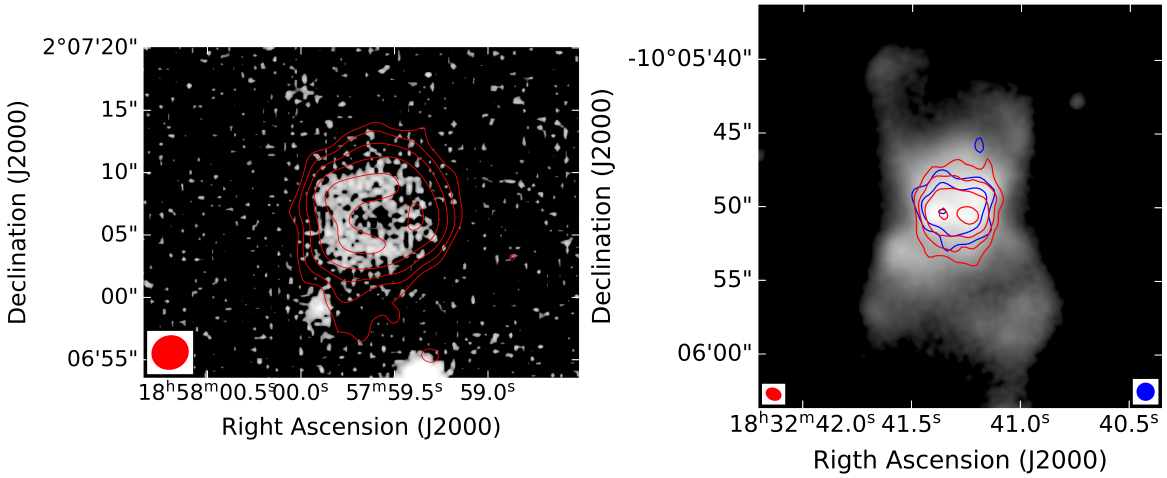

FIGURE 9.1: ***Left.*** Contour emission map at 4.8 GHz of PHR J1857+0207 from the reprocessing of GLOSTAR data overlaid with a Hα image in logarithmic scale taken from HASH. The contours increment in steps of $3\sigma \times 2^n$ starting from $n = 0$, where $\sigma = 0.10$ mJy beam^{-1} is the rms of the continuum map. ***Right.*** Same as the left panel but for M 3-28 ($\sigma = 0.15$ mJy beam^{-1}) overlaid to an optical wideband r-filter image in logarithmic scale taken from the archive of PanSTARRs. In addition, the contour emission map at 5 GHz (blue) from the CORNISH survey is presented in steps of $3\sigma \times 2^n$ starting from $n = 0$, where $\sigma = 0.10$ mJy beam^{-1} is the rms of the continuum map.

Using the corresponding fluxes of the emission lines of Hα and Hβ, and a theoretical Hα/Hβ intensity ratio of 2.85 and the extinction-correction law of Seaton (1979), we obtained a logarithmic extinction coefficient at Hβ, c(Hβ), of 1.78±0.05 for M 3-28 and 1.88±0.15 for HaTr 11. Table 9.3 lists the intrinsic intensities in these two objects obtained with the corresponding values of c(Hβ). For G62.702 we provide the observed fluxes.

9.4.3 Spectral properties and physical conditions

An inspection of Fig. 9.2 shows that most objects present very strong [N II] emission lines as compared with the Hα one. To quantify the [N II](6548+6584)/Hα line intensity ratio, we have measured the flux of these lines in our spectra and also in published spectra of other objects in Table 9.1, and we note that extinction correction is not relevant because the three lines are very close in wavelength. Table 9.4 lists the results which, in some cases, should be seen with caution because the [N II]λ6548 emission line contains a relatively large error due to noise.

Except in StMul and PHR J1815-1457 where [N II] is not detected, and in G029.2+00.0 where the [N II] line could not be separated from the Hα line (see Table 9.4), virtually all objects present a [N II]/Hα ratio higher than 1, being Kn 7, Pa 112 and, particularly, J1821-1353 extreme cases.

To analyze the spectral properties of the ionized emission in all sources with available spectra, including our own observations of M 3-28, HaTr 11, and G62.702+0.006, we have

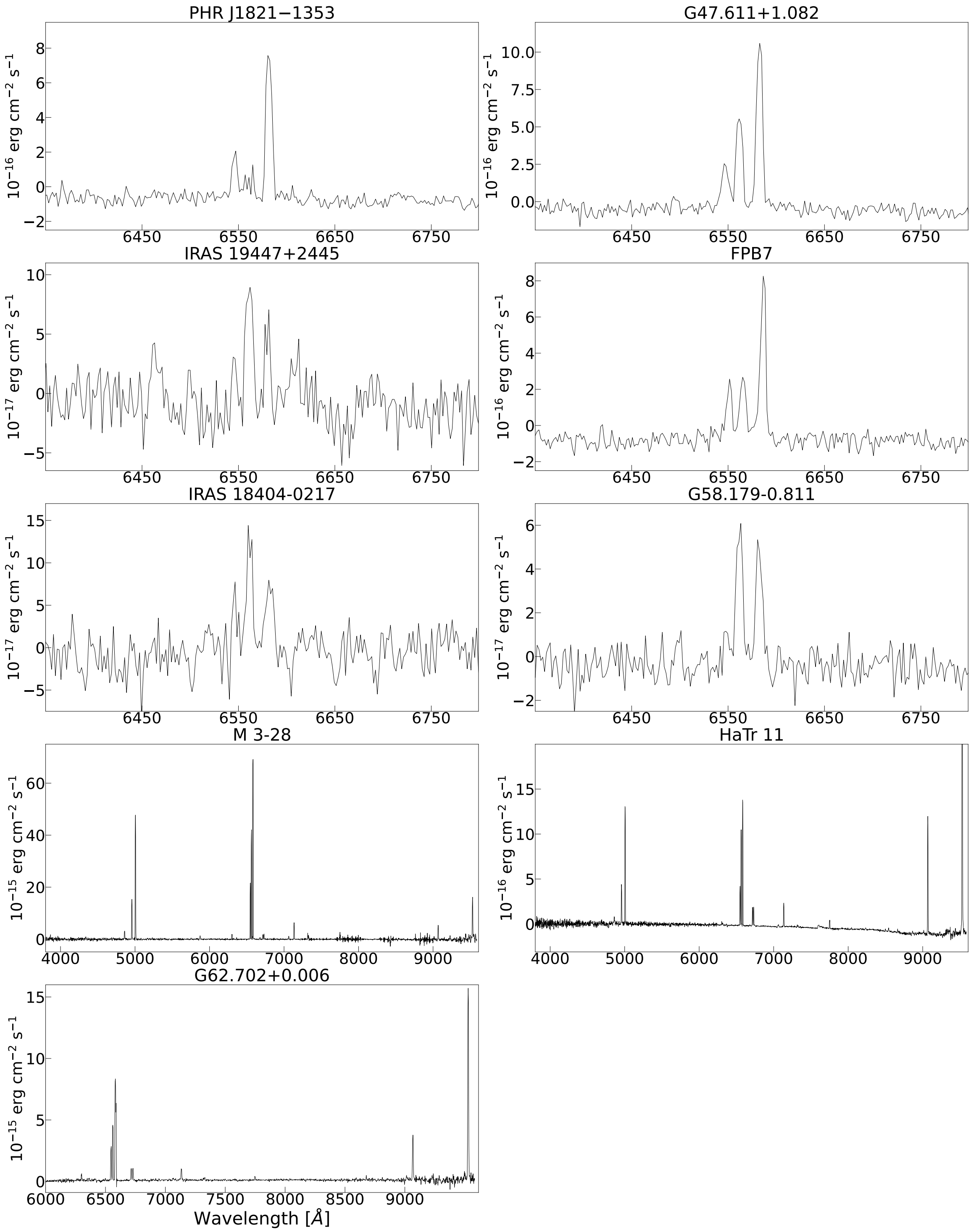

FIGURE 9.2: Optical spectra of the sources listed in Table 9.1. The names, flux units, and wavelength range are indicated on the corresponding panel.

TABLE 9.3: Intrinsic line intensities ($I(H\beta)$=100) in PNe with more emission lines than Hα and [N II]$\lambda\lambda$6548,6584.

Emission line	M 3-28	HaTr 11	G62.702[a]
4340 Hγ	47.23 ± 3.60	–	–
4861 Hβ	100.00 ± 2.5	100.00 ± 9.9	–
4959 [O III]	391.6 ± 10.5	443.5 ± 9.5	–
5007 [O III]	1143.0 ± 27.9	1289.82 ± 9.25	–
5755 [N II]	12.83 ± 1.08	–	–
5876 He I	18.0 ± 0.7	–	–
6300 [O I]	16.6 ± 2.9	12.5 ± 0.5	3.60
6363 [O I]	5.34 ± 2.37	6.16 ± 0.33	–
6548 [N II]	155.61 ± 2.24	116.3 ± 3.9	22.28
6563 Hα	285.0 ± 2.2	285.0 ± 3.9	36.8
6584 [N II]	487.65 ± 2.22	358.7 ± 3.8	94.9
6678 He I	5.09 ± 1.38	–	–
6716 [S II]	12.03 ± 1.17	51.7 ± 0.7	8.39
6731 [S II]	13.38 ± 1.13	51.53 ± 0.65	8.56
7065 He I	7.13 ± 1.28	10.85 ± 0.40	–
7137 [Ar III]	35.48 ± 2.06	55.1 ± 0.6	8.6
7319 [O II]	7.79 ± 1.40	14.42 ± 0.31	1.6
7330 [O II]	5.92 ± 0.42	–	1.56
7751 [Ar III]	9.0 ± 0.6	–	2.37
9015 P 10	3.02 ± 0.25	–	–
9069 [S III]	14.43 ± 0.28	106.96 ± 0.98	32.7
9229 P 9	4.94 ± 0.41	–	–
9535 [S III]	41.70 ± 0.70	328.63 ± 2.06	137
$F(H\beta)$[a]	30.2 ± 0.08	7.43 ± 0.73	–
$c(H\beta)$	1.79 ± 0.04	1.88 ± 0.15	–

[a] Line fluxes in units of 10^{-15} erg cm^{-2} s^{-1} because the blue spectrum was not observed (see text).

determined electron temperatures (T_e) and electron densities (N_e). However, the limited wavelength coverage and signal-to-noise of most spectra restricted the simultaneous determination of both physical parameters to only one source, which we describe in detail below. Table 9.4 shows the corresponding values for N_e.

Among the emission lines available in the spectra, only for M 3-28 we were able to determine values for both electron temperature ($T_e = 13500^{+700}_{-1200}$ K) and electron density ($N_e = 1100^{+2000}_{-900}$ cm^{-3}) using the emission line ratios [N II]$\lambda\lambda$6548+6584/5755 and [S II]$\lambda\lambda$6716/6731, respectively. For spectra without reddening correction, we determined N_e assuming the [S II]$\lambda\lambda$6716/6731 lines are affected by similar reddening. Given that this ratio is highly insensitive to changes in T_e, we assumed T_e = 10000 K in all sources (except M 3-28, for which we used the T_e obtained above), to compute values of N_e. This calculation failed for PHR J1813−1543 and G58.179−0.811, suggesting the presence of a high-density ionized gas ($N_e > 10^4$ cm^{-3}). In the remaining cases, the N_e we determined are in the range of 110 and 1400 cm^{-3}. Values of $T_e \simeq 10\,800$ K and $N_e \simeq 100$ cm^{-3} previously reported for M 3-28 by Kaler et al. (1996), and values for N_e of 5400^{+13400}_{+2700} and 2700^{+4100}_{-1400} cm^{-3} for Kn 7

TABLE 9.4: [N II](6548+6583)/Hα emission-line ratios and electron densities.

Object[a]	[N II]/Hα	N_e (cm^{-3})	Reference
PHR J1813−1543	1.56	–	HASH
PHR J1821−1353	24.3	$\sim 1270^{b}$	This work
M 3-28	2.21	1100^{+2000}_{-900}	This work
Pa 112	8.70	–	HASH
Pe 1-14	2.15	$\sim 1400^{b,c}$	Acker et al. (1992)
FBP7	2.68	–	This work
IRAS 18404−0217	1.33	–	This work
G029.2+00.0	1.04	–	Thompson et al. (1991)
MPA J1852−0044	2.61	–	HASH
PHR J1857+0207	0.45	–	HASH
HaTr 11	1.67	600 ± 60	This work
G47.611+1.082	2.22	$\sim 110^{b}$	This work
Kn 11	5.80	$\sim 510^{b}$	Sabin et al. (2010)
	3.80	2700^{+4100}_{-1400}	Hsia et al. (2010)
Kn 7	4.76	$\sim 540^{b}$	Sabin et al. (2010)
	4.71	5400^{+13400}_{+2700}	Hsia et al. (2010)
G58.179−0.811	1.16	–	This work
IRAS 19447+2445	0.80	–	This work
G62.702+0.006	3.17	$\sim 650^{b,d}$	This work
	3.0	$\sim 950^{b}$	Sabin et al. (2010)

[a] In bold, objects without available flux-calibrated spectra; emission-line ratios are derived from counts.
[b] Blue spectral range not available; N_e computed from undereddened fluxes assuming $T_e = 10\,000$ K.
[c] Based on counts because a flux-calibrated spectrum is not available.

and Kn 11, respectively, have been reported by Hsia & Zhang (2014). These values differ from the ones we obtain, but we cannot confirm variability as the cause for this difference because our observational setup is different to them.

9.4.4 Near-infrared spectroscopy

Figure 9.3 shows the K-band (2.0-2.3 μm) near-infrared spectra of the observed targets. The spectrum of IRAS 18404−0217 exhibits recombination lines of He I, He II, and Brγ, together with H_2 emission lines. The initial section of the spectrum of G29.578−0.268 is affected by a broad telluric absorption, although it is clear that the emission line of H_2 at 2.12 μm is more prominent than the emission line of Brγ. No emission lines were detected in the spectrum of G33.448+00.318. The spectrum of G019.2356+00.4951 is not shown there since it is unfortunately severely affected by broad telluric features.

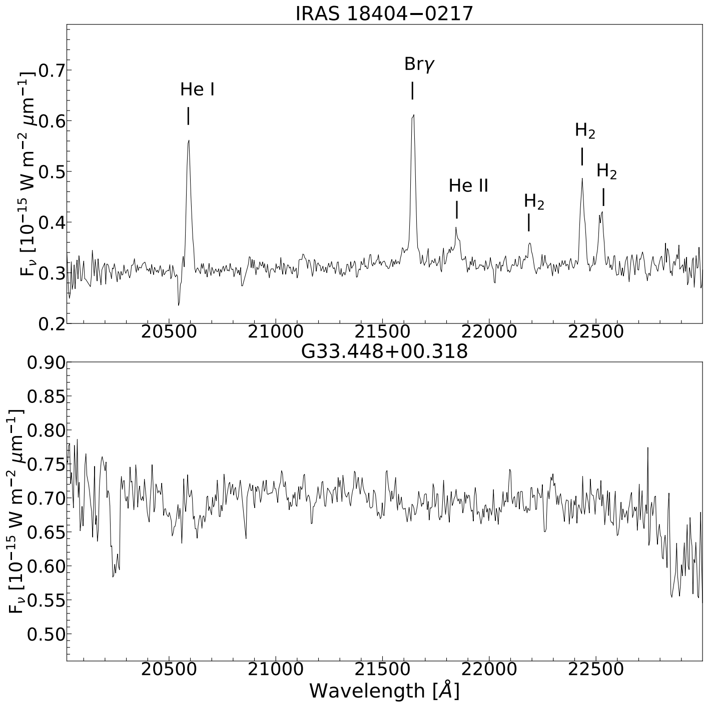

FIGURE 9.3: *K*-band near-infrared spectra of sources as indicated in each panel.

9.5 Discussion

9.5.1 Characteristics of the identified sources and possible interpretations

We have carried out a cross-identification procedure between radio surveys and catalogued PNe and PN candidates, selecting sources that show radio spectral indices consistent with non-thermal emission. This procedure has led to the identification of 22 objects whose radio continuum cannot be explained only by thermal (free–free) emission.

Where optical spectroscopy is available, many display high [N II]/Hα ratios (≥ 1), while the derived N_e are heterogeneous: some objects show relatively low values ($N_e \sim 10^2$–10^3 cm^{-3}), whereas in others N_e cannot be reliably constrained, and in one case (M 3-28) we found a much higher N_e.

The non-thermal radio continuum emission may be associated with toroidal structures, as observed in PHR J1857+0207 and M 3-28 (Fig. 9.1). Additionally, an inspection of public MeerKAT images at 1.28 GHz reveals radio emission in PHR 1813−1543 (Fig. 9.4, left) and PHR J1821−1353 (Fig. 9.4, right). However, only in the latter source does the continuum clearly originate from a bipolar structure. Similar morphological characteristics are found in other objects reported to exhibit non-thermal radio continuum emission at frequencies below 1 GHz (Hajduk et al. 2025).

Close post-common envelope (CE) binaries tend to show bipolar morphologies, strong low-ionization emission lines and, in many cases, relatively low N_e (see Wesson et al. 2018,

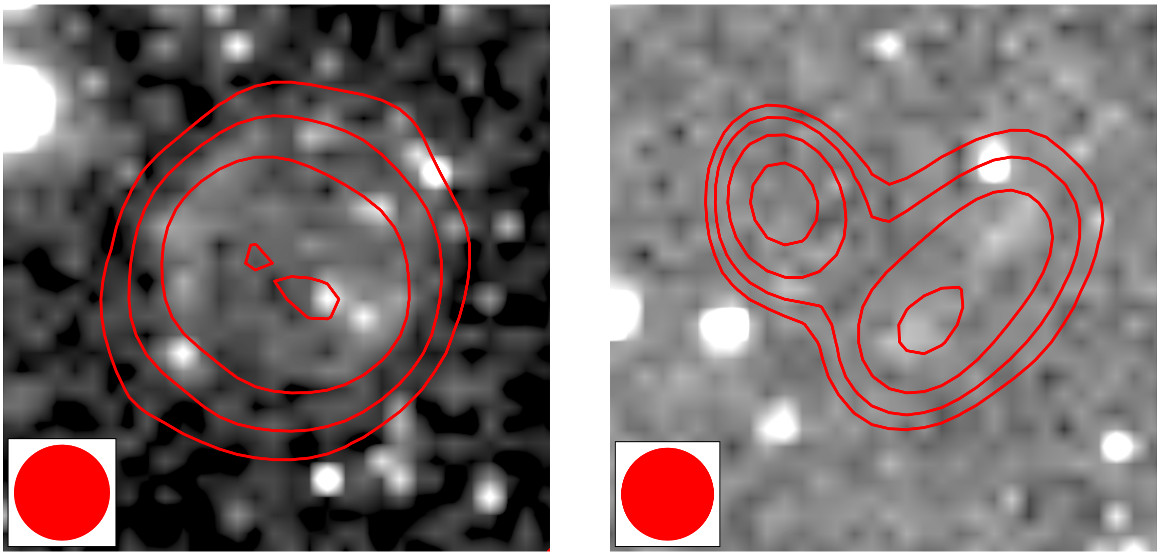

Figure 9.4: Contour maps of 1.28 GHz continuum emission from MeerKAT, overlaid on Hα images from VPHAS+, for PHR J1813-1543 (left) and PHR J1821-1353 (right). The contours in both images increment in steps of $3\sigma \times 2^n$ starting from $n = 0$, where $\sigma = 41\,\mu$Jy beam^{-1}. The filled circles indicates the synthesized beam (FWHM=8.″0). The field size in both images is 50.″0 × 50.″0.

and refences therein). Given that such kind of morphologies and emission properties are observed in some of the identified sources in this chapter, these objects may therefore be related to post–CE binary systems, as previously suggested by Hajduk et al. (2025).

Finally, a small fraction of the sample may instead be tracing the nascent PN phase. The prototypical case is IRAS 15103–5754, where an initially non-thermal radio spectrum rapidly evolved toward thermal emission as photoionization began (Suárez et al. 2015). A similar scenario may apply to sources in our sample that show time- and frequency-dependent spectral indices. In addition, objects such as PHR J1813–1543 and G58.179–0.811, whose ionized emission is compatible with $N_e > 10^4$ cm^{-3}, could represent very young and compact PNe. In this context, non-thermal radio continuum emission may trace both post-CE systems and the onset of the PN phase.

9.5.2 Non-thermal radio spectral indices

The observed radio spectral indices $-1.7 \leq \alpha \leq -0.3$ are inconsistent with thermal (free–free) emission, and instead indicate a non-thermal origin (Condon 1992).

Several radio spectral indices vary systematically with frequency band, angular resolution, and observing epoch. Overall, ∼35-40% of the sample exhibits frequency- and/or resolution-dependent spectral indices. In several sources, moderately negative or nearly flat spectral indices at 1–2 GHz become significantly steeper at 4–8 GHz (e.g., M 3-28, Pa 112, IRAS 18404−0217, PHR J1857+0207, IRAS 18551+0159, and G029.2+00.0), while in other cases positive low-frequency indices coexist with negative high-frequency values (G029.2+00.0

and IRAS 18551+0159). Additionally, four objects (M 3-28, PHR J1857+0207, IRAS 18454+0001, and Pa 112) display significant changes in α between different 4–8 GHz epochs observed with different angular resolutions. This behavior can be explained by the coexistence of spatially extended thermal (free-free) emission and compact non-thermal components: at low frequencies and coarse angular resolution a photoionized nebula dominates the measured flux density, whereas at higher frequencies and higher resolution diffuse thermal emission may be resolved out by interferometric filtering.

Apart from these possible instrumental effects, the presence of a photoionized region can also induce a decrease of non-thermal emission at low frequencies, which would result in an increase of the value of spectral index (e.g., flattening or positive values) in that frequency range. Possible mechanisms, could be the opacity of the ionized region (which follows $\tau \propto \nu^{-2.1}$), collisions of high-energy electrons with the protons in the plasma, or Razin effect (Suárez et al. 2015).

Confirming whether the variations of spectral index arise from the filtering of extended free-free emission, or from a radiative suppression on non-thermal emission would require dedicated, multi-frequency, multi-epoch and multi-configuration radio interferometric observations, complemented by maps of spectroscopic diagnostics (see Section 9.5.3).

9.5.3 Classification of the identified sources

Non-thermal PNe and candidates are, in principle, characterized by the lack of evidence of the presence of thermal (free-free) emission in their radio continuum spectrum. Consequently, an essential issue is how to confirm the presence of photoionization using near-infrared and optical spectra. Ideally, the most robust approach would require modeling the ionized emission produced by a mixture of shocks and photoionization, and directly comparing the hybrid models with the observed spectra. However, such hybrid models are not yet available. Instead, ionized emission has so far been modeled independently, either as originating exclusively from shocks (Allen et al. 2008; Sutherland & Dopita 2017) or from photoionization alone (Ferland et al. 2017). The full collection of synthetic spectra generated by these models is available in the Mexican Million Models Database (3MDB; Morisset et al. 2015; Alarie & Morisset 2019). This database can be used to examine the spectral behavior of individual emission lines associated with each ionization mechanism and to construct diagnostic diagrams, such as the one presented below.

To assess whether photoionization contributes to the observed ionized emission, we focus on emission-line diagnostics other than H recombination lines used for interstellar extinction correction. These lines provide a robust diagnostic of an ionizing radiation field because their emissivities depend weakly on T_e, in contrast to collisionally excited lines whose intensities depend exponentially on T_e and can be strongly enhanced in radiative shocks (Osterbrock & Ferland 2006; Allen et al. 2008). Hence, collisionally excited lines can be less discriminating

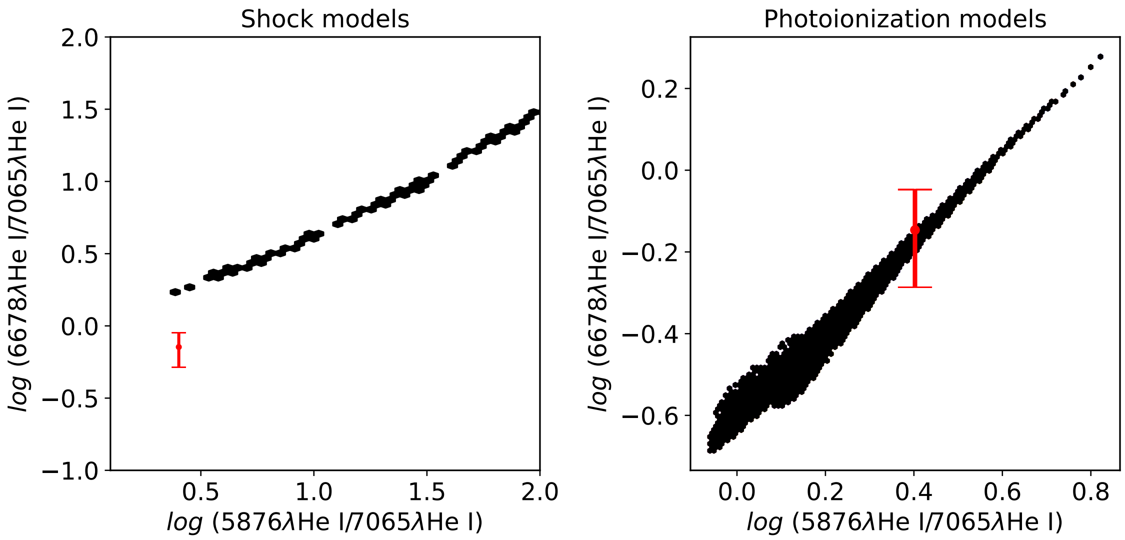

FIGURE 9.5: Line ratio diagnostic diagram for the recombination lines of H γ, He I λ5876, and He I λ6678. The regions occupied by shock (left) and photoionization (right) models are shown in black. The red point marks the position of M 3–28. The length and width of the red bar span the positional uncertainty. See Appendix 6.D for more details on the grid parameters.

when both ionization mechanisms may coexist, while recombination lines provide a more direct and conservative diagnostic of photoionization.

Among the available spectra in the literature and our own observations, only our spectra of M 3-28 exhibits recombination lines apart from those of H, namely He I λ5876, He Iλ6678, and He Iλ7065 (Table 9.5). Considering that the 3MDB has not yet incorporated the spectral response of the Pa 10 line for the photoionization models, we thus constructed the diagnostic diagram shown in Fig. 9.5 using Hγ, He I λ5876, and He Iλ6678. The position of this source in the diagnostic diagram (red star and its error bar) lies outside the region covered by shock models, while remaining consistent with photoionization models. This incompatibility with shocks alone indicates that the observed intensities of these recombination lines require a significant contribution from photoionization. Hence, this diagnostic diagram supports the PN nature of M 3-28, as suggested before by Kaler et al. (1996) and Manchado et al. (1996b).

Apart for this case of M 3-28, the sources reported in Table 9.4 with [N II]/H$\alpha \geq 1$ can only be classified as PN candidates. In particular, for IRAS 18404–0217 and G29.578-0.268, two sources previously classified as PN candidates based on its infrared emission (Irabor et al. 2018), our near infrared spectra (Fig. 9.3) show recombination lines and H2 emission, consistent with this classification (Marquez-Lugo et al. 2013; Gledhill & Forde 2015). On the other hand, G33.448+00.318, a source previously classified as PN candidate based on photometric data (Irabor et al. 2018), shows no emission lines in its near-infrared spectrum, implying that it may not be a PN.

9.6 Conclusions

From our cross-identification procedure, we selected 23 objects with non-thermal radio continuum emission. The observed radio spectral indices ($-1.1 \leq \alpha \leq -0.3$) provide evidence for the presence of non-thermal emission in a regime traditionally assumed to be dominated by purely thermal processes. This implies that magnetic fields could be key in the PN formation.

The combination of toroidal structures and/or bipolar morphologies, low N_e and high [N II]/Hα ratios, observed in some of our objects, is also observed in post-CE binary systems but more investigation is required to firmly established this apparent link.

Alternatively, the presence of non-thermal radio continuum emission at cm wavelengths could also be a tracer of the nascent PN phase. This interpretation is also compatible with scenarios involving close post-CE binary systems, where shocks and magnetic fields may coexist with the onset of photoionization.

Approximately $\sim$40% of the selected sources exhibits significant variations in α, which depend systematically on observing frequency, angular resolution, and epoch. This behavior could be explained by the superposition of a photoionized region and compact non-thermal structures, such as the case of M 3-28. Multi-frequency, multi-configuration, and multi-epoch radio continuum observations are needed to disentangle possible thermal and non-thermal emission components in these sources and to avoid spurious technical effects (such as resolving out extended emission).

Among the selected objects with non-thermal radio continuum emission, M 3-28 has been classified as a PN based on recombination-line diagnostics (He I λ5876, He I λ6678, and He I λ7065), 19 as PN candidates, one (G33.448 +00.318) is discarded as a PN, and two (G19.2356+0.4951 and IRAS 18551 +0159) are classified as evolved star candidates.

Chapter 10

Conclusions and Future Research

The main results of this thesis can be summarized as follows:

- We increased the number of known maser-emitting PNe and candidates from 10 to 23 (2 PNe and 11 candidates), and the number of non-thermal PNe and candidates in the centimeter regime from 1 to 23 (2 PNe and 20 candidates). The significant increase in the number of confirmed and candidate PNe with maser and/or non-thermal radio continuum emission opens the possibility, for the first time, to carry out robust statistical investigations of the nascent PN phase.
- We identified 3 WFs and one WF candidate, increasing the number of confirmed WFs from 15 to 18, including the first low-velocity WFs with ionized emission identified to date, an emerging group of sources whose study could be relevant to determine the chronology of the onset of ionization in evolved stars.
- The analysis of maser-emitting PNe and candidates shows that they are not a homogeneous group. Their wide distribution in infrared color–color diagrams suggests that PNe of different properties can host maser emission.
- In addition to the new OHPN IRAS 07027−7934 and the previously reported H_2OPN IRAS 18061−2505, which host PAHs and [WC] central stars with O-rich envelopes, PAHs are present in one additional OHPN (IRAS 17393−2727) and in three OHPN candidates (IRAS 16029−5055, IRAS 17375−2759, and IRAS 19176+1251). These results indicate that some of these objects may show mixed chemistry, with C-rich central stars or inner circumstellar regions, and could represent an emerging group of PNe that underwent a recent thermal pulse and/or common-envelope evolution.
- We report that the nature of the newly identified source IRAS 18443−0231 is consistent with a nascent PN from a magnetized WF: it shows strong and variable non-thermal radio continuum emission and near-infrared spectroscopy indicates ionized emission compatible with photoionization. This source could thus be one of the youngest PN known.

- Low-velocity WFs exhibit CO absorption bands characteristic of cool giant stars, while other classical, high-velocity WFs show H_2, Brγ, and He I emission lines consistent with shocks around post-AGB stars or photoionization from PNe. This suggests that the difference between low- and high- velocity WFs reflects intrinsically different evolutionary stages.

- In the non-thermal PN candidate IRAS 22568+6141, we reported on an energetic event occurred around 1990, and that manifested itself as a sudden and rapid increase in the nebular brightness. The observed spectral variability between 2021 and 2023 shows that it is recombining and cooling. Some emission line ratios and the emission line profiles observed in 2021 reveal that the spectrum is excited by shocks. Changes in the physical conditions in the shocks or a nova-like eruption might explain the observed variability, but a late thermal pulse in the central star provides a simple and consistent explanation for this energetic event and for its subsequent photometric and spectral evolution.

- In the OHPN Vy 2-2, our intermediate resolution spectra revealed many previously unreported nebular recombination (e.g., N^+) and forbidden (e.g., [Ni II]) emission lines, as well as stellar recombination emission lines. Some of these emission lines were crucial in accurately determining the new value of the *adf*(O^{2+})=13.6±2.6, which is unusually high for PNe. The high-resolution spectra allowed us to identify four kinematical components in the nebula: two components related to the central region and two components tracing bipolar lobes. The emission lines indicate that the inner region presents a higher excitation than the lobes. Our data does not show significant shock excitation in the main ionized shell. We derived a kinematical age of $\simeq$210 yr for this nascent PN. Although the stellar emission lines detected in Vy 2-2 suggest a *wels* type central star, they may be related to an irradiated close companion. This possibility is compatible with the unusually high *adf*, the observed nebular structures, and other emission properties, which suggest that Vy 2-2 may host a post-CE binary. Therefore, Vy 2-2 would be an illustrative observational case of the CE evolutionary phase. Chemical abundances and circumstellar mass estimates indicate $M_\mathrm{i} \lesssim 0.9\,M_\odot$ for the progenitor star of Vy 2-2.

- The non-thermal radio spectral indices we report for 22 PNe and candidates provide evidence that radiative processes such as synchrotron emission may be present during this evolutionary phase, further challenging the traditional view of these objects as purely thermal radio sources. This would imply that intense magnetic-field activity operates during the earliest stages of PN formation and may play a fundamental role in their shaping.

10.1 Future Research

At the dawn of the new golden era of observational astrophysics, our work has unearthed a population of invaluable objects located across the northern and southern sky whose emission properties correspond with those of evolved stars transiting between the brief post-AGB and the nascent PN phases that enable deepening our understanding of the earliest stages of PN formation. We will continue this work in the future, expanding and characterizing new nascent PNe.

- We will apply intermediate-resolution long-slit near-infrared K-band (2–2.3 μm) spectroscopy with the NTT to maser-emitting PN candidates to confirm their PN nature, including confirmed maser-emitting PNe for comparison. This approach will allow us to assess the contribution of photoionization to their ionized emission using diagnostic diagrams based on shock and photoionization models, including our previously and newly developed diagrams. These diagnostic tools constitute a novel methodological contribution and provide a powerful framework for the classification of obscured sources, particularly in the context of upcoming datasets from facilities such as the James Webb Space Telescope (JWST).

- We presented growing evidence that the central stars of these maser-emitting PNe and candidates could be carbon-rich. We are carrying out a survey for HCN masers in all confirmed and candidate PNe with OH and/or H_2O masers, aiming at the first detection of HCN masers in these sources. This would confirm their dual chemistry and open a new window to study the morphology, kinematics, and physical properties of nascent PNe at scales < 10 AU through follow-up high angular resolution radio observations with ALMA.

- We have started a detailed characterization of the WF IRAS 18443–0231. Using the EVN, we aim to determine whether the spatio-kinematics of the S-shaped H_2O masers trace precessing mass loss, and to measure their magnetic field direction and strength, providing key constraints for models of magnetic shaping of PNe. Complementary VLA observations in bands L, X, and K will allow us to monitor the maser distribution, characterize the radio continuum spectrum and its variability, and map the spectral index to disentangle thermal and non-thermal emission components.

- Our recent photometric and spectroscopic observations of IRAS 22568+6141 reveal that the Hβ flux has decreased by factors of $\sim$6 and $\sim$4 compared to 2021 and 2023, indicating that the ionized emission is declining at an accelerated rate. We have initiated a long-term monitoring program of its variable optical emission, consistent with a cooling central star and a recombining PN, to be complemented with high-resolution spectroscopy to track its morphokinematical evolution.

- Next-generation radio facilities will enable sensitive, wide-field surveys capable of detecting faint maser emission and non-thermal radio continuum from previously undetectable sources. As a first step, we will exploit the Galactic ASKAP survey to identify new candidate OHPNe. Building on this, the Square Kilometre Array (SKA) will allow the systematic discovery of maser-emitting and non-thermal PNe across the Galaxy, as well as the study of their time-variable ionized emission, maser structures, and non-thermal continuum on human timescales.

- Complementary high-resolution, spatially-resolved spectroscopy using optical and near-infrared integral field units will be crucial to disentangle the contributions of shocks and photoionization in the ionized emission within individual objects. This can be achieved with facilities such as Keck, Gemini, VLT, or the JWST, allowing the investigation of dust, PAHs, and obscured inner regions, in addition to the ionized emission. ALMA observations will bridge these approaches by enabling the simultaneous study of ionized, molecular, and dust emission.

- We aim to develop a probabilistic artificial intelligence (AI) pipeline to systematize and homogenize the analysis of shocks and photoionization in nascent PNe. This pipeline will perform automated spectral measurements (line detection, Gaussian fitting, and flux estimation) and use supervised models trained on synthetic spectra to estimate probabilities of shock and photoionization contributions. AI emulators of model grids will enable the inference of physical parameters such as shock velocities, magnetic field strengths, effective temperatures, and electron densities. In this context, this work lays the foundations for a new Big Data era, where the synergy of wide-field Galactic surveys and the AI pipeline could systematically identify, classify, and analyze a new generation of nascent PNe. Furthermore, the AI pipeline could provide a robust classification, for the first time, of sources as post-AGB stars or PNe.

Bibliography

Aaquist, O. B. 1993, A&A, 267, 260

Aaquist, O. B. & Kwok, S. 1991, ApJ, 378, 599

Abazajian, K. N., Adelman-McCarthy, J. K., Agüeros, M. A., et al. 2009, ApJS, 182, 543

Acker, A., Marcout, J., Ochsenbein, F., et al. 1992, The Strasbourg-ESO Catalogue of Galactic Planetary Nebulae. Parts I, II.

Acker, A. & Neiner, C. 2003, A&A, 403, 659

Acker, A., Raytchev, B., Koeppen, J., & Stenholm, B. 1991, A&A, 89, 237

Akras, S., Guzman-Ramirez, L., Leal-Ferreira, M. L., & Ramos-Larios, G. 2019, ApJS, 240, 21

Alarie, A. & Morisset, C. 2019, Rev.Mex.Ast., 55, 377

Allen, M. G., Groves, B. A., Dopita, M. A., Sutherland, R. S., & Kewley, L. J. 2008, ApJS, 178, 20

Amada, K., Imai, H., Hamae, Y., et al. 2022, AJ, 163, 85

Anderson, L. D., Bania, T. M., Balser, D. S., & Rood, R. T. 2011, ApJS, 194, 32

Anderson, L. D., Zavagno, A., Barlow, M. J., García-Lario, P., & Noriega-Crespo, A. 2012, A&A, 537, A1

Anglada, G., Estalella, R., Pastor, J., Rodriguez, L. F., & Haschick, A. D. 1996, ApJ, 463, 205

Anglada, G., Rodríguez, L. F., & Carrasco-González, C. 2018, A&ARv, 26, 3

Anglada, G., Rodriguez, L. F., Torrelles, J. M., et al. 1989, ApJ, 341, 208

Arkhipova, V. P., Burlak, M. A., Esipov, V. F., Ikonnikova, N. P., & Komissarova, G. V. 2017, Astronomy Letters, 43, 831

Arkhipova, V. P., Ikonnikova, N. P., Kniazev, A. Y., & Rajoelimanana, A. 2013, Astronomy Letters, 39, 201

Arrieta, A. & Torres-Peimbert, S. 2003, ApJS, 147, 97

Asplund, M., Grevesse, N., Sauval, A. J., & Scott, P. 2009, AR&A, 47, 481

Astropy Collaboration, Price-Whelan, A. M., Lim, P. L., et al. 2022, ApJ, 935, 167

Astropy Collaboration, Price-Whelan, A. M., Sipőcz, B. M., et al. 2018, AJ, 156, 123

Astropy Collaboration, Robitaille, T. P., Tollerud, E. J., et al. 2013, A&A, 558, A33

Avison, A., Quinn, L. J., Fuller, G. A., et al. 2016, MNRAS, 461, 136

Bachiller, R., Forveille, T., Huggins, P. J., & Cox, P. 1997, A&A, 324, 1123

Bains, I., Cohen, M., Chapman, J. M., Deacon, R. M., & Redman, M. P. 2009, MNRAS, 397, 1386

Balick, B. 1987, AJ, 94, 671

Balick, B., Alexander, J., Hajian, A. R., et al. 1998, AJ, 116, 360

Balick, B. & Frank, A. 2002, ARA&A, 40, 439

Balick, B., Frank, A., & Liu, B. 2020, ApJ, 889, 13

Balick, B., Guerrero, M. A., & Ramos-Larios, G. 2021, ApJ, 907, 104

Balick, B., Preston, H. L., & Icke, V. 1987, AJ, 94, 1641

Baud, B., Habing, H. J., Matthews, H. E., & Winnberg, A. 1979a, A&AS, 35, 179

Baud, B., Habing, H. J., Matthews, H. E., & Winnberg, A. 1979b, A&AS, 36, 193

Baud, B., Habing, H. J., Matthews, H. E., & Winnberg, A. 1981, A&A, 95, 156

Becker, R. H., White, R. L., Helfand, D. J., & Zoonematkermani, S. 1994, ApJS, 91, 347

Becker, R. H., White, R. L., & Proctor, D. D. 1992, AJ, 103, 544

Benson, P. J. & Little-Marenin, I. R. 1996, ApJS, 106, 579

Benson, P. J., Little-Marenin, I. R., Woods, T. C., et al. 1990, ApJS, 74, 911

Beuther, H., Bihr, S., Rugel, M., et al. 2016, A&A, 595, A32

Beuther, H., Walsh, A., Wang, Y., et al. 2019, A&A, 628, A90

Black, J. H. & van Dishoeck, E. F. 1987, ApJ, 322, 412

Blandford, R. D. & Königl, A. 1979, ApJ, 232, 34

Blöcker, T. 1995, A&A, 299, 755

Blöcker, T. 2001, Astrophysics and Space Science, 275, 1

Bloecker, T. 1995, A&A, 299, 755

Boboltz, D. A. & Marvel, K. B. 2005, ApJL, 627, L45

Boboltz, D. A. & Marvel, K. B. 2007, ApJ, 665, 680

Boffin, H. M. J. & Jones, D. 2019, The Importance of Binaries in the Formation and Evolution of Planetary Nebulae

Boffin, H. M. J., Miszalski, B., Rauch, T., et al. 2012, Science, 338, 773

Bollen, D., Kamath, D., Van Winckel, H., De Marco, O., & Wardle, M. 2021, MNRAS, 502, 445

Bondi, H. & Hoyle, F. 1944, MNRAS, 104, 273

Borkowski, K. J., Blondin, J. M., & Harrington, J. P. 1997, ApJL, 482, L97

Bouvis, K., Akras, S., Monteiro, H., et al. 2025, A&A, 700, A155

Bowers, P. F. & Johnston, K. J. 1994, ApJS, 92, 189

Breen, S. L., Ellingsen, S. P., Contreras, Y., et al. 2013, MNRAS, 435, 524

Brown, M. J. I., Moustakas, J., Smith, J.-D. T., et al. 2014, ApJS, 212, 18

Bujarrabal, V., Alcolea, J., Neri, R., & Grewing, M. 1994, ApJL, 436, L169

Bujarrabal, V., Alcolea, J., Neri, R., & Grewing, M. 1997, A&A, 320, 540

Bujarrabal, V., Castro-Carrizo, A., Alcolea, J., & Sánchez Contreras, C. 2001, A&A, 377, 868

Bujarrabal, V., Castro-Carrizo, A., Alcolea, J., et al. 2013, A&A, 557, L11

Bujarrabal, V., Neri, R., Alcolea, J., & Kahane, C. 2003, A&A, 409, 573

Bujarrabal, V., Planesas, P., Gomez-Gonzalez, J., Martin-Pintado, J., & del Romero, A. 1986, A&A, 162, 157

Caballero, J. A., Guàrdia, J., López del Fresno, M., et al. 2016, in Society of Photo-Optical Instrumentation Engineers (SPIE) Conference Series, Vol. 9910, Observatory Operations: Strategies, Processes, and Systems VI, ed. A. B. Peck, R. L. Seaman, & C. R. Benn, 99100E

Cala, R. A., Gómez, J. F., & Miranda, L. F. 2024a, in IAU Symposium, Vol. 380, Cosmic Masers: Proper Motion Toward the Next-Generation Large Projects, ed. T. Hirota, H. Imai, K. Menten, & Y. Pihlström, 343–346

Cala, R. A., Gómez, J. F., Miranda, L. F., et al. 2025a, A&A, 703, A268

Cala, R. A., Gómez, J. F., Miranda, L. F., et al. 2024b, A&A, 692, A24

Cala, R. A., Gómez, J. F., Miranda, L. F., et al. 2022, MNRAS, 516, 2235

Cala, R. A., Miranda, L. F., Gómez, J. F., et al. 2024c, A&A, 691, A321

Cala, R. A., Miranda, L. F., Gómez, J. F., & Ohnaka, K. 2025b, A&A, 703, L7

Carrasco-González, C., Rodríguez, L. F., Anglada, G., et al. 2010, Science, 330, 1209

Carsenty, U. & Solf, J. 1982, A&A, 106, 307

CASA Team, Bean, B., Bhatnagar, S., et al. 2022, PASP, 134, 114501

Casali, M., Adamson, A., Alves de Oliveira, C., et al. 2007, A&A, 467, 777

Caswell, J. L. 1997, MNRAS, 289, 203

Caswell, J. L., Fuller, G. A., Green, J. A., et al. 2010, MNRAS, 404, 1029

Caswell, J. L., Fuller, G. A., Green, J. A., et al. 2011, MNRAS, 417, 1964

Caswell, J. L., Haynes, R. F., & Goss, W. M. 1980, Australian Journal of Physics, 33, 639

Cerrigone, L., Trigilio, C., Umana, G., Buemi, C. S., & Leto, P. 2011, MNRAS, 412, 1137

Cerrigone, L., Umana, G., Trigilio, C., et al. 2017, MNRAS, 468, 3450

Cesaroni, R., Palagi, F., Felli, M., et al. 1988, A&AS, 76, 445

Chambers, K. C., Magnier, E. A., Metcalfe, N., et al. 2016, arXiv e-prints, arXiv:1612.05560

Chapman, J. M. 1988, MNRAS, 230, 415

Chengalur, J. N., Lewis, B. M., Eder, J., & Terzian, Y. 1993, ApJS, 89, 189

Cho, C.-Y., Cho, S.-H., Kim, S., et al. 2017, ApJS, 232, 13

Cho, S.-H. & Kim, J. 2010, ApJ, 719, 126

Christianto, H. & Seaquist, E. R. 1998, AJ, 115, 2466

Clark, B. G. 1980, A&A, 89, 377

Claussen, M. J., Sahai, R., & Morris, M. R. 2009, ApJ, 691, 219

Clayton, G. C. & De Marco, O. 1997, AJ, 114, 2679

Cohen, M. & Barlow, M. J. 2005, MNRAS, 362, 1199

Cohen, M., Barlow, M. J., Liu, X.-W., & Jones, A. F. 2002, MNRAS, 332, 879

Cohen, M., Van Winckel, H., Bond, H. E., & Gull, T. R. 2004, AJ, 127, 2362

Condon, J. J. 1992, ARA&A, 30, 575

Condon, J. J., Cotton, W. D., Greisen, E. W., et al. 1998, AJ, 115, 1693

Cooper, H. D. B., Lumsden, S. L., Oudmaijer, R. D., et al. 2013, MNRAS, 430, 1125

Corradi, R. L. M. & Schwarz, H. E. 1995, A&A, 293, 871

Cox, P., Boulanger, F., Huggins, P. J., et al. 1998, ApJL, 495, L23

Dale, D. A., Bendo, G. J., Engelbracht, C. W., et al. 2005, ApJ, 633, 857

David, P., Le Squeren, A. M., & Sivagnanam, P. 1993, A&A, 277, 453

Davis, L. E., Seaquist, E. R., & Purton, C. R. 1979, ApJ, 230, 434

Dawson, J. R., Breen, S. L., & Gaskap-Oh Team. 2024, in IAU Symposium, Vol. 380, Cosmic Masers: Proper Motion Toward the Next-Generation Large Projects, ed. T. Hirota, H. Imai, K. Menten, & Y. Pihlström, 486–490

Dawson, J. R., Jones, P. A., Purcell, C., et al. 2022, MNRAS, 512, 3345

Day, F. M., Pihlström, Y. M., Claussen, M. J., & Sahai, R. 2010, ApJ, 713, 986

de Gregorio-Monsalvo, I., Gómez, Y., Anglada, G., et al. 2004, ApJ, 601, 921

De Marco, O. 2009, PASP, 121, 316

De Marco, O., Long, J., Jacoby, G. H., et al. 2015, MNRAS, 448, 3587

De Marco, O. & Soker, N. 2002, PASP, 114, 602

De Marco, O. & Soker, N. 2011, PASP, 123, 402

de Ruyter, S., van Winckel, H., Maas, T., et al. 2006, A&A, 448, 641

Deacon, R. M., Chapman, J. M., & Green, A. J. 2004, ApJS, 155, 595

Deacon, R. M., Chapman, J. M., Green, A. J., & Sevenster, M. N. 2007, ApJ, 658, 1096

Decin, L., Homan, W., Danilovich, T., et al. 2019, Nature Astronomy, 3, 408

Decin, L., Montargès, M., Richards, A. M. S., et al. 2020, Science, 369, 1497

Deguchi, S., Fujii, T., Ita, Y., et al. 2007, PASJ, 59, 559

Deguchi, S., Matsunaga, N., & Fukushi, H. 2005, PASJ, 57, L25

Deguchi, S., Nakashima, J.-I., & Balasubramanyam, R. 2001, PASJ, 53, 305

Delgado-Inglada, G., Morisset, C., & Stasińska, G. 2014, MNRAS, 440, 536

Depoy, D. L. & Shields, J. C. 1994, ApJ, 422, 187

Desmurs, J.-F., Baudry, A., Sivagnanam, P., & Henkel, C. 2002, A&A, 394, 975

Desmurs, J.-F., Baudry, A., Sivagnanam, P., et al. 2010, A&A, 520, A45

Desmurs, J. F., Bujarrabal, V., Colomer, F., & Alcolea, J. 2000, A&A, 360, 189

Deutsch, A. J. 1956, ApJ, 123, 210

Diamond, P. J., Kemball, A. J., Junor, W., et al. 1994, ApJL, 430, L61

Dike, V., Morris, M. R., Rich, R. M., et al. 2021, AJ, 161, 111

Dopita, M. A. 1978, ApJS, 37, 117

Dorman, B., Rood, R. T., & O'Connell, R. W. 1993, ApJ, 419, 596

Douglas, J. N., Bash, F. N., Bozyan, F. A., Torrence, G. W., & Wolfe, C. 1996, AJ, 111, 1945

Drew, J. E., Gonzalez-Solares, E., Greimel, R., et al. 2014, MNRAS, 440, 2036

Duchesne, S. W., Grundy, J. A., Heald, G. H., et al. 2024, PASA, 41, e003

Duerbeck, H. W. & Benetti, S. 1996, ApJ, 468, L111

Dunham, M. M., Arce, H. G., Allen, L. E., et al. 2013, AJ, 145, 94

Dunham, M. M., Crapsi, A., Evans, II, N. J., et al. 2008, ApJS, 179, 249

Dzib, S. A., Yang, A. Y., Urquhart, J. S., et al. 2023, A&A, 670, A9

Eder, J., Lewis, B. M., & Terzian, Y. 1988, ApJS, 66, 183

Edgar, R. 2004, NewAR, 48, 843

Edwards, J. L. & Ziurys, L. M. 2014, ApJL, 794, L27

Elitzur, M. 1992, ARA&A, 30, 75

Ellingsen, S. P., Voronkov, M. A., Breen, S. L., Caswell, J. L., & Sobolev, A. M. 2018, MNRAS, 480, 4851

Engels, D. 2002, A&A, 388, 252

Engels, D. & Bunzel, F. 2015, A&A, 582, A68

Engels, D. & Jiménez-Esteban, F. 2007, A&A, 475, 941

Engels, D. & Lewis, B. M. 1996, A&AS, 116, 117

Engels, D., Schmid-Burgk, J., & Walmsley, C. M. 1986, A&A, 167, 129

Etoka, S. & Diamond, P. J. 2010, MNRAS, 406, 2218

Fan, H., Nakashima, J.-i., Engels, D., et al. 2024, ApJS, 270, 13

Fang, X., Guerrero, M. A., Miranda, L. F., et al. 2015, MNRAS, 452, 2445

Fang, X. & Liu, X. W. 2013, MNRAS, 429, 2791

Fang, X., Storey, P. J., & Liu, X.-W. 2011, A&A, 530, A18

Fedriani, R., Caratti o Garatti, A., Koutoulaki, M., et al. 2020, A&A, 633, A128

Ferland, G. J., Chatzikos, M., Guzmán, F., et al. 2017, Rev.Mex.Ast., 53, 385

Fomalont, E. 1981, National Radio Astronomy Observatory Newsletter, 3, 3

Forster, J. R. & Caswell, J. L. 1989a, A&A, 213, 339

Forster, J. R. & Caswell, J. L. 1989b, A&A, 213, 339

Forster, J. R. & Caswell, J. L. 1999a, A&AS, 137, 43

Forster, J. R. & Caswell, J. L. 1999b, A&AS, 137, 43

Fragkou, V., Parker, Q. A., Bojičić, I. S., & Aksaker, N. 2018, MNRAS, 480, 2916

Franco, J., Tenorio-Tagle, G., & Bodenheimer, P. 1990, ApJ, 349, 126

Frew, D. J., Bojičić, I. S., & Parker, Q. A. 2013, MNRAS, 431, 2

Froese Fischer, C. & Tachiev, G. 2004, Atomic Data and Nuclear Data Tables, 87, 1

Fujii, T., Deguchi, S., Ita, Y., et al. 2006, PASJ, 58, 529

Gaia Collaboration, Babusiaux, C., van Leeuwen, F., et al. 2018, A&A, 616, A10

Gaia Collaboration, Brown, A. G. A., Vallenari, A., et al. 2021, A&A, 649, A1

Gaia Collaboration, Prusti, T., de Bruijne, J. H. J., et al. 2016, A&A, 595, A1

Gaia Collaboration, Vallenari, A., Brown, A. G. A., et al. 2023, A&A, 674, A1

García-Hernández, D. A., Manchado, A., García-Lario, P., et al. 2006, ApJ, 640, 829

García-Hernández, D. A., Perea-Calderón, J. V., Bobrowsky, M., & García-Lario, P. 2007, ApJL, 666, L33

Garcia Lario, P., Manchado, A., Riera, A., Mampaso, A., & Pottasch, S. R. 1991, A&A, 249, 223

Garcia-Segura, G. 1997, ApJL, 489, L189

García-Segura, G. 2010, A&A, 520, L5

García-Segura, G., López, J. A., & Franco, J. 2005, ApJ, 618, 919

García-Segura, G., Manchado, A., Toalá, J. A., Guerrero, M. A., & Castro-Tirado, A. J. 2025, MNRAS, 543, 3867

García-Segura, G., Ricker, P. M., & Taam, R. E. 2018, ApJ, 860, 19

García-Segura, G., Taam, R. E., & Ricker, P. M. 2020, ApJ, 893, 150

García-Segura, G., Villaver, E., Langer, N., Yoon, S.-C., & Manchado, A. 2014, ApJ, 783, 74

Garwood, R. W., Perley, R. A., Dickey, J. M., & Murray, M. A. 1988, AJ, 96, 1655

Gathier, R., Pottasch, S. R., Goss, W. M., & van Gorkom, J. H. 1983, A&A, 128, 325

Genzel, R., Lutz, D., Sturm, E., et al. 1998, ApJ, 498, 579

Gesicki, K., Zijlstra, A., Hajduk, M., et al. 2024, A&A, 689, A17

Gieseking, F., Becker, I., & Solf, J. 1985, ApJL, 295, L17

Ginsburg, A., Anderson, L. D., Dicker, S., et al. 2020, ApJS, 248, 24

Gledhill, T. M. & Forde, K. P. 2012, MNRAS, 421, 346

Gledhill, T. M. & Forde, K. P. 2015, MNRAS, 447, 1080

Gledhill, T. M., Forde, K. P., Lowe, K. T. E., & Smith, M. D. 2011, MNRAS, 411, 1453

Gold, K. R., Schmidt, D. R., & Ziurys, L. M. 2024, ApJ, 976, 196

Goldman, S. R., van Loon, J. T., Zijlstra, A. A., et al. 2017, MNRAS, 465, 403

Gómez, J. F., de Gregorio-Monsalvo, I., Lovell, J. E. J., et al. 2005, MNRAS, 364, 738

Gómez, J. F., Imai, H., Uscanga, L., et al. 2023, in Highlights on Spanish Astrophysics XI, ed. M. Manteiga, L. Bellot, P. Benavidez, A. de Lorenzo-Cáceres, M. A. Fuente, M. J. Martínez, M. Vázquez Acosta, & C. Dafonte, 210

Gómez, J. F., Miranda, L. F., Uscanga, L., & Suárez, O. 2018a, in IAU Symposium, Vol. 336, Astrophysical Masers: Unlocking the Mysteries of the Universe, ed. A. Tarchi, M. J. Reid, & P. Castangia, 377–380

Gómez, J. F., Niccolini, G., Suárez, O., et al. 2018b, MNRAS, 480, 4991

Gómez, J. F., Rizzo, J. R., Suárez, O., et al. 2011, ApJL, 739, L14

Gómez, J. F., Rizzo, J. R., Suárez, O., et al. 2015a, A&A, 578, A119

Gómez, J. F., Suárez, O., Bendjoya, P., et al. 2015b, ApJ, 799, 186

Gómez, J. F., Suárez, O., Gómez, Y., et al. 2008, AJ, 135, 2074

Gómez, J. F., Suárez, O., Rizzo, J. R., et al. 2017, MNRAS, 468, 2081

Gómez, J. F., Uscanga, L., Green, J. A., et al. 2016, MNRAS, 461, 3259

Gómez, J. F., Uscanga, L., Suárez, O., Rizzo, J. R., & de Gregorio-Monsalvo, I. 2014, Rev. Mex Ast., 50, 137

Gómez, Y., Moran, J. M., & Rodríguez, L. F. 1990, Rev.Mex.Ast., 20, 55

Gómez, Y., Rodríguez, L. F., Contreras, M. E., & Moran, J. M. 1994, RXAA, 28, 97

Gómez, Y., Tafoya, D., Anglada, G., et al. 2009, ApJ, 695, 930

Gonçalves, D. R., Corradi, R. L. M., Mampaso, A., & Perinotto, M. 2003, ApJ, 597, 975

Gonçalves, D. R., Mampaso, A., Corradi, R. L. M., et al. 2004, MNRAS, 355, 37

Gonidakis, I., Chapman, J. M., Deacon, R. M., & Green, A. J. 2014, MNRAS, 443, 3819

Gonzalez, G., Lambert, D. L., Wallerstein, G., et al. 1998, ApJS, 114, 133

Gordon, Y. A., Boyce, M. M., O'Dea, C. P., et al. 2021, ApJS, 255, 30

Górny, S. K., Stasińska, G., Escudero, A. V., & Costa, R. D. D. 2004, A&A, 427, 231

Green, J. A., Caswell, J. L., Fuller, G. A., et al. 2008, MNRAS, 385, 948

Green, J. A., McClure-Griffiths, N. M., Caswell, J. L., Robishaw, T., & Harvey-Smith, L. 2012, MNRAS, 425, 2530

Groenewegen, M. A. T., van den Hoek, L. B., & de Jong, T. 1995, A&A, 293, 381

Gruenwald, R. & Aleman, A. 2007, A&A, 461, 1019

Guerrero, M. A., Cazzoli, S., Rechy-García, J. S., et al. 2021, ApJ, 909, 44

Guerrero, M. A. & De Marco, O. 2013, A&A, 553, A126

Guerrero, M. A., Fang, X., Miller Bertolami, M. M., et al. 2018, Nature Astronomy, 2, 784

Guerrero, M. A., Miranda, L. F., Ramos-Larios, G., & Vázquez, R. 2013, A&A, 551, A53

Guerrero, M. A., Miranda, L. F., Riera, A., et al. 2008, ApJ, 683, 272

Hajduk, M., Shimwell, T., White, G., et al. 2025, A&A, 703, L5

Hajduk, M., Todt, H., Hamann, W.-R., et al. 2020, MNRAS, 498, 1205

Hajduk, M., van Hoof, P. A. M., Śniadkowska, K., et al. 2018, MNRAS, 479, 5657

Hajduk, M., van Hoof, P. A. M., Zijlstra, A. A., et al. 2024, A&A, 688, L21

Hajduk, M., Zijlstra, A. A., Herwig, F., et al. 2005, Science, 308, 231

Hale, C. L., McConnell, D., Thomson, A. J. M., et al. 2021, PASA, 38, e058

Hall, P. J., Wright, A. E., Troup, E. R., Wark, R. M., & Allen, D. A. 1990, MNRAS, 247, 549

Hambly, N. C., Collins, R. S., Cross, N. J. G., et al. 2008, MNRAS, 384, 637

Haro, G. 1952, Boletin de los Observatorios Tonantzintla y Tacubaya, 1, 1

Hartigan, P., Raymond, J., & Hartmann, L. 1987, ApJ, 316, 323

Harvey-Smith, L., Hardwick, J. A., De Marco, O., et al. 2018, MNRAS, 479, 1842

Helfand, D. J., Zoonematkermani, S., Becker, R. H., & White, R. L. 1992, ApJS, 80, 211

Henize, K. G. 1967, ApJS, 14, 125

Herschel, W. 1791, Philosophical Transactions of the Royal Society of London Series I, 81, 71

Hewett, P. C., Warren, S. J., Leggett, S. K., & Hodgkin, S. T. 2006, MNRAS, 367, 454

Ho, P. T. P. & Townes, C. H. 1983, ARA&A, 21, 239

Hofner, P. & Churchwell, E. 1996, A&A, 120, 283

Hora, J. L., Latter, W. B., & Deutsch, L. K. 1999, ApJS, 124, 195

Houck, J. R., Roellig, T. L., van Cleve, J., et al. 2004, ApJS, 154, 18

Hrivnak, B. J., Kwok, S., & Geballe, T. R. 1994, ApJ, 420, 783

Hsia, C.-H., Kwok, S., Zhang, Y., Koning, N., & Volk, K. 2010, ApJ, 725, 173

Hsia, C.-H. & Zhang, Y. 2014, A&A, 563, A63

Huarte-Espinosa, M., Frank, A., Blackman, E. G., et al. 2012, ApJ, 757, 66

Huggins, P. J., Bachiller, R., Cox, P., & Forveille, T. 1996, A&A, 315, 284

Huggins, W. & Miller, W. A. 1864a, Philosophical Transactions of the Royal Society of London Series I, 154, 413

Huggins, W. & Miller, W. A. 1864b, Philosophical Transactions of the Royal Society of London Series I, 154, 437

Hyung, S., Lee, S.-J., & Otsuka, M. 2023, ApJS, 265, 2

Iben, Jr., I., Kaler, J. B., Truran, J. W., & Renzini, A. 1983, ApJ, 264, 605

Icke, V., Preston, H. L., & Balick, B. 1989, AJ, 97, 462

Imai, H. 2007, in IAU Symposium, Vol. 242, Astrophysical Masers and their Environments, ed. J. M. Chapman & W. A. Baan, 279–286

Imai, H., Deguchi, S., Nakashima, J.-i., Kwok, S., & Diamond, P. J. 2013, ApJ, 773, 182

Imai, H., Hamae, Y., Amada, K., et al. 2023, , 75, 1183

Imai, H., Morris, M., Sahai, R., Hachisuka, K., & Azzollini F., J. R. 2004, A&A, 420, 265

Imai, H., Nakashima, J.-i., Diamond, P. J., Miyazaki, A., & Deguchi, S. 2005, ApJ, 622, L125

Imai, H., Obara, K., Diamond, P. J., Omodaka, T., & Sasao, T. 2002, Nature, 417, 829

Irabor, T., Hoare, M. G., Burton, M., et al. 2023, MNRAS, 520, 1073

Irabor, T., Hoare, M. G., Oudmaijer, R. D., et al. 2018, MNRAS, 480, 2423

Ivanova, N., Justham, S., Chen, X., et al. 2013, A&AR, 21, 59

Ivezic, Z., Nenkova, M., & Elitzur, M. 1999, arXiv e-prints, astro

Iwanek, P., Soszyński, I., Kozłowski, S., et al. 2022, ApJS, 260, 46

Izumiura, H., Catchpole, R., Deguchi, S., et al. 1995, ApJS, 98, 271

Jacoby, G. H., Hillwig, T. C., & Jones, D. 2020, MNRAS, 498, L114

Jacoby, G. H. & Van de Steene, G. 2004, A&A, 419, 563

Jewell, P. R., Snyder, L. E., Walmsley, C. M., Wilson, T. L., & Gensheimer, P. D. 1991, A&A, 242, 211

Jewell, P. R., Walmsley, C. M., Wilson, T. L., & Snyder, L. E. 1985, ApJL, 298, L55

Jones, D. & Boffin, H. M. J. 2017, Nature Astronomy, 1, 0117

Jordan, C. H., Walsh, A. J., Lowe, V., et al. 2015, MNRAS, 448, 2344

Jura, M., Turner, J., Balm, & S. P. 1997, ApJ, 474, 741

Kahn, F. D. 1954, BAIN, 12, 187

Kaler, J. B., Kwitter, K. B., Shaw, R. A., & Browning, L. 1996, PASP, 108, 980

Kanarek, G., Shara, M., Faherty, J., Zurek, D., & Moffat, A. 2015, MNRAS, 452, 2858

Kaplan, K. F., Dinerstein, H. L., & Jaffe, D. T. 2026, AJ, 171, 219

Karakas, A. I. & Lattanzio, J. C. 2014, PASA, 31, e030

Khouri, T., Vlemmings, W. H. T., Tafoya, D., et al. 2021, Nature Astronomy, 6, 275

Kimeswenger, S. 2001, Rev. Mex. Ast., 37, 115

Kingsburgh, R. L. & Barlow, M. J. 1994, MNRAS, 271, 257

Knapp, G. R., Bowers, P. F., Young, K., & Phillips, T. G. 1995, ApJ, 455, 293

Kohoutek, L. 2001, A&A, 378, 843

Kwok, S. 1975, ApJ, 198, 583

Kwok, S. 2010, PASA, 27, 174

Kwok, S. & Feldman, P. A. 1981, ApJL, 247, L67

Kwok, S., Hrivnak, B. J., Zhang, C. Y., & Langill, P. L. 1996, ApJ, 472, 287

Kwok, S., Purton, C. R., & Fitzgerald, P. M. 1978, ApJ, 219, L125

Kwok, S., Purton, C. R., & Keenan, D. W. 1981, ApJ, 250, 232

Lacy, M., Baum, S. A., Chandler, C. J., et al. 2020, PASP, 132, 035001

Ladeyschikov, D. A., Bayandina, O. S., & Sobolev, A. M. 2019, AJ, 158, 233

Lawlor, T. M. 2021, MNRAS, 504, 667

Lawlor, T. M. 2023, MNRAS, 519, 5373

Lawlor, T. M. & MacDonald, J. 2003, ApJ, 583, 913

Lawrence, A., Warren, S. J., Almaini, O., et al. 2007, MNRAS, 379, 1599

Lebzelter, T., Mowlavi, N., Lecoeur-Taibi, I., et al. 2023, A&A, 674, A15

Lee, S.-J., Hyung, S., & Otsuka, M. 2022, ApJ, 938, 71

Leone, F., Corradi, R. L. M., Martínez González, M. J., Asensio Ramos, A., & Manso Sainz, R. 2014, A&A, 563, A43

Lewis, B. M. 1989, ApJ, 338, 234

Lewis, B. M. 1994, ApJS, 93, 549

Lewis, B. M. 1997, ApJS, 109, 489

Lewis, B. M. & Engels, D. 1988, Nature, 332, 49

Lewis, M. O., Pihlström, Y. M., Sjouwerman, L. O., et al. 2020, ApJ, 892, 52

Likkel, L. 1989, ApJ, 344, 350

Likkel, L. & Morris, M. 1988, ApJ, 329, 914

Likkel, L., Morris, M., & Maddalena, R. J. 1992, A&A, 256, 581

Liu, X.-W., Barlow, M. J., Cohen, M., et al. 2001, MNRAS, 323, 343

Livio, M., Salzman, J., & Shaviv, G. 1979, MNRAS, 188, 1

Livio, M. & Soker, N. 1988, ApJ, 329, 764

Lo, K. Y. 2005, ARA&A, 43, 625

Lopez, J. A., Meaburn, J., & Palmer, J. W. 1993, ApJL, 415, L135

Lopez, J. A., Vazquez, R., & Rodriguez, L. F. 1995, ApJL, 455, L63

López-Martín, L., López, J. A., Esteban, C., et al. 2002, A&A, 388, 652

Loup, C., Forveille, T., Nyman, L. A., & Omont, A. 1990, A&A, 227, L29

Lumsden, S. L., Puxley, P. J., & Hoare, M. G. 2001a, MNRAS, 320, 83

Lumsden, S. L., Puxley, P. J., & Hoare, M. G. 2001b, MNRAS, 328, 419

Luridiana, V., Morisset, C., & Shaw, R. A. 2015, A&A, 573, A42

Lyu, J. & Rieke, G. 2022, Universe, 8, 304

Manchado, A., Guerrero, M. A., Stanghellini, L., & Serra-Ricart, M. 1996a, The IAC morphological catalog of northern Galactic planetary nebulae

Manchado, A., Manteiga, M., González-Santamaría, I., & Villaver, E. 2025, in IAU Symposium, Vol. 384, IAU Symposium, ed. O. De Marco, A. Zijlstra, & R. Szczerba, 403–404

Manchado, A. & Pottasch, S. R. 1989, A&A, 222, 219

Manchado, A., Stanghellini, L., & Guerrero, M. A. 1996b, ApJL, 466, L95

Manchado, A., Stanghellini, L., Villaver, E., et al. 2015, ApJ, 808, 115

Manion, J. A., Huie, R. E., Levin, R. D., et al. 2015, NIST Chemical Kinetics Database, NIST Standard Reference Database 17, data version 2015.09

Marcolino, W. L. F. & de Araújo, F. X. 2003, AJ, 126, 887

Mari, M. B., Akras, S., & Gonçalves, D. R. 2023a, MNRAS, 525, 1998

Mari, M. B., Gonçalves, D. R., & Akras, S. 2023b, MNRAS, 518, 3908

Marigo, P., Girardi, L., Bressan, A., et al. 2017, ApJ, 835, 77

Maron, O., Kijak, J., Kramer, M., & Wielebinski, R. 2000, A&AS, 147, 195

Marquez-Lugo, R. A., Ramos-Larios, G., Guerrero, M. A., & Vázquez, R. 2013, MNRAS, 429, 973

Martin, S. C. 1997, ApJL, 478, L33

Martín-Hernández, N. L., Vermeij, R., Tielens, A. G. G. M., van der Hulst, J. M., & Peeters, E. 2002, A&A, 389, 286

Marton, G., Gezer, I., Madarász, M., et al. 2024, A&A, 688, A203

Masci, F. J., Laher, R. R., Rusholme, B., et al. 2019, PASP, 131, 018003

Matsuura, M., Bernard-Salas, J., Lloyd Evans, T., et al. 2014, MNRAS, 439, 1472

McNabb, I. A., Fang, X., Liu, X. W., Bastin, R. J., & Storey, P. J. 2013, MNRAS, 428, 3443

Meaburn, J. & Walsh, J. R. 1989, A&A, 223, 277

Medina, S.-N. X., Dzib, S. A., Urquhart, J. S., et al. 2024, A&A, 689, A196

Medina, S.-N. X., Urquhart, J. S., Dzib, S. A., et al. 2019, A&A, 627, A175

Mellema, G. & Frank, A. 1995, MNRAS, 273, 401

Menten, K. M. 1991, ApJL, 380, L75

Menten, K. M., Wyrowski, F., Keller, D., & Kamiński, T. 2018, A&A, 613, A49

Menzies, J. W. & Wolstencroft, R. D. 1990, MNRAS, 247, 177

Messier, C. 1781, Catalogue des Nébuleuses et des Amas d'Étoiles (Catalog of Nebulae and Star Clusters), Connoissance des Temps ou des Mouvements Célestes, for 1784, p. 227-267

Miller Bertolami, M. M. 2016, A&A, 588

Mirabel, I. F., Rodriguez, L. F., Cordier, B., Paul, J., & Lebrun, F. 1992, Nature, 358, 215

Miranda, L. F., Blanco, M., Guerrero, M. A., & Riera, A. 2012, MNRAS, 421, 1661

Miranda, L. F., Fernández, M., Alcalá, J. M., et al. 2000, MNRAS, 311, 748

Miranda, L. F., Gómez, Y., Anglada, G., & Torrelles, J. M. 2001, Nature, 414, 284

Miranda, L. F. & Solf, J. 1991, A&A, 252, 331

Miranda, L. F. & Solf, J. 1992, A&A, 260, 397

Miranda, L. F., Suárez, O., Olguín, L., et al. 2021, arXiv e-prints [[arXiv]2105.05186]

Miranda, L. F., Torrelles, J. M., Guerrero, M. A., Aaquist, O. B., & Eiroa, C. 1998, , 298, 243

Miranda, L. F., Torrelles, J. M., & Lillo-Box, J. 2022, A&A, 657, L9

Miranda, L. F., Vázquez, R., Olguín, L., Guillén, P. F., & Matías, J. M. 2024, A&A, 687, A123

Miszalski, B., Acker, A., Parker, Q. A., & Moffat, A. F. J. 2009, A&A, 505, 249

Miszalski, B., Corradi, R. L. M., Boffin, H. M. J., et al. 2011a, MNRAS, 413, 1264

Miszalski, B., Jones, D., Rodríguez-Gil, P., et al. 2011b, , 531, A158

Mohamed, S. & Podsiadlowski, P. 2007, in Astronomical Society of the Pacific Conference Series, Vol. 372, 15th European Workshop on White Dwarfs, ed. R. Napiwotzki & M. R. Burleigh, 397

Molster, F. J., Waters, L. B. F. M., Tielens, A. G. G. M., & Barlow, M. J. 2002, A&A, 382, 184

Monet, D. G., Levine, S. E., Canzian, B., et al. 2003, AJ, 125, 984

Montoro-Molina, B. 2024, PhD thesis, University of Granada, Spain

Montoro-Molina, B., Guerrero, M. A., Pérez-Díaz, B., et al. 2022, MNRAS, 512, 4003

Moore, C. E. 1945, Contributions from the Princeton University Observatory, 20, 1

Morisset, C., Delgado-Inglada, G., & Flores-Fajardo, N. 2015, Rev.Mex.Ast., 51, 103

Morris, M. 1981, ApJ, 249, 572

Morris, M. 1987, PASP, 99, 1115

Müller, H. S. P., Schlöder, F., Stutzki, J., & Winnewisser, G. 2005, Journal of Molecular Structure, 742, 215

Munday, J., Jones, D., García-Rojas, J., et al. 2020, MNRAS, 498, 6005

Murphy, T., Mauch, T., Green, A., et al. 2007, MNRAS, 382, 382

Murphy, T., Sadler, E. M., Ekers, R. D., et al. 2010, MNRAS, 402, 2403

Nakashima, J.-I. & Deguchi, S. 2003a, PASJ, 55, 229

Nakashima, J.-I. & Deguchi, S. 2003b, PASJ, 55, 203

Nordhaus, J. & Blackman, E. G. 2006, MNRAS, 370, 2004

Norris, R. P., Allen, D. A., Haynes, R. F., & Wright, A. E. 1984, PASA, 5, 562

Nyman, L. A., Hall, P. J., & Olofsson, H. 1998, A&AS, 127, 185

Ogbodo, C. S., Green, J. A., Dawson, J. R., et al. 2020, MNRAS, 493, 199

Ohnaka, K., Boboltz, D. A., Mulitz-Schimel, G., Izumiura, H., & Wittkowski, M. 2013, A&A, 559, A120

Olnon, F. M. 1975, A&A, 39, 217

Olofsson, H., Bergman, P., Lucas, R., et al. 2000, A&A, 353, 583

Ondratschek, P. A., Röpke, F. K., Schneider, F. R. N., et al. 2022, A&A, 660, L8

Oomen, G.-M., Van Winckel, H., Pols, O., & Nelemans, G. 2019, A&A, 629, A49

Oomen, G.-M., Van Winckel, H., Pols, O., et al. 2018, A&A, 620, A85

Orosz, G., Gómez, J. F., Imai, H., et al. 2019, MNRAS, 482, L40

Orosz, G., Imai, H., Dodson, R., et al. 2017, AJ, 153, 119

Ortega, M. E., Petriella, A., & Paron, S. 2024, MNRAS, 532, 4446

Ortiz-León, G. N., Menten, K. M., Kamiński, T., et al. 2020, A&A, 638, A17

Osterbrock, D. E. 1964, ARA&A, 2, 95

Osterbrock, D. E. 1989, Astrophysics of gaseous nebulae and active galactic nuclei

Osterbrock, D. E. & Ferland, G. J. 2006, Astrophysics of gaseous nebulae and active galactic nuclei

Otsuka, M., Izumiura, H., Tajitsu, A., & Hyung, S. 2008, , 682, L105

Oudmaijer, R. D., Jones, E. R. M., & Vioque, M. 2022, MNRAS, 516, L61

Oudmaijer, R. D., Waters, L. B. F. M., van der Veen, W. E. C. J., & Geballe, T. R. 1995, A&A, 299, 69

Ouyang, X.-J., Zhang, Y., Zhang, C.-P., et al. 2024, ApJ, 972, 96

Paczyński, B. 1971, ARA&A, 9, 183

Paczynski, B. 1976, in IAU Symposium, Vol. 73, Structure and Evolution of Close Binary Systems, ed. P. Eggleton, S. Mitton, & J. Whelan, 75

Panagia, N. & Felli, M. 1975, A&A, 39, 1

Parker, Q. A., Acker, A., Frew, D. J., et al. 2006, MNRAS, 373, 79

Parker, Q. A., Bojičić, I. S., & Frew, D. J. 2016, in Journal of Physics Conference Series, Vol. 728, Journal of Physics Conference Series (IOP), 032008

Parthasarathy, M., Acker, A., & Stenholm, B. 1998, A&A, 329, L9

Parthasarathy, M., Garcia-Lario, P., de Martino, D., et al. 1995, A&A, 300, L25

Parthasarathy, M., Garcia-Lario, P., Pottasch, S. R., et al. 1993, A&A, 267, L19

Payne, H. E., Phillips, J. A., & Terzian, Y. 1988, ApJ, 326, 368

Peña, M., Parthasarathy, M., Ruiz-Escobedo, F., & Manick, R. 2022, MNRAS, 515, 1459

Peeters, E., Spoon, H. W. W., & Tielens, A. G. G. M. 2004, ApJ, 613, 986

Peimbert, M., Peimbert, A., & Delgado-Inglada, G. 2017, PASP, 129, 082001

Perea-Calderón, J. V., García-Hernández, D. A., García-Lario, P., Szczerba, R., & Bobrowsky, M. 2009, A&A, 495, L5

Pereira-Santaella, M., Diamond-Stanic, A. M., Alonso-Herrero, A., & Rieke, G. H. 2010, ApJ, 725, 2270

Pérez-Sánchez, A. F., Tafoya, D., García López, R., Vlemmings, W., & Rodríguez, L. F. 2017, A&A, 601, A68

Pérez-Sánchez, A. F., Vlemmings, W. H. T., & Chapman, J. M. 2011, MNRAS, 418, 1402

Podsiadlowski, P. & Mohamed, S. 2007, Baltic Astronomy, 16, 26

Pollacco, D. L. & Bell, S. A. 1993, MNRAS, 262, 377

Pollacco, D. L. & Bell, S. A. 1994, MNRAS, 267, 452

Popescu, C. C., Tuffs, R. J., Dopita, M. A., et al. 2011, A&A, 527, A109

Pottasch, S. R., Bignell, C., & Zijlstra, A. 1987, A&A, 177, L49

Pottasch, S. R., Dennefeld, M., & Mo, J. 1986, A&A, 155, 397

Preite-Martinez, A. 1988, A&AS, 76, 317

Purcell, C. R., Hoare, M. G., Cotton, W. D., et al. 2013, ApJS, 205, 1

Purcell, C. R., Longmore, S. N., Walsh, A. J., et al. 2012, MNRAS, 426, 1972

Pérez-Sánchez, A. F., Vlemmings, W. H. T., Tafoya, D., & Chapman, J. M. 2013a, MNRAS, 436, L79

Pérez-Sánchez, A. F., Vlemmings, W. H. T., Tafoya, D., & Chapman, J. M. 2013b, MNRAS, 436, L79

Qiao, H.-H., Breen, S. L., Gómez, J. F., et al. 2020, ApJS, 247, 5

Qiao, H.-H., Walsh, A. J., Breen, S. L., et al. 2018, ApJS, 239, 15

Qiao, H.-H., Walsh, A. J., Gómez, J. F., et al. 2016a, ApJ, 817, 37

Qiao, H.-H., Walsh, A. J., Green, J. A., et al. 2016b, ApJS, 227, 26

Raga, A. C. & Bohm, K. H. 1986, ApJ, 308, 829

Ramos-Larios, G., Guerrero, M. A., Suárez, O., Miranda, L. F., & Gómez, J. F. 2009, A&A, 501, 1207

Ramos-Larios, G., Guerrero, M. A., Suárez, O., Miranda, L. F., & Gómez, J. F. 2012, A&A, 545, A20

Ramos-Larios, G., Santamaría, E., Guerrero, M. A., et al. 2016, MNRAS, 462, 610

Rayner, J. T., Cushing, M. C., & Vacca, W. D. 2009, ApJS, 185, 289

Reid, M. J. 1976, ApJ, 207, 784

Reid, M. J. & Menten, K. M. 2007, ApJ, 671, 2068

Reid, M. J. & Moran, J. M. 1981a, ARA&A, 19, 231

Reid, M. J. & Moran, J. M. 1981b, , 19, 231

Reid, M. J., Schneps, M. H., Moran, J. M., et al. 1988, ApJ, 330, 809

Reimers, D. 1977, A&A, 57, 395

Reindl, N., Rauch, T., Miller Bertolami, M. M., Todt, H., & Werner, K. 2017, MNRAS, 464, L51

Reindl, N., Rauch, T., Parthasarathy, M., et al. 2014, A&A, 565, A40

Ressler, M. E., Aller, A., Jones, D., et al. 2025, AJ, 169, 236

Reynolds, S. P. 1986, ApJ, 304, 713

Richards, A. M. S., Etoka, S., Gray, M. D., et al. 2012, A&A, 546, A16

Ricker, P. M. & Taam, R. E. 2012, ApJ, 746, 74

Riera, A., García-Lario, P., Manchado, A., Bobrowsky, M., & Estalella, R. 2003, A&A, 401, 1039

Rinehart, S. A., Houck, J. R., Smith, J. D., & Wilson, J. C. 2002, MNRAS, 336, 66

Rizzo, J. R., Gómez, J. F., Miranda, L. F., et al. 2013, A&A, 560, A82

Robitaille, T. P., Whitney, B. A., Indebetouw, R., & Wood, K. 2007, ApJS, 169, 328

Rodríguez-Flores, E. R., Corradi, R. L. M., Mampaso, A., et al. 2014, A&A, 567, A49

Rodríguez-Kamenetzky, A., Pasetto, A., Carrasco-González, C., et al. 2025, ApJ, 978, L31

Ruiz-Escobedo, F. & Peña, M. 2022, MNRAS, 510, 5984

Rynkun, P., Gaigalas, G., & Jönsson, P. 2019, A&A, 623, A155

Sabin, L., Hull, C. L. H., Plambeck, R. L., et al. 2015, MNRAS, 449, 2368

Sabin, L., Zhang, Q., Miranda, L. F., & Gómez-Muñoz, M. A. 2025, MNRAS, 538, 2421

Sabin, L., Zhang, Q., Zijlstra, A. A., et al. 2014, MNRAS, 438, 1794

Sabin, L., Zijlstra, A. A., & Greaves, J. S. 2007, MNRAS, 376, 378

Sabin, L., Zijlstra, A. A., Wareing, C., et al. 2010, PASA, 27, 166

Sahai, R., Morris, M., Sánchez Contreras, C., & Claussen, M. 2007, AJ, 134, 2200

Sahai, R., Morris, M. R., & Villar, G. G. 2011, AJ, 141, 134

Sahai, R. & Trauger, J. T. 1998, AJ, 116, 1357

Sánchez Contreras, C., Báez-Rubio, A., Alcolea, J., Bujarrabal, V., & Martín-Pintado, J. 2017, A&A, 603, A67

Sánchez Contreras, C., Bujarrabal, V., Miranda, L. F., & Fernández-Figueroa, M. J. 2000, A&A, 355, 1103

Sánchez Contreras, C., Cortijo-Ferrero, C., Miranda, L. F., Castro-Carrizo, A., & Bujarrabal, V. 2010, ApJ, 715, 143

Sánchez Contreras, C., Desmurs, J. F., Bujarrabal, V., Alcolea, J., & Colomer, F. 2002, A&A, 385, L1

Sánchez Contreras, C. & Sahai, R. 2001, ApJ, 553, L173

Sánchez Contreras, C. & Sahai, R. 2012, ApJS, 203, 16

Santander-García, M., Rodríguez-Gil, P., Corradi, R. L. M., et al. 2015, Nature, 519, 63

Sault, R. J., Teuben, P. J., & Wright, M. C. H. 1995, in Astronomical Society of the Pacific Conference Series, Vol. 77, Astronomical Data Analysis Software and Systems IV, ed. R. A. Shaw, H. E. Payne, & J. J. E. Hayes, 433

Schaefer, B. E. & Edwards, Z. I. 2015, ApJ, 812, 133

Schmidt, D. R., Woolf, N. J., Zega, T. J., & Ziurys, L. M. 2018, Nature, 564, 378

Schmidt, D. R. & Ziurys, L. M. 2019, ApJL, 881, L38

Schwarz, H. E. 1992, A&A, 264, L1

Seaquist, E. R. & Davis, L. E. 1983, ApJ, 274, 659

Seaquist, E. R., Ivison, R. J., & Hall, P. J. 1995, MNRAS, 276, 867

Seaton, M. J. 1979, MNRAS, 187, 73

Sevenster, M. N. 2002, AJ, 123, 2772

Sevenster, M. N., Chapman, J. M., Habing, H. J., Killeen, N. E. B., & Lindqvist, M. 1997a, A&AS, 122, 79

Sevenster, M. N., Chapman, J. M., Habing, H. J., Killeen, N. E. B., & Lindqvist, M. 1997b, A&A, 124, 509

Sevenster, M. N., van Langevelde, H. J., Moody, R. A., et al. 2001, A&A, 366, 481

Simpson, J. P., Cotera, A. S., Burton, M. G., et al. 2012, MNRAS, 419, 211

Sivagnanam, P., Le Squeren, A. M., Minh, F. T., & Braz, M. A. 1990, A&A, 233, 112

Sjouwerman, L. O., Pihlström, Y. M., Lewis, M. O., et al. 2024, in IAU Symposium, Vol. 380, Cosmic Masers: Proper Motion Toward the Next-Generation Large Projects, ed. T. Hirota, H. Imai, K. Menten, & Y. Pihlström, 292–299

Skrutskie, M. F., Cutri, R. M., Stiening, R., et al. 2006, AJ, 131, 1163

Soker, N. 1996, ApJ, 468, 774

Soker, N. 1997, ApJS, 112, 487

Soker, N. 2024, Galaxies, 12, 29

Soker, N. & Livio, M. 1989, ApJ, 339, 268

Soker, N. & Livio, M. 1994, ApJ, 421, 219

Solf, J. 1994, A&A, 282, 567

Spitzer Science, C. 2009, VizieR Online Data Catalog: GLIMPSE Source Catalog (I + II + 3D) (IPAC 2008), VizieR On-line Data Catalog: II/293. Originally published in: IPAC, Caltech (2008)

Sterling, N. C., Porter, R. L., & Dinerstein, H. L. 2015, ApJS, 218, 25

Storey, P. J., Sochi, T., & Badnell, N. R. 2014, MNRAS, 441, 3028

Storey, P. J. & Zeippen, C. J. 2000, MNRAS, 312, 813

Strom, S. E., Grasdalen, G. L., & Strom, K. M. 1974, ApJ, 191, 111

Strömgren, B. 1939, ApJ, 89, 526

Suárez, O., García-Lario, P., Manchado, A., et al. 2006, A&A, 458, 173

Suárez, O., Gómez, J., Bendjoya, P., et al. 2015, ApJ, 806, 105

Suárez, O., Gómez, J. F., & Miranda, L. F. 2008, ApJ, 689, 430

Suárez, O., Gómez, J. F., Miranda, L. F., et al. 2009, A&A, 505, 217

Suárez, O., Gómez, J. F., & Morata, O. 2007, A&A, 467, 1085

Surendiranath, R. 2002, A&A, 390, 667

Sutherland, R. S. & Dopita, M. A. 2017, ApJS, 229, 34

Szabó, Z. M., Belloche, A., Menten, K. M., et al. 2025, A&A, 694, A329

Szczerba, R., Siódmiak, N., Stasińska, G., & Borkowski, J. 2007, A&A, 469, 799

Szymczak, M. & Gérard, E. 2004, A&A, 423, 209

Sánchez Contreras, C., Alcolea, J., Rodriguez Cardoso, R., et al. 2022, A&A, 665, A88

Tafoya, D., Gómez, Y., Anglada, G., et al. 2007, AJ, 133, 364

Tafoya, D., Gómez, Y., Patel, N. A., et al. 2009, ApJ, 691, 611

Tafoya, D., Imai, H., Gómez, J. F., et al. 2020, ApJ, 890, L14

Tafoya, D., Imai, H., Gomez, Y., et al. 2011, PASJ, 63, 71

Tayal, S. S. 2011, ApJS, 195, 12

Tayal, S. S. & Zatsarinny, O. 2010, ApJS, 188, 32

Taylor, A. R., Pottasch, S. R., & Zhang, C. Y. 1987, A&A, 171, 178

te Lintel Hekkert, P., Caswell, J. L., Habing, H. J., et al. 1991, A&AS, 90, 327

te Lintel Hekkert, P. & Chapman, J. M. 1996, A&A, 119, 459

te Lintel Hekkert, P., Habing, H. J., Caswell, J. L., Norris, R. P., & Haynes, R. F. 1988, A&A, 202, L19

te Lintel Hekkert, P., Versteege-Hensel, H. A., Habing, H. J., & Wiertz, M. 1989, A&AS, 78, 399

Thompson, D. J., Djorgovski, S., & de Carvalho, R. R. 1991, PASP, 103, 487

Toalá, J. A., Ramos-Larios, G., Guerrero, M. A., & Todt, H. 2019, MNRAS, 485, 3360

Turner, B. E. 1979, A&AS, 37, 1

Tylenda, R., Acker, A., & Stenholm, B. 1993, A&AS, 102, 595

Uno, Y., Imai, H., Shinano, K., et al. 2021, MNRAS, 502, 3012

Urquhart, J. S., Busfield, A. L., Hoare, M. G., et al. 2007, A&A, 461, 11

Urquhart, J. S., Busfield, A. L., Hoare, M. G., et al. 2008, A&A, 487, 253

Urquhart, J. S., Hoare, M. G., Purcell, C. R., et al. 2009, A&A, 501, 539

Urquhart, J. S., Morgan, L. K., Figura, C. C., et al. 2011, MNRAS, 418, 1689

Uscanga, L., Gómez, J. F., Miranda, L. F., et al. 2014, MNRAS, 444, 217

Uscanga, L., Gómez, J. F., Suárez, O., & Miranda, L. F. 2012, A&A, 547, A40

Uscanga, L., Gómez, Y., Raga, A. C., et al. 2008, MNRAS, 390, 1127

Uscanga, L., Imai, H., Gómez, J. F., et al. 2023, ApJ, 948, 17

Van de Steene, G. C. & Jacoby, G. H. 2001, A&A, 373, 536

van de Steene, G. C. & Pottasch, S. R. 1995, A&A, 299, 238

Vassiliadis, E. & Wood, P. R. 1993, ApJ, 413, 641

Vassiliadis, E. & Wood, P. R. 1994, ApJS, 92, 125

Vázquez, R., López-Martín, L., Miranda, L. F., et al. 2000, A&A, 357, 1031

Verbena, J. L., Bujarrabal, V., Alcolea, J., Gómez-Garrido, M., & Castro-Carrizo, A. 2019, A&A, 624, A107

Verdes-Montenegro, L., Torrelles, J. M., Rodriguez, L. F., et al. 1989, ApJ, 346, 193

Vlemmings, W. H. T., Amiri, N., van Langevelde, H. J., & Tafoya, D. 2014, A&A, 569, A92

Vlemmings, W. H. T., Diamond, P. J., & Imai, H. 2006, Nature, 440, 58

Vyssotsky, A. N., Miller, W. J., & Walther, M. E. 1945, PASP, 57, 314

Walsh, A. J., Breen, S. L., Bains, I., & Vlemmings, W. H. T. 2009, MNRAS, 394, L70

Walsh, A. J., Breen, S. L., Britton, T., et al. 2011, MNRAS, 416, 1764

Walsh, A. J., Purcell, C. R., Longmore, S. N., et al. 2014, MNRAS, 442, 2240

Wang, Y., Beuther, H., Rugel, M. R., et al. 2020, A&A, 634, A83

Wang, Y., Bihr, S., Rugel, M., et al. 2018, A&A, 619, A124

Wardle, M. & Yusef-Zadeh, F. 2002, Science, 296, 2350

Weaver, K. A., Meléndez, M., Mushotzky, R. F., et al. 2010, ApJ, 716, 1151

Weidmann, W. A. & Gamen, R. 2011, A&A, 526, A6

Weidmann, W. A., Mari, M. B., Schmidt, E. O., et al. 2020, A&A, 640, A10

Weidmann, W. A., Méndez, R. H., & Gamen, R. 2015, A&A, 579, A86

Weiler, K. W. & Sramek, R. A. 1988, ARA&A, 26, 295

Wesson, R., Jones, D., García-Rojas, J., Boffin, H. M. J., & Corradi, R. L. M. 2018, MNRAS, 480, 4589

Wesson, R., Liu, X. W., & Barlow, M. J. 2003, MNRAS, 340, 253

Wesson, R., Liu, X. W., & Barlow, M. J. 2005, MNRAS, 362, 424

White, R. L., Becker, R. H., & Helfand, D. J. 2005, AJ, 130, 586

Whitelock, P. A. & Menzies, J. W. 1986, MNRAS, 223, 497

Wilson, O. C. 1950, ApJ, 111, 279

Winnberg, A., Terzides, C., & Matthews, H. E. 1981, AJ, 86, 410

Wong, K. T., Menten, K. M., Kamiński, T., et al. 2018, A&A, 612, A48

Wood, D. O. S. & Churchwell, E. 1989, ApJ, 340, 265

Xie, J.-Y., Nakashima, J.-i., & Zhang, Y. 2025, ApJ, 978, 114

Xu, Y., Reid, M. J., Menten, K. M., & Zheng, X. W. 2006, ApJS, 166, 526

Yang, A. Y., Dzib, S. A., Urquhart, J. S., et al. 2023, A&A, 680, A92

Yoon, D.-H., Cho, S.-H., Kim, J., Yun, Y. j., & Park, Y.-S. 2014, ApJS, 211, 15

Yung, B. H. K., Nakashima, J.-i., & Henkel, C. 2014, ApJ, 794, 81

Yung, B. H. K., Nakashima, J.-i., Hsia, C.-H., & Imai, H. 2017, MNRAS, 465, 4482

Yung, B. H. K., Nakashima, J.-i., Imai, H., et al. 2011, ApJ, 741, 94

Yung, B. H. K., Nakashima, J.-i., Imai, H., et al. 2013, ApJ, 769, 20

Zhang, C. Y. & Kwok, S. 1991, A&A, 250, 179

Zhang, Y. & Liu, X.-W. 2005, ApJL, 631, L61

Zijlstra, A. A., Chapman, J. M., te Lintel Hekkert, P., et al. 2001, MNRAS, 322, 280

Zijlstra, A. A., Gaylard, M. J., te Lintel Hekkert, P., et al. 1991, A&A, 243, L9

Zijlstra, A. A., te Lintel Hekkert, P., Pottasch, S. R., et al. 1989, A&A, 217, 157

Zoonematkermani, S., Helfand, D. J., Becker, R. H., White, R. L., & Perley, R. A. 1990, ApJS, 74, 181

Zou, Y., Frank, A., Chen, Z., et al. 2020, MNRAS, 497, 2855